

Development and Validation of Models for Predicting Leakage from Degraded Tube-to-Tubesheet Joints During Severe Accidents

AVAILABILITY OF REFERENCE MATERIALS IN NRC PUBLICATIONS

NRC Reference Material

As of November 1999, you may electronically access NUREG-series publications and other NRC records at NRC's Library at www.nrc.gov/reading-rm.html. Publicly released records include, to name a few, NUREG-series publications; *Federal Register* notices; applicant, licensee, and vendor documents and correspondence; NRC correspondence and internal memoranda; bulletins and information notices; inspection and investigative reports; licensee event reports; and Commission papers and their attachments.

NRC publications in the NUREG series, NRC regulations, and Title 10, "Energy," in the *Code of Federal Regulations* may also be purchased from one of these two sources.

1. The Superintendent of Documents

U.S. Government Publishing Office
Washington, DC 20402-0001
Internet: bookstore.gpo.gov
Telephone: (202) 512-1800
Fax: (202) 512-2104

2. The National Technical Information Service

5301 Shawnee Road
Alexandria, VA 22312-0002
www.ntis.gov
1-800-553-6847 or, locally, (703) 605-6000

A single copy of each NRC draft report for comment is available free, to the extent of supply, upon written request as follows:

Address: **U.S. Nuclear Regulatory Commission**
Office of Administration
Multimedia, Graphics, and Storage &
Distribution Branch
Washington, DC 20555-0001
E-mail: distribution.resource@nrc.gov
Facsimile: (301) 415-2289

Some publications in the NUREG series that are posted at NRC's Web site address www.nrc.gov/reading-rm/doc-collections/nuregs are updated periodically and may differ from the last printed version. Although references to material found on a Web site bear the date the material was accessed, the material available on the date cited may subsequently be removed from the site.

Non-NRC Reference Material

Documents available from public and special technical libraries include all open literature items, such as books, journal articles, transactions, *Federal Register* notices, Federal and State legislation, and congressional reports. Such documents as theses, dissertations, foreign reports and translations, and non-NRC conference proceedings may be purchased from their sponsoring organization.

Copies of industry codes and standards used in a substantive manner in the NRC regulatory process are maintained at—

The NRC Technical Library

Two White Flint North
11545 Rockville Pike
Rockville, MD 20852-2738

These standards are available in the library for reference use by the public. Codes and standards are usually copyrighted and may be purchased from the originating organization or, if they are American National Standards, from—

American National Standards Institute

11 West 42nd Street
New York, NY 10036-8002
www.ansi.org
(212) 642-4900

Legally binding regulatory requirements are stated only in laws; NRC regulations; licenses, including technical specifications; or orders, not in NUREG-series publications. The views expressed in contractor prepared publications in this series are not necessarily those of the NRC.

The NUREG series comprises (1) technical and administrative reports and books prepared by the staff (NUREG-XXXX) or agency contractors (NUREG/CR-XXXX), (2) proceedings of conferences (NUREG/CP-XXXX), (3) reports resulting from international agreements (NUREG/IA-XXXX), (4) brochures (NUREG/BR-XXXX), and (5) compilations of legal decisions and orders of the Commission and Atomic and Safety Licensing Boards and of Directors' decisions under Section 2.206 of NRC's regulations (NUREG-0750).

DISCLAIMER: This report was prepared as an account of work sponsored by an agency of the U.S. Government. Neither the U.S. Government nor any agency thereof, nor any employee, makes any warranty, expressed or implied, or assumes any legal liability or responsibility for any third party's use, or the results of such use, of any information, apparatus, product, or process disclosed in this publication, or represents that its use by such third party would not infringe privately owned rights.

Development and Validation of Models for Predicting Leakage from Degraded Tube-to-Tubesheet Joints During Severe Accidents

Manuscript Completed: July 2010
Date Published: July 2020

Prepared by:
S. Majumdar
K. Kasza
C. Bahn
W.J. Shack

Argonne National Laboratory
Argonne, IL 60439

Patrick Purtscher, NRC Project Manager

PROPRIETARY INFORMATION NOTICE

This report does not contain information that is proprietary to Westinghouse Electric Company. The U.S. Nuclear Regulatory Commission (NRC) has also prepared a proprietary version of this report for internal distribution as a Technical Letter Report (TLR).

In order to conform to the Commission's regulations concerning the protection of proprietary information so submitted to the NRC, as set forth in Title 10 Section 2.390, of the *Code of Federal Regulations* (10 CFR 2.390), the proprietary information in the proprietary version of this document is contained within brackets and, where the proprietary information has been deleted in the non-proprietary version, only the brackets remain (the information within the brackets in the proprietary version having been deleted). The justification for claiming the information as proprietary is indicated in both versions by means of lower case letters (a) through (f), located as a superscript immediately following the brackets enclosing each bracketed item of proprietary information, or in the margin opposite such information. These lower case letters refer to the types of information Westinghouse customarily holds in confidence, as identified in Sections (4)(ii)(a) through (4)(ii)(f) of the affidavit accompanying the transmittal of these documents pursuant to 10 CFR 2.390(b)(1)

ABSTRACT

This report documents the development and validation of analytical models to predict steam generator (SG) tube leakage that can be expected from cracks within the tube-to-tubesheet junction at high temperature. It is recognized that the problem of predicting the leakage from cracked tubes within the tube sheet (TS) during severe accidents is too complex to be solved by either purely analytical or purely experimental means. In this study Argonne National Laboratory (ANL) adopted a combined analytical-experimental approach. The experiments were designed to simulate several key aspects of the tubesheet behavior during a postulated station blackout severe accident. The resultant predicted leak rates were determined through these efforts.

Pressure and leak rate tests were conducted at high temperatures on 12 tube-to-collar junction specimens with independent pressurization of the tube and the leakage path (crevice). A finite element model of the specimen was used to calculate the variation of contact pressure and tube-to-tubesheet gap over time. A leak rate model was developed based on plane Couette-Poiseuille flow along the interface between two rough contacting surfaces. The model parameters were determined from the leak rate tests.

A finite element model was developed for a Westinghouse Model 51 SG tube-to-tubesheet interface, including the divider plate, lower head and a short segment of the SG shell. The model was used to analyze first, the spatial variation of the temperature with time, and second, the variations of contact pressure and gap along the tube-to-tubesheet interface as functions of time during the postulated station blackout severe accident. The leak rate model was used to predict the leak rates during the severe accident.

Results in this report indicate that leakage could occur through the tube-to-tubesheet joints in station blackout accident conditions, and there are significant variations in the leak rates calculated for different paths. In addition, results show that the leak rate remains low for three hours, after which the rate is predicted to increase. In the absence of tests with realistic interface and boundary conditions, the present results should be considered as best estimates.

FOREWORD

There is concern with a proposal to limit inspection for steam generator (SG) defects inside the thick tubesheet region. It has been argued that the joint between the sheet and the tubes is so tight, that even if cracks grow completely through the tubes, the primary water cannot leak to the secondary side of a nuclear power plant. The staff has expressed concerns that an initially tight seal may not remain so over time. To investigate this, a combination of experimental validation and model development was performed, by ANL and the U.S. Nuclear Regulatory Commission, respectively, to estimate the magnitude of this potential leakage.

Tube-to-collar test specimens were designed to simulate the contact pressures generated in a real SG tube-to-tubesheet junction due to hydraulic expansion and thermal expansion mismatch between the tube and tubesheet. The tubes and the leakage paths (crevices) in the test specimens were independently pressurized. The tests showed a steady decrease of leak rate with increasing temperature from room temperature, reduced to almost zero at $\sim 500^{\circ}\text{C}$. In tests where the crevice pressure was held constant and the temperature of the specimen was increased continuously, leakage resumed at temperatures between $670\text{-}690^{\circ}\text{C}$ and increased at an increasing rate with temperature to high values ($>5,000$ mg/min) until the test was stopped. However, if the crevice was kept mostly depressurized and a crevice pressure applied only intermittently to measure the leak rates, no such large leakage was observed. Thus, it was concluded that large leakage is not possible unless the crevice is pressurized for a sufficiently long time to relax the contact pressure and open a gap at the tube-to-collar interface by deforming the collar by creep.

Results showed that under a postulated station blackout severe accident, leakage flow could occur. There was significant variation in the leak rates calculated for different paths. The results showed that leak rate remains low for three hours, then the leak rate is predicted to increase. In the absence of tests with realistic interface and boundary conditions, the present results should be considered as best estimates to approximate potential field conditions.

TABLE OF CONTENTS

ABSTRACT	iii
FOREWORD.....	v
LIST OF FIGURES.....	xi
LIST OF TABLES	xxv
EXECUTIVE SUMMARY	xxix
ACKNOWLEDGMENTS	xxxi
ACRONYMS AND ABBREVIATIONS	xxxiii
SYMBOLS	xxxv
1 INTRODUCTION.....	1
2 BACKGROUND.....	3
3 PROBLEM DESCRIPTION AND APPROACH.....	5
4 MATERIALS PROPERTIES DATA.....	9
4.1 Physical Properties.....	9
4.1.1 Thermal Expansion Coefficients	9
4.2 Mechanical Properties.....	13
4.2.1 Alloy 600	13
4.2.2 SA508 Steel	23
5 LEAK RATE MODELS.....	29
5.1 Leak Rate Model.....	29
5.1.1 Flow in the Annulus between Two Rigid Cylinders.....	29
5.1.2 Flow in the Annulus between Tube and Collar (or Tubesheet)	31
5.2 Contact Mechanics.....	31
5.3 Validation of Leak Rate Model Using Westinghouse Data	32
5.3.1 Pullout Tests.....	33
5.3.2 Contact Pressure.....	36
5.3.3 Conclusions.....	40
6 DESIGN OF TUBE-TO-COLLAR JUNCTION TEST SPECIMEN	41
6.1 Development of Elastic Properties of Equivalent Tubesheet Material.....	41
6.2 Tubesheet and Collar Stiffness Analyses	45
6.2.1 Tube-to-Tubesheet Junction	45
6.2.2 Tube-to-Collar Junction	46
6.3 Selection of Collar Dimensions	46
6.4 Specimen Design	47
6.4.1 Selection of Hydraulic Expansion Pressure.....	47
6.5 Test Matrix.....	53

7	LEAK RATE TESTS.....	55
7.1	Description of Test Facility.....	55
7.2	Leak Rate Specimen Geometrical Characteristics.....	56
7.3	Screening Tests.....	58
7.4	Initial Test Results.....	60
7.4.1	Specimen 10-7/8 (EX-82-1).....	60
7.4.2	Specimen 9-7/8 (NX 8520).....	63
7.4.3	Specimen 8-7/8 (EX-82-1).....	68
7.5	Results with Revised Protocol.....	68
7.5.1	Specimen 11-7/8 (NX 8520).....	68
7.5.2	Specimen 04-7/8 (NX 8520).....	71
7.5.3	Specimen 05-7/8 (EX-82-1).....	74
7.5.4	Specimen 03-7/8 (NX 8520).....	77
7.5.5	Specimen 02-3/4 (NX 8524).....	79
7.5.6	Specimen 07-7/8 (NX 8520).....	82
7.6	Special Tests Designed to Study Mechanisms.....	86
7.6.1	Trends Observed in Leakage Tests and Revised Protocol.....	86
7.6.2	Specimen 01-3/4 (NX 8524).....	89
7.6.3	Specimen 01-7/8 (NX-8520).....	93
7.6.4	Specimen 03-3/4 (NX 8524).....	97
7.6.5	Test 06-7/8 (EX-82-1).....	101
7.6.6	Test 02-7/8 (EX-82-1).....	105
8	ANALYSIS OF TESTS.....	111
8.1	Contact Pressure and Gap Analysis.....	111
8.1.1	Dimensional Model for the Tube-to-Collar Junction.....	111
8.1.2	Transition from Closed to Open Contact.....	116
8.2	Leakage Analysis of Tests.....	117
8.2.1	Ring Assembly Model.....	118
8.2.2	Initial Room Temperature Tests.....	119
8.2.3	Leakage Analysis of Tests with Creep.....	120
8.2.4	Crevice Gas Pressure Distribution.....	122
8.2.5	Detailed Analysis Results of a Representative Sample of Tests.....	123
9	LEAKAGE PREDICTIONS FOR TUBE-TO-TUBESHEET JUNCTIONS DESIGN DURING BASIS ACCIDENTS.....	133
9.1	Assessment of Leak Model for Design Basis Accidents.....	133
9.1.1	Comparison to Room Temperature Tests with Water.....	133
9.2	Contact Pressure Analysis.....	144
9.2.1	Effective Plastic Properties of Tubesheet.....	144
9.2.2	FEA Results.....	149
9.3	Leak Rate Predictions for Normal Operation and Design Basis Accidents.....	154
9.3.1	Simplified Leak Rate Model.....	157
9.3.2	Approximate Bounds to Leak Rates.....	158
10	LEAKAGE PREDICTIONS FOR TUBE-TO-TUBESHEET JUNCTIONS SEVERE DURING ACCIDENTS.....	161
10.1	Thermal Analysis.....	161
10.1.1	Thermal Hydraulic Input Data from CFD and RELAP 5 Analysis.....	163
10.1.2	Development of Thermal Properties for Equivalent Tubesheet Material.....	165

10.1.3	Thermal Analysis of Tube-to-Tubesheet Junction	169
10.2	Contact Pressure Analysis	172
10.2.1	Development of Creep Properties of Tubesheet.....	172
10.2.2	Results from FEA.....	175
10.3	Leak Rate Prediction for Severe Accident	186
10.3.1	Leak Rate Model	186
10.3.2	Predicted Leak Rates.....	187
10.4	Tube Rupture/Pullout During Severe Accidents.....	190
10.4.1	Free Span SG Tube Rupture.....	190
10.4.2	Tube Pullout	192
11	CONCLUSIONS	195
12	REFERENCES	197

LIST OF FIGURES

Figure 3-1	Typical TS Geometry.....	5
Figure 3-2	Cut Away View of Model 51 SG.....	6
Figure 3-3	Typical Deformation Profile of the SGT after Tube Expansion	7
Figure 3-4	TS and Divider Plate, Showing Displaced Shape of TS During MSLB and Severe Accidents.....	7
Figure 4-1	Thermal Expansion Strains Measured by ANTER Corp. and PMIC Corp.	9
Figure 4-2	Kink in the Thermal Expansion Coefficient Data (blue) in Air Measured by PMIC Corp and a Smooth Fitted Curve (red).....	10
Figure 4-3	Coefficients of Thermal Expansion as Calculated from the Expansion Data	10
Figure 4-4	Comparison of Mean Thermal Expansion Coefficients of (a) A508 and (b) Alloy 600	11
Figure 4-5	Comparison of Thermal Expansion Coefficients of Alloy 600 and A508 Measured by ANTER Corp. with those Reported by Westinghouse	12
Figure 4-6	Comparison of Thermal Expansion Coefficients of Alloy 600 and A508.....	12
Figure 4-7	Variation of Contact Pressure with Temperature Calculated by Using Thermal Expansion Coefficient Data.....	13
Figure 4-8	Room Temperature Stress-strain Curves of (a) 22.2 mm (0.875) Diameter Dogbone Specimens.....	15
Figure 4-9	Room Temperature Stress-strain Curves of (a) 22.2 mm (0.875 in.) Diameter and (b) 19.05 mm (0.75 in.) Diameter Alloy 600 Tube Sheet Specimens	15
Figure 4-10	Creep Strain vs. Time Plots for Tests Conducted at 550°C on Alloy 600 Heats (a) EX-82-1, (b) NX 8520L and (c) NX 8524.....	16
Figure 4-11	Creep Strain vs. Time Plots for Tests Conducted at 650°C on Alloy 600 Heats (a) EX-82-1, (b) NX 8520L an (c) NX 8524.....	17
Figure 4-12	Creep Strain vs. Time Plots for Tests Conducted at 732°C and 93 MPa (13.5 ksi) on Alloy 600 Heats EX-82-1, NX 8520L and NX 8524.....	18

Figure 4-13	Larson Miller Plots for the Time to Rupture Data on Alloy 600 Conducted by INL and ANL	18
Figure 4-14	Measured and Fitted Creep Strain vs. Time Plots for Tests Conducted on Heat NX 8520 Alloy 60021	21
Figure 4-15	Measured and Fitted Creep Strain vs. Time Plots for Tests Conducted on Heat NX 8520 Alloy 600	21
Figure 4-16	Measured and Fitted Creep Strain vs. Time Plots for Tests Conducted on Heat EX-82-1 Alloy 600	22
Figure 4-17	Predicted vs. Observed Steady State Creep Rates for Alloy 600 Tubes	22
Figure 4-18	Histograms of Room Temperature (a) Yield and (b) Ultimate Tensile Strengths of SA508	23
Figure 4-19	Tensile Stress Strain Curves of A508 Specimens with (a)-(c) 3 hour PWHT and (d) 4 hour PWHT at Room Temperature.....	24
Figure 4-20	Creep Strain vs. Time Plot for a Test Conducted at 550°C on A508	25
Figure 4-21	Creep Strain vs. Time Plots for Tests Conducted on A508 at (a) 650°C and (b) 750°C.....	25
Figure 4-22	Larson Miller Plot for the Time to Rupture Data on A508 Conducted by INL and ANL.....	26
Figure 4-23	Measured and Fitted Creep Strain vs. Time Plots for Tests Conducted on A508 Steel.....	27
Figure 4-24	Predicted vs. Observed Steady State Creep Rates for A508	27
Figure 5-1	Schematic Illustration of Contact Between a Rough Surface and a Smooth Surface	31
Figure 5-2	Representation of Flow Across Asperities Where the Parameter γ Characterizes the Shape and Orientation of the Asperities	32
Figure 5-3	Variation of the Thermal Expansion Coefficients of [] ^{a,c,e} , A508 Forging and Alloy 600 Tube with Temperature	33
Figure 5-4	Effect of Friction Factor and Tube Expansion Pressure on the Pullout Load vs. Displacement Plot	34
Figure 5-5	Comparison of Calculated vs. Observed Initial Slip Loads for the Pullout Tests at 600°F	35
Figure 5-6	Variation of the Calculated Contact Pressure Along the Specimen Length at Room Temperature and 600°F in the Absence of Internal	

	Pressure [The dashed curves are for an expansion pressure of 221 MPa (314 MPa (2 ksi)); the solid curves are for an expansion pressure of 228 MPa (33 ksi)].....	36
Figure 5-7	Variation of the Contact Pressure at Room Temperature and 600°F with Internal Pressure.....	37
Figure 5-8	Non-dimensional Pressure Drop Profiles for (a) Incompressible Flows with Initial Pressures of 1900 and 2650 psi; (b) Incompressible and Compressible Flows with an Initial Pressure of 1900 psi; and (c) Two-phase Flows at 600°F with Initial Pressures of 1900 and 2650 psi	38
Figure 6-1	Plan Views of a Quarter of a Tubesheet Unit Cell for Square Arrays with (a) 32.5 mm (1.28 in.) Pitch and 22.6 mm (0.891 in.) Tube Hole Diameter for 22.2 mm (0.875 in.) Diameter SG Tubes and (b) 27.2 mm (1.07 in.) Pitch and 19.4 mm (0.765 in.) Tube Hole Diameter for 19.1 mm (0.75 in.) Diameter SG Tubes	42
Figure 6-2	Typical Deformed and Undeformed Shapes of a Unit Cell Corresponding to a (a) Normal Strain and (b) a Shear Strain.....	42
Figure 6-3	Elastic Constants of SA-508 and Effective In-Plane Isotropic Elastic Constants for a TS with Square Array of Holes with (a) 19.4 mm (0.765 in.) Diameter Holes Set at a Pitch of 27.2 mm (1.07 in.) and (b) 22.6 mm (0.891 in.) Diameter Holes Set at a Pitch of 32.8 mm (1.28 in.).....	44
Figure 6-4	Young's Modulus and Shear Modulus of SA508 (red) and Effective Transverse Elastic Constants and Effective In-Plane Shear Moduli (blue) for a TS with Square Array of Holes with (a) 19.4 mm (0.765 in.) Diameter Holes Set at a Pitch of 27.2 mm (1.07 in.) and (b) 22.6 mm (0.891 in.) Diameter Holes Set at a Pitch of 32.8 mm (1.28 in.).....	44
Figure 6-5	Axisymmetrical Model of a Tubesheet with a Single Hole	45
Figure 6-6	Axisymmetric Model of a Collar with Hole	46
Figure 6-7	Variation of Radial Displacement at the Hole Surface of a Collar and a Tubesheet of Various Radii at 172 MPa (25 Ksi) Applied at the Surface of the Hole with Diameter (a) 19.4 mm (0.765 in.) and (b) 22.6 mm (0.891 in.)	47
Figure 6-8	Tube-to-Collar Specimen Design for (a) 19.1 mm (0.75 in.) and (b) 22.2 mm (0.875 in.) Diameter Tubes	48
Figure 6-9	Variation of Tube-to-Collar Contact Pressure with Temperature for Various Hydraulic Expansion Pressures and Zero and 17.2 MPa (2.5 ksi) Differential Pressures Acting on (a) 19.1 mm (0.75 in.) Diameter (Heat NX8524) and (b) 22.2 mm (0.875 in.) Diameter (Heat EX-82-1)	

	Tubes	49
Figure 6-10	Variation of Contact Pressure with Expansion Pressure in (a) 19.1 mm (0.75 in.) Diameter and (b) 22.2 mm (0.875 in.) Diameter Tube-to-Collar Joints at Room Temperature at Internal Pressures of 0 and 17.2 MPa (2.5 ksi).....	51
Figure 6-11	Variation of Tube-to-Collar Contact Pressure with Temperature for Zero and 17.2 MPa (2.5 ksi) Differential Pressures Acting on (a) 19.1 mm (0.75 in.) Diameter Tubes (Heat NX8524) Expanded with 214 MPa (31 ksi) Hydraulic Pressure and (b) 22.2 mm (0.875 in.) Diameter (Heat EX-82-1) Tubes Expanded with 234 MPa (34 ksi) Hydraulic Pressure	52
Figure 6-12	Variation of Tube-to-Collar Contact Pressure with Temperature for Zero and 17.2 MPa (2.5 ksi) Differential Pressures Acting on 22.2 mm (0.875 in.) Diameter Tubes (Heat NX8520) Expanded with 234 MPa (34 ksi) Hydraulic Pressure	53
Figure 7-1	Calculated Variation of Contact Pressure with Tube Internal Pressure for Leak Rate Specimens with (a) 22 mm (0.875 in.) Diameter and (b) 19 mm (0.75 in.) Diameter Tubes	57
Figure 7-2	Close up Views of Leak Specimen Seal Weld and Leak Path Exit Gap of Specimen 10-7/8.....	60
Figure 7-3	Leakage Data for Room Temperature Tests on Specimen 10-7/8	61
Figure 7-4	Leak Rate History for Specimen 10-7/8 during Heating from Room Temperature to 300°C (572°F)	62
Figure 7-5	Leak Rate History of Specimen 10-7/8 during Hold at 600°C (1112°F)....	63
Figure 7-6	Leak Rate History of Specimen 09-7/8 during Heating to 700°C (1300°F).....	67
Figure 7-7	Specimen 11-7/8 in the As-received State.....	69
Figure 7-8	Leak Rate and Pressure History of Specimen 11-7/8 during Stages 2, 3 and 4 testing.....	70
Figure 7-9	Specimen 11-7/8 in the Post-test Condition.....	70
Figure 7-10	Specimen 04-7/8 in the As-received Condition	72
Figure 7-11	Pressure and Leak Rate History of Specimen 04-7/8 at High Temperature during Stages 2-4 Loading	73
Figure 7-12	Post-test Picture of Specimen 04-7/8	73

Figure 7-13	Specimen 05-7/8 in the As-received Condition	74
Figure 7-14	Pressure, Leak Rate and Temperature History of Specimen 05-7/8 at High Temperature during Stages 2-4 Loading	75
Figure 7-15	Post-test Picture of Specimen 05-7/8	76
Figure 7-16	Specimen 03-7/8 in the As-received Condition	77
Figure 7-17	Pressure and Leak Rate History of Specimen 03-7/8 at High Temperature during Stages 2-4 Loading	78
Figure 7-18	Post-test Picture of Specimen 03-7/8	78
Figure 7-19	Specimen 02-3/4 in the As-received Condition	80
Figure 7-20	Pressure, Leak Rate and Temperature History of Specimen 02-3/4 at High Temperature during Stage 2	81
Figure 7-21	Post-Test Picture of Specimen 02-3/4	81
Figure 7-22	Specimen 07-7/8 in the As-received Condition	83
Figure 7-23	Modified Stage 2 (Five Stages) Pressure-temperature Leak Rate History of Specimen 07-7/8	84
Figure 7-24	Specimen 07-7/8 in the Post-test Condition	86
Figure 7-25	Variation of the Temperature at Onset of Large Leakage with Leak Path Length of the Specimens with 22 Mm (0.875 In.) Diameter Tubes	87
Figure 7-26	Variation of the Temperature at Onset of Large Leakage with Initial Leak Rate at Room Temperature of the Specimens with 22 mm (0.875 in.) Diameter Tubes	87
Figure 7-27	Specimen 01-3/4 in the As-received Condition	89
Figure 7-28	Stage 4 Pressure-temperature-leak Rate History of Specimen 01-3/4	92
Figure 7-29	Specimen 01-3/4 in the Post-test Condition	92
Figure 7-30	Specimen 01-7/8 in the As-received Condition	94
Figure 7-31	Stage 6 Pressure-Temperature-Leak Rate Data for Specimen 01-7/8	96
Figure 7-32	Specimen 01-7/8 in the Post-test Condition	97
Figure 7-33	Specimen 03-3/4 in the Pre-test Condition	98

Figure 7-34	Pressure, Leak Rate and Temperature History of Specimen 03-3/4 at High Temperature During Stage 2.....	99
Figure 7-35	Specimen 03-3/4 in the Post-test Condition.....	100
Figure 7-36	SEM Micrographs for the Cross-sectional View of the Inside Collar Surface Showing Metal Part (upper) and Mounting Polymer (lower) Region Divided by Oxide Layer with (A) Secondary Electron Image and (B) Back-Scattered Electron Image (3,000X magnification); EDS Analysis for (C) Spot "1" and (d) Spot "2" in (a).....	101
Figure 7-37	Specimen 06-7/8 in the Pre-test Condition	102
Figure 7-38	Thermocouples Attached to Specimen 06-7/8 Located Near the Jet Exiting the Leakage Path.....	102
Figure 7-39	Stage 2 Elevated Temperature Testing of Specimen 06-7/8.....	104
Figure 7-40	Specimen 06-7/8 in the Post-test Condition.....	105
Figure 7-41	Specimen 02-7/8 in the Pre-test Condition	106
Figure 7-42	Variation of (a) Specimen Pressure and Temperature and (b) Leak Rate and Specimen Temperature with Time for Test 02-7/8 during Stage 2.....	107
Figure 7-43	Variation of (a) Specimen Pressure and Temperature and (b) Leak Rate and Specimen Temperature with Time for Test 02-7/8 during Stage 3.....	108
Figure 7-44	Expanded View of Variation of Specimen, Collar and Gas Temperatures and Leak Rate for Test 02-7/8 during Stage 3	109
Figure 8-1	Variation of Contact Pressure with Time -1D Model vs. FEA	115
Figure 8-2	Variation of Gap Opening with Time -1D Model vs. FEA.....	115
Figure 8-3	Variations of Contact Pressure and Gap Opening with Temperature for Test 05-7/8	116
Figure 8-4	Effective Gap Width Used When the Contact Changes between Closed and Open	117
Figure 8-5	Specimen Divided into a Number of Composite Rings.....	118
Figure 8-6	Flow Rates as a Function of Fluid Driving Pressure for Specimens 06-7/8 and 08-7/8	120
Figure 8-7	Time vs. Temperature Plot for a Tube with an Internal Pressure of 17.2 MPa (2.5 ksi)	121

Figure 8-8	(a) Calculated Variation of Contact Pressure with Time for Various Values of Crevice Pressure and (b) the Data Replotted as Variation of Contact Pressure with Crevice Pressure at Various Times	122
Figure 8-9	Variation of Gap Opening with Crevice Pressure at Various Times.....	122
Figure 8-10	Axial Variation of Normalized Crevice Gas Pressure in Specimen 11-7/8 During Stage 1 and Stage 5 Testing.	123
Figure 8-11	Variation of Contact Pressure with Temperature for Test 11-7/8 Calculated by (a) FEA and (b) 1-D Model.....	124
Figure 8-12	Comparison of Test Leak Rates at Room Temperature and 710°C with Those Predicted by FEA and the 1-D Model for Specimen 11-7/8.....	125
Figure 8-13	Comparison of Test Leak Rates (Specimen 11-7/8, Stage 5) at Room Temperature with those Predicted by the 1-D Model at Tube Pressures of (a) 14 MPa (2 ksi) and (b) 10.3 MPa (1.5 ksi).....	125
Figure 8-14	Computed Relaxation of Contact Pressure of Specimen 01-3/4 During the First 4 Hour Hold at 670°C	126
Figure 8-15	Comparison of Test Leak Rates (symbols) at Room Temperature during Stage 3 Testing of 01-3/4 vs. Crevice Pressure with those Predicted by (a) FEA and (b) 1D Model	127
Figure 8-16	Comparison of Test Leak Rates (symbols) at Room Temperature during Stage 5 Testing of 01-3/4 vs. Crevice Pressure with those Predicted by (a) FEA and (b) 1D Model	127
Figure 8-17	Comparison of Test Leak Rates at Room Temperature and 670°C vs. Crevice Pressure with those Predicted by FEA and the 1-D Model for Specimen 01-3/4	128
Figure 8-18	Original PMIC Data for Thermal Expansion Coefficient of A508 (red filled circles), B&W Fit to the Data (deep blue filled triangle), ANL Fit to the Data (light blue filled diamond), and PMIC Data for Alloy 600 (green filled squares).....	129
Figure 8-19	Calculated Contact Pressures using B&W and ANL Ffits to the PMIC Expansion Coefficient Data for A508	130
Figure 8-20	Comparison of the Measured Leak Rates with Those Predicted by the 1-D Model using the B&W and ANL Fits to the PMIC Thermal Expansion Coefficient Data for A508	130
Figure 8-21	Predicted vs. Observed Leak Rate for Test 02-7/8	131

Figure 9-1	Comparison of Observed and Predicted Leak Rates for Tests with Water at Room Temperature (The dashed lines indicate a factor of 1.5).....	134
Figure 9-2	Leak Rate Error Factors for Tests with Water at Room Temperature....	134
Figure 9-3	Dependence of Leak Rate of Water at Room Temperature and an Internal Pressure $p_i = 13.2$ MPa with Initial Contact Pressure.....	135
Figure 9-4	Dependence of Normalized Flow Rate on Temperature for Two Initial Contact Pressures.....	136
Figure 9-5	Comparison of Measured Leak Rates at 70°F (21.1°C) and 600°F (315.6°C) at Different Internal Pressures with the Corresponding Predicted Values	136
Figure 9-6	Comparison of the Predicted Measured Pressure Distributions for Test NOP 1	138
Figure 9-7	Comparison of the Predicted Measured Pressure Distributions for Test NOP 2	138
Figure 9-8	Comparison of the Predicted Measured Pressure Distributions for Test NOP 3	139
Figure 9-9	Comparison of the Predicted Measured Pressure Distributions for Test SLB 1	139
Figure 9-10	Comparison of the Predicted Measured Pressure Distributions for Test SLB 2	140
Figure 9-11	Comparison of the Predicted Measured Pressure Distributions for Test SLB 3	140
Figure 9-12	Comparison of the Predicted Measured Pressure Distributions for Test SLB 4	141
Figure 9-13	Comparison of the Predicted Measured Pressure Distributions for Test SLB 5	141
Figure 9-14	Comparison of the Predicted Measured Pressure Distributions for Test SLB 6	142
Figure 9-15	Leak Rate Error Factors for Tests with Two Phase Flows At 600°F	143
Figure 9-16	Change in Leak Rate as the Contact Pressure is Changed with the Temperature and Fluid Driving Pressure Fixed at Nominal Values	143
Figure 9-17	Average Stress-Strain Curves of SA508 Steel Used for Deriving Equivalent Stress-Strain Curves of the Tubesheet	146

Figure 9-18	Variation of Yield Stress of SA508 and Effective Tubesheet Material with Temperature for Hole Diameter of (a) 19.4 Mm (0.765 In.) and (b)22.6 Mm (0.891 In.).....	147
Figure 9-19	Calculated Equivalent Stress-Strain Curves at Various Temperatures of the Tubesheet with 19.4 Mm (0.765 In.) Holes in the (a) in-Plane and in the (b) Transverse Directions.....	147
Figure 9-20	Calculated Equivalent Stress-Strain Curves at Various Temperatures of the Tubesheet with 22.6 Mm (0.891 In.) Holes in the (a) in-Plane and in the (b) Transverse Directions.....	148
Figure 9-21	Calculated Shear Stress-Plastic Strain Curves at Various Temperatures of the Tubesheet with 19.4 Mm (0.765 In.) Holes for (a) in-Plane Shear and (b) Transverse Shear Loading.....	149
Figure 9-22	Calculated Shear Stress-Plastic Strain Curves at Various Temperatures of the Tubesheet with 22.6 Mm (0.891 In.) Holes for (a) in-Plane Shear and (b) Transverse Shear Loading.....	149
Figure 9-23	Comparison of Distributions of Contact Pressure at the Tube-to-Tubesheet Interface Following Hydraulic Expansion Computed by the Old Model and the Updated Model.....	151
Figure 9-24	Comparison of Distributions of Contact Pressure Computed by the Old Model, the Updated Quarter Model and the Updated Full Model Due to Loadings During (a) NO and (b) MSLB.....	151
Figure 9-25	Displaced Shape of the Tube Cross-section at the Top of Tubesheet during (a) NO and (b) MSLB (The Diametral Expansion (u_R) of the Tube along a Tubesheet Radial Direction is less than that in the Orthogonal Direction, Suggesting a Small Ovalization of the Tube Cross-section).....	152
Figure 9-26	Variation of Diametral Growth of the Tube Cross-Section with Angular Location During NO and MSLB at (a) Tubesheet Midsurface and (b) Top of Tubesheet.....	153
Figure 9-27	Circumferential Variation of Contact Pressure at the Tubesheet Midsurface and at the Top of Tubesheet during NO and MSLB (Dashed lines indicate contact pressures calculated assuming that the crevice is pressurized with the secondary fluid).....	153
Figure 9-28	Axial Distribution of Contact Pressure along Four Paths Situated 90° Apart in the Circumferential Direction of the Tube during MSLB.....	154
Figure 9-29	Calculated Leak Rate vs. Iteration Number for Normal Operation and Main Steam Line Break Conditions (Dashed lines show predictions by a simplified model).....	156

Figure 9-30	Distribution of (a) Contact Pressure and (b) Crevice Pressure along the Length of the Tube during NO	156
Figure 9-31	Distribution of (a) Contact Pressure and (b) Crevice Pressure along the Length of the Tube during MLB	157
Figure 9-32	Calculated Crevice Pressure Distribution and the Uniform Crevice Pressure Distribution Assumed for Calculating the Contact Pressures during (a) NO and (b) MSLB.....	158
Figure 9-33	Calculated Crevice Pressure Distribution and the Parabolic Crevice Pressure Distribution Assumed for Calculating the Contact Pressures during (a) NO and (b) MSLB.....	159
Figure 9-34	Calculated Leak Rate vs. Iteration Number (solid lines) for (a) Normal Operation and (b) Main Steam Line Break Conditions (Dashed lines represent bounds)	159
Figure 10-1	Thermal Loading of Tubes and Tubesheet	162
Figure 10-2	Thermal Loading of a Single Tube under Consideration and of the Equivalent Tubesheet Material	163
Figure 10-3	Definition of Tubesheet Cells H1-H24 Used in CFD Analysis.....	164
Figure 10-4	Variations of (a) Inlet Gas Temperatures and (b) Heat Transfer Coefficient with Time for Tubesheet Cells 1-21 Obtained from CFD Analysis.....	164
Figure 10-5	Finite Element Model of Model 51 SG Showing the Tubesheet, Location of the SG Tube, Divider Plate and the Various Cells used in the CFD Analysis.....	165
Figure 10-6	Variation of Effective Thermal Conductivity Properties of Tubesheet with Temperature	166
Figure 10-7	Variation of Specific Heat of A508 with Temperature	167
Figure 10-8	Time Variation of the Maximum Temperatures in the Unit Cell and the Equivalent Solid Cell Subjected to Hot Inlet Conditions	168
Figure 10-9	Temperature Distribution (In °C) at 13,760 S in (a) Tubesheet Unit Cell Subjected to HTC and Gas Temperature Corresponding to Hot Inlet Condition and (b) Tubesheet Equivalent Solid Cell Subjected to Equivalent Volumetric Heating Rate	168
Figure 10-10	Temperature Distribution at the Inside Surface of the Lower Head of a Model 51 SG at time t=13,760 s	169

Figure 10-11	Temperature Distribution at the Bottom Surface of a Model 51 Tubesheet at 13,760 S (The line with the arrowheads represent the radial path along which the temperatures in Fig. 10-12 are plotted).....	170
Figure 10-12	Temperature Distribution in the Solid Rim, Tubesheet and Tube Wall along the Radial Path through the Hot Region of the Tubesheet Bottom Surface shown in Fig. 10-11 during the Severe Accident.....	170
Figure 10-13	Axial Temperature Distribution in the Tube at Various Times.....	171
Figure 10-14	Comparison of Temperature Histories of the Gas Inside the Hottest Tube, Hottest Tube (ID) within the Tubesheet and Exposed Part of the Hottest Tube (ID).....	172
Figure 10-15	Variation of Creep Rate Coefficient A with Temperature for Tubesheets with (a) 23 mm (0.891 in.) Diam. Holes at a Pitch of 33 mm (1.28 in.) and (b) 19 mm (0.765 in.) Diam. Holes at a Pitch of 27 mm (1.07 in.) (Parameter units are as labelled).....	175
Figure 10-16	Deformation of the Top Surface of the Tubesheet at 11,700 s.....	176
Figure 10-17	Tubesheet Deformation at 13,590 s at the (a) Top and (b) Bottom Surfaces, Showing Enhanced Deformation in the Hot Inlet Zone Due to Creep.....	176
Figure 10-18	Variations of Contact Pressure (a) Along Four Axial Paths at Various Times and (b) with Time at Four Circumferential Locations at the Tubesheet Midplane during the Severe Accident (Crevice pressure = 0).....	178
Figure. 10-19	(a) Circumferential Variations of the Contact Pressure at the Tubesheet Mid Plane at Various Times during the Severe Accident and (b) Highly Magnified Deformed Tube Cross-section at the Tubesheet Mid Plane at t=13760 s (The arrow points toward the center of the tubesheet).....	178
Figure 10-20	(a) Axial Variation of Crevice Opening Displacement along Four Paths at Two Times and (b) Circumferential Variation of Crevice Opening Displacement at the Top of Tubesheet at Various Times during the Severe Accident (Crevice Pressure = 0).....	179
Figure 10-21	Time Variations of Crevice Opening Displacements at Four Circumferential Locations at the Top of Tubesheet (Crevice pressure = 0).....	180
Figure 10-22	Variations of Contact Pressure (a) Along Four Axial Paths at Various Times and (b) With Time at Four Circumferential Locations at the Tubesheet Midplane during the Severe Accident [Uniform crevice pressure = 16.2 MPa (2.35 ksi)].....	181

Figure 10-23	Circumferential Variations of the Contact Pressure at the Tubesheet Mid Plane at Various Times during the Severe Accident [Uniform crevice pressure = 16.2 MPa (2.35 ksi)].....	182
Figure 10-24	(a) Axial Variation of Crevice Opening Displacement Along Four Paths at Two Times and (b) Circumferential Variation of Crevice Opening Displacement at the Top of Tubesheet at Various Times during the Severe Accident [Uniform crevice pressure = 16.2 MPa (2.35 ksi)]	182
Figure 10-25	Time Variations of Crevice Opening Displacements at Four Circumferential Locations at the Top of Tubesheet [Crevice pressure = 16.2 MPa (2.35 ksi)]	183
Figure 10-26	Variations of Contact Pressure (a) Along Four Axial Paths at Various Times and (b) With Time at Four Circumferential Locations at the Tubesheet Midplane during the Severe Accident [Parabolic crevice pressure distribution with maximum crevice pressure = 16.2 MPa (2.35 ksi)]	184
Figure 10-27	Circumferential Variations of the Contact Pressure at the Tubesheet Mid Plane at Various Times during the Severe Accident [Parabolic crevice pressure distribution with maximum crevice pressure = 16.2 MPa (2.35 ksi)]	185
Figure 10-28	(a) Axial Variation of Crevice Opening Displacement Along Four Paths at Two Times and (b) Circumferential Variation of Crevice Opening Displacement at the Top of Tubesheet at Various Times during the Severe Accident [Parabolic crevice pressure distribution with maximum crevice pressure = 16.2 MPa (2.35 ksi)]	185
Figure 10-29	Time Variations of Crevice Opening Displacements at Four Circumferential Locations at the Top of Tubesheet [Parabolic crevice pressure distribution with maximum crevice pressure = 16.2 MPa (2.35 ksi)]	186
Figure 10-30	Calculated Leak Rate (using roughness= 2 μm) vs Time for Model 51 SG with (a) Uniform Crevice Pressure Distribution and (b) Parabolic Crevice Pressure Distribution Along Four Axial Paths.....	188
Figure 10-31	Calculated Cumulative Leakage vs. Time for a Model 51 SG for Two Types of Crevice Pressure Distribution (roughness=2 μm)	188
Figure 10-32	Calculated Leak Rate (using roughness=5 μm) vs. Time for Model 51 SG with (a) Uniform Crevice Pressure Distribution and (b) Parabolic Crevice Pressure Distribution Along Four Axial Paths.....	189
Figure 10-33	Calculated Cumulative Leakage (roughness=5 μm) vs. Time for a Model 51 SG for Two Types of Crevice Pressure Distribution.....	189

Figure 10-34	Variation of Crack Depth and m_p with 3 Δp_{NO} for Three Different Crack Lengths (1ksi=6.895 MPa).....	190
Figure 10-35	Variations of Pressure Differential Δp and Average Tube Wall Temperatures of an Average and the Hottest Tube with Time during the Severe Accident	191
Figure 10-36	Mean and $\pm 95\%$ Confidence Bounds Values of Time to Rupture vs. Stress Magnification Factor for (a) the Hottest and (b) Average Tubes Containing Cracks in the Free Span Region	192
Figure 10-37	Variation of Pullout Force and Frictional Resistant Force with Time (The frictional forces are computed from contact pressures predicted by FEA with zero and a parabolic distribution of crevice pressure)	193

LIST OF TABLES

Table 4-1	Elemental Analysis (wt. %) of 19 mm (0.75 in.) and 22 mm (0.875 in.) Diameter Alloy 600 Tubing Material	14
Table 4-2	Room Temperature Tensile Properties of Alloy 600 Tubes Measured in the Axial Direction.....	14
Table 4-3	Parameters for Primary and Steady State Creep of Three Heats of Alloy 600 Tubes.....	20
Table 4-4	Primary and Steady State Creep Parameters (Ksi, °C, H) for A508	28
Table 5-1	Predicted Leak Rates for the Callaway Tube/Tubesheet Test Specimens (drops/minute).....	40
Table 6-1	Initial Test Matrix for Leak Rate Tests.....	54
Table 7-1	Average Geometrical Properties of the Specimens.....	56
Table 7-2	Surface Roughness of 6 Tubes and 5 Collars from Six Leak Rate Specimens	57
Table 7-3	Results from initial Screening Tests on Specimens with Zero Internal Tube Pressure.....	59
Table 7-4	Room Temperature Testing of Specimen 09-7/8	65
Table 7-5	Low Temperature Testing of Specimen 09-7/8; Leak Rate Data (LR) with $P_t = P_{lp} = \sim 2500$ psi.....	66
Table 7-6	Final Room Temperature (26°C) Testing of Specimen 09-7/8; Leak Rate Data (LR) for Four P_{lp} pressures with $P_t = 2524$ psi.....	67
Table 7-7	Stage 1 Initial Room Temperature Testing of Specimen 11-7/8	69
Table 7-8	Stage 5 Final Room Temperature Tests of Specimen 11-7/8.....	71
Table 7-9	Stage 1 Initial Room Temperature Testing of Specimen 04-7/8	72
Table 7-10	Stage 5 Final Room Temperature Tests of Specimen 04-7/8.....	74
Table 7-11	Stage 1 Initial Room Temperature Testing of Specimen 05-7/8	75
Table 7-12	Stage 5 Final Room Temperature Tests of Specimen 05-7/8.....	76
Table 7-13	Stage 1 Initial Room Temperature Testing of Specimen 03-7/8	77
Table 7-14	Stage 3 Final Room Temperature Tests of Specimen 03-7/8.....	79

Table 7-15	Stage 1 Initial Room Temperature Testing of Specimen 02-3/4.....	80
Table 7-16	Stage 3 Final Room Temperature Tests of Specimen 02-3/4	82
Table 7-17	Stage 1 Room Temperature Testing of Specimen 07-7/8	83
Table 7-18	Stage 3 Room Temperature Testing of Specimen 07-7/8	84
Table 7-19	Stage 4 Discrete Data for Leak Rate Maximums and Minimums of Specimen 07-7/8	85
Table 7-20	Final Room Temperature Testing of Specimen 07-7/8.....	85
Table 7-21	Stage 1 Initial Room Temperature Testing of Specimen 01-3/4.....	90
Table 7-22	Stage 3 Room Temperature Tests of Specimen 01-3/4.....	91
Table 7-23	Stage 5 Final Room Temperature Tests of Specimen 01-3/4	93
Table 7-24	Stage 3 Room Temperature Tests of Specimen 01-7/8	95
Table 7-25	Stage 5 Room Temperature Tests of Specimen 01-7/8	95
Table 7-26	Stage 7 Room Temperature Tests of Specimen 01-7/8 with Nitrogen.....	96
Table 7-27	Stage 8 Room Temperature Tests of Specimen 01-7/8 with Air.....	97
Table 7-28	Stage 1 Room Temperature Tests of Specimen 03-3/4	98
Table 7-29	Stage 3 Room Temperature Tests of Specimen 03-3/4 with Air.....	99
Table 7-30	Stage 1 Initial Room Temperature Testing of Specimen 06-7/8	103
Table 7-31	Stage 3 Final Room Temperature Testing of Specimen 06-7/8.....	104
Table 7-32	Stage 1 Initial Room Temperature Testing of Specimen 02-7/8.....	106
Table 7-33	Stage 4 Final Room Temperature Testing of Specimen 02-7/8.....	109
Table 8-1	Initial Estimates of Roughness for B&W Specimens	121
Table 8-2	Leak Rate Parameters Determined from Room Temperature Stage 1 Tests on Specimen 11-7/8.....	124
Table 8-3	Leak Rate Parameters Determined from Room Temperature Stage 1 Tests on Specimen 01-3/4.....	126
Table 8-4	Leak Rate Parameters Determined from Room Temperature Stage 1 Tests on Specimen 02-7/8.....	128

Table 9-1	Conditions for Tube–Collar Crevice Pressure Profile Tests	137
Table 9-2	Parametric Estimates of Changes in Leak Rate (LR) During Design Basis Accidents Under Two Different Contact Stress Assumptions.....	144
Table 9-3	Loading Assumed for Stress Analyses of Model 51 SG with []° diameter Alloy 600 tubes	150

EXECUTIVE SUMMARY

During severe accidents, there is a concern that superheated steam from the primary side may be discharged outside the containment by a breach of a sufficient number of SG tubes. Such SGs in the field may have cracks that are contained within the tubesheet. It is customary to assume that during design basis accidents, these cracks would not constitute a breach of the tube wall because the high contact pressure at the tube-to-tubesheet interface would prevent any leakage of the coolant from the primary to the secondary side. However, during severe accidents, the high contact pressures may be relaxed out by creep and the interface region could provide a low resistance path for the primary coolant to leak out into the secondary side. This report documents the detailed analysis involving a Westinghouse Model 51 SG of the tube-to-tubesheet interface to provide estimated values of leakage from such cracks under postulated (Case 8B) station blackout severe accident conditions. Case 8B is a station blackout with a stuck opened PORV on one SG. The tests and models discussed in this report are based on the postulated pressurization of the tube-to-tubesheet gap (crevice) due to SG tube cracking and subsequent leakage of the RCS into this gap.

Model Development

A 2-D axisymmetric finite element model and a simplified 1-dimensional model of the specimen were developed and used to calculate the variation of contact pressure and gap at the tube-to-collar interface with time. The analyses included stresses due to hydraulic expansion, thermal stresses due to mismatch in thermal expansion coefficients between the tube and the collar and stresses induced by tube and crevice pressures. The high temperature mechanical properties needed for analysis were obtained from literature in addition to a limited number of tensile and creep tests conducted on three heats of Alloy 600 tubes and a single heat of A508 steel. Tests were also performed to obtain thermal expansion coefficient data for a single heat of Alloy 600 and A508 steel as functions of temperature up to 700°C. Both the finite element model and simplified models were successful in predicting the temperature at which there was a complete loss of contact pressure, leading to onset of large leakage.

A 1-D leak rate model was developed based on plane Couette-Poiseuille flow applied to the interface between two plane rough surfaces in contact. The leak rates of most of the tests could be predicted to within a factor of 2-3 by appropriate choices of three adjustable parameters of the model. All three parameters were determined from the initial leak rate tests at room temperature before the high temperature tests were performed.

A finite element model of a Westinghouse Model 51 tube-to-tubesheet joint was developed. The model included a single SG tube (hot tube) embedded inside the tubesheet (with a solid rim), the divider plate, the lower head and a short segment of the SG shell. The inhomogeneous tubesheet with tube holes was replaced by a homogeneous tubesheet with equivalent anisotropic properties. The anisotropic properties were determined from finite element analysis (FEA) of the tubesheet unit cell. The heat transfer from the tube to the tubesheet for the single tube was analyzed in details, while the heat flow from the rest of the tubes to the tubesheet was approximated by volumetric heat fluxes. The heat transfer data for the hot tube was obtained from a computational fluid dynamics (CFD) analysis performed by NRC/RES, and those for the rest of the components were obtained from RELAP 5 model. First, a thermal conduction analysis was conducted with FEA (ABAQUS). The temperature data from the thermal conduction analysis were input into an elastic-plastic-creep structural FEA that included the tube pressure, crevice pressure and the primary pressure acting on the lower surface of the tubesheet. The analysis provided the contact pressure and interfacial gap variation along the length of the tube as functions of time.

Experimental Validation

Tube-to-collar test specimens were designed to simulate the contact pressures generated in a real SG tube-to-tubesheet junction due to hydraulic expansion and thermal expansion mismatch between the tube and the tubesheet. However, these tests were not designed to simulate the more complex behavior of a real SG tube-to-tubesheet junction, such as, tubesheet bowing, tube hole ovalization, etc. Twelve tube-to-collar specimens were fabricated by B&W, Canada. ANL conducted pressure and leak rate tests at high temperatures, representative of thermal transients under Case 8B severe accident conditions. The tubes and the leakage paths (crevices) in the test specimens were independently pressurized. The tests showed a steady decrease of leak rate with increasing temperature from room temperature. The leak rate reduced to almost zero at $\approx 500^{\circ}\text{C}$. In tests where the crevice pressure was held constant and the temperature of the specimen was increased continuously, leakage resumed at temperatures between $670\text{-}690^{\circ}\text{C}$ and increased at an increasing rate with temperature to high values (>5000 mg/min) until the test was stopped. However, if the tube-to-tubesheet crevice was kept mostly depressurized and the crevice pressure increased only intermittently to measure the leak rates, no such large leakage was observed. Thus, it was concluded that large leakage is not possible unless the crevice is pressurized for a sufficiently long time to relax the contact pressure and open a gap at the tube-to-collar interface by deforming the collar by creep. (A schematic of this is shown in Fig. 44.)

Specimens with 1.9 mm (0.75 in.) diameter tubes behaved essentially the same way as 22 mm (0.875 in.) diameter tubes. Also, specimens with three different heats of Alloy 600 tubes behaved essentially the same way. The onset of large leakage during the temperature ramp was delayed slightly with increasing leakage path length.

A test, in which the crevice pressure inlet was sealed off and a 0.8 mm (0.03125 in.) hole was drilled in the tube wall, behaved essentially the same way as specimens whose tubes and crevices were pressurized independently. It is thus likely that crevices in tubes containing through-wall cracks within the tubesheet of a real SG will also be pressurized.

Results

The stress analysis result showed a significant variation of contact pressure and gap in the tube circumferential direction, suggesting that circumferential flow would occur. However, since the leak rate model is based on axisymmetric geometry and ignores any circumferential flow, leak rates were calculated for four axial paths located 90° apart in the circumferential direction of the tube. There was significant variation in the leak rates calculated for the four paths. The results showed that the predicted path-averaged leak rate and cumulative leakage remain low ($<10^{-3}$ kg/min and 2×10^{-3} kg/tube) at 13,460 s, the mean rupture time for the hottest tubes. Although these results are based on a simplified description of the leakage flow, even if multiplied by a factor of 5000, the resulting leak rates are too small to depressurize or alter the course of the severe accident transient significantly.

A tube pullout analysis showed that the end cap loading acting on the hottest tube is insufficient to overcome the fictional resistant force (using $H^*=0.45$ m [17.75 in.]) and cause a pullout before a free span crack of interest will rupture during the severe accident.

ACKNOWLEDGMENTS

The author wishes to thank Kenneth Karwoski for his support. This work was sponsored by the Office of Nuclear Regulatory Research, U. S. Nuclear Regulatory Commission, under Job Code N6583; Program Managers Matthew Rossi and Patrick Purtscher.

ACRONYMS AND ABBREVIATIONS

ANL	Argonne National Laboratory
CFD	Computational Fluid Dynamics
EPRI	Electric Power Research Institute
FEA	Finite Element Analysis
FEM	Finite Element Model
HTC	Heat Transfer Coefficient
LWR	Light Water Reactor
MA	Mill Annealed
MSLB	Main Steam Line Break
NO	Normal Operation
NRC	Nuclear Regulatory Commission
PORV	Power Operated Relief Valve
PWR	Pressurized Water Reactor
SCC	Stress Corrosion Cracking
SG	Steam Generator
SGT	Steam Generator Tube
SGTR	Steam Generator Tube Rupture
Thk.	Thickness
TS	Tube Sheet
TTS	Top of Tube Sheet

SYMBOLS

E	Elastic modulus
P	Applied load
P_{\max}	Maximum applied load
R	Radius of Tube Sheet and collar
r_o, r_i	Outer, inner radii of tube
T	Temperature
t	Time
W	Specimen width
σ_f	Flow stress, defined as the average of yield and ultimate stress
σ_u	Ultimate stress
σ_y	Yield stress
ν	Poisson ratio

1 INTRODUCTION

The purpose of the present study is to develop analytical models to predict the leakage that can be expected from cracks within the tube-to-tube sheet junction at high temperature and experimentally validate the models. It is recognized that the problem of predicting the leakage from cracked tubes within the tube sheet (TS) during severe accidents is too complex to be solved by either purely analytical or purely experimental means. In this study a combined analytical-experimental approach was adopted. The experiments were designed to simulate several key aspects of the TS behavior during severe accidents, but not all, and provide validation of the model. The leak rate model parameters were developed from these experimental tests. One important aspect of the problem that was not simulated in the tests is the phenomenon of TS bowing; this was addressed analytically by finite element analysis. Finally, the models are used together with finite element analyses to predict a range of leakages that can be expected from through-wall cracks under the TS. The magnitudes of these leak rates were compared with the RCP leak rates assumed in the RELAP 5 analysis. If the leak rates were significant, they may materially influence the progress of the severe accident transient, which in turn may affect the failure time sequence of the RCS components.

In NUREG-1570,^[1] the NRC assessed the potential for containment bypass due to SG tube rupture (SGTR) induced by severe accident conditions. One possible accident scenario is thermally induced tube rupture following an unmitigated station blackout leading to core melt. Such an accident can lead to a situation in which the hot leg and SG are filled with a single-phase mixture of superheated steam and hydrogen. A counter-current natural circulation flow pattern is established in the hot leg and it is during this time that the temperatures rise significantly in the reactor coolant system. The specific scenario used for the analysis in this report is referred to as Case 8B in Reference 3. Case 8B is a station blackout with a stuck opened power-operated relief valve (PORV) on one SG. Thermal hydraulic analyses show that the primary system pressure drops for the first 5,000 seconds due to the significant heat removal from the primary system by the SGs as they are boiling dry. The SGs are completely dry at approximately 6,000 seconds, which reduces their heat transfer capacity and the primary system pressure begins to rise. After about 6500 seconds, the primary pressure rises to the PORV set point pressure and then oscillates around this pressure as the PORVs cycle between opened and closed. The temperature of the fluid entering the SG is nearly constant for the first 9,173 seconds. The void fraction is 1.0 at 9,173 seconds, i.e., the fluid is only steam and hydrogen, and at this time, the temperature starts to rise significantly above the temperatures associated with design basis conditions. This is also close to the time when the counter-current natural circulation flows are assumed to begin.

The current thermal hydraulic analyses of these transients assume various levels of leakage from the reactor coolant pump (RCP), but do not currently consider the possible leakage from cracks that may be present in the SG tube-to-tubesheet junction. Excessive leakage from through-wall cracks within the tube-to-tubesheet junctions during severe accidents raises two concerns. First, it may lead to containment bypass even without tube rupture, and second, it may materially affect the thermal hydraulic response of the reactor coolant system (RCS) during the progress of the severe accidents which the RELAP 5 calculations will fail to predict correctly unless such leakages are explicitly taken into account. High temperature-induced creep, expected to occur in the SG tubes and TS during the latter stages of severe accidents, could significantly increase the leakage compared to that during main steam line break (MSLB) because of two effects. First, cracks can open wider during severe accidents due to creep and increase the leakage area and second, creep can relax the interfacial pressure at the tube-to-tubesheet junction and reduce the resistance to leakage from cracks within the TS.

2 BACKGROUND

During postulated PWR severe accidents, there is a concern that effluents from a degraded core may be allowed to bypass the containment if structural failures are experienced in the SG tubes (SGTs). However, if other RCS components (e.g., hot leg or surge line) fail before the SGTs, containment bypass may be averted. RCS component failure predictions will aid in determining the related RCS thermal hydraulic response and the relative order of the RCS failure sequences, the risk importance, and the associated uncertainties.

In order to predict structural failure times of various RCS components, the coolant temperature and pressure histories during the severe accident transients are needed as inputs to the structural analyses. The inputs for the structural analyses are generated from thermal hydraulic (TH) analyses of various severe accident scenarios using the TH code RELAP 5.[2] Under certain scenarios, the results of the TH analyses can depend critically on the reduction of primary coolant inventory due to leakage through all available paths. In the recent series of sensitivity analyses that was conducted by Information Systems Laboratories, RCP leakage was considered as the only leakage path.[3] It is known that many of the currently operating pressurized water reactor (PWR) SGs contain cracks in the tubes in the TS regions. Under normal operating conditions such cracks may not leak, but at high temperatures leakage through these cracks provides an additional path for loss of primary coolant and could potentially influence the progress of the severe accident transient. The sensitivity calculations suggest that a cumulative leak rate on the order of 1 kg/s (from all tube-to-tubesheet junctions) may be the threshold beyond which such leak rates may make a difference. Using the developed model, validated with experimental data, the following analyses and tests were conducted to help estimate the possible range of leak rates from cracks located within the TS.

The leak rate from cracks in the SGTs under the TS during severe accidents will be controlled by a large number of factors. The key to correctly predict the leakage lies in our ability to obtain reasonable estimates of the resistance to leakage flow from all sources. The sources for resistance to the leakage flow are as follows

- (1) Debris carried from the reactor core with the coolant (which may clog the cracks).
- (2) Turns in the coolant flow from inside the tube through the crack into the tube-to-tubesheet annular interface.
- (3) Flow resistance of the crack (crack opening area, roughness of crack, etc.).
- (4) Flow resistance of the tube-to-tubesheet annular interface (depends on the contact pressure, TS bowing, flow path length, surface roughness of the mating surfaces, temperature, pressure, flow velocity, and potential oxidation of TS hole surface). This resistance is influenced by the location of the crack relative to the top of TS (TTS) (if it can be shown that cracks lying within the TS at a depth greater than a predetermined distance will not leak, it might be possible to eliminate the need to inspect the full depth of the TS for cracks.).
- (5) Deposits at the top of the TS which may or may not effectively block the leakage flow. (Recently leak tests were conducted at ANL on tube-to-tubesheet junction sections removed from a retired SG; among two specimens, both with intact deposits at the TTS and with through-wall circumferential cracks, one leaked while the other did not when tested under the same pressure)

Of the five contributors to the total flow resistance listed above, the first and the last are the most difficult to quantify because they vary greatly between SGs and even from tube to tube

within the same SG. In this study, the contributions from these two factors to the flow resistance were ignored, recognizing that such an assumption will tend to lead to overestimates of the leakage. Also, it is estimated that the contributions from items 2 and 3 should be small compared to those from item 4. Therefore, the contributions to flow resistance from items 2 and 3 were ignored, recognizing again that such an assumption will tend to lead to overestimates of the leakage, and the experimental and analytical efforts were designed to quantify the flow resistances due to item 4.

[

]a,c,e

Although varying somewhat, the critical dimensions such as the tubesheet thickness, solid rim thickness, tube hole diameter and tube diameters are relatively constant. Since the testing was conducted on []a,c,e diameter tubes, the Model 51F and Model D5 geometries were chosen for the detailed severe accident leakage analysis.

3 PROBLEM DESCRIPTION AND APPROACH

A review of the TS geometry of most of Westinghouse SGs showed that a typical TS is a porous circular plate with a radius of ~ []^{a,c,e} and thickness of ~ []^{a,c,e} (Fig.3-1). The TS is welded to the SG shell at the top and to the hemispherical lower head at the bottom. A divider plate []^{a,c,e} divides the space between the TS and the lower head [] thick)]^{a,c,e} into inlet and outlet plenums (Fig.). The SG shell []^{a,c,e}, TS, lower head and the divider plate are made out of carbon steel. The divider plate, which is welded to both the TS and the lower head, adds a small bending stiffness to the TS. The TS, which contains thousands of tube holes arranged either in a square or a hexagonal array (Fig 3-1), has a significantly lower bending stiffness than a solid plate of the same thickness. The hole diameters are generally slightly larger []^{a,c,e} than the SGT outer diameter. The SGTs in the old SGs are made of Alloy 600 while the newer SGs have Alloy 690 tubes. During the fabrication of the SG, the tubes are expanded into the TS hole either hydraulically or mechanically. In this report, the chosen source of leakage was from SG tube cracks lying within the TS thickness in SGs with hydraulically expanded mill-annealed Alloy 600 tubes arranged in a square array.

[

a,c,e

Figure 3-1 Typical TS Geometry

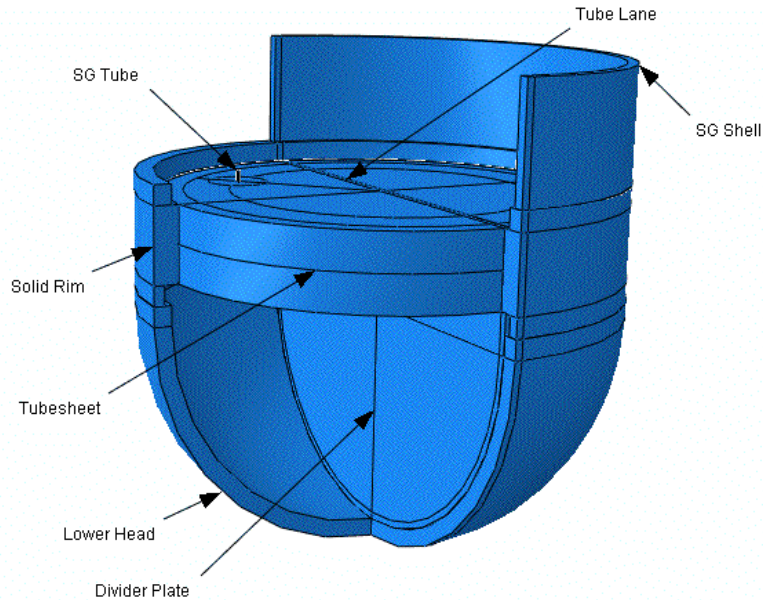


Figure 3-2 Cut Away View of Model 51 SG

During the tube expansion process, great care is taken to ensure that while the portion of the tube lying inside the TS is expanded, the rest of the tube lying outside the TS is unexpanded (Fig. 3-3). Besides the large bending residual stresses in the tube wall itself, the expansion process also introduces a significant contact pressure between the SGT outer surface and the tube hole surface within the TS. The contact pressure distribution is relatively uniform after fabrication at room temperature. Because of the tube internal pressure and a difference in the thermal expansion coefficients of carbon steel and Alloy 600, the contact pressure increases significantly during normal operation. The pressure difference between the primary and secondary fluids causes the TS to flex (or bow) upwards, which leads to a non-uniform distribution of the contact pressure in the axial direction of the tubes. During MSLB and severe accidents, the secondary side is depressurized which causes additional bending (Fig.3-4) of the TS and increased non-uniformity in the contact pressure distribution with the possibility of a portion of the tubes lying within some distance from the top of TS to lose contact with the TS hole surface. During latter stages of severe accidents when the temperature of the coolant reaches levels where both the tube and the TS start to deform by thermal creep, the contact pressure distribution changes as a function of time with the possibility of further loss of contact between the tube and the TS.

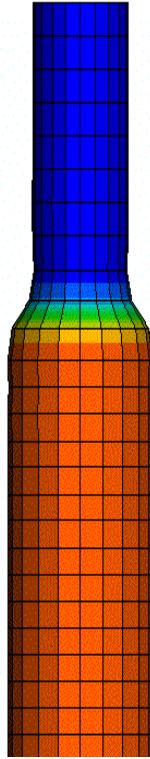


Figure 3-3 Typical Deformation Profile of the SGT after Tube Expansion

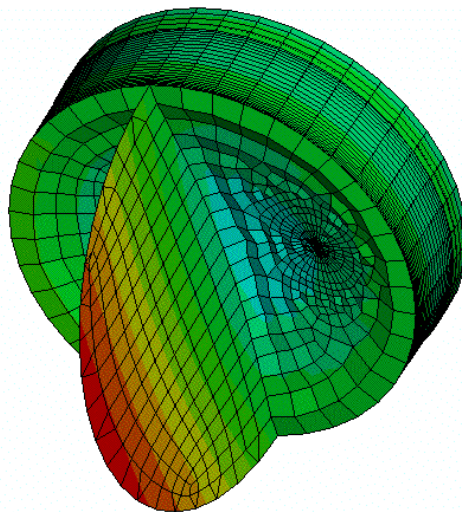


Figure 3-4 TS and Divider Plate, Showing Displaced Shape of TS During MSLB and Severe Accidents

The analytical prediction of the changing contact pressure with time, temperature and pressure is a challenge. The problem is further complicated by the fact that there is no easy way to experimentally measure the contact pressure and validate the calculations. Although utilities have attempted to measure the contact pressure by conducting tube pullout tests at room temperature, the results are often difficult to interpret because of Poisson's contraction of the tube during pullout. The interpretation of a few pullout tests that have been conducted by industry at temperature is complicated by the change in the contact pressure brought about by the differential thermal expansion between the tube and the TS. Since the ultimate objective is to calculate leakage through the tube-to-tubesheet interfacial annulus, the plan was to validate the overall models with leakage tests directly rather than try to first validate a model for calculating contact pressure. Successful experimental validation of the overall leakage model, with tests conducted on a range of specimen dimensions at a number of test pressures and temperatures, will demonstrate that the models for calculating contact pressure reasonably approximate the effects of pressure and temperature.

Conducting realistic leakage tests on tube-to-tubesheet joint specimens that include effects such as TS bowing at high temperature would be very expensive and was outside the work scope of the project. Historically, industry has conducted leakage tests on simpler tube-to-collar specimens and carried out parallel analyses to demonstrate to NRC that leakage during design-basis accidents from cracks lying deep within the TS is acceptably small. In an analogous fashion, the leakage model developed in this project was validated through leakage tests on tube-to-collar test specimens, although the tests were conducted at much higher temperatures than have been done by industry so far. The validation included a series of ABAQUS FEAs to calculate the changing contact pressure with time for each test. Successful validation will provide confidence in the ability to carry out the next step, which is to calculate the contact pressure in an actual tube-to-tubesheet junction as a function of time during severe accidents by FEAs that will take into account both creep deformation and TS bowing. The results from the FEAs are then used in the leak rate model to estimate the leakage rate during severe accidents.

To ensure that the tube-to-collar specimens have surface roughness and contact pressures that are close to those in an actual SG, a subcontract was issued to Babcock and Wilcox, Canada for the fabrication of the specimens using the hydraulic expansion procedures that they normally would use during fabrication of SGs for the utilities. The specimens included 19 mm (0.75 in.) diameter as well as 22 mm (0.875 in.) diameter Alloy 600 tubes. The collar dimensions were selected so that the computed contact pressures are comparable to those in tube-to-tubesheet joints in a real SG after tube expansion.

4 MATERIALS PROPERTIES DATA

4.1 Physical Properties

4.1.1 Thermal Expansion Coefficients

Among the key properties that control the contact pressure at the tube-to-collar interface are the coefficients of thermal expansion of Alloy 600 and A508 steel. Tube samples of Heat EX-82-1 of Alloy 600 and a block of A 508 were sent to two vendors – ANTER Corp. and PMIC Corp. Data for Alloy 600 were measured by both vendors in air. To prevent oxidation from affecting the data, the measurements for A508 steel were made by ANTER in argon environment and by PMIC in vacuum. A repeat measurement on A508 (the same specimen) was made by PMIC in air. The 6th order polynomial fits to the expansion data for Alloy 600 and A508 are plotted in Figs. 4-1 a-b, respectively. Although the expansion data as measured by the two vendors appear to be close, the calculated thermal expansion coefficients for A508 as based on the expansion data measured by PMIC in air has a kink, as shown in Fig.4-2. The mean thermal expansion coefficients for all cases, except the PMIC data for A508 in air, were obtained from the 6th order polynomial fits to the expansion data. The PMIC data for A508 in air was obtained by smoothing the data as shown in Fig. 4-2.

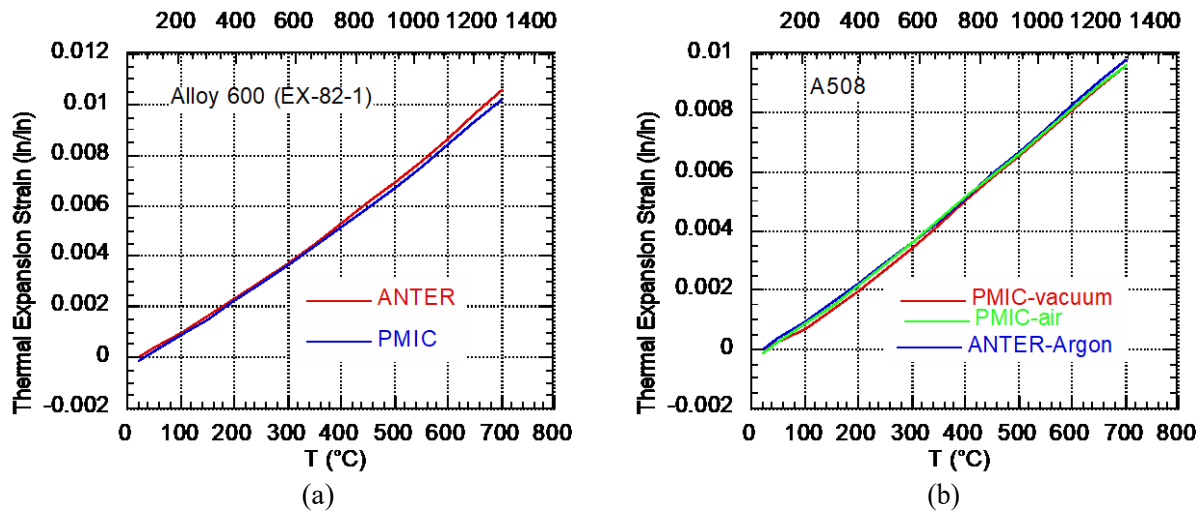


Figure 4-1 Thermal Expansion Strains Measured by ANTER Corp. and PMIC Corp

The mean thermal expansion coefficient data as measured by PMIC and ANTER for both materials are plotted in Fig. 4-3. The data for each material as measured by the two vendors are fairly close, except for the PMIC data on A508 in vacuum which fall significantly below those in air at low temperatures. It should be noted that PMIC resorted to testing in vacuum after it was unable to carry out the measurements in an argon environment. The data measured by ANTER and PMIC are compared with those tabulated in the ASME Code Section II in Fig. 4-4a-b. The ASME Code data for both materials are higher than those measured by the two vendors. The thermal expansion coefficient values for both materials as reported by Westinghouse are compared with the ANTER data in Fig. 4-5.

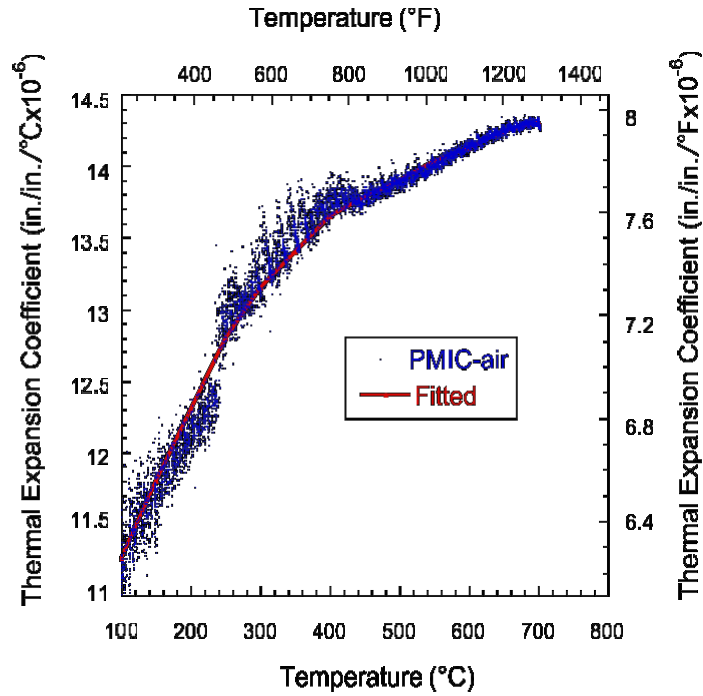


Figure 4-2 Kink in the Thermal Expansion Coefficient Data (blue) in Air Measured by PMIC Corp and a Smooth Fitted Curve (red)

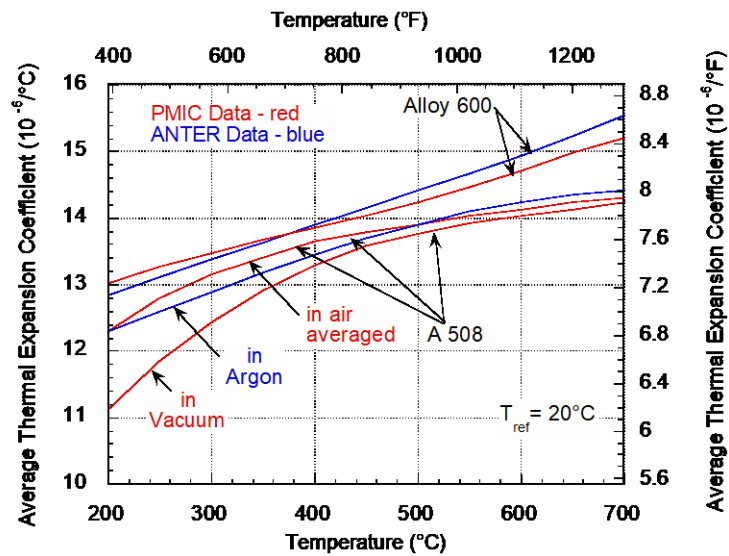


Figure 4-3 Coefficients of Thermal Expansion as Calculated from the Expansion Data

Thermal expansion coefficients of Alloy 600 and A508 as measured by ANTER Corp. are compared with those reported by PMIC for Alloy 600 in air and for A508 in vacuum and air in Figs. 4-4 a-b, respectively. The values of thermal expansion coefficients can have a significant influence on the variation of contact pressure with temperature, as shown in Figs. 4-5a-b. The leakage tests (to be discussed in Section 8.2.5) conducted at ANL suggest that the measured leakage behavior is more in agreement with the predictions based on the PMIC vacuum data on A508 modified by ANL at low temperatures (Fig. 4-6 a) than with those based on either the PMIC data in air or the ANTER data in argon (Fig. 4.7 b).

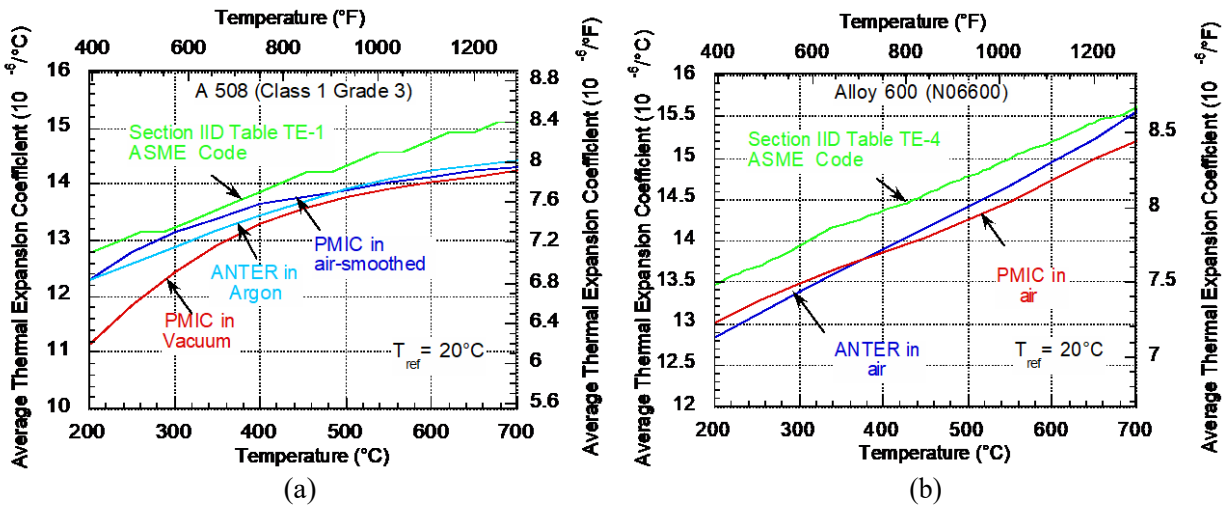


Figure 4-4 Comparison of Mean Thermal Expansion Coefficients of (a) A508 and (b) Alloy 600

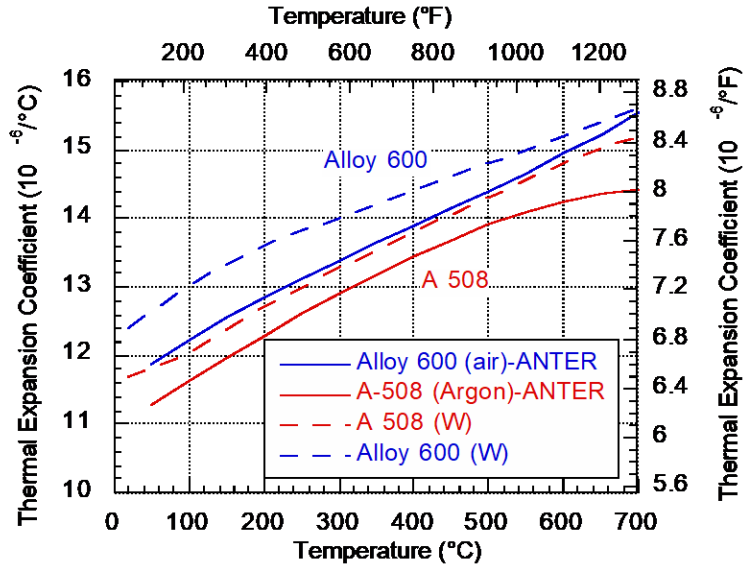


Figure 4-5 Comparison of Thermal Expansion Coefficients of Alloy 600 And A508 Measured by ANTER Corp. with those reported by Westinghouse

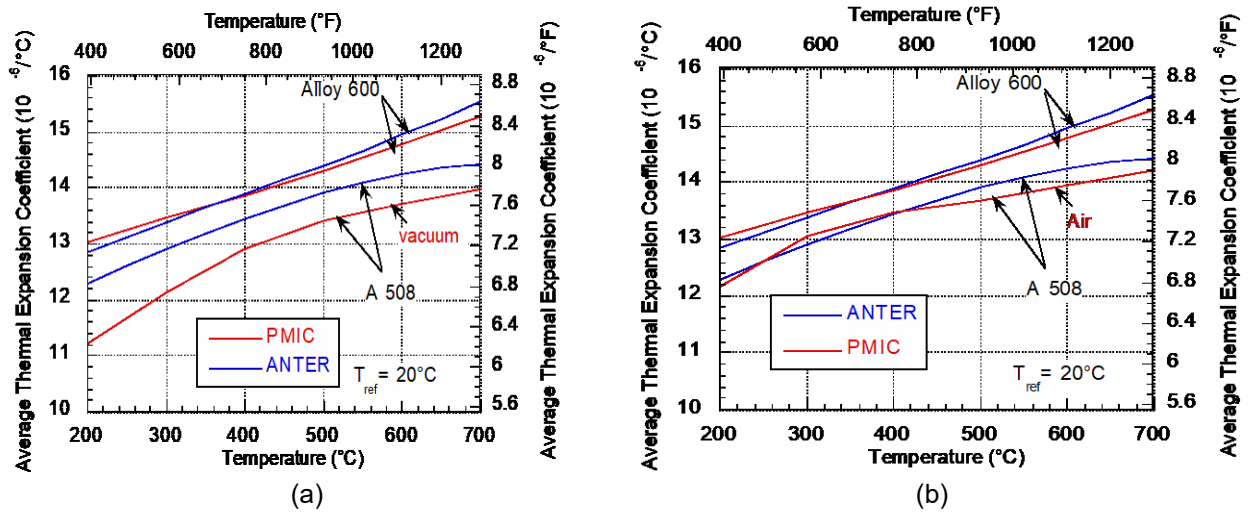


Figure 4-6 Comparison of Thermal Expansion Coefficients of Alloy 600 and A508

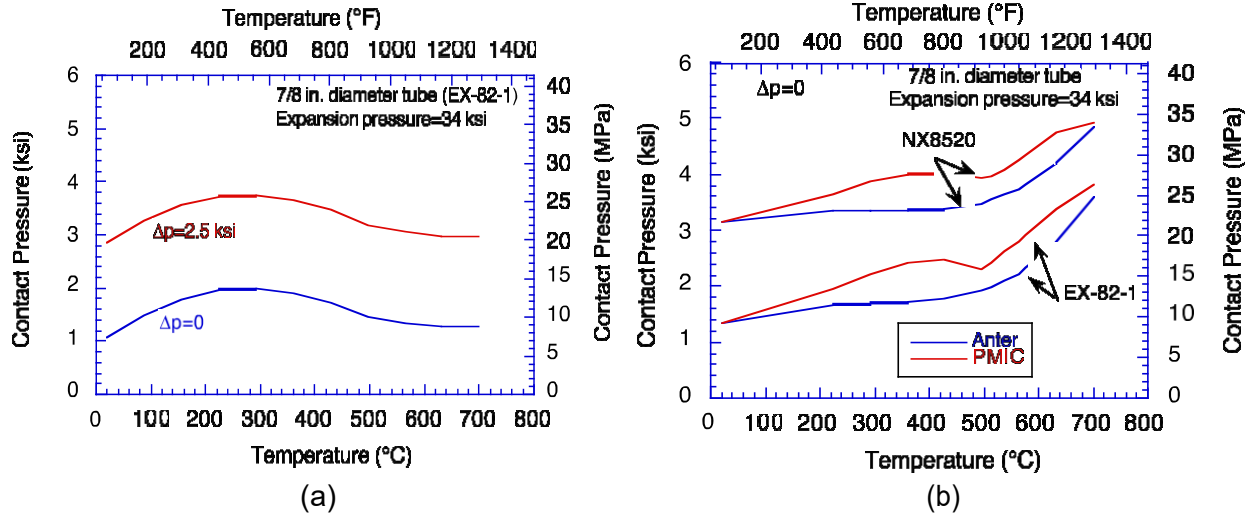


Figure 4-7 Variation of Contact Pressure with Temperature Calculated by using Thermal Expansion Coefficient Data

4.2 Mechanical Properties

4.2.1 Alloy 600

Tube-to-collar junction specimens were made with 22 and 19 mm (0.875 and 0.75 in., respectively) diameter Alloy 600 tubes. The chemical composition and tensile properties of the Alloy 600 tubes are given in Tables 4-1 and 4-2, respectively. The 22 mm (0.875 in.) diameter tubes are from two heats, EX-82-1 and NX-8520. The 19 mm (0.75 in.) diameter tubes are from heat NX-8524.

Table 4-1 Elemental Analysis (wt. %) of 19 mm (0.75 in.) and 22 mm (0.875in.) Diameter Alloy 600 Tubing Material

Element	Specifications ASTM B163	NX8520 0.875 in. dia	NX8524 ^a 0.75 in. dia	NX8524 ^b 0.75 in. dia	EX-82-1 ^c 0.875 in. dia
Ni	72.0 min.	75.63 - 75.77	74.66	74.95	75.05
Cr	14.0-17.0	15.28 - 15.40	15.21	14.84	15.21
Fe	6.0-10.0	7.96 - 8.03	9.16	9.11	8.30
Mn	1.0 max.	0.19	0.20	0.20	0.18
Cu	0.5 max.	0.02	<0.01	0.01	0.17
C	0.15 max	0.022	0.022	0.023	0.035
S	0.015 max.	<0.001	<0.001	<0.001	0.001
Si	0.5 max.	0.18 - 0.21	0.20	0.17	0.23
Al	d	0.21	0.24	0.22	0.15
Ti	d	0.26 - 0.34	0.29	0.35	0.18
Co	d	0.02	0.01	0.02	0.03
P	d	0.004	0.003	0.005	0.009
B	d	0.002 - 0.004	0.004	0.002	0.002
N	d	<0.01	<0.01	<0.01	0.004

^a Top of ingot

^b Bottom of ingot

^c Check analysis for Tubing from PNNL with a label, EX-82-1/2675

^d Not specified.

Table 4-2 Room Temperature Tensile Properties of Alloy 600 Tubes Measured in the Axial Direction

Heat No.	Diam. mm (in.)	Yield MPa (ksi)	UTS MPa (ksi)	% Elongation
8520L	22.2 (0.875)	293 (42.5)	696 (101)	36
8524	19.05 (0.75)	308 (44.7)	682 (99)	25
EX-82-1	22.2 (0.875)	357 (51.8)	683 (99)	43

4.2.1.1 Tensile Tests

Tensile tests were conducted at room temperature on double dogbone specimens fabricated from tubes of the three heats of Alloy 600. Typical axial stress-strain curves of the Alloy 600 tubes are plotted in Figs. 4-8 a-b.

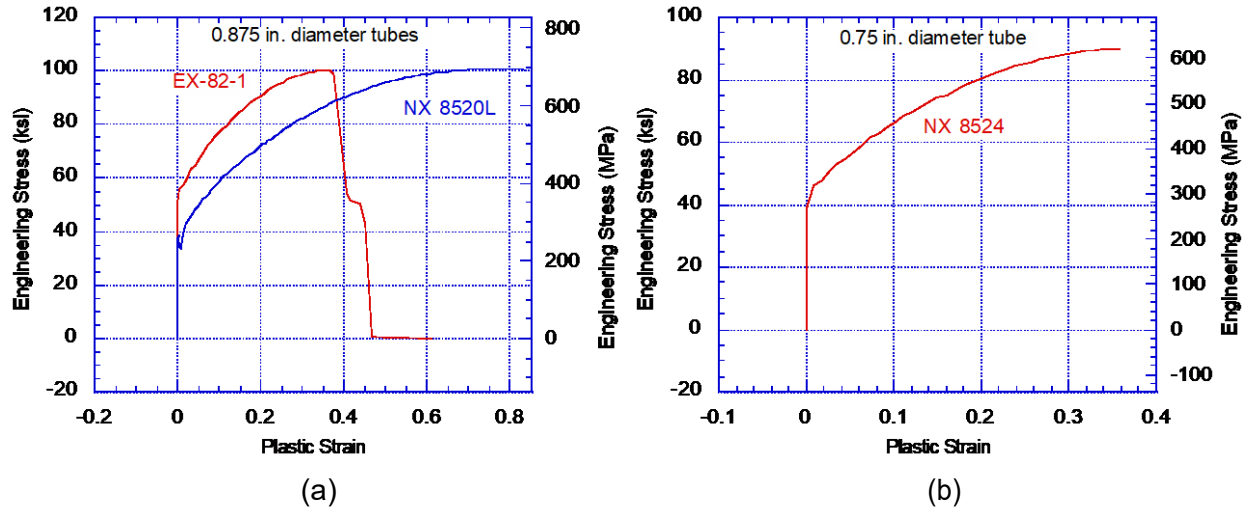


Figure 4-8 Room Temperature Stress-strain Curves of (a) 2.2 mm (0.875 in.) Diameter Dogbone Specimens

Longitudinal slices were cut from the same set of tubes and flattened before tensile dogbone sheet specimens were machined. The cold work introduced by the flattening process may have elevated the flow stress. The stress-strain curves in the low strain regime are shown in Figs 4.9 a-b. Note that the yield strengths are slightly higher for the sheet specimens than for the double dogbone specimens. The ultimate tensile strengths for the two types of specimens are close.

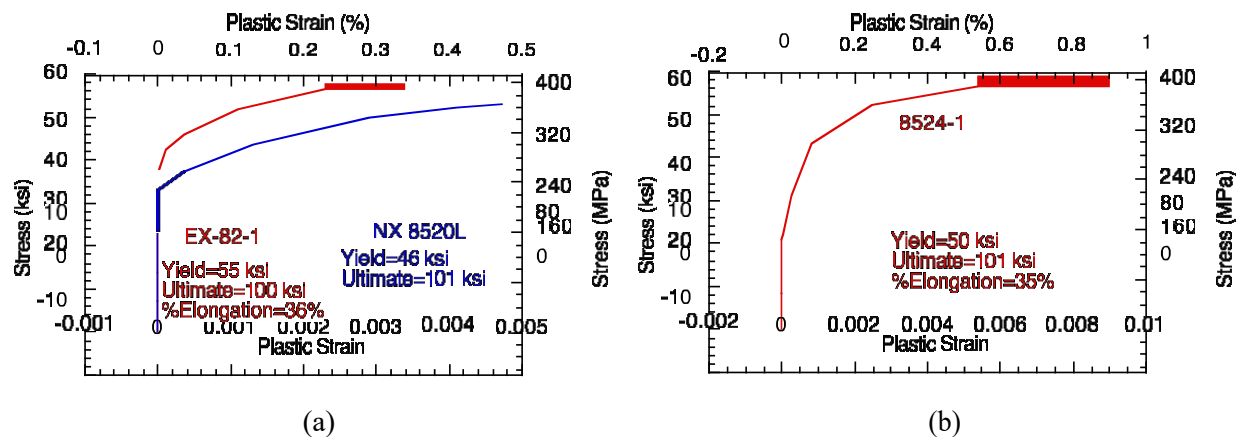


Figure 4-9 Room Temperature Stress-strain Curves of (a) 22.2 mm (0.875 in.) Diameter and (b) 19.05 mm (0.75 in.) Diameter Alloy 600 Tube Sheet Specimens

4.2.1.2 Creep Tests

Sheet specimens of the Alloy 600 tubes were also tested for creep. The purpose of these tests was to determine the early creep deformation behavior, which would have an influence on the contact pressure relaxation of the tube-to-collar junction specimens during high temperature testing. Therefore, these tests were interrupted after 100 hours if no rupture had occurred by then. Creep strain vs. time plots for tests conducted at 15 and 172 MPa (25 ksi) at 550°C on heats EX-82-1, NX 8520L and NX 8524 are shown in Figs. 4-10 a-c.

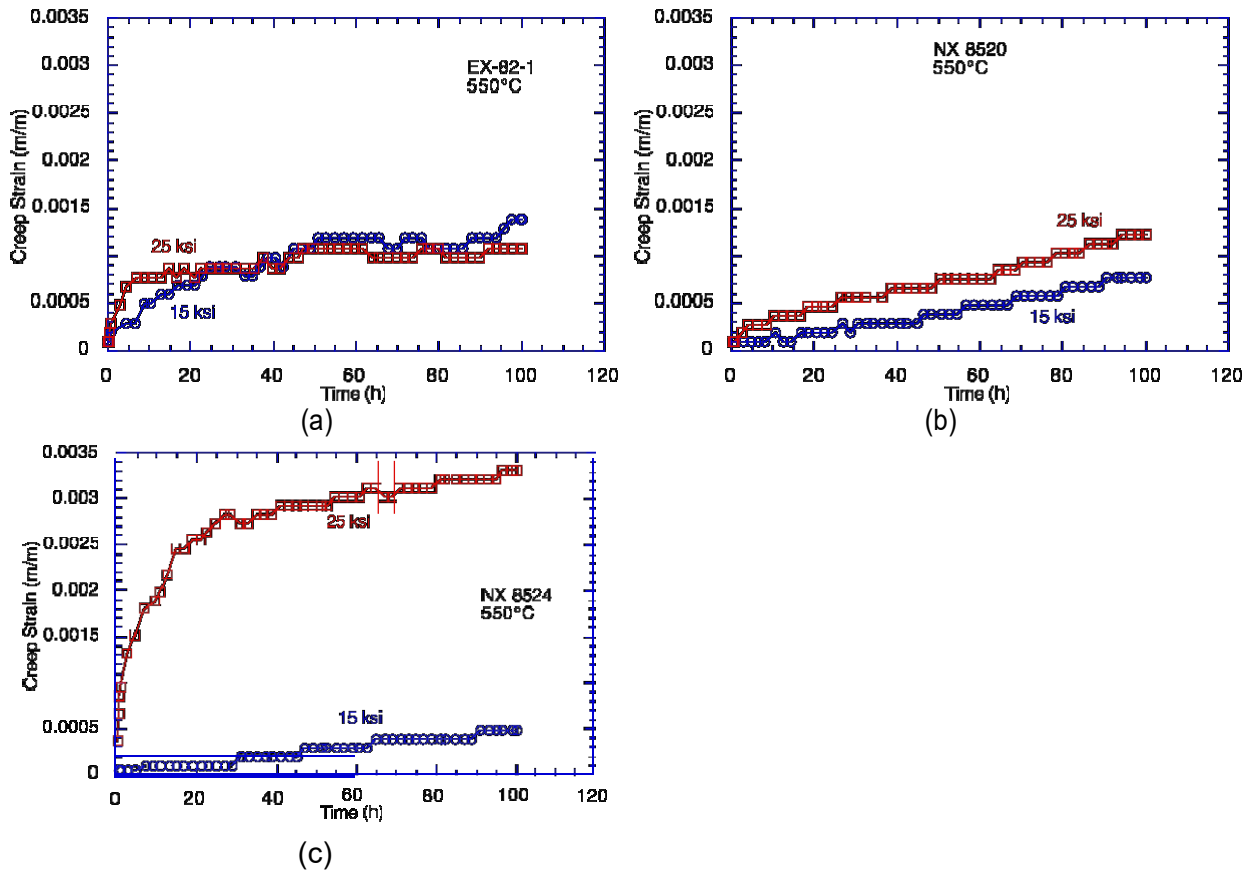


Figure 4-10 Creep Strain vs. Time Plots for Tests Conducted at 550°C on Alloy 600 Heats (a) EX-82-1, (b) NX 8520L and (c) NX 8524

Similar plots for tests conducted at 69 and 138 MPa (10 and 20 ksi) at 650°C are shown in Figs. 4-11 a-c.

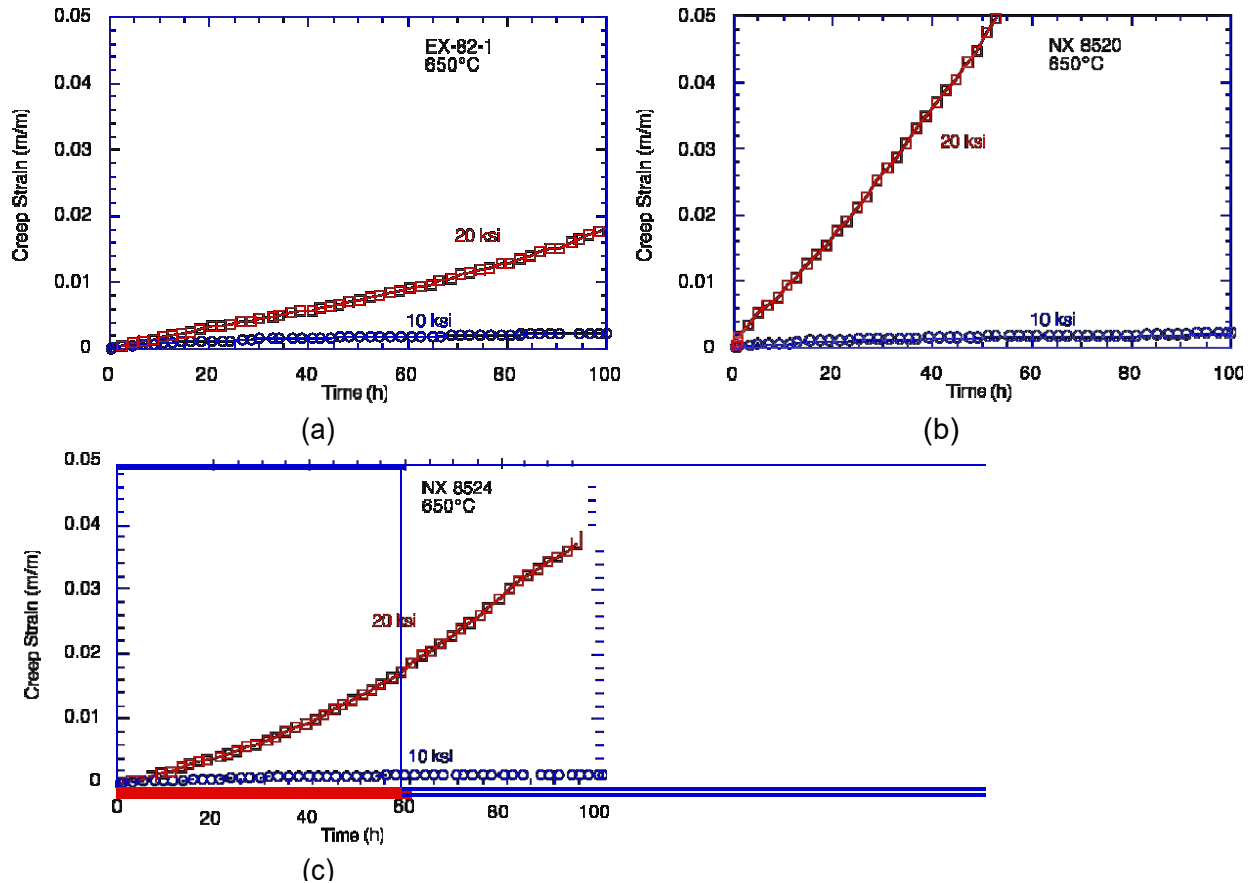


Figure 4-11 Creep Strain vs. Time Plots for Tests Conducted at 650°C on Alloy 600 Heats (a) EX-82-1, (b) NX 8520L and (c) NX 8524

Plots for all three heats tested at 93 MPa (13.5 ksi) at 732°C are shown in Fig. 4-12. The last test conditions (temperature and stress) was selected because the INL reported data from a different heat of Alloy 600 at the same conditions. Like the INL tests, these tests did not show any primary creep. Figure 4-13 shows that the minimum creep rate for all three of our heats were less than that exhibited by the INL heat. Unlike the other tests, the three tests at 732°C were continued until rupture. The Larson-Miller parameter data for the creep rupture times of the ANL tests are superimposed on the same plot for the INL tests in Fig. 4-13, which shows that the ANL creep rupture time data for all three heats fall close to the best-fit line for the INL tests.[4].

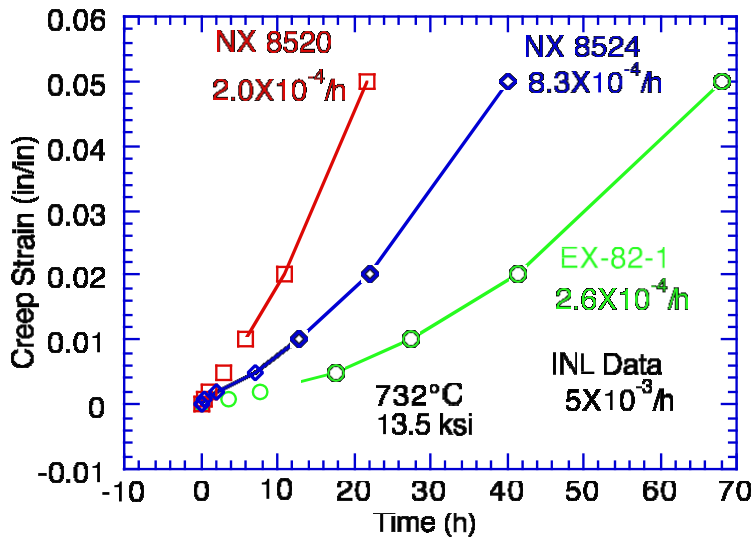


Figure 4-12 Creep Strain vs. Time Plots for Tests Conducted at 732°C and 93 MPa (13.5 ksi) on Alloy 600 Heats EX-82-1, NX 8520L and NX 8524

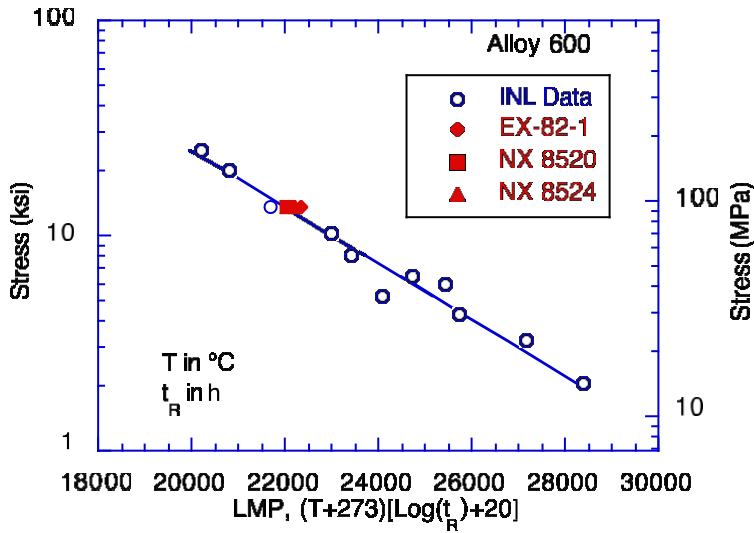


Figure 4-13 Larson Miller Plots for the Time to Rupture Data on Alloy 600 Conducted by INL and ANL

4.2.1.3 Creep Rate Equation

The creep curves were fitted with the following equations

$$\epsilon_c = \epsilon_{c,p} + \epsilon_{c,s} \quad (1)$$

where $\epsilon_{c,p}$ =primary creep and $\epsilon_{c,s}$ =steady state creep,

$$\epsilon_{c,p} = A_1 \sigma^{n_1} \exp\left(-\frac{Q_1}{T}\right) \left[1 - \exp\left(-\frac{t}{t_0}\right)\right] \quad (2a)$$

and

$$\epsilon_{c,s} = A_2 t \sigma^{n_2} \exp\left(-\frac{Q_2}{T}\right) \quad (2b)$$

The parameters for the various heats are given in Table 4-3. The fitted curves are compared with the measured curves in Figs. 4-14 – 4-16. Creep deformation at short times are fitted to within a factor of 2. The predicted vs. observed steady state creep rates together with the $\pm 95\%$ confidence bounds are shown in Fig. 4-17

Table 4-3 Parameters for Primary and Steady State Creep of Three Heats of Alloy 600 Tubes

Material	Primary creep parameters	Steady state creep parameters
NX 8520 Alloy 600	$A_1 = \begin{cases} 1.35 \times 10^{-3} & \text{for } T = 550^\circ\text{C} \\ 5.0 & \text{for } T > 550^\circ\text{C} \end{cases}$ $n_1 = \begin{cases} 2 & \text{for } T = 550^\circ\text{C} \\ 0.03 & \text{for } T > 550^\circ\text{C} \end{cases}$ $Q_1 = 7100 \text{ K}$ $t_0 = \begin{cases} 0.3 & \text{for } T = 550^\circ\text{C} \\ 20.0 & \text{for } T > 550^\circ\text{C} \end{cases}$	$A_2 = 3.89 \times 10^5$ $n_2 = 4.35$ $Q_2 = 30897 \text{ K}$
NX 8524 Alloy 600	$A_1 = \begin{cases} 5.0 \times 10^{-8} & \text{for } T = 550^\circ\text{C} \\ 0.09 & \text{for } T > 550^\circ\text{C} \end{cases}$ $n_1 = \begin{cases} 5 & \text{for } T = 550^\circ\text{C} \\ 0.03 & \text{for } T > 550^\circ\text{C} \end{cases}$ $Q_1 = 5015 \text{ K}$ $t_0 = \begin{cases} 0.1 & \text{for } T = 550^\circ\text{C} \end{cases}$	$A_2 = 5.0 \times 10^4$ $n_2 = 2.91$ $Q_2 = 26063 \text{ K}$
EX-82-1 Alloy 600	$A_1 = \begin{cases} 1.5 \times 10^{-3} & \text{for } T = 550^\circ\text{C} \\ 0.29 & \text{for } T > 550^\circ\text{C} \end{cases}$ $n_1 = \begin{cases} 2 & \text{for } T = 550^\circ\text{C} \\ 0.03 & \text{for } T > 550^\circ\text{C} \end{cases}$ $Q_1 = 4937 \text{ K}$ $t_0 = \begin{cases} 12 & \text{for } T = 550^\circ\text{C} \end{cases}$	$A_2 = 9.5 \times 10^4$ $n_2 = 2.73$ $Q_2 = 26837 \text{ K}$

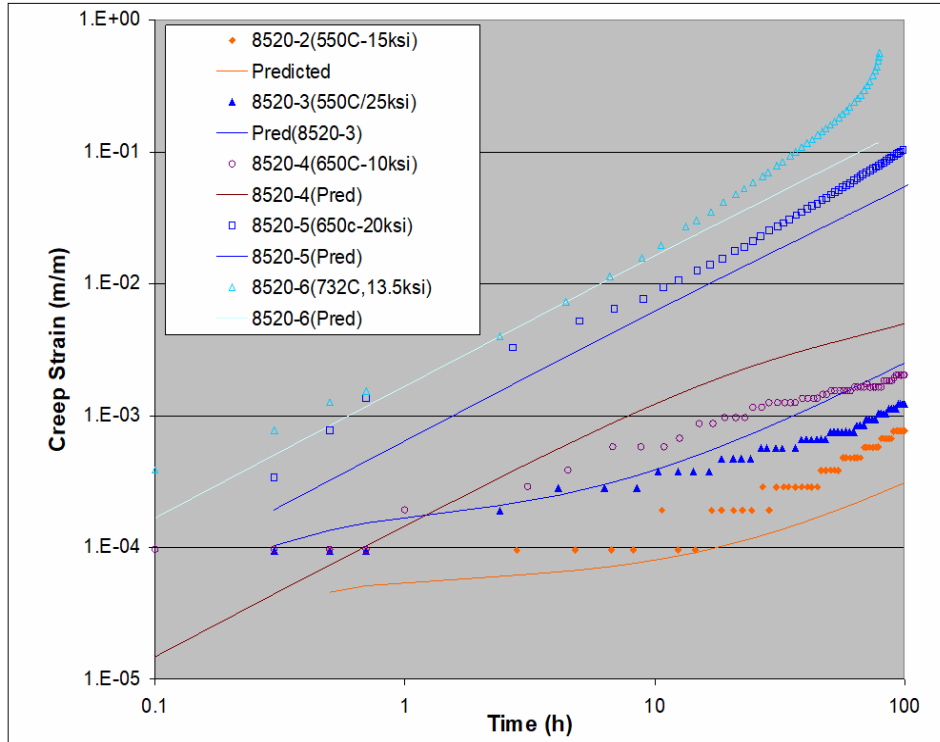


Figure 4-14 Measured and Fitted Creep Strain vs. Time Plots for Tests Conducted on Heat NX 8520 Alloy 600

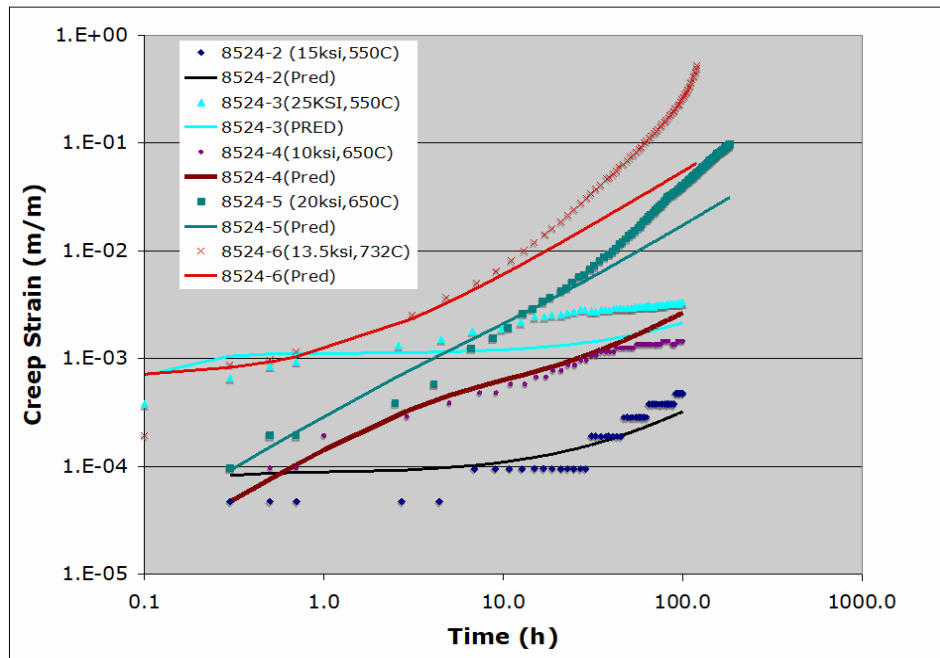


Figure 4-15 Measured and Fitted Creep Strain vs. Time Plots for Tests Conducted on Heat NX 8524 Alloy 600

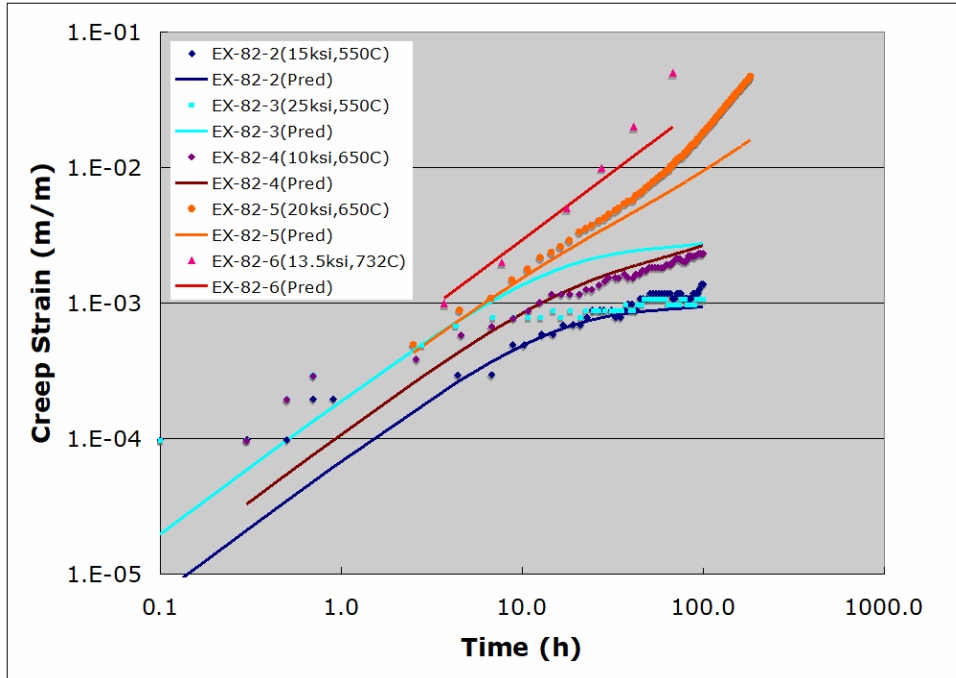


Figure 4-16 Measured and Fitted Creep Strain vs. Time Plots for Tests Conducted on Heat EX-82-1 Alloy 600

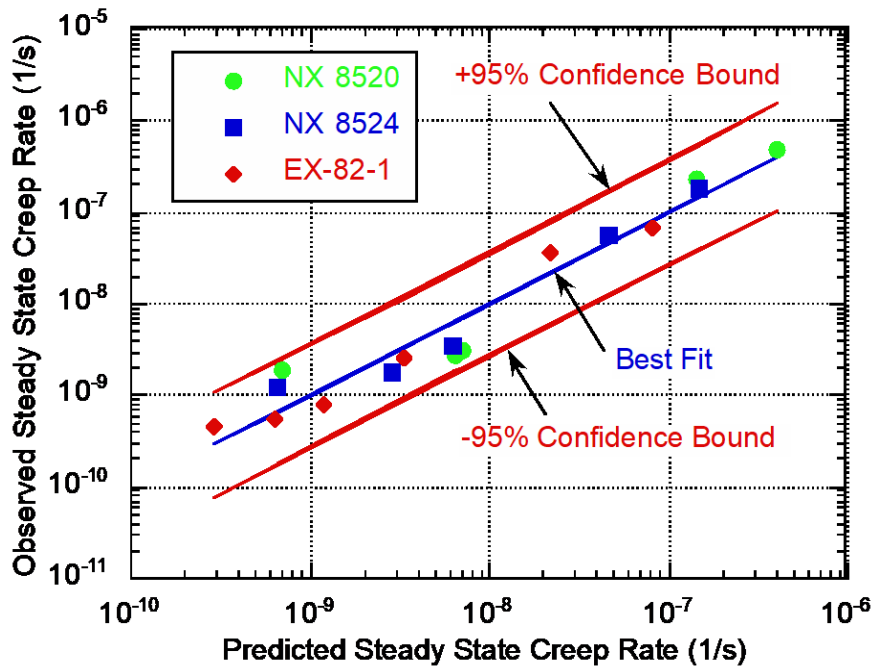


Figure 4-17 Predicted vs. Observed Steady State Creep Rates for Alloy 600 Tubes

4.2.2 SA508 Steel

The SA508 steel was obtained from a large forging. The material test report showed that the material is SA508 Class 1 Grade 3 (formerly Class 3). Following high temperature annealing, it was water quenched at 870°C (1600°F) for 11 hours and tempered at 649°C (1200°F) for 15 h. Histograms of the reported yield and ultimate tensile strengths are plotted in Figs 4-18 respectively.

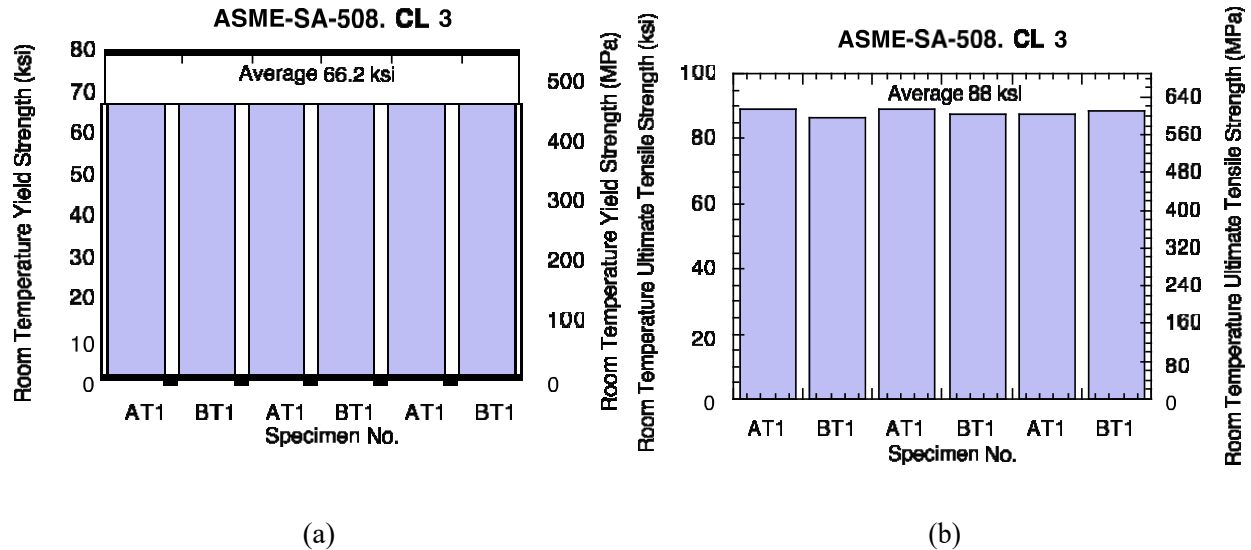


Figure 4-18 Histograms of Room Temperature (a) Yield and (b) Ultimate Tensile Strengths of SA508

4.2.2.1 Tensile Tests

The tensile tests were conducted on 6.35 mm (0.25 in.) diameter standard ASTM specimens fabricated from a block of A508 that was sent to ANL by a vendor. It had on it a 3-hr/1125°F post weld heat treatment (PWHT), which is a standard heat treatment that is applied to all of clad tubesheets prior to drilling of holes. However, when the vendor fabricated the tube-to-collar leak rate specimens for ANL, they gave the material an extra hour at 1125°F to help machining the collars. ANL tested three specimens without the extra hour of PWHT. The stress-strain curves are plotted in Figs. 4-19 a-c. ANL also tested a specimen with an additional hour of PWHT; the result is plotted in Fig. 4-19 d. The extra hour of PWHT appears to have minimal effect on the stress-strain curve. However, Figs. 4-19 a-b and 4-19 a-c show that the 3 hour PWHT does reduce the yield and ultimate tensile strengths significantly.

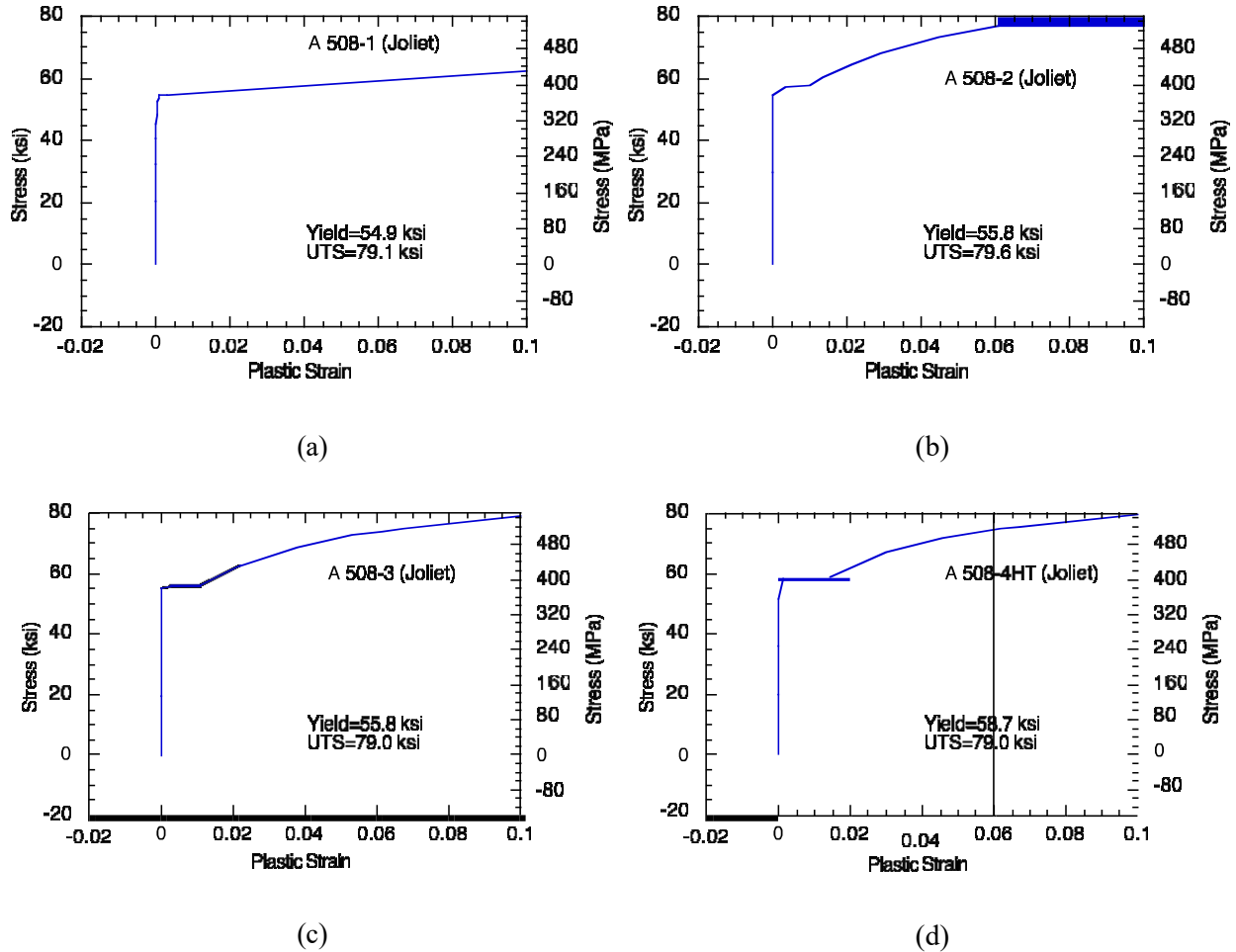


Figure 4-19 Tensile Stress Strain Curves of A508 Specimens with (a)-(c) 3 hour PWHT and (d) 4 hour PWHT at Room Temperature

4.2.2.2 Creep Tests

The creep tests were conducted on 6.35 mm (0.25 in.) diameter standard ASTM specimens fabricated from the same block of A 508 that was used for the tensile tests. It had on it a 4-hr/1125°F post weld heat treatment (PWHT). Creep strain vs. time plot for a test conducted at 103 MPa (15 ksi) at 550°C is shown in Fig. 4-20. Similar plots for tests conducted at 8 and 12.14 MPa (2 ksi) at 650°C and 5 and 12.14 MPa (2 ksi) at 750°C are shown in Figs. 4-21 a-b, respectively. Note that primary creep was observed only for the test at 550°C. Like the tests run by INL, the higher temperature tests did not display appreciable primary creep. [4]

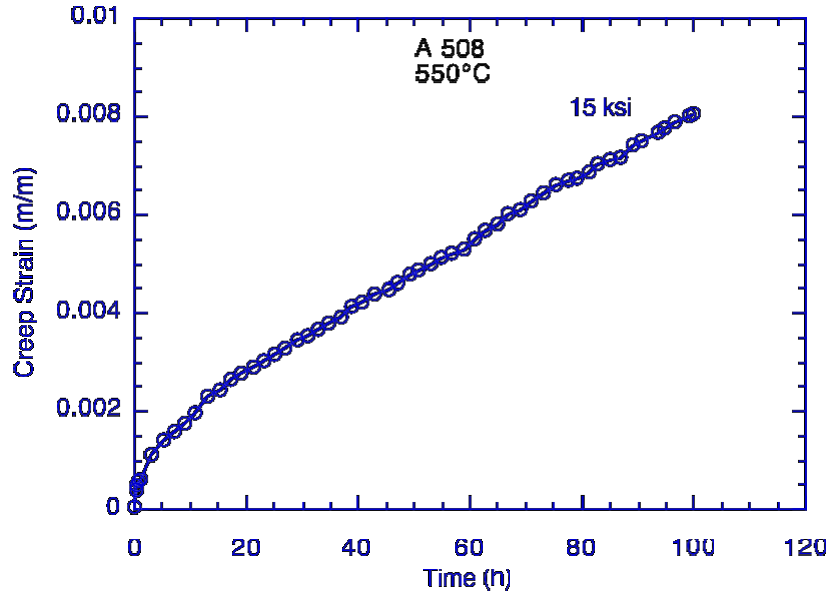


Figure 4-20 Creep Strain vs. Time Plot for a Test Conducted at 550°C on A508

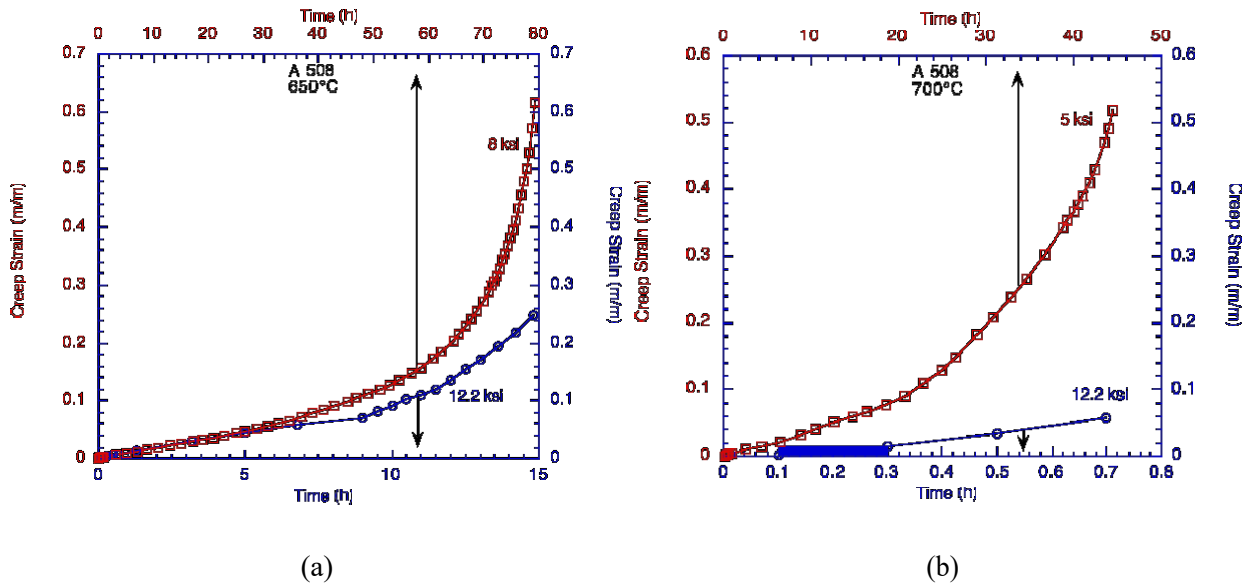


Figure 4-21 Creep Strain vs. Time Plots for Tests Conducted on A508 at (a) 650°C and (b) 750°C

The Larson-Miller parameter data for the creep rupture times of the ANL tests are superimposed on the same plot for the INL tests in Fig. 4-22, which shows that the ANL data fall consistently below the best-fit line for the INL tests. [4] The shorter rupture times can be attributed to the PWHT given to the ANL specimens.

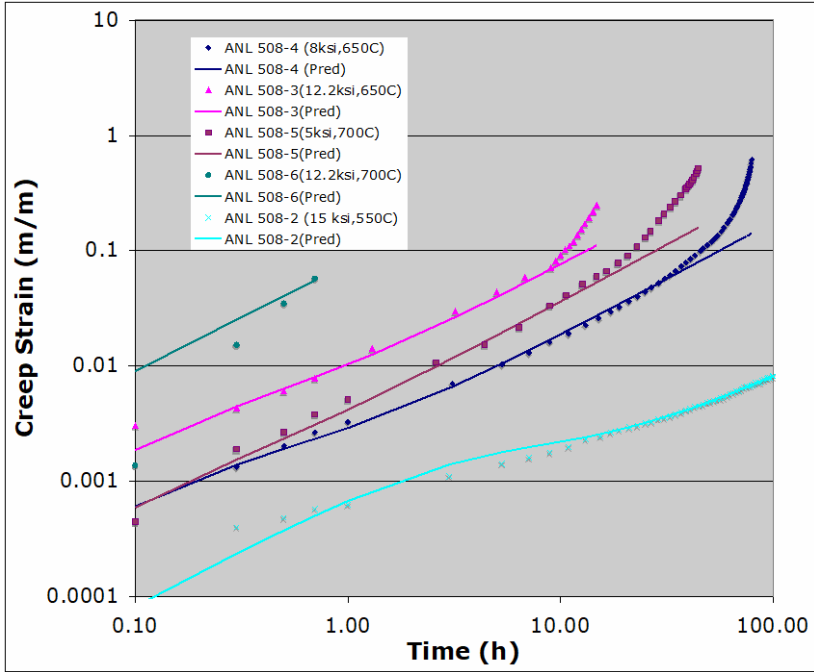


Figure 4-23 Measured and Fitted Creep Strain vs. Time Plots for Tests Conducted on A508 Steel

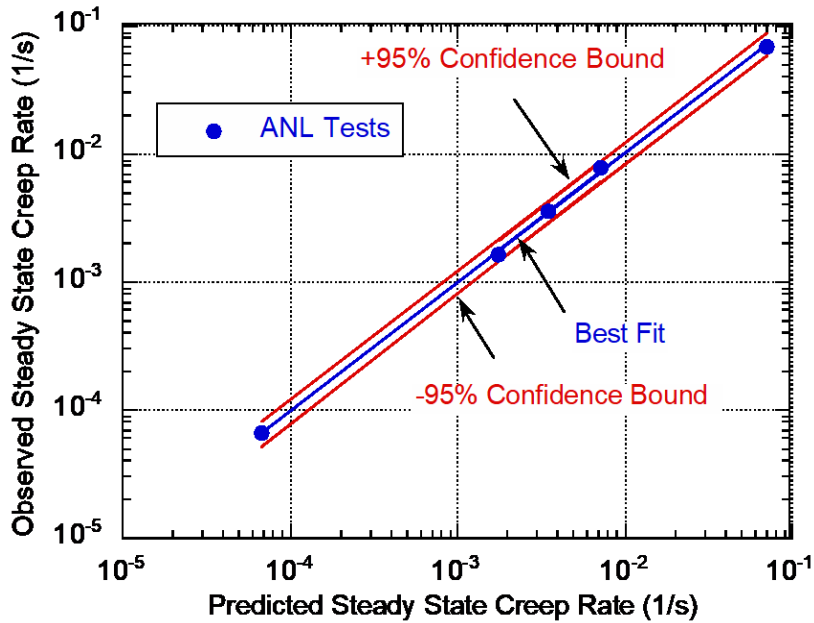


Figure 4-24 Predicted vs. Observed Steady State Creep Rates for A508

Table 4-4 Primary and Steady State Creep Parameters (Ksi, °C, H) for A508

Material		Primary creep parameters	Steady state creep parameters
A 508 steel		$A_1 = 0.102$ $n_1 = 2.285$ $Q_1 = 8551 \text{ K}$ $t_0 = \begin{cases} 2 & \text{for } T = 550^\circ\text{C} \\ 0.21 & \text{for } T = 650^\circ\text{C} \\ 0.27 & \text{for } T = 732^\circ\text{C} \end{cases}$	$A_2 = 3.0 \times 10^{13}$ $n_2 = 3.37$ $Q_2 = 40966 \text{ K}$

5 LEAK RATE MODELS

5.1 Leak Rate Model

A leak rate model was developed and benchmarked against the Callaway test results. [9] The flow between the tube and the tubesheet is assumed to be dominated by viscous losses. The mass flow per unit length around the circumference, q , is

$$q = -\frac{1}{K} \frac{\rho(p_f)}{\mu} \frac{dp_f}{dz} \quad (5)$$

where p_f is the fluid pressure, μ the viscosity, ρ the density, and K is the loss coefficient = $12/d^3$ where d is the distance between the tube and tubesheet. Equation (5) is strictly applicable to incompressible plane Couette-Poiseuille flow.

For compressible flows, a similar result is obtained if the compressibility terms are neglected in the momentum equation; this assumption is valid as long as the velocities are much less than sonic.⁵[5]

Two-Phase Flow

For two-phase flows, it was assumed that the flow is incompressible as long as p_f is greater than the saturation pressure p_{sat} and that the flow flashes instantly to steam and acts as perfect gas once p_f is less than p_{sat}

$$q = \frac{-1}{\mu L_\ell} \int_{p_1}^{p_{sat}} \frac{\rho(p_f) dp_f}{K} \text{ in the liquid phase and} \quad (6a)$$

$$q = \frac{-1}{L_g} v_{sat} \int_{p_{sat}}^{p_2} \frac{(p_f/p_{sat}) dp_f}{K} \text{ in the gas phase.} \quad (6b)$$

Continuity requires that the mass flow in the liquid phase and the gas phase be equal and the combined lengths of the liquid region and the gaseous region must equal the geometric length L

$$L_\ell + L_g = L \quad (7)$$

5.1.1 Flow in the Annulus between Two Rigid Cylinders

For flow through the annular region between two rigid cylinders separated by a fixed distance d , the loss coefficient $K = 12/d^3$ independent of z .

5.1.1.1 Incompressible Flow

In the case of incompressible flow, the pressure gradient along the length (z) is a constant given by

$$\frac{dp_f}{dz} = -\frac{p_1 - p_o}{L} \quad (8)$$

where L is the axial length of the annulus, p_1 is the fluid inlet pressure and p_o is the fluid exit pressure. The mass flow rate can be obtained by integrating the flow rate given by Eq. (5) around the circumference.

5.1.1.2 Compressible Flow

In the case of single-phase compressible gas flow, if it is assumed that the compressibility terms can be neglected in the momentum equation, it takes the simplified form

$$\frac{\partial p_f}{\partial z} = \mu \frac{\partial^2 u}{\partial y^2} \quad (9)$$

As noted previously, Equation (9), is valid for compressible flows if the velocities are much less than sonic.⁵ Equation (9) can be integrated with respect to y twice and, after satisfying the no-slip boundary conditions at $y = 0$ and $y = h$, gives the same parabolic velocity profile as the incompressible case. The mass flow rate, which is independent of z, can then be shown to be the same as Eq. (5).

p_f was interpreted to be the thermodynamic pressure, which can be related to the gas density by the ideal gas law. Since the gas density will vary along the length, Eq (5) has to be integrated along the tube length,

$$q = \frac{-d^3}{12\mu L} \int_{p_1}^{p_2} \rho(p_f) dp_f \quad (10)$$

for perfect gases $\rho \sim p_f$, therefore,

$$q = \frac{-d^3}{12L} \frac{\rho_1}{\mu} \int_{p_1}^{p_2} \left(\frac{\rho(p_f)}{\rho_1}\right) dp_f = \frac{-d^3}{12Lv_1 p_1} \int_{p_1}^{p_2} p_f dp_f \quad (11)$$

where v_1 is the kinematic viscosity at pressure p_1 . For $p_2 = 0$,

$$q = \frac{d^3 p_1}{24Lv_1} \quad (12)$$

By integrating the RHS of Eq. (10) from p_1 to $p_f(z)$ and LHS from 0 to z, noting that q is a constant,

$$q = \frac{d^3}{24zv_1 p_1} (p_1^2 - p_f^2) \quad (13)$$

which on substituting for q from Eq (12) gives

$$\frac{p_f}{p_1} = \sqrt{1 - \left(\frac{z}{L}\right)^2} \quad (14)$$

Thus, the fluid pressure varies parabolically along the length and unlike in the incompressible case, the fluid pressure gradient is not a constant. This result can be shown to hold for both the isothermal and the adiabatic case.⁶

5.1.2 Flow in the Annulus between Tube and Collar (or Tubesheet)

In the case of flow in the annulus between the tube and the collar (or tubesheet), both of which are non-rigid, K will be a function of z because d will vary along the length with changing contact pressure. At high temperatures, K will also be a function of time and temperature because of creep deformation. Thus, generally the leak rate has to be obtained by numerical integration.

5.2 Contact Mechanics

The contact between a smooth surface and a rough surface is shown schematically in Fig. 5-1. The leakage between the surfaces depends on the roughness which creates separation between the surfaces. A higher contact pressure, p_c deforms the asperities and decreases the effective distance between the two surfaces. The flow area between the surfaces is controlled not only by the distance between the surfaces, but blockage of open area between the surfaces by the asperities. Figure 5-2 shows a cross-section of the plane of the flow and illustrates how the asperities can block the flow. The blockage of the flow by asperities depends on their number, size, orientation, and shape. The parameter γ in Fig. 5-2 characterizes the shape and orientation of the asperities. Greenwood and Williamson⁷ have developed a model that relates the average distance d between the two surfaces to the contact pressure and the statistical distribution of asperity sizes. Their model was developed for an arbitrary distribution, but takes on a simple analytical form if the distribution is assumed to be exponential. Since the roughness distribution is usually assumed to be Gaussian and an exponential distribution gives similar results, the simple analytical form has been used.

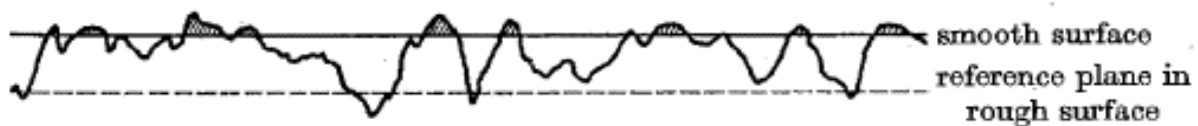


Figure 5-1 Schematic Illustration of Contact Between a Rough Surface and a Smooth Surface

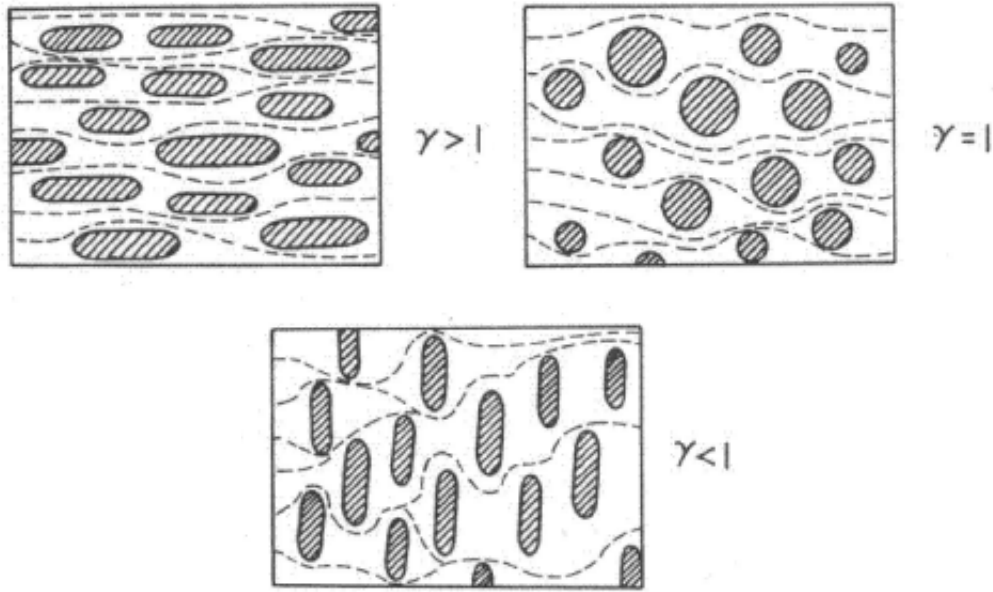


Figure 5-2 Representation of Flow Across Asperities Where the Parameter γ Characterizes the Shape and Orientation of the Asperities

In this case, the relation between the contact pressure p_c and the average distance d between the surfaces is given by

$$p_c = \alpha e^{-h} \quad (15)$$

where $h = d/\sigma$ and σ is the standard deviation of the surface roughness. For two smooth plates separated by a distance, the solution for viscous dominated flow is the well-known Couette flow and the loss coefficient K is proportional to $1/d^3$. Patir and Cheng⁸ have considered the case where the plates are not smooth and the flow channel is partially blocked by asperities. In this case

$$K = \frac{12}{\phi d^3} = \frac{12}{\phi \sigma^3 h^3} \quad (16)$$

where $\phi = 1 - 0.90e^{-0.56h}$ represents the fraction of the channel blocked by the asperities for the isotropic case $\gamma = 1$. As h gets large, a smaller fraction of the channel is blocked by the asperities q ; as $h \rightarrow \infty$, $\phi \rightarrow 1$ and K reduces to the value for Couette flow.

5.3 Validation of Leak Rate Model Using Westinghouse Data

A series of pullout and leakage tests that was carried out by Westinghouse (WCAP-15932-P)⁹ on tube-to-collar junction specimens (to simulate tube-to-tubesheet junctions) can be used to estimate the friction and contact pressures existing in these specimens and benchmark the ANL leakage model. [

]a,c,e

[

]a,c,e

Figure 5-3 Variation of the Thermal Expansion Coefficients of []a,c,e, A508 Forging and Alloy 600 Tube with Temperature

5.3.1 Pullout Tests

Pullout tests were conducted by Westinghouse at [

] a,b,c For the purpose of calculating the contact pressure during the leak rate tests, the initial slip loads are of the greatest relevance. Therefore, the 600°F pullout tests were analyzed by FEA up to the initial slip loads. Analysis of the test beyond the initial slip is difficult because of the gouging and scratching that occur once the tube starts to pull out over significant distances. Westinghouse did not analyze the tube expansion process, but analyzed the pullout tests using a shear lag model to account for the variation of the axial stress with distance into the tube sheet, the resulting Poisson effect on the contact stress, and a friction factor of []a,c,e to estimate the values of the contact pressure existing prior to the pullout tests.

The tube expansion process as well as the tube pullout tests were analyzed by using elastic-plastic FEA including contact and slippage at the interface. Several analyses were conducted, as shown in Fig. 5-4, to determine the effect of the friction factor on the pullout load for different expansion pressures, which resulted in different contact pressures. The tube expansion pressure, i.e., the contact pressure, has a more significant effect on the pullout curve than the friction factor. After reviewing the literature on the relevant friction factors, a value of friction factor = 0.4 was selected as a best estimate value. The contact pressure at 600°F is

significantly higher than that at room temperature because mismatch between the thermal expansion coefficients of Alloy 600 and []^{a,c,e} (Fig. 5-3). The calculated pullout load-displacement results plotted in Fig. 5-5 show that the initial slip loads of the pullout tests are consistent with a tube expansion pressure of 228 MPa (33 ksi), which is, somewhat higher than the reported value of []^{a,c,e}, but is not unreasonable.

[

] ^{a,c,e}

Figure 5-4 Effect of Friction Factor and Tube Expansion Pressure on the Pullout Load vs. Displacement Plot

[

]a,c,e

Figure 5-5 Comparison of Calculated vs. Observed Initial Slip Loads for the Pullout Tests at 600°F

5.3.2 Contact Pressure

Analysis of the pullout tests by either FEA or the shear lag model shows that the contact pressures at 600°F must be on the order of []^{a,c,e}. Figure 5-6 shows the distribution of the calculated contact pressure along the length of the specimen at 600°F corresponding to expansion pressures of 33 (solid lines) and 221 MPa (314 MPa (2 ksi)) (dashed lines) and yield stress of the tube of []^{a,c,e} as reported by Westinghouse for the tubes in the experiments.^[9] As noted, to match the pullout data, an expansion pressure of 228 MPa (33 ksi) was assumed. With this expansion pressure, the contact pressure is ~ []^{a,b,c} at room temperature and []^{a,b,c} at 600°F. Although the total contact pressures (2000 psi) calculated in this report and Westinghouse agree, the splitting of the contact pressure between the expansion process and the thermal mismatch effect differs significantly. Westinghouse did not directly calculate the stresses due to the expansion process, but they estimate that the thermal component of the contact pressure is only []^{a,b,c} and thus that the bulk of the contact pressure is due to the expansion process, which is exactly opposite to the results of the calculations used in this report. ANL believes that this is because Westinghouse used thermal expansion properties of A508 in their calculations although the specimen collars were []^{a,c,e} which has a different thermal expansion coefficient (Fig. 5-3). The implied residual pressure of 1500 psi is totally inconsistent with the reported yield strengths and expansion pressures once account is taken of the actual thermal expansion properties of []^{a,c,e}

[

] ^{a,c,e}

Figure 5-6 Variation of the Calculated Contact Pressure Along the Specimen Length at Room Temperature and 600°F in the Absence of Internal Pressure [The dashed curves are for an expansion pressure of 221 MPa (314 MPa (2 ksi)); the solid curves are for an expansion pressure of 228 MPa (33 ksi)]

[

]a,c,e

Figure 5-7 Variation of the Contact Pressure at Room Temperature and 600°F with Internal Pressure

Since the Westinghouse leak rate tests were conducted with internal pressure, the distribution of the contact pressure at room temperature and 600°F were calculated for two values of internal pressure, as shown in Fig. 5-7. Comparison of Figs 5-6 and 5-7 shows that internal pressure increases the contact pressure significantly.

A simplified expression for the contact pressure can be deduced from the ABAQUS results

$$p_{co} = 0.79 p_i + 2.9(T - 70) + p_{residual} \quad (17)$$

where p_i is the internal pressure (psi), T the temperature (°F), and $p_{residual}$ is the contact pressure due to the hydraulic expansion. It is not clear how to model the effect of the fluid pressure in the space between the tubesheet and the tube on the contact pressure, i.e., whether to account for the reduction in area over which the fluid acts. Additional experiments in which the internal pressure and the fluid pressure are varied in a controlled manner are needed for a better understanding. For the purposes of the current calculations, it was assumed that the actual area in metal to metal contact is small and that the fluid pressure acts directly to reduce the contact pressure

$$p_c = p_{co} - p_f \quad (18)$$

For the Callaway experiments, the fluid pressure near the flow holes between the inner portion of the tube and the tube sheet simulator is assumed to be equal to the internal pressure and it drops to atmospheric at the top of the tubesheet simulator. This should give conservative results since in the actual situation, a crack would be constrained by the tubesheet and the crack opening will be tight so that there could be a pressure loss through the tube. For single phase conditions, the flow rate is proportional to the length L of the region of contact pressure, but the pressure drop is not linear since the loss coefficient varies because the contact pressure varies along the length of the tube in accordance with Eq. (18). Examples of pressure-drop profiles for incompressible, compressible, and two-phase flows are shown in Fig. 5.8.

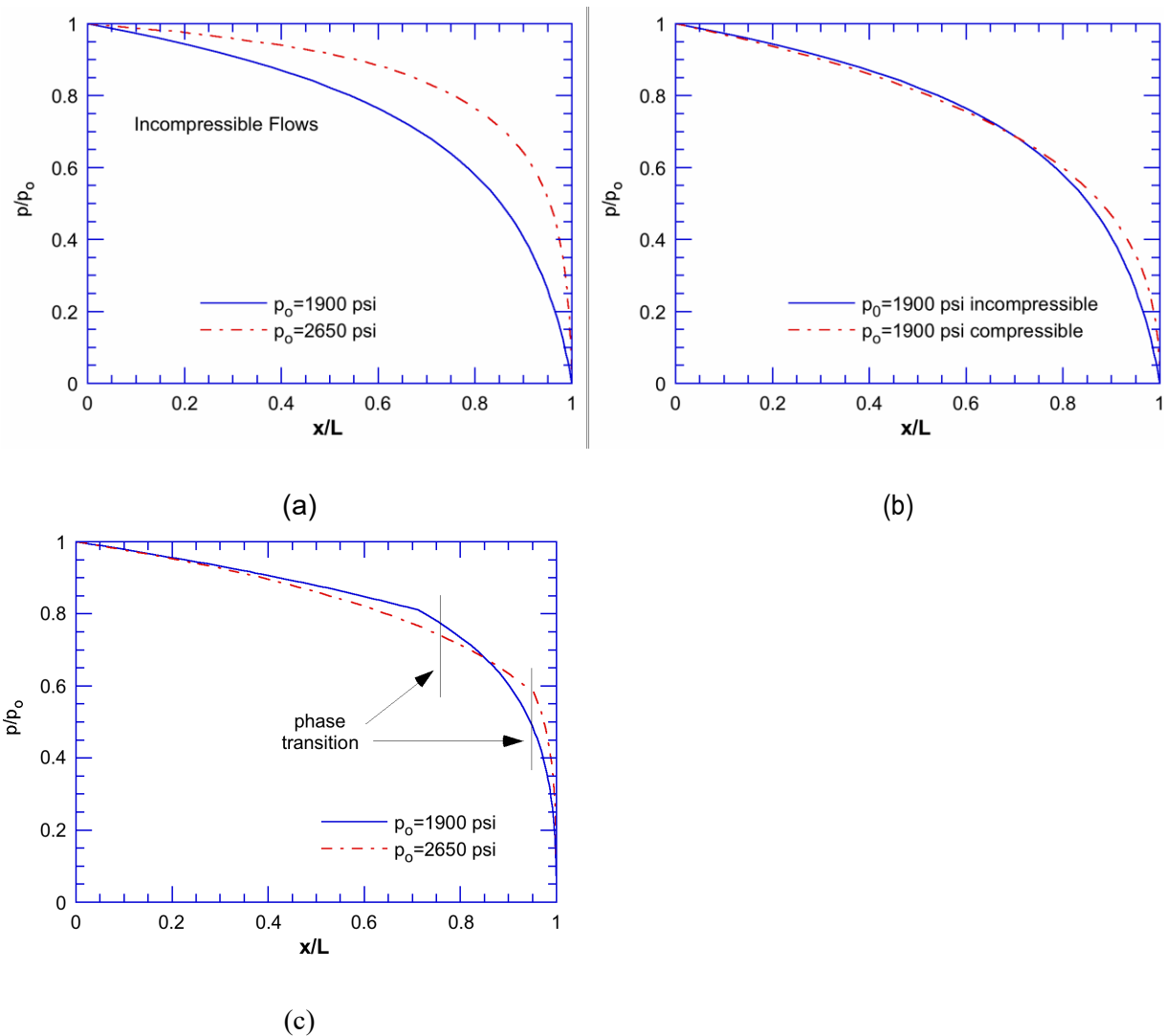


Figure 5-8 Non-dimensional Pressure Drop Profiles for (a) Incompressible Flows with Initial Pressures of 1900 and 2650 psi; (b) Incompressible and Compressible Flows with an Initial Pressure of 1900 psi; and (c) Two-phase Flows at 600°F with Initial Pressures of 1900 and 2650 psi

There are basically three parameters in the roughness model. One is the surface roughness, which based on information from B&W should be between 3-6 μm (125-250 μin) and in practice is probably closer to the lower end of the range. Another is a cut-off on the Gaussian distribution for the roughness. Gaussian distributions have infinite tails, which is unrealistic for surface roughness. One solution would be to use distributions which are finite, but a simple alternative is to truncate the Gaussian distribution. Truncation at the 95/5 percentile would give a distribution width of 3.3σ ; truncation at the 99/1 percentile would give a width of 4.6σ . The third parameter, (α in Eq. (15)), depends on the elastic properties, roughness, density of asperities, and asperity shape, is more difficult to estimate a priori.

It is difficult to try to fit the leakage model to the Callaway test results [9], because few details are given about the tests. The tests were done with specimens with normal collar fits and specimens with oversize clearances that would tend to reduce the initial contact pressures due

to the expansion. The summary of the test results in Fig. 6.18 of the WCAP [9] gives results in terms of a contact pressure that includes only the internal pressure and temperature induced stresses, not the contribution from the initial hydraulic expansion. Thus what appears to be scatter in the plot may actually reflect an expected variation due to the variation in contact pressure due to different conditions for the initial expansion. In addition, the contact pressures given in Fig. 6.18 appear to include a thermal contribution based on properties of A508 while the actual collars are []^{a,c,e} which has different thermal expansion properties.

The analysis of the pullout tests suggest that the highest contact pressures due to the hydraulic expansion are about []^{a,b,c}. Sensitivity studies show that for the high yield stress materials used for the Callaway tests, hydraulic expansion at the reported pressures would result in low contact stresses. Thus the contact stresses due to hydraulic expansion examined range from 0–450 psi and 100–450 psi.

[

] ^{a,b,c}

The three fitting parameters for the roughness model were varied to try to match the reported results. The high contact pressure results for an internal pressure of [

] ^{a,b,c} are the best defined tests. The contact pressures were assumed to have a high and low value, depending on whether the collars were nominally sized or oversized. The fitting was done for three sets of expansion contact stresses, one where the contact pressures were varied as part of the fitting process, one with contact pressures of 50 and 500 psi, and one with 100 and 450 psi. The results are summarized in Table 2. Measured values are [] ^{a,b,c} at room temperature and [] ^{a,b,c} at 600°F. The agreement for all sets of contact pressures is reasonably good. The values for the roughness and the effective width of the Gaussian distribution for the roughness are consistent with typical values.

It is difficult to compare with Fig. 6.18 of the WCAP [9], because it appears that the contact pressures are incorrect due to incorrect coefficients of thermal expansion. The points plotted in Fig. 6.18 also must represent average values of K, since the contact pressure and K actually vary along the length. It is not clear how these average values were defined for the two-phase flow case.

Table 5-1 Predicted Leak Rates for the Callaway Tube/Tubesheet Test Specimens (drops/minute)

Parameters varied in data fitting	Model Parameters					Range of Leak Rates	
	log10 a	Roughness (μm)	Gauss Width	pc oversize collars (psi)	pc nominal collars (psi)	RT Tests	600°F Tests
All	2.34	4.32	3.06	0.00	537.76	[] ^{a,b,c}	[] ^{a,b,c}
Fix Contact Pressures	2.33	4.58	2.88	50.00	500.00	92-238	17-102
Fix Contact Pressures	2.31	4.99	2.62	100.00	450.00	103-220	18-93

5.3.3 Conclusions

The process of hydraulic tube expansion at []^{a,c,e} creates a uniform residual contact pressure of 3.5 MPa (0.5 ksi) between the []^{a,c,e} diameter Alloy 600 tube and the []^{a,c,e} collar. The residual plastic strain in the tube is 2%.

At 600°F, the contact pressure increases to 14 MPa (2 ksi) and remains uniformly distributed along the length.

The variations in the contact pressures due to the thermal and expansion effects, calculated indirectly by Westinghouse, are different than those calculated by ANL. This may be due to an incorrect choice of thermal expansion coefficients for the test samples by Westinghouse.

The experimentally observed initial slip loads at 600°F can be predicted by assuming a tube expansion pressure of []^{a,c,e} which is slightly higher than the reported value of []^{a,c,e}.

When the tube is subjected to an internal pressure of []^{a,c,e} the contact pressure at 600°F increases to 23.4 MPa (3.4 ksi), which will have an important effect on limiting the leak rate.

A leak rate model has been developed based on the Greenwood and Williamson model for rough surfaces and the Patir and Cheng model for fluid flow in channels blocked by asperities. Combined with the contact stresses predicted by the FEA analysis, the parameters in the model can be chosen to give good agreement with the reported data. The values of the parameters determined by the fitting procedure are not inconsistent with those expected from the physical assumptions of the model.

6 DESIGN OF TUBE-TO-COLLAR JUNCTION TEST SPECIMEN

If the tube-to-collar specimen is to truly simulate the leakage behavior of the tube-to-tubesheet junction, both must have the same contact pressure at all times during the severe accident. At a practical level, this is something impossible to achieve. At a minimum, the contact pressures developed after tube expansion should be comparable in both cases. This can be achieved if the collar is designed such that its radial elastic stiffness is the same as that of the tubesheet. Nonetheless, the contact pressure distribution during the severe accident transient would be different in the two cases even if the tube-to-collar specimens were subjected to the same severe accident transient as the tube-to-tubesheet junction. As mentioned earlier, the tube-to-collar specimens were not subject to transient thermal loading during the tests. Instead, ANL relied on their analytical ability to calculate contact pressures and leak rates using leak rate correlations. Therefore, ANL developed leakage rate correlations experimentally under constant temperature conditions over a sufficiently wide range of contact pressures to support application of the correlations to the accident situation. To do this effectively ANL needed the ability to independently control the tube internal pressure and the driving leakage pressure in our tests.

6.1 Development of Elastic Properties of Equivalent Tubesheet Material

As mentioned before, the TS is a porous plate with thousands of holes drilled transverse to the plate midplane. The presence of the holes makes the in-plane properties of the plate different from its transverse properties, i.e., it is orthotropic (transversely isotropic). In an FEA of the plate, the inhomogeneous porous plate is generally replaced by a homogeneous solid plate of equal thickness with equivalent orthotropic elastic properties.

The orthotropic elastic constants for the equivalent homogeneous TS were determined from elastic FEA of the unit cells (Figs. 6-1a-b), by applying successively displacements corresponding to unit strain of a single component of the strain tensor while keeping all the other components equal to zero. At the same time, sufficient constraints were applied to ensure that the displacements of neighboring cells are mutually compatible. Typical deformed and undeformed shapes of a unit cell corresponding to a normal strain and a shear strain are shown in Figs. 6-2 a-b, respectively.

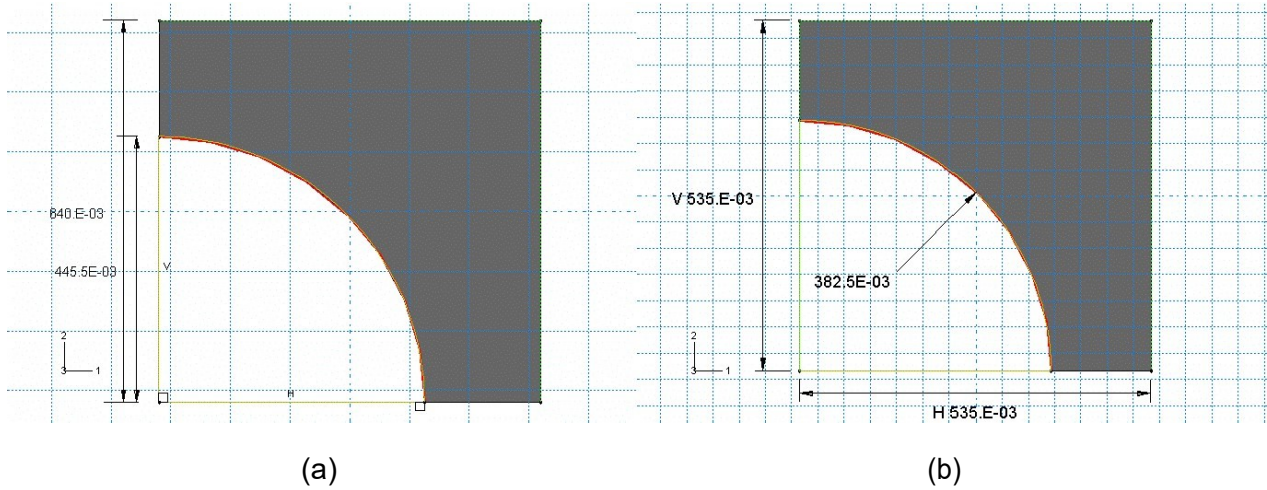


Figure 6-1 Plan Views of a Quarter of a Tubesheet Unit Cell for Square Arrays with (a) 32.5 mm (1.28 in.) Pitch and 22.6 mm (0.891 in.) Tube Hole Diameter for 22.2 mm (0.875 in.) Diameter SG Tubes and (b) 27.2 mm (1.07 in.) Pitch and 19.4 mm (0.765 in.) Tube Hole Diameter for 19.1 mm (0.75 in.) Diameter SG Tubes

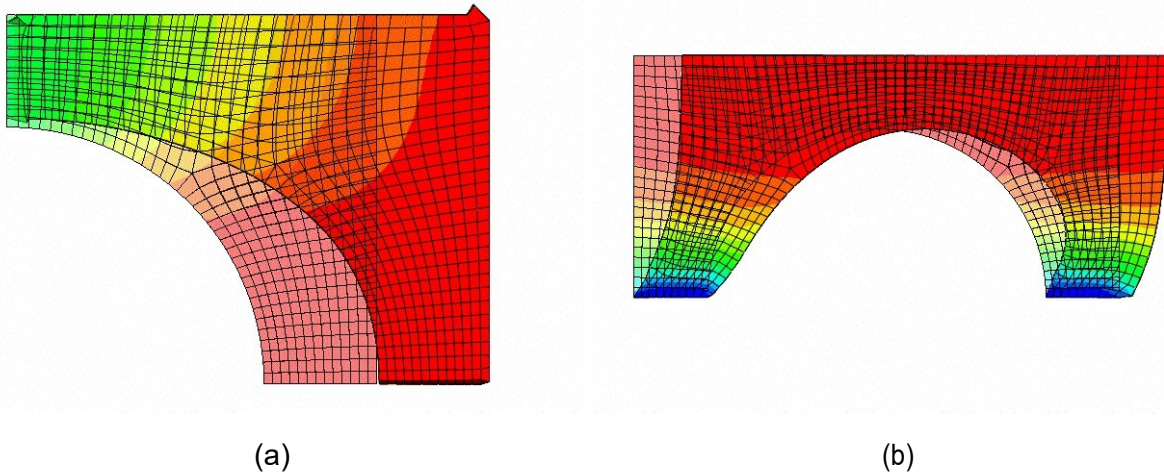


Figure 6-2 Typical Deformed and Undeformed Shapes of a Unit Cell Corresponding to a (a) Normal Strain and (b) a Shear Strain

Using r (radial or 1), z (axial or 2) and θ (circumferential or 3) coordinates for the tubesheet, the orthotropic elastic stress-strain law can be represented by Eq. (19).

$$\begin{Bmatrix} \sigma_r \\ \sigma_z \\ \sigma_\theta \\ \tau_{rz} \\ \tau_{r\theta} \\ \tau_{z\theta} \end{Bmatrix} = \begin{bmatrix} D_{1111} & D_{1122} & D_{1133} & 0 & 0 & 0 \\ D_{1122} & D_{2222} & D_{1122} & 0 & 0 & 0 \\ D_{1133} & D_{1122} & D_{1111} & 0 & 0 & 0 \\ 0 & 0 & 0 & D_{1212} & 0 & 0 \\ 0 & 0 & 0 & 0 & D_{1313} & 0 \\ 0 & 0 & 0 & 0 & 0 & D_{1212} \end{bmatrix} \begin{Bmatrix} \varepsilon_r \\ \varepsilon_z \\ \varepsilon_\theta \\ \gamma_{rz} \\ \gamma_{r\theta} \\ \gamma_{z\theta} \end{Bmatrix} \quad (19)$$

The elastic constants D_{ijkl} for the TS with 22.2 and 19.1 mm (0.875 and 0.75 in.) diameter tubes were determined as functions of temperature and incorporated them into the finite element code ABAQUS. Alternatively, the elastic constants can be expressed in terms of in-plane effective Young's moduli and Poisson's ratios, effective transverse moduli, and effective shear moduli. The in-plane effective Young's moduli and Poisson's ratios for the two arrays under consideration are plotted as functions of temperature in Figs. 6-3 a-b. The corresponding transverse effective moduli and effective shear moduli are plotted in Figs. 6-4 a-b. As expected, the in-plane elastic stiffnesses are significantly smaller than the transverse elastic stiffnesses. Also, note that the effective elastic constants for the two geometries are quite similar to each other.

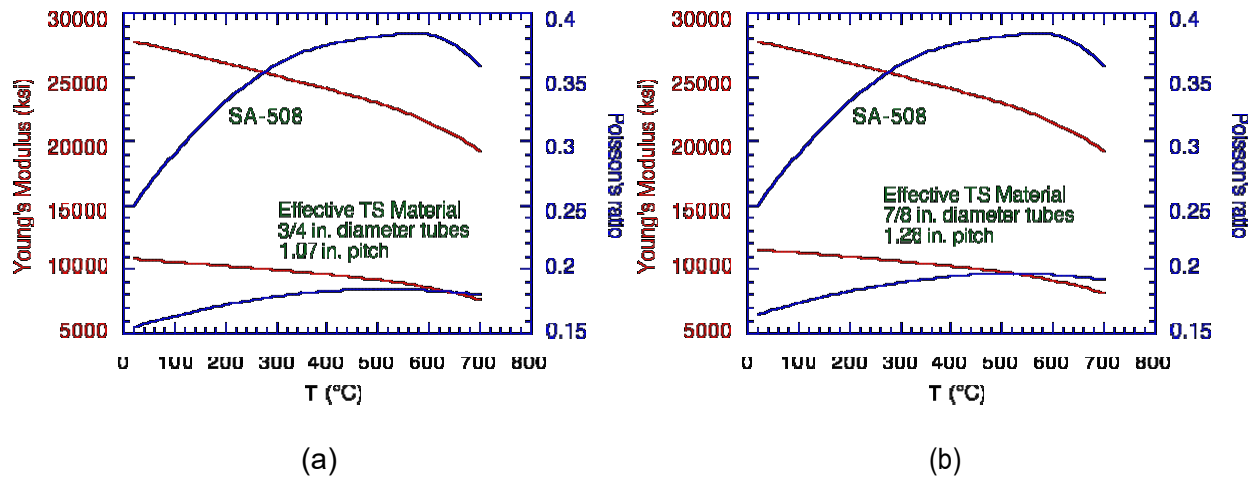


Figure 6-3 Elastic Constants of SA-508 and Effective In-Plane Isotropic Elastic Constants for a TS with Square Array of Holes with (a) 19.4 mm (0.765 in.) Diameter Holes Set at a Pitch of 27.2 mm (1.07 in.) and (b) 22.6 mm (0.891 in.) Diameter Holes Set at a Pitch of 32.8 mm (1.28 in.)

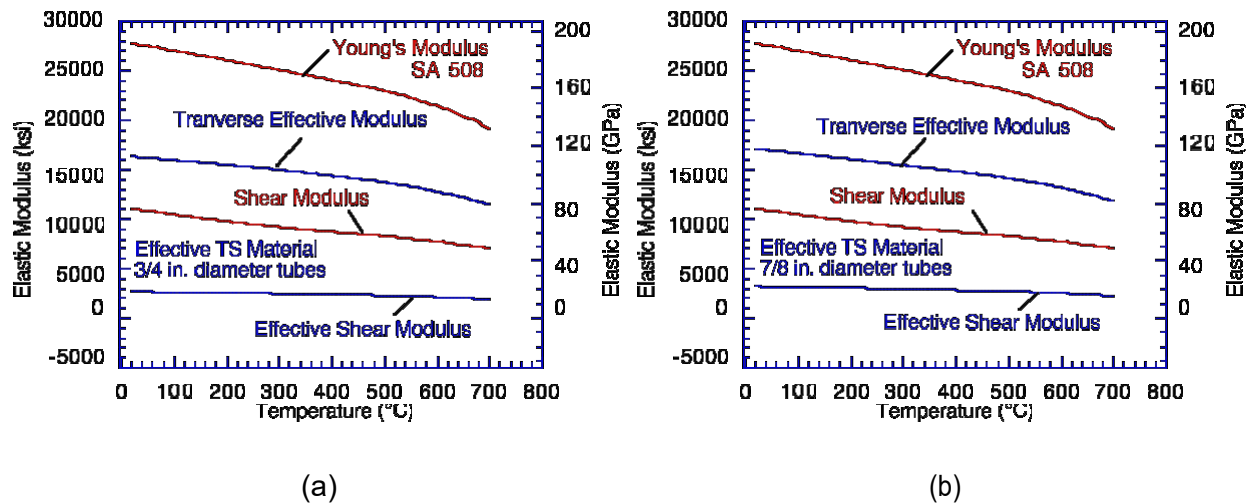


Figure 6-4 Young's Modulus and Shear Modulus of SA508 (red) and Effective Transverse Elastic Constants and Effective In-Plane Shear Moduli (blue) for a TS with Square Array of Holes with (a) 19.4 mm (0.765 in.) Diameter Holes Set at a Pitch of 27.2 mm (1.07 in.) and (b) 22.6 mm (0.891 in.) Diameter Holes Set at a Pitch of 32.8 mm (1.28 in.)

6.2 Tubesheet and Collar Stiffness Analyses

The design of the tube-to-collar junction specimen was intended to ensure that the contact pressure created during hydraulic expansion of the tube-to-collar specimen would be the same as that created in a real tube-to-tubesheet junction. To do this, first an elastic analysis of a tubesheet with a single hole (without a tube) at the center of the tubesheet was performed, an arbitrary radial pressure was applied on the hole surface, and the radial stiffness of the tubesheet was calculated. Similarly, elastic analyses of the collar of the tube-to-collar specimen (without the tube) was conducted and determined its radial stiffness as a function of the outer diameter of the collar. Finally, the outer collar diameter was selected so that the two stiffnesses were equal.

6.2.1 Tube-to-Tubesheet Junction

Two-dimensional axisymmetric finite element models of a 533.4 mm (21 in.) thick, 1270 mm (50 in.) radius, SA508 steel TS with a 22.6 mm (0.891 in.) diameter tube hole (22.2 mm [0.875 in.] diameter Alloy 600 tube) and a similar tubesheet with a 19.4 mm (0.765 in.) diameter tube hole (19.1 mm [0.75 in.] diameter Alloy 600 tube) at its center were developed. The hole was surrounded by a thin ring of solid A508 whose radius was 13.6 mm (0.535 in.) for the 19.4 mm (0.765 in.) hole and 16.3 mm (0.64 in.) for the 22.6 mm (0.891 in.) hole. The inhomogeneous tubesheet beyond the solid ring was replaced by homogeneous tubesheets with equivalent orthotropic elastic properties as determined in section 6.1.1. A typical geometry of the setup is shown in Fig. 6-5. The radial elastic deformation was determined from a FEA of the model with an arbitrary radial pressure of 172 MPa (25 ksi) acting on the hole surface.

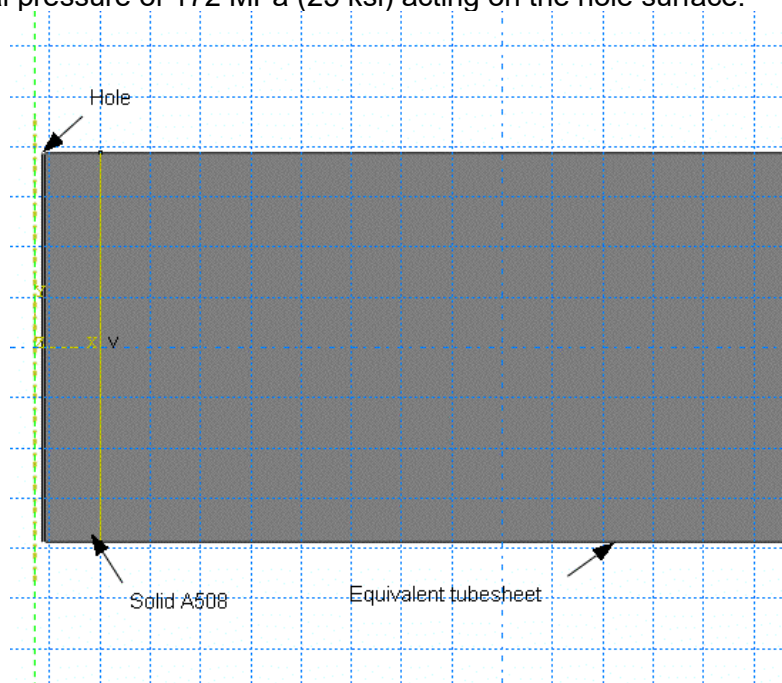


Figure 6-5 Axisymmetrical Model of a Tubesheet with a Single Hole

6.2.2 Tube-to-Collar Junction

A typical axisymmetric model of the collar with a central hole is shown in Fig. 6-6. The hole diameter in the collar is the same as the hole diameter in the corresponding tubesheet. The collar is often called a tubesheet simulant because it replaces the actual tubesheet in the laboratory tests. The radial elastic deformation was determined from a series of FEA of the collar with various outer radius and with the same arbitrary radial pressure of 172 MPa (25 ksi) acting on the hole surface.

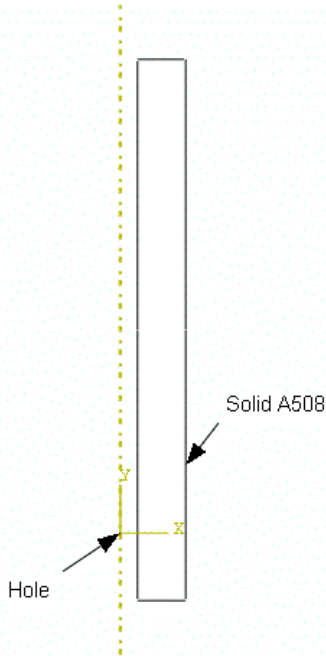


Figure 6-6 Axisymmetric Model of a Collar with Hole

6.3 Selection of Collar Dimensions

The variation of radial displacement at the inner surface of a collar as a function of its outer diameter for hole diameters of 19.4 and 22.6 mm (0.765 and 0.891 in.) are plotted in Figs. 6-7a-b, respectively. An arbitrary pressure of 172 MPa (25 ksi) is applied. The same figures also show the radial displacement at the surface of the hole in a tubesheet as a function of the radius of the tubesheet for two different tubesheet geometries. Note that the radial displacement of the tubesheet is relatively insensitive to its outer diameter. The intersections of the two sets of curves determine the outer diameters of the collars.

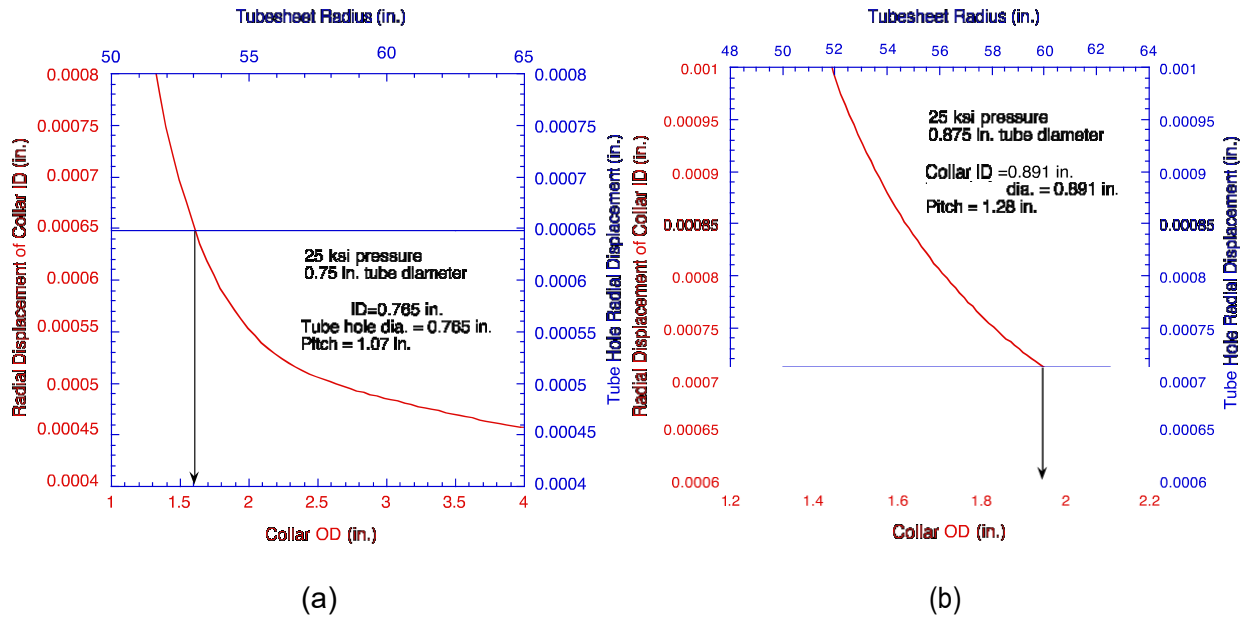


Figure 6-7 Variation of Radial Displacement at the Hole Surface of a Collar and a Tubesheet of Various Radii at 172 MPa (25 Ksi) Applied at the Surface of the Hole with Diameter (a) 19.4 mm (0.765 in.) and (b) 22.6 mm (0.891 in.)

6.4 Specimen Design

Based on our collar analyses, the two geometries shown in Figs 6-8a-b were chosen for the test specimens. The expanded lengths are 50.8, 101.6, and 203.2 mm (2, 4 and 8 in.), which represent the distances of cracks from the top of tubesheet. The tubes can be internally pressurized through the hole in one of the end plugs. The crevice can be independently pressurized through the annular inlet plenum and the 3.2 mm (0.125 in.) diameter lateral hole in the collar. The integrity of the seal weld is critical, and its leak tightness was checked by the vendor by helium leak tests prior to delivery.

6.4.1 Selection of Hydraulic Expansion Pressure

To select representative hydraulic expansion pressures, Westinghouse and Babcock and Wilcox (B&W), Canada were contacted for data. [

]a,c,e

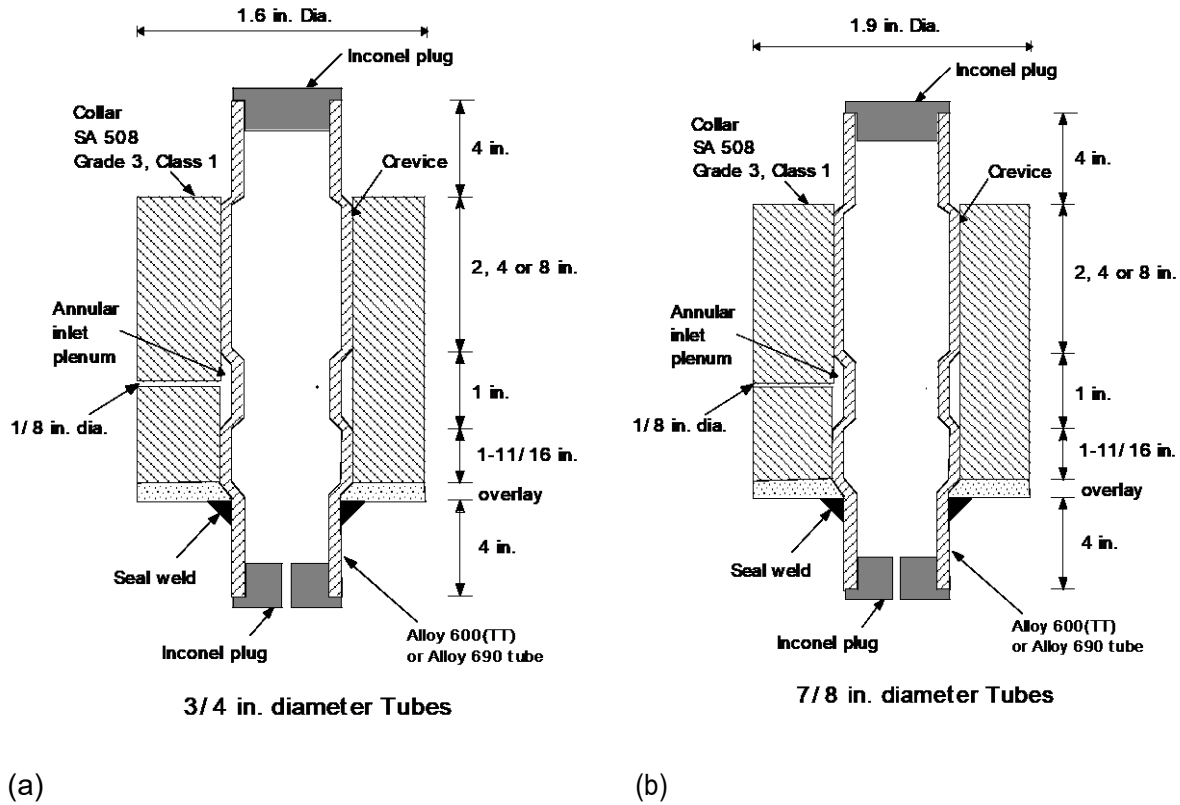


Figure 6-8 Tube-to-Collar Specimen Design for (a) 19.1 mm (0.75 in.) and (b) 22.2 mm (0.875 in.) Diameter Tubes

The expansion pressures would be different for triangular pitch. For SGs built between early 1979 through 1981, the process specification revisions (Rev 4 through 10) provide only an intensifier pressure control specification of [

]a,c,e

B&W, Canada uses Alloy 690 tubes with 35200 to 35700 psig hydraulic pressure for 19.1 mm (0.75 in.) tube (Thk. = 1.07 ± 0.10 mm [0.042 ± 0.004 in.]) and 37500 to 38000 psig hydraulic pressure for 22.2 mm (0.875 in.) tube (Thk. = $1.24 \pm .13$ mm [0.049 ± 0.005 in.]). They do not use Alloy 600 tubes in their SGs. B&W, Canada advised us that, based on their experience, the joints will be “loose” if expanded with 214 MPa (31 ksi) expansion pressure. Their recommended pressures for our specimens, based on Westinghouse numbers that they have access to, are 31000 to 31500 psig for 19.1 mm (0.75 in.) tubes and 33500 to 34000 psig for 22.2 mm (0.875 in.) tubes.

A series of analyses were conducted to investigate the effect of hydraulic expansion pressure, tube internal pressure and temperature on the tube-to-collar contact pressure. The thermal stress calculations reported in this section were conducted using ASME code values of thermal expansion coefficients. In all cases, an initial diametral clearance of 0.38 mm (0.015 in.) was assumed to exist between the tube OD and the collar ID surfaces. The results for 19.1 mm (0.75 in.) diameter tubes (heat NX8524, yield stress = 296 MPa (43 ksi)) and 22.2 mm (0.875 in.) diameter tubes (heat EX-82-1, yield stress = 359 MPa (52 ksi)) at zero and 17.2 MPa (2.5 ksi) internal pressures are plotted in Figs. 6-9a-b, respectively. For clarity, the results for heat NX 8520L of the 22.2 mm (0.875 in.) diameter tubes are not presented here but will be discussed later. The change in the contact pressure with temperature due to differential thermal expansion coefficients between Alloy 600 and A508 steel was included. The contact pressures plotted in Figs. 6-9a-b represent the maximum contact pressures that will be relaxed by creep with time depending on the temperature. The hatched areas in Figs 6-9a-b represent the calculated spread in the contact pressures at various temperatures due to a variation in the hydraulic expansion pressure between 214 and 234 MPa (31 and 34 ksi). The maximum contact pressure initially increases with temperature reaching a maximum at 300°C beyond which it decreases. Figure 6-9a shows that a minimum contact pressure of 12.4 MPa (1.8 ksi) between the collar and the 19.1 mm (0.75 in.) tube is generated at room temperature, at $\Delta P=0$, and for a hydraulic expansion pressure of 214 MPa (31 ksi). The maximum contact pressure for the same tube is 35 MPa (5 ksi), which is generated at 300°C, at $\Delta P=17.2$ MPa (2.5 ksi), and for a hydraulic expansion pressure of 234 MPa (34 ksi). Figure 6-9b shows that the corresponding minimum and maximum contact pressures for the 22.2 mm (0.875 in.) tube are 2.1 and 26.2 MPa (0.3 and 3.8 ksi), respectively.

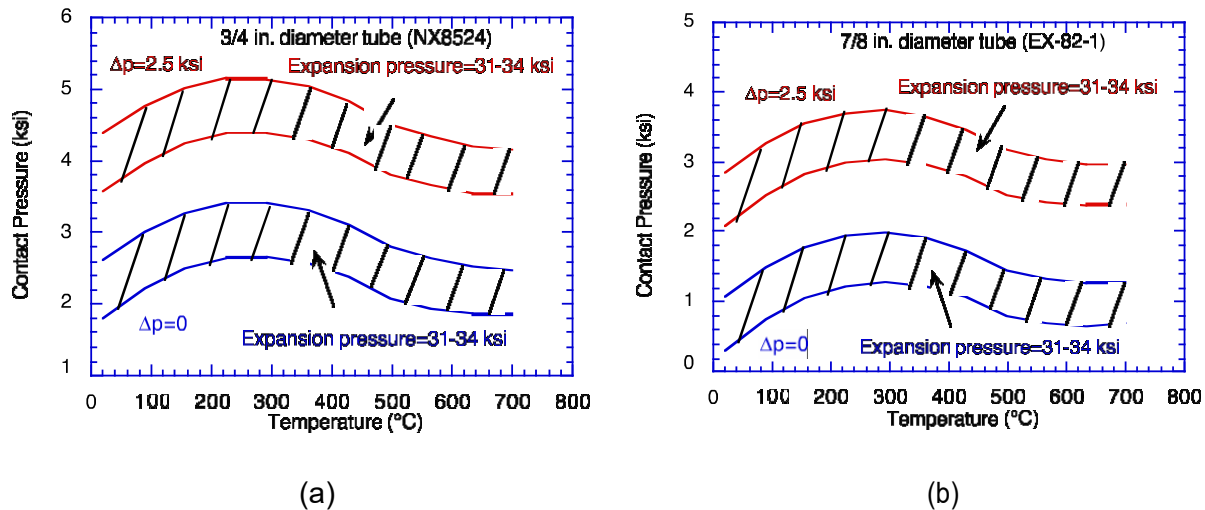


Figure 6-9 Variation of Tube-to-Collar Contact Pressure with Temperature for Various Hydraulic Expansion Pressures and Zero and 17.2 MPa (2.5 ksi) Differential Pressures Acting on (a) 19.1 mm (0.75 in.) Diameter (Heat NX8524) and (b) 22.2 mm (0.875 in.) Diameter (Heat EX-82-1) Tubes

It should be noted that, depending on the hydraulic expansion pressure used, the contact pressures during normal operation ($T=300^{\circ}\text{C}$ and $\Delta P=1.3$ ksi) for uncracked tubes will be somewhere between 24.1 and 29.6 MPa (3.5 and 4.3 ksi) for the 19 mm (0.75 in.) tubes and

between 15.2 and 19.3 MPa (2.2 and 2.8 ksi) for the 22 mm (0.875 in.) tubes, both distributed uniformly along the length.

At the start of the severe accident, the ranges of contact pressure possible for tubes with cracks are the same as those during normal operation. Again, all these values represent the absolute maximum values possible for contact pressures all occurring at the start of the severe accident. With increasing temperature, the contact pressures will be reduced because of a decrease in the difference in thermal expansion coefficients of the tube and the tubesheet. During the severe accident, when the temperature is increasing and the secondary side pressure is decreasing, their effects on the contact pressure will be counter acting, i.e., the increasing temperature will tend to reduce the contact pressure but the reducing secondary side pressure will tend to increase the contact pressure. Once the secondary side is fully depressurized, the pressure differential (ΔP) will stay relatively constant at 16.2 MPa (2.35 ksi) during most of the severe accident. If creep effects are ignored, the maximum possible contact pressure at the interface can range between 24.8 and 29 MPa (3.6 and 4.2 ksi) for the 19.1 mm (0.75 in.) diameter tube and between 16.5 and 20.7 MPa (2.4 and 3.0 ksi) for the 22.2 mm (0.875 in.) diameter tubes. These contact pressures may be further reduced with time due to thermally induced creep.

If the tubes have through-wall leaking cracks within the tubesheet, the leakage through the annulus will create a pressure differential (ΔP) field across the tube wall that will vary in the direction of the leakage. The boundary conditions on the leaking fluid will dictate that (1) the fluid pressure in the annulus at the crack location is 16.2 MPa (2.35 ksi), i.e., pressure differential on the tube wall is zero and (2) the fluid pressure at the leakage flow exit at the top of tubesheet is zero, i.e., the pressure differential is 16.2 MPa (2.35 ksi). This axial variation in the pressure differential (ΔP varying between 0 and 16.2 MPa (2.35 ksi)) acting on the tube will create a corresponding variation in the contact pressure that will be minimum at the crack location and maximum at the top of tubesheet. The exact variation will be calculated automatically with the one-dimensional leakage flow model. Therefore, it was necessary to develop the leakage correlation for a wide range of contact pressures – from 24.8 and 29 MPa (3.6 and 4.2 ksi) for the 19.1 mm (0.75 in.) tubes and from 16.5 and 20.7 MPa (2.4 and 3.0 ksi) for the 22.2 mm (0.875 in.) tubes. The minimum values of the ranges may have to be further lowered if significant relaxation of the contact pressure occurs due to creep.

Our initial plan for determining the leakage flow vs. contact pressure correlation curves was to derive them from tests conducted at room temperature, the range of contact pressures that can be generated by varying the hydraulic expansion pressure and tube internal pressure at room temperature are of interest. Our experimental set up limits our ability to vary the tube internal pressure and the crevice inlet plenum pressure independently between 0 and 17.2 MPa (2.5 ksi). The variation of the contact pressure with the hydraulic expansion pressure and at 0 and 17.2 MPa (2.5 ksi) tube differential pressures are plotted for 19.1 and 22.2 mm (0.75 and 0.875 in.) diameter tubes in Figs. 6-10a-b, respectively.

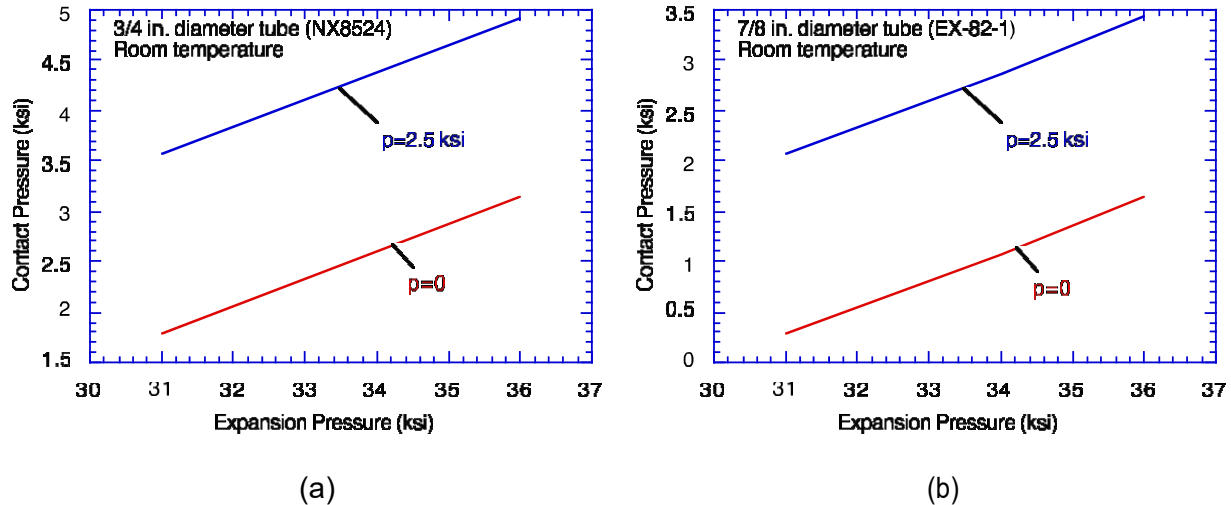


Figure 6-10 Variation of Contact Pressure with Expansion Pressure in (a) 19.1 mm (0.75 in.) Diameter and (b) 22.2 mm (0.875 in.) Diameter Tube-to-Collar Joints at Room Temperature at Internal Pressures of 0 and 17.2 MPa (2.5 ksi)

For the 19.1 mm (0.75 in.) tubes, contact pressures can be generated between 12.4 and 24.1 MPa (1.8 and 3.5 ksi) by using a hydraulic expansion pressure of 214 MPa (31 ksi) and varying the tube differential pressure between 0 and 17.2 MPa (2.5 ksi). The remaining range of contact pressures can be generated between 3.5 and 4.14 MPa (2 ksi) by using a hydraulic expansion pressure of 234 MPa (34 ksi) and varying the tube differential pressure between 1.3 and 17.2 MPa (2.5 ksi). Alternatively, the same range of contact pressure can be generated by using an expansion pressure of 214 MPa (31 ksi), but conducting the test at 300°C with a tube differential pressure varying between 1.4 and 17.2 MPa (2.5 ksi).

For the 22.2 mm (0.875 in.) diameter tubes, contact pressures can be generated between 2.1 and 14.5 MPa (0.3 and 2.1 ksi) by using a hydraulic expansion pressure of 214 MPa (31 ksi) and varying the tube differential pressure between 0 and 17.2 MPa (2.5 ksi) at room temperature. The remaining range of contact pressures can be generated between 14.5 and 20.7 MPa (2.1 and 3.0 ksi) by using a hydraulic expansion pressure of 234 MPa (34 ksi) and varying the tube differential pressure between 2.0 and 17.2 MPa (2.5 ksi).

Thus, depending on the number of contact pressures at which one plans to obtain leakage rate data, the specimens can be fabricated with either 31 or 234 MPa (34 ksi) hydraulic expansion pressures. Thus, covering the entire range of contact pressures expected between normal operating temperature and 700°C can be achieved by suitably choosing the tube differential pressure at room temperature. If using only a single hydraulic expansion pressure of 214 MPa (31 ksi), some of the tests at 300°C must be performed.

Based on the data provided by the vendors and the series of analyses conducted by ANL, ANL decided to use 31,000 psig for expanding all of the 19.1 mm (0.75 in.) tubes and 34,000 psig for expanding all of the 22.2 mm (0.875 in.) tubes. This ensured that the reference contact pressures for both sized tubes are approximately equal and that there was sufficient overlap in contact pressure in the tests to determine whether tube diameter has any significant effect on the leak rate correlations. Test data on heats NX 8520L and NX 8524 (with comparable tensile properties) will capture the effect of tube diameter on the leak rate and those on EX-82-1 and NX 8520L (both of the same diameter) will capture the effect of yield strength on leak rate. The

interfacial contact pressures generated in the tubes during expansion can be simulated at pressures between 214 and 234 MPa (31 and 34 ksi) by selecting appropriate internal pressures and test temperatures. The contact pressure vs. temperature plots in Figs. 6-11a-b and 6-12 represent the maximum contact pressures at any given temperature without accounting for relaxation by creep.

For the 19.1 mm (0.75 in.) tubes, contact pressures can be generated between 12.4 and 30.3 MPa (1.8 and 4.4 ksi) by varying the tube differential pressure between 0 and 17.2 MPa (2.5 ksi). For the 22.2 mm (0.875 in.) diameter tubes, by varying the tube differential pressure between 0 and 17.2 MPa (2.5 ksi), contact pressures can be generated between 1.0 and 25.5 MPa (3.7 ksi) for heat EX-82-1 and between 20.7 and 38.6 MPa (3 and 5.6 ksi) for heat NX 8520L. The higher end of the contact pressure for heat EX-82-1 has to be generated by tests at 300°C. Note that every tube that is subjected to severe accident starts from normal operating conditions when the contact pressures are at their maximum level. The maximum contact pressures created during normal operation are 30.3 (4.4 ksi) for the 19.1 mm (0.75 in.) tubes and 25.5 MPa (3.7 ksi) for heat EX-82-1 and 38.6 MPa (5.6 ksi) for heat NX 8520L of the 22.2 mm (0.875 in.) tubes.

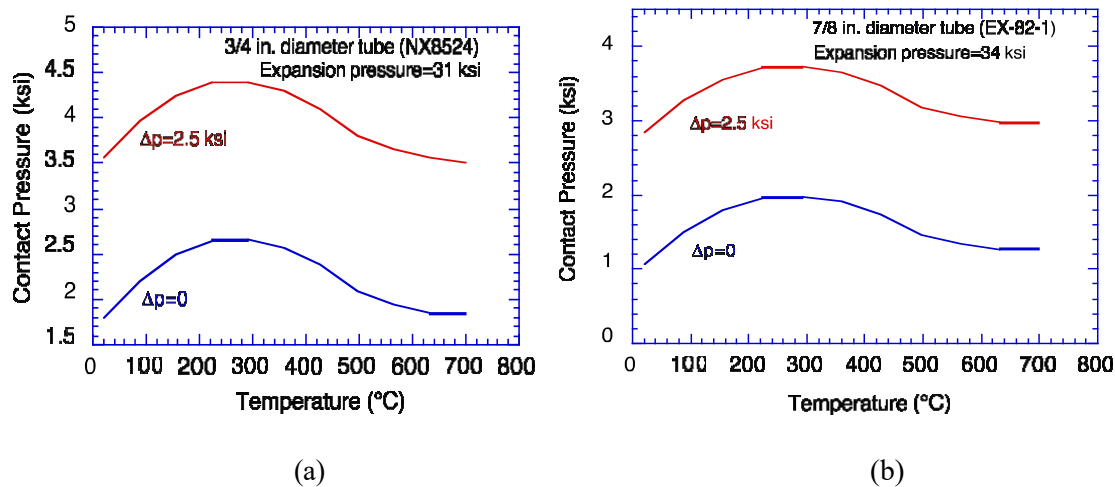


Figure 6-11 Variation of Tube-to-Collar Contact Pressure with Temperature for Zero and 17.2 MPa (2.5 ksi) Differential Pressures Acting on (a) 19.1 mm (0.75 in.) Diameter Tubes (Heat NX8524) Expanded with 214 MPa (31 ksi) Hydraulic Pressure and (b) 22.2 mm (0.875 in.) Diameter (Heat EX-82-1) Tubes Expanded with 234 MPa (34 ksi) Hydraulic Pressure

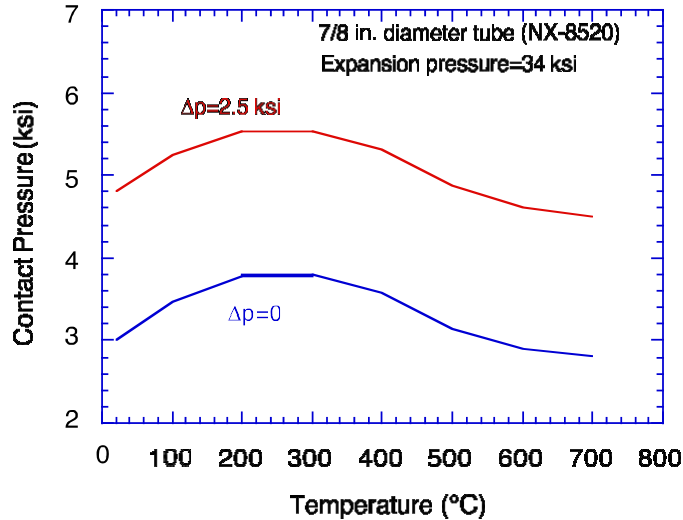


Figure 6-12 Variation of Tube-to-Collar Contact Pressure with Temperature for Zero and 17.2 MPa (2.5 ksi) Differential Pressures Acting on 22.2 mm (0.875 in.) Diameter Tubes (Heat NX8520) Expanded with 234 MPa (34 ksi) Hydraulic Pressure

6.5 Test Matrix

Table 6-1-1 shows the initial test matrix for the 12 leak rate specimens. The nominal initial diametral gap used was 0.41 mm (0.016 in.). This test matrix was later revised based on an initial set of tests, which will be discussed later. To expand the database for leak rate over a range of contact pressures, every specimen was tested at low ($\leq 300^\circ\text{C}$) as well as high temperature ($\geq 500^\circ\text{C}$). The low temperature ($\leq 300^\circ\text{C}$) tests are designed to help develop the leak rate correlations as functions of contact pressure and leakage path length. There should be sufficient overlap in the contact pressure between the tests at these low temperatures to check whether temperature has any effect on the leak rate correlation that is not accounted for in the model. The high temperature tests are designed primarily as validation tests.

Most of the test specimens were made from 22.2 mm (0.875 in.) diameter tubes. However, the tests for the 19.1 mm (0.75 in.) diameter specimens were designed such that there are overlaps in the calculated contact pressures between the 19.1 and 22.2 mm (0.75 and 0.875 in.) tube specimens. This allowed us to verify the predicted dependence of the leak rate on tube diameter.

As mentioned earlier, Babcock and Wilcox (B&W), Canada was contracted to fabricate the specimens using procedures that they follow to fabricate PWR SGs.

Table 6-1 Initial Test Matrix for Leak Rate Tests

Spec. No.	Heat No.	Tube OD, mm (in.)	Hydraulic Expansion		Test Pressure		Test Temp. (°C)	Target Contact Pressure Range (ksi)
			Length, mm (in.)	Pressure (ksi)	Tube Internal (ksi)	Inlet Plenum (ksi)		
W-1	NX8520 L	22.2 (0.875)	50.8 (2)	34	0, 1.25, 2.5	0 - 2.5	20-300 [500, 600, 700]	3.0-5.6
W-2	NX8520 L		101.6 (4)	34				3.0-5.6
W-3	EX-82-1		203.2 (8)	34				1.0-3.7
W-4	NX8524	19.1 (0.75)	203.2 (4)	31				1.8-4.4
W-5	EX-82-1	22.2 (0.875)	50.8 (2)	34	0, 1.25, 2.5	0 - 2.5	20-300 [600, 700]	1.0-3.7
W-6	EX-82-1		101.6 (4)	34				1.0-3.7
W-7	NX8520 L		203.2 (8)	34				3.0-5.6
W-8	NX8520 L	22.2 (0.875)	50.8 (2)	34	0, 1.25, 2.5	0 - 2.5	20-300 [700]	3.0-5.6
W-9	NX8524	19.1 (0.75)	101.6 (4)	31			20-300 [700]	1.8-4.4
W-10	EX-82-1	22.2 (0.875)	203.2 (8)	34			20-300 [700]	1.0-3.7
W-11	EX-82-1	22.2 (0.875)	101.6 (4)	34	0, 1.25, 2.5	0-2.5	20-300 [600, 700]	1.0-3.7
W-12 ^a	NX8520 L	22.2 (0.875)	101.6 (4)	34			20-300 [600, 700]	3.0-5.6

^a This specimen will be tested without the initial thermal cycle

7 LEAK RATE TESTS

7.1 Description of Test Facility

To conduct the tube-to-collar leak experiments a facility was built, which was designed to allow testing under room temperature as well as under prototypic severe accident conditions at pressures of up to 17.2 MPa (2.5 ksi) and temperatures up to 700°C.

Leakage was simulated through the hydraulically-formed contact interface leak path between the tube and the collar. To achieve this, nitrogen gas pressure was supplied to an annular inlet plenum through a 3.2 mm (0.125 in.) supply line welded into the collar (Figs. 7-1a-b). The leak path nitrogen supply annular inlet plenum was formed between two hydraulically expanded zones. The expansion zone, which forms the leak path, is a test parameter chosen as 50.8, 101.6, or 203.2 mm (2, 4, or 8 in.) in length. The contact pressure resulting from the expansion process will strongly influence the potential for leakage as will the amount of creep that occurs over time at the elevated temperature and the differential thermal expansions of the tube and collar materials. In order to allow flexibility in the assessment of the role of contact pressure, varying levels of internal tube pressurization with nitrogen gas was used. This nitrogen is supplied through an end plug in the SG tube, and contact pressure is controlled separately from the leak path annular inlet plenum pressure. To assure that test specimen leakage can only occur along the leak path a seal weld is applied between the tube and the collar. The other end of the test specimens is not sealed between the tube and collar allowing gas to escape if leakage occurs. The test specimens are pressurized by two high-pressure nitrogen supply lines fed by separate source bottles outside of the pit.

The major subsystems of the facility are

- A Furnace test module (1)/controller (2)
- B Room temperature test module
- C Nitrogen pressurization system
- D Leak rate and temperature measurement instrumentation
- E Computer data acquisition system

Two methods / types of instrumentation were used to measure leak flow rate

- 1) For low-flow measurements, pressure decay versus time from a small 500cc intermittently isolated chamber was used.
- 2) For high-flow measurements, a NIST calibrated commercial mass flow meter of upper range 2000 SCCM was used.

The two instruments are connected in series and are located between the nitrogen pressurization source tank and the test specimen located in the pit. They have an intermediate range of measurement overlap for redundancy.

7.2 Leak Rate Specimen Geometrical Characteristics

The tube outside diameters (OD) and thicknesses of all the specimens were measured before they were shipped to B&W. B&W measured the tube inner diameters (IDs) after they were expanded into the collar. From these measurements the initial gaps were estimated. Average dimensions of the specimens are summarized in Table 7-1. Although the standard deviations of the gaps are appreciable relative to their mean values, the calculated contact pressures do not change appreciably even if the gaps are changed by twice the standard deviations from their respective means. Therefore, average dimensions and average gaps were used for calculating contact pressure of each specimen type of a given nominal tube diameter. In addition to the geometrical properties, B&W also measured the surface roughness of two specimens of each type and their collars. Their measurement results, listed in Table 7-2, show large variations from specimen to specimen and even within the same specimen. In general, surface roughness of the collar is greater than that of the tubes.

Table 7-1 Average Geometrical Properties of the Specimens

Tube Diam. in. (mm)	Heat	Pre-Fab Avg ^a OD in. (mm)	Pre-Fab Avg ^a Thickness in. (mm)	Pre-Fab Avg ^a ID in. (mm)	Post-Fab Avg ^b ID in. (mm)	Initial Diametral Gap in. (mm)	
						Mean	Std. Dev.
7/8 (22)	EX-82-1	0.871 (22)	0.048 (1.2)	0.775 (20)	0.784 (20)	0.0091 (0.23)	0.0014 (0.04)
7/8 (22)	NX 8520	0.873 (22)	0.049 (1.2)	0.776 (20)	0.784 (20)	0.0088 (0.23)	0.0011 (0.03)
3/4 (19)	NX 8524	0.749 (19)	0.041 (1.0)	0.667 (17)	0.674 (17)	0.0067 (0.17)	0.0014 (0.04)

^a Pre-Fabrication Average

^b Post-Fabrication Average

Table 7-2 Surface Roughness of 6 Tubes and 5 Collars from Six Leak Rate Specimens

Specimen # (Tube Heat)	Alloy 600 Tube OD ^{a)} min (mm)						Carbon Steel Collar ID ^{b)} min (mm)			
	END				MIDDLE		END			
	1		2				1		2	
#01-3/4 (NX8524)	27.2 (0.69)	33.0 (0.84)	33.1 (0.84)	32.5 (0.83)	28.3 (0.72)	32.1 (0.82)	135.6 (3.44)	142.6 (3.62)	91.8 (2.33)	99.6 (2.53)
#02-3/4 (NX8524)	25.3 (0.64)	16.9 (0.43)	18.5 (0.47)	21.4 (0.54)	14.7 (0.37)	23.4 (0.59)	NM ^{c)}	NM	NM	NM
#01-7/8 (NX8520LT)	30 (0.76)	35 (0.89)	38 (0.97)	48 (1.22)	41 (1.04)	43 (1.09)	27 (0.69)	21 (0.53)	45 (1.14)	36 (0.91)
#03-7/8 (NX8520LT)	26.5 (0.67)	19.9 (0.51)	16.1 (0.41)	16.6 (0.42)	14.0 (0.36)	15.6 (0.40)	66.9 (1.70)	77.5 (1.97)	200.8 (5.10)	136.5 (3.47)
#02-7/8 (EX-82-1)	38 (0.97)	41 (1.04)	37 (0.94)	43 (1.09)	33 (0.84)	42 (.07)	22 (0.56)	27 (0.69)	45 (1.14)	60 (1.52)
#05-7/8 (EX-82-1)	12.5 (0.32)	13.7 (0.35)	7.8 (0.20)	16.9 (0.43)	14.9 (0.38)	26.5 (0.67)	70.3 (1.79)	59.9 (1.52)	93.9 (2.39)	99.8 (2.53)

a) For tubing, both ends and mid areas were measured (2 points per position).

b) For carbon steel, both ends were measured (2 points per position).

c) Not Measured

Note 1 μin=0.03μm

The calculated variation of the contact pressure with tube internal pressure for specimens of the two different tube diameters are plotted in Figs. 7-1 a-b, respectively. Although the tubes from heats EX-82-1 and NX 8520 have the same diameter, the calculated contact pressures are different due to their different flow stress properties.

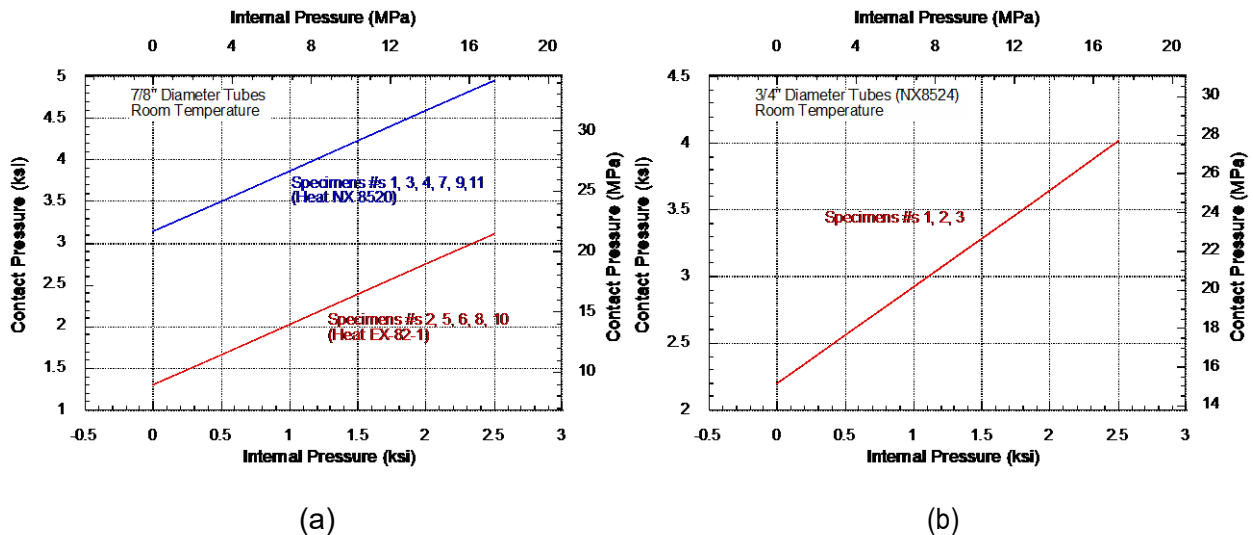


Figure 7-1 Calculated Variation of Contact Pressure with Tube Internal Pressure for Leak Rate Specimens with (a) 22 mm (0.875 in.) Diameter and (b) 19 mm (0.75 in.) Diameter Tubes

7.3 Screening Tests

Before conducting the leakage tests, screening tests were performed on all 14 B&W tube-to-collar specimens at room temperature to determine unpressurized leak rates. A 3.175 mm (0.125 in.) OD stainless steel (SS) tubing was welded to the side hole of the carbon steel collar using a SS weld adapter between tubing and collar. The leak path pressure was increased through the 3.175 mm (0.125 in.) OD SS tubing and leak rates were measured at 3.45 and 6.89 MPa (500 and 1000 psig) without pressurizing the tube interior. Once the leak rates were measured, the leak path pressure was reduced to zero and held for 30 minutes. The leak path was then re-pressurized to 6.89 MPa (1000 psig) and measured the leak rates to make sure the first 6.89 MPa (1000 psig) pressurization did not permanently change contact pressure. The results of the screening tests are given in Table 7-3. Note that although the leak rates generally increased when the pressure was increased from 3.5 to 6.9 MPa (0.5 to 1 ksi), the increases were much more significant for heat EX-82-1 than for heat NX 8520 or NX 8524, reflecting the higher initial contact pressures for heat NX 8520 and NX 8524 than heat EX-82-1. The screening test showed that specimen 01-7/8 was not expanded adequately.

Table 7-3 Results from Initial Screening Tests on Specimens with Zero Internal Tube Pressure

Specimen # (Heat #)	Leak Rate ^a (mg/min)			Leak Path Length mm (in.)	Initial contact pressure ksi (MPa)
	0.5 ksi (3.5 MPa)	1 ksi (6.9 MPa)	1 ksi (6.9 MPa) ^b		
#01-3/4 (NX8524)	0.5	3.5	4.3	102 (4)	3 (21)
#02-3/4 (NX8524)	0.3	13.8	16.8	102 (4)	3 (21)
#03-3/4 (NX8524)	12.4	57.4	60.9	102 (4)	3 (21)
#01-7/8 (NX8520 LT)	2190 @ 0.1 ksi (0.69 MPa)			51 (2)	3 (21)
#02-7/8 (EX-82-1)	11.3	445	482	51 (2)	1 (7)
#03-7/8 (NX8520 LT)	8.1	81.9	83.3	51 (2)	3 (21)
#04-7/8 (NX8520 LT)	0.8	2.7	2.7	102 (4)	3 (21)
#05-7/8 (EX-82-1)	No Leak	24.3	23.8	102 (4)	1 (7)
#06-7/8 (EX-82-1)	4.5	319	287	102 (4)	1 (7)
#07-7/8 (NX8520 LT)	No Leak	1.3	1.4	102 (4)	3 (21)
#08-7/8 (EX-82-1)	37.3	823	1100	203 (8)	1 (7)
#09-7/8 (NX8520 LT)	No Leak	3.9	5.6	203 (8)	3 (21)
#10-7/8 (EX-82-1)	No Leak	46.0	48.2	203 (8)	1 (7)
#11-7/8 (NX8520 LT)	0.2	1.5	1.6	203 (8)	3 (21)

a Leak rates were measured by the pressure decay method at room temperature for all but #01-7/8 for which it was measured by a flow meter. Only leak path pressure was applied.

b This test was done 30 minutes after the first 6.89 MPa leak test was done and depressurized.

7.4 Initial Test Results

Before deciding on a standard test protocol, three sets of initial exploratory tests were conducted on specimens 10-7/8 (EX-82-1) and 9-7/8 (NX 8520) and 8-7/8 (EX-82-1) to determine the responses of the specimens to various temperature and pressure histories. The nominal contact pressures in the EX-82-1 and NX 8520 specimens at room temperature were estimated to be 6.9 and 20.7 MPa (1 and 3 ksi), respectively. In the first two tests, a series of leak rate measurements were conducted on each specimen at 20, 100, 200 and 300°C; at each temperature the tube internal pressure was held constant successively at zero, 1250 and 2500 psi and leak rate measurements were made with inlet plenum pressure held constant at several levels between 0 and 17.2 MPa (2.5 ksi). After completing the low temperature measurements, each specimen was tested at high temperature at 500, 600 and 700°C. In the third test on specimen 8-7/8, no leak rate testing was done with low temperature holds. Instead, the unpressurized specimen was first heated to 700°C. After thermal equilibration, the tube was first pressurized to 17.2 MPa (2.5 ksi) followed by pressurization of the leak path side.

7.4.1 Specimen 10-7/8 (EX-82-1)

In order to obtain a better understanding of the leakage behavior of the specimens to tube pressure and leakage path pressure that would help establish a test procedure, a series of pressure tests was conducted on specimen 10-7/8 at room temperature, low temperature ($\leq 300^\circ\text{C}$) and high temperature ($> 300^\circ\text{C}$). The leak path (P_{lp}) and tube (P_t) pressures were never allowed to exceed 17.2 MPa (2.5 ksi). In addition, P_t was always increased first to the desirable level before P_{lp} was raised to the desired value for a given test to minimize relaxation of contact pressure and to prevent a gap from opening. Because the initial contact pressure was estimated to be 6.9 MPa (1 ksi), P_{lp} was never allowed to exceed P_t by more than 6.9 MPa (1 ksi). Between test stages, the leak path of the specimen was depressurized before depressurizing the tube interior. For the elevated temperature creep tests, both P_{lp} and P_t were maintained at ambient until the temperature of the specimen located in the high temperature furnace was stabilized at the desired temperature; then the specimen was pressurized. Close up views of the seal weld and the leak path exit ends of the specimen are shown in Fig. 7-2. The leakage path length of the specimen is 203 mm (8 in.) and the tube material is EX-82-1.



Figure 7-2 Close up Views of Leak Specimen Seal Weld and Leak Path Exit Gap of Specimen 10-7/8

7.4.1.1 Low Temperature Tests

Leakage data for all the tests are plotted in Fig. 7-3. The maximum pressure difference between P_{lp} and P_t at the end of each test is shown with an arrow on Fig 7-3. The leak rate generally increased significantly when the pressure difference reached a value of 6.9 MPa (1 ksi). In one case significant increase was observed even at 3.45 MPa (0.5 ksi), indicating that significant variability is to be expected. Note that as long as P_t was greater than or equal to P_{lp} , the leakage rate remained relatively low. At the conclusion of the room temperature tests, the leak rates were observed to be quite reproducible, indicating that any particulate matter in the crevice was cleared out during testing.

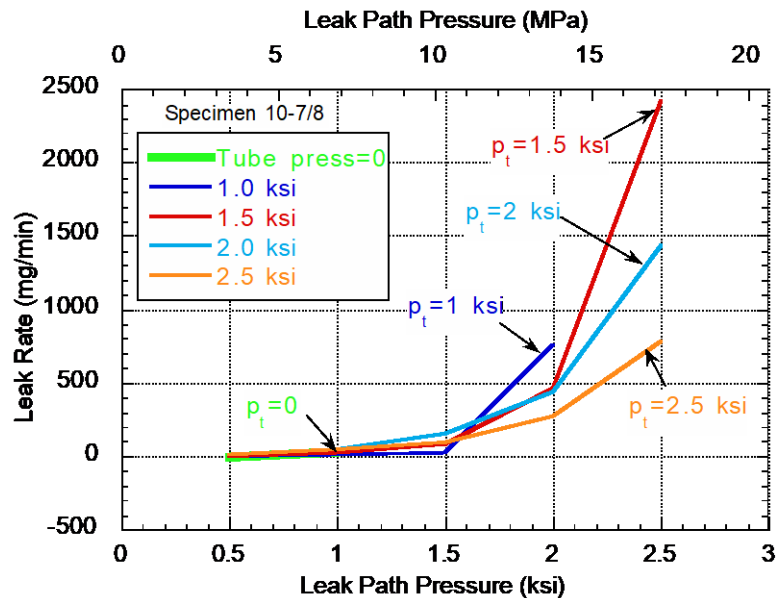


Figure 7-3 Leakage Data for Room Temperature Tests on Specimen 10-7/8

With the establishment of a stable (non-deforming) specimen under pressure cycling, a very low temperature heat up of the specimen to 45°C (113°F) involving a two hour dwell at this condition was performed. The specimen was maintained under constant pressure of $P_t = 2500$ psi and $P_{lp} = 2500$ psi for the entire test. During the entire heat up from an initial room temperature of 28°C (83° F) to a final temperature of 45°C (113°F) the leak rate continuously dropped from an initial 1715 mg/min to a final 1496 mg/min which is a 13% decrease from its starting value. Both the changing gas properties as a function of temperature and the differential thermal expansion between the collar and tube, (which changes the leak path contact pressure quite dramatically for a small increase in specimen temperature), have a strong effect on leak rate. It was also noted during testing that a small 3-5 psi change in P_t was sufficient for us to detect and measure a change in the leak rate.

Next, a programmed furnace was used to heat up sequentially from 100°C (212°F) to 200°C (392°F), and then 300°C (572°F) with furnace temperature dwells of 1, 1, and 2 hours, respectively, for the three temperatures to allow thermal equilibrium of the specimen to occur. All testing was done with the tube pressure $P_t = P_{lp} = 2500$ psi. The leak rate, plotted in Fig. 7-4, decreased over the entire range of the heat up from its initial room temperature value of 1622 mg/min to a stable value of 122 mg/min at the end of the 2 hour dwell at 300°C (572°F). The

test confirmed the increasing contact pressure between the collar and tube because of differential thermal expansion of the two materials. Also, the leak rate was reproducible with pressure cycling at 300°C (572°F).

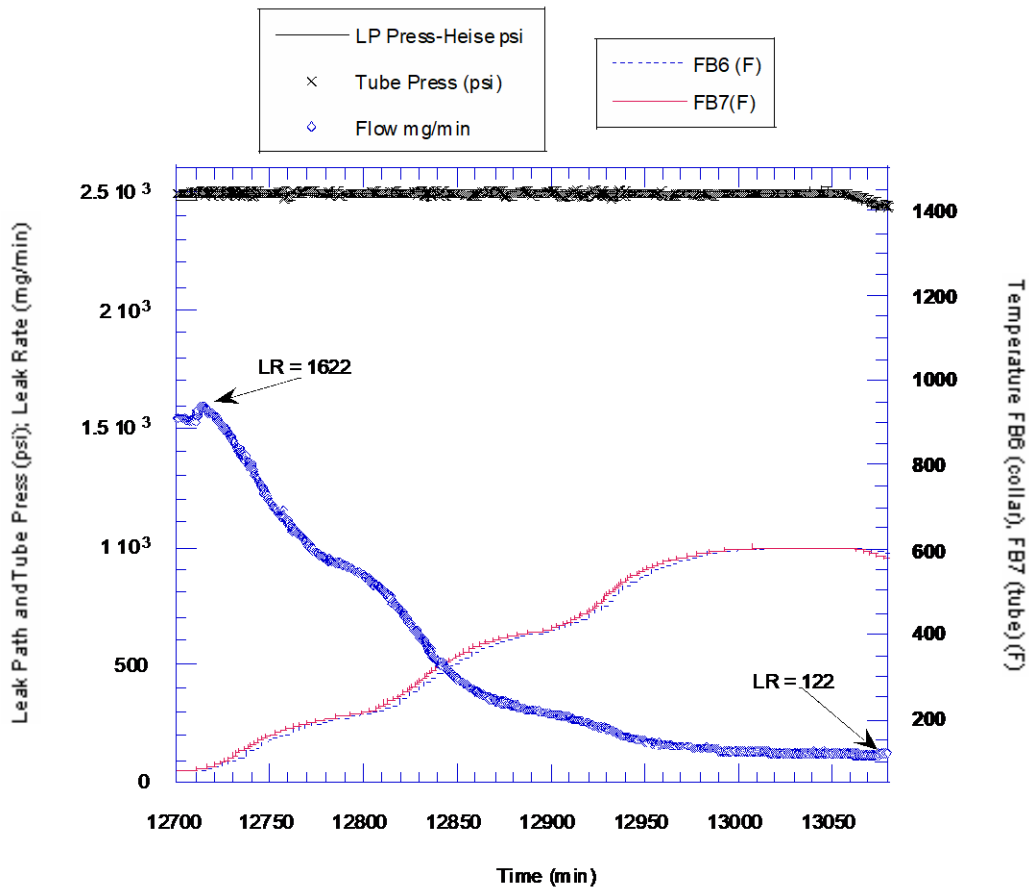


Figure 7-4 Leak Rate History for Specimen 10-7/8 during Heating from Room Temperature to 300°C (572°F)

7.4.1.2 High Temperature Tests

The next day the temperature was ramped from room temperature up to 600°C (1112°F) with a 2 hour dwell during which time the specimen was pressurized to $P_t = P_{ip} = 2500$ psi and the influence of higher temperatures on leak rate was investigated. As shown in Fig. 7-5, when the pressures were raised from zero to the desired values while at ~ 600°C, the leak rate remained near zero. Again this result showed that the high contact pressure generated due to differential thermal expansion was not sufficiently relaxed by thermal creep that occurred during 2 hour dwell at 600°C (1112°F). The specimen was then allowed to partially cool overnight to 100°C under reduced pressure. However, even though no leakage occurred during the high temperature hold, creep did occur as demonstrated by the test conducted the following day.

Testing started on the following day when the furnace temperature was ramped up at 150°C/hr in two phases with P_t held at a constant value of 2500 psi. The two phases were as follows

- (1) first heated to 300°C (572°F) and held for 0.5 hour with $P_t = P_{lp} = 2500$ psi
- (2) then ramped up to 700°C (1292°F) at 150°C/h with the pressures acting dynamically

During the two-phase heat-up, the reproducibility of leak-rate was checked at two of the previous days temperatures 300°C and 600°C (572°F to 1112°F). Due to very high leak rates encountered at temperatures below 300°C - 400°C (572°F to 752°F), ANL had to shut off the leak path gas supply line intermittently to conserve gas. For example, at 300°C with $P_t = P_{lp} = 2500$ psi, the leak rate measured by the isolated chamber pressure decay method was 4912 mg/min. This is a much larger leak rate than the 122 mg/min that had occurred earlier at 300°C under the same pressure loading. Thus, the high temperature hold at 600°C for 2 hours reduced the leak path resistance significantly even though no leakage was observed during the hold time itself.

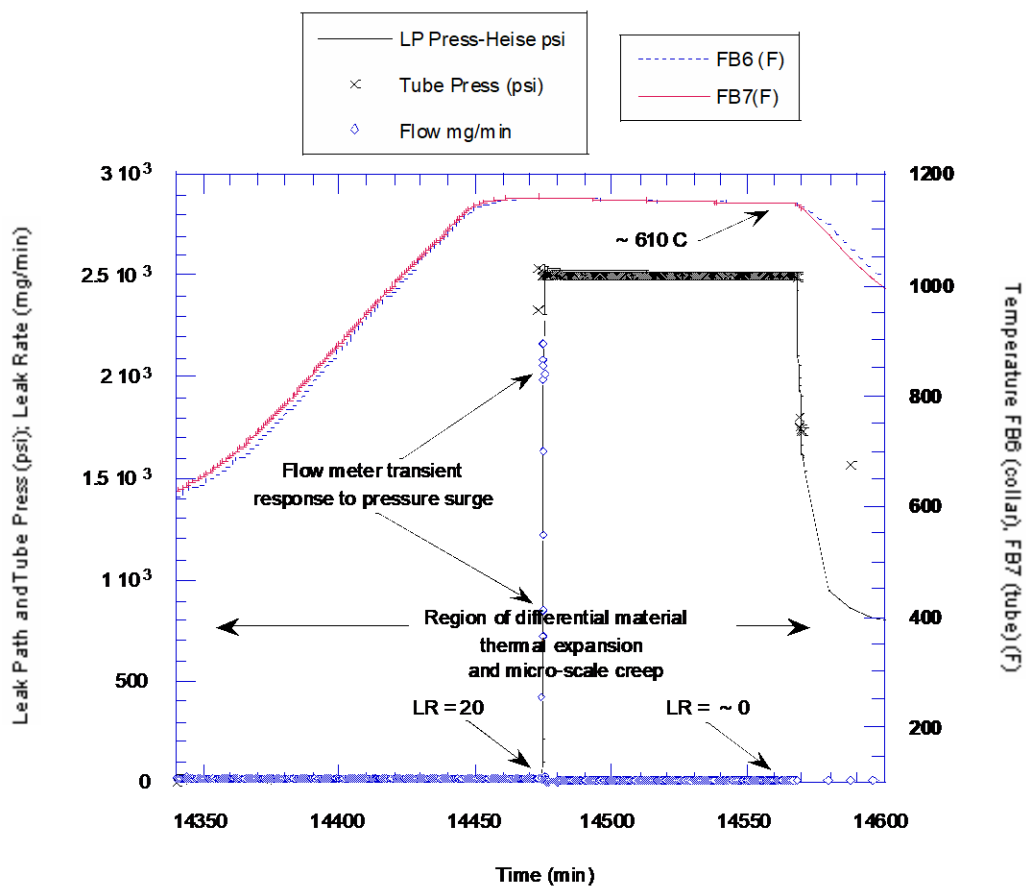


Figure 7-5 Leak Rate History of Specimen 10-7/8 during Hold at 600°C (1112°F)

7.4.2 Specimen 9-7/8 (NX 8520)

As for specimen 10-7/8, a series of pressure tests was conducted on specimen 09-7/8 at room temperature, low temperature ($\leq 300^\circ\text{C}$) and high temperature ($> 300^\circ\text{C}$). The leak path (P_{lp}) and tube (P_t) pressures were never allowed to exceed 17.2 MPa (2.5 ksi). In addition, P_t was

always increased first to the desirable level before P_{ip} was raised to the desired value for a given test to minimize relaxation of contact pressure and to prevent a gap from opening. Because the initial contact pressure was estimated to be 20.7 MPa (3 ksi), it was unexpected for gaps to open up between the tube and the collar during testing. Initial screening test had indicated that the leak rate in this specimen was low (Table 7-4). As before, between test stages, the leak path of the specimen was depressurized before depressurizing the tube interior. For the elevated temperature creep tests, both P_{ip} and P_t were maintained at ambient until the temperature of the specimen located in the high temperature furnace was stabilized at the desired temperature; then the specimen was pressurized. The leakage path length of the specimen is 203 mm (8 in.) and the tube material is NX 8520 which has a lower yield and higher creep rate than EX-82-1.

7.4.2.1 Low Temperature Tests

The leak rate was measured sequentially with $P_t = P_{ip} = 990$ psi and then with $P_t = P_{ip} = 2522$ psi both yielding very low leak rates of 4.1 and 1.0 mg/min respectively. These leak rates are too small to measure with our commercial flow meter and were measured by our isolated chamber pressure decay method.

Next, with $P_{ip} = \sim 2420$ psi, P_t was lowered from 20.7 to 6.9 MPa (2.5 ksi to 1 ksi), then to 0 MPa and then raised back to 17.4 MPa (2.518 ksi) each time measuring the leak rate. Finally, the specimen was tested with $P_t = 6.79$ MPa (0.985 ksi) and $P_{ip} = 7.86$ MPa (1.14 ksi). As shown in Table 7-4, the pressure cycling dramatically increased the leak rates over those encountered earlier.

Table 7-4 Room Temperature Testing of Specimen 09-7/8

Phase		P _t (psi)	P _{lp} (psi)	LR (mg/min)
1	a	990	990	4.1
	b	2522	2522	1.0
2 (pressure cycling)	a	1000	2460	506
	b	0	2409	11,000*
	c	2518	2400	5100*
	d	985	1140	1198
3 (behavior after cycling)	a	2491	500	39
	b	2493	1000	99
	c	2490	1500	236
	d	2485	1960	942
	e	2490	2400	4870
	f	2485	987	99

* estimated using isolated pressure decay chamber; exceeded limit of commercial flow meter and decay chamber

Following Phase 2 pressure cycling, to generate leak rate data for P_t nominally equal to (2.49 ksi) for a range of increasing P_{lp} values from 3.5 to 16.6 MPa (0.500 to 2.400 ksi) (Phases 3a-e) and finally Phase 3b was duplicated in Phase 3f to check on data reproducibility. As shown in Table 7-4, the leak rate increases with increasing P_{lp} and reached a maximum of 4870 mg/min with P_t = 17.2 MPa (2.49 ksi) and P_{lp} = 16.6 MPa (2.4 ksi) which is much greater than encountered for the initial test 1b. Furthermore, the data obtained after Phase 2 pressure cycling is reproducible as is evident by comparing leak rates from Phases 2c and 3e and 3b and 3f.

Table 7-5 shows the leak rate data for low temperature testing of specimen 09-7/8 along with the initial leak rate under room temperature at the beginning of the heat up. For this test, the specimen was initially at room temperature and then heated up sequentially to 100, 200, and 300°C with a 1.5-hour dwell at each temperature to ensure thermal stabilization of the specimen. The objective was to obtain leak rate data under pressurization of P_t = P_{lp} = (2.5 ksi). As shown in Table 7-4, for Phase 3 testing under this pressure pair the leak rate was very large = 4870 mg/min which is comparable to 4690 mg/min in Table 7-5. As before, the leak rate steadily decreased with increasing temperature.

Table 7-5 Low Temperature Testing of Specimen 09-7/8; Leak Rate Data (LR) with $P_t = P_{lp} = \sim 2500$ psi

Temperature (°C)	P_t (psi)	P_{lp} (psi)	LR (mg/min)
27	2523	2410	4690
100	2507	2470	1615
200	2502	2505	275
300	2504	2485	89

7.4.2.2 High Temperature Tests

The specimen with $P_t = P_{lp} = 0$ psi was heated up at a rate of 150°C/hr to 600°C and held for a 3 hour dwell during which the specimen was pressurized to $P_t = P_{lp} = \sim 2500$ psi and the leak rate (LR) was measured several times over the dwell to see if the leak was stable or if creep would lower the contact pressure and increase the leak rate. Over the 3 hour dwell, no increase in leak rate was detected; the leak rate had reduced from the level reported in Table 2 in Stage 2 testing at 300°C of LR = 89 mg/min due to differential thermal expansion to an even smaller value of nominally 6 mg/min. Finally, after the three hour dwell at 600°C and with $P_t = P_{lp}$ kept at 2500 psi, the furnace was ramped up to 650°C and held for a one hour dwell to see if creep would increase the leak rate. But, during the 1 hour hold, the leak rate remained nominally 6 mg/min, indicating no influence of creep on the leak rate.

Upon completion of testing, specimen 09-7/8 was allowed to cool overnight un-pressurized. The next morning after the specimen had cooled to 100°C it was heated up at a rate of 150°C/hr with $P_t = P_{lp} = 0$ psi until the specimen temperature reached 600°C at which time P_t and P_{lp} were raised to 2500 psi. The leak rate at 600°C was 365 mg/min which was higher than that measured the day before (6 mg/min) at the same temperature but the LR declined as the heat up continued to 650°C (1202°F). At 650°C, the leak rate had reduced to 252 mg/min which was also higher than the measured LR (6 mg/min) the day before at the same temperature. This suggests that creep occurred when the specimen was held at these two temperatures the day before. Upon heating above 650°C, the leak rate continued to decrease until at $\sim 1265^\circ\text{F}$ (685°C) the leak rate showed a small upward trend (Fig.7-6). Within 3 minutes when the specimen reached a temperature of 1299°F (704°C), the LR abruptly increased to greater than an estimated 8181 mg/min. The test was stopped because the range of both flow meters had been exceeded and ANL was unable to maintain P_{lp} at the desired level of 2500 psi.

After allowing specimen 09-7/8 to cool for two days it was tested at room temperature (26°C) with $P_t = 2524$ psi with increasing values of P_{lp} until the flow range of the commercial flow meter was exceeded (~ 2320 mg/min). Table 7-6-6 shows the leak rate data and the corresponding pressure pairs (P_t , P_{lp}). The LR even at very small values of P_{lp} is large and at $P_{lp} = 385$ psi has reached 2221 mg/min, the limit of the commercial flow meter. These values of LR far exceed those of earlier room temperature testing of the specimen in Stage 1 after pressure cycling

(see Table 7-4) indicating that the creep occurring at temperatures of 600-700°C have irreversibly lowered the leak path resistance to flow.

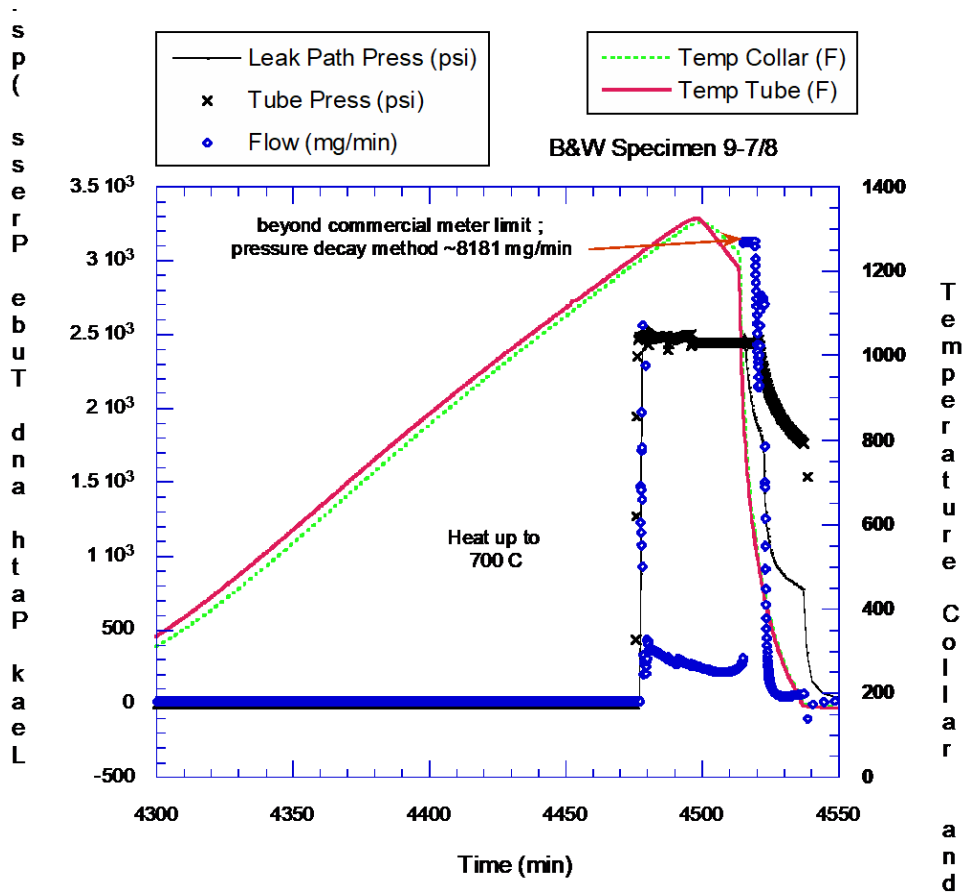


Figure 7-6 Leak Rate History of Specimen 09-7/8 during Heating to 700°C (1300°F)

Table 7-6 Final Room Temperature (26°C) Testing of Specimen 09-7/8; Leak Rate Data (LR) for Four P_{lP} Pressures with P_t = 2524 psi

P _t (psi)	P _{lP} (psi)	LR (mg/min)
2524	94	145
2524	193	522
2524	294	1242
2524	385	2221

7.4.3 Specimen 8-7/8 (EX-82-1)

To simplify the analysis of contact stress, the test on specimen 8-7/8 (203 mm [8 in.] long) did not involve cycling of the pressures either at room temperature or at low temperatures. A single heat up ramp rate of 150°C/hr to 700°C was used during which time the specimen was not pressurized. After the temperature of the specimen and furnace had equilibrated, the tube pressure P_t was increased to 2500 psi followed by increasing the leakage path pressure. This test protocol was not satisfactory because upon pressurizing at 700°C the leak rate almost instantaneously jumped to > 13,000 mg/min.

7.5 Results with Revised Protocol

Our original intent was to independently vary the internal and leak path pressures to obtain a wide range of contact pressures. However, our initial tests showed that application of a leak path pressure greater than the internal pressure produced irreversible changes in the contact pressure. Therefore, the following test protocol was adopted consisting of five stages

- (1) At room temperature, the specimen is pressurized in three successive steps with 1500, 2000 and 2500 psi applied to both the tube and the leakage path.
- (2) In the second stage, the un-pressurized specimen is heated at a rate of 150°C/hr to 500°C.
- (3) In the third stage, the specimen is pressurized to [2500psi, 2500psi] at 500°C
- (4) In the fourth stage, the pressurized specimen is slowly heated at a rate of 50°C/hr to 700°C
- (5) After cooldown to room temperature, stage 1 is repeated to determine the effect of high temperature exposure on the leakage rate at room temperature.

The slow heating rate in stage 4 allowed us to identify the temperature at which rapid leakage was initiated due to creep. Also, the ramp rate was sufficiently slow to allow us to maintain the tube temperature close to the collar temperature at all times during the ramp.

Each high temperature test was analyzed for creep in order to determine the variation of contact pressure with time and location. Together with the one-dimensional leak rate correlations, they were used to predict the leak rate history, which was compared with the measured leak rates.

The results are discussed in the following sections in the order the tests were carried out.

7.5.1 Specimen 11-7/8 (NX 8520)

This is a specimen with 203 mm (8 in.) leak path length. The specimen in the as-received state is shown in Fig. 7-7. The results of the room temperature tests under step 1 loading are included in Table 7-7, which shows that the leak rates at all three pressures are quite low, which is to be expected because the calculated contact pressure is 3 ksi.



Figure 7-7 Specimen 11-7/8 in the As-received State

Table 7-7 Stage 1 Initial Room Temperature Testing of Specimen 11-7/8

Tube Pressure (T) (psi)	Leak Path Pressure (LP) (psi)	Leak Rate (mg/min)
1,505	1,494	1.2
2,001	2,001	2.3
2,498	2,497	2.5

The leak rate and pressure history during the high temperature test under stages 2-4 are shown in Fig. 7-8. As before, the leak rate was essentially zero until 1800 minutes when the temperature reached 710°C (1310°F) at which point the leak rate increased rapidly to 15,000 mg/min (our measurement limit) and still rising. This behavior is very similar to that of the initial tests on specimens 8-7/8, 9-7/8 and 10-7/8. The collar, which is made of A508 steel that was tempered at 649°C (1200°F), loses its creep strength above the tempering temperature. The creep deformation of the collar led to the high leak rate. FEA of the specimen, which will be discussed later, confirmed that. The specimen (Fig.7.) in the post-test condition showed that the collar was oxidized significantly during the test.

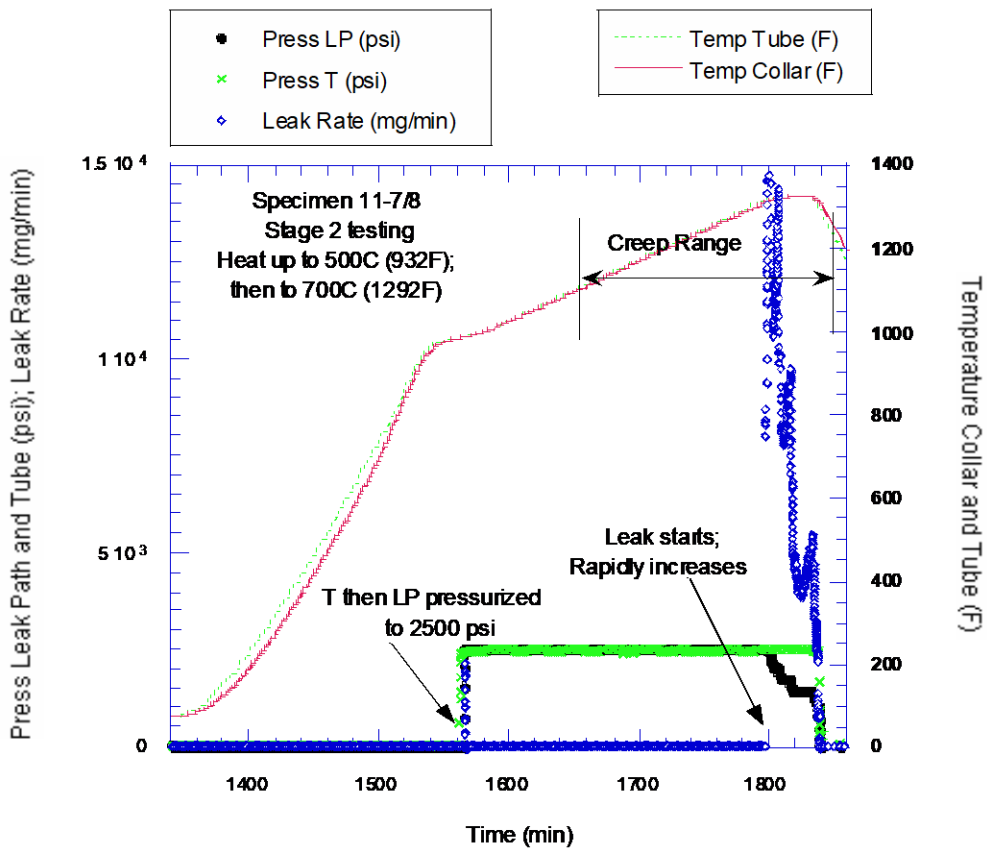


Figure 7-8 Leak Rate and Pressure History of Specimen 11-7/8 during Stages 2, 3 and 4 testing



Figure 7-9 Specimen 11-7/8 in the Post-Test Condition

Results from the post-test room temperature pressure cycling under stage 5 are shown in Table 7-8. With the internal tube pressure at 1500, 2000 and 2500 psi, ANL was unable to pressurize the leak path pressure to 2500 psi because of excessive leakage, which confirmed that the prior high temperature exposure had reduced the leakage path flow resistance significantly. Comparison of Tables 7.7 and 7-8 shows the large increases in leak rates during stage 5 compared to stage 1 even when the leakage path pressures were much lower.

Table 7-8 Stage 5 Final Room Temperature Tests of Specimen 11-7/8

Tube Pressure (T) (psi)	Leak Path Pressure (LP) (psi)	Leak Rate (mg/min)
2,506	85	815
2,502	147	1,987
2,500	290	5,755
2,497	444	10,695
2,003	445	11,329
2,003	291	6,169
2,003	147	2,188
2,003	76	764
1,510	74	825
1,512	152	2,516
1,511	287	6,481
1,512	442	11,782

7.5.2 Specimen 04-7/8 (NX 8520)

This is a specimen with 102 mm (4 in.) leak path length. The specimen in the as-received state is shown in Fig. 7-10. The results of the room temperature tests under step 1 loading are included in Table 7-9, which shows that the leak rates at all three pressures are relatively low, which is to be expected because the calculated contact pressure is 3 ksi.



Figure 7-10 Specimen 04-7/8 in the As-received Condition

Table 7-9 Stage 1 Initial Room Temperature Testing of Specimen 04-7/8

Tube Pressure (T) (psi)	Leak Path Pressure (LP) (psi)	Leak Rate (mg/min)
1,495	1,493	7.1
2,001	1,993	9.7
2,495	2,492	11.1

The leak rate and pressure history during the high temperature test under stages 2-4 are shown in Fig.7-11. As before, the leak rate was essentially zero until the temperature was close to 675°C (1247°F) at which point the leak rate increased rapidly from zero to 13,950 mg/min (our measurement limit) in 18 minutes. The leak rate was reduced when the leakage path pressure was reduced to 2000, but began to rise again until the pressure was reduced further to 1500 psi and finally to 0. The specimen (Fig.7-12) in the post-test condition showed that the collar was oxidized significantly during the test.

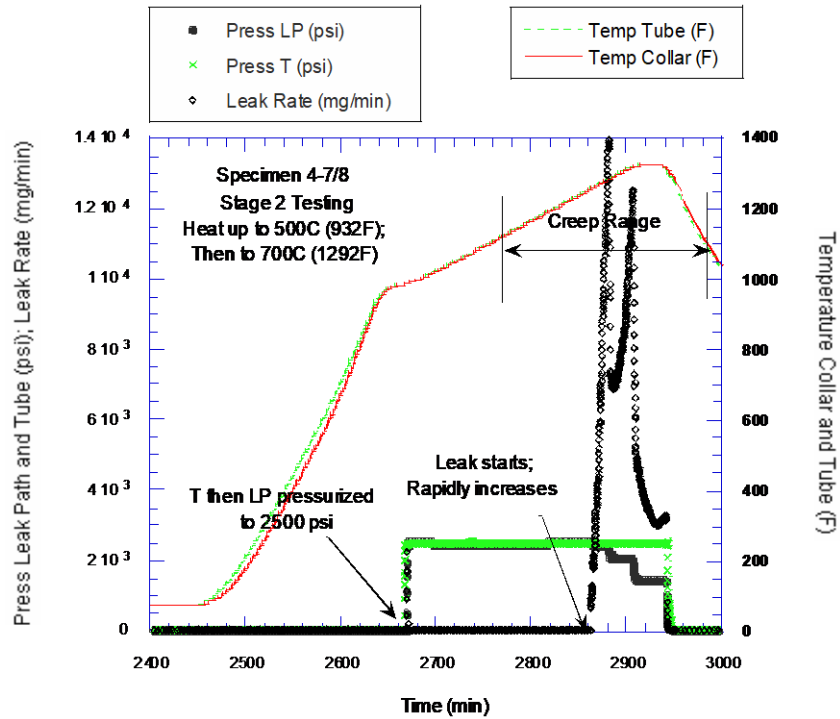


Figure 7-11 Pressure and Leak Rate History of Specimen 04-7/8 at High Temperature during Stages 2-4 Loading



Figure 7-12 Post-test Picture of Specimen 04-7/8

Results from the post-test room temperature pressure cycling under stage 5 are shown in Table 7-10. With the tube pressure at 1500, 2000 and 2500 psi, ANL was unable to pressurize the leak path pressure to 2500 psi because of excessive leakage, which confirmed that the prior high temperature exposure had reduced the leakage path flow resistance significantly. Comparison of Tables 7-9 and 7-10 shows the large increases in leak rates during stage 5 compared to stage 1 even when the leakage path pressures were much lower.

Table 7-10 Stage 5 Final Room Temperature Tests of Specimen 04-7/8

Tube Pressure (T) (psi)	Leak Path Pressure (LP) (psi)	Leak Rate (mg/min)
2,514	105	1,138
2,511	203	3,171
2,508	300	5,718
2,504	454	10,162
2,003	455	10,861
2,004	303	6,099
2,005	203	3,376
2,007	102	1,182
1,508	101	1,292
1,492	207	3,835
1,492	306	6,682
1,492	455	11,671

7.5.3 Specimen 05-7/8 (EX-82-1)

This is a specimen with 102 mm (4 in.) leak path length. The specimen in the as-received state is shown in Fig. 7-13. The results of the room temperature tests under step 1 loading are included in Table 12, which shows that although the leak rates at all three pressures are relatively low but they are higher than those for specimen 04-7/8, which is to be expected because the calculated contact pressure for this specimen is only 1 ksi.



Figure 7-13 Specimen 05-7/8 in the As-received Condition

Table 7-11 Stage 1 Initial Room Temperature Testing of Specimen 05-7/8

Tube Pressure (T) (psi)	Leak Path Pressure (LP) (psi)	Leak Rate (mg/min)
1,503	1507	14.4
2,000	1996	32.1
2,500	2499	238.0

The leak rate and pressure history during the high temperature test under stages 2-4 are shown in Fig. 7-14. As in the case of specimen 04-7/8, the leak rate was very low until the temperature reached 678°C (1252°F) at which point the leak rate increased rapidly to 13,000 mg/min and still rising. The leak rate was reduced when the leakage path pressure was reduced to 2000 psi, but began to rise again until the pressure was reduced further to 1500 psi when the leak rate was reduced again but began to rise again until the pressure was finally reduced to 0. The specimen (Fig.7-15) in the post-test condition showed that the collar was oxidized significantly during the test.

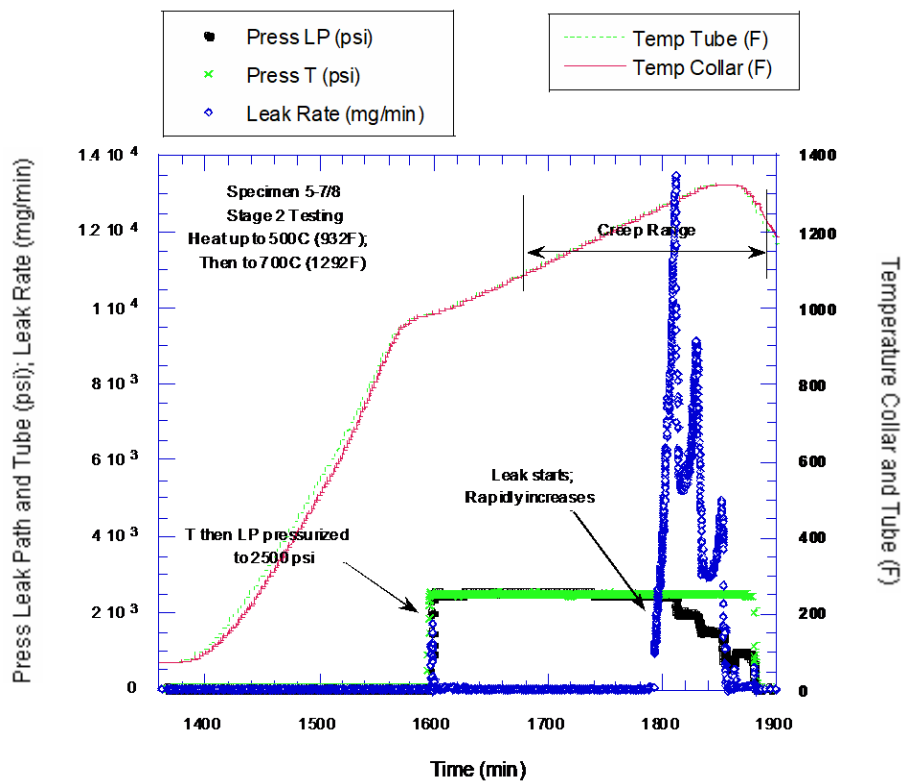


Figure 7-14 Pressure, Leak Rate and Temperature History of Specimen 05-7/8 at High Temperature during Stages 2-4 Loading



Figure 7-15 Post-test Picture of Specimen 05-7/8

Results from the post-test room temperature pressure cycling under stage 5 are shown in Table 7-12. With the tube pressure at 1500, 2000 and 2500 psi, ANL was unable to pressurize the leak path pressure to 2500 psi because of excessive leakage, which confirmed that the prior high temperature exposure had reduced the leakage path flow resistance significantly. Comparison of Tables 7-11 and 7-12 shows the large increases in leak rates during stage 5 compared to stage 1 even when the leakage path pressures were much lower, which is to be expected because of thermal creep effects during stage 5. Comparison of Table 7-10 and 7-12 shows that the specimen with EX-82-1 Alloy 600 tubes had much lower leak rates during post-test room temperature testing than the specimen with NX 8520 Alloy 600 tube. This is consistent with the lower creep strength of NX 8520 than EX-82-1.

Table 7-12 Stage 5 Final Room Temperature Tests of Specimen 05-7/8

Tube Pressure (T) (psi)	Leak Path Pressure (LP) (psi)	Leak Rate (mg/min)
2497	92	334
2495	196	1,331
2494	294	2,888
2491	603	11,115
1983	597	13,269
1983	463	8,627
1983	293	3,799
1983	202	1,930
1983	146	1,051
1486	143	1,366
1488	267	4,014
1487	399	8,125
1487	489	11,472

7.5.4 Specimen 03-7/8 (NX 8520)

This is a specimen with 51 mm (2 in.) leak path length. The specimen in the as-received state is shown in Fig. 7-16. The results of the room temperature tests under step 1 loading are included in Table 7-13, which shows that although the leak rates at all three pressures are relatively low but they are higher than those for specimen 04-7/8 (Table 7-9), which is of the same material but longer.

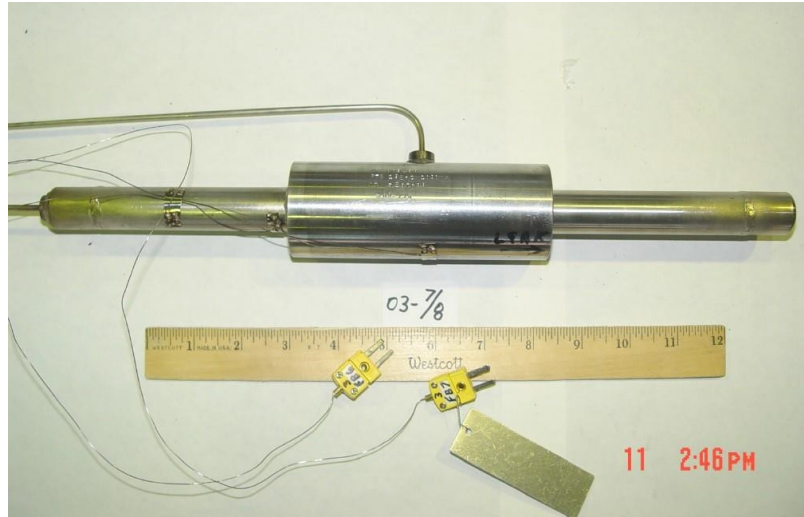


Figure 7-16 Specimen 03-7/8 in the As-received Condition

Table 7-13 Stage 1 Initial Room Temperature Testing of Specimen 03-7/8

Tube Pressure (T) (psi)	Leak Path Pressure (LP) (psi)	Leak Rate (mg/min)
1,500	1,500	59
1,999	2,001	92
2,497	2,498	128

The leak rate and pressure history during the high temperature test under stages 2-4 are shown in Fig.7-17. As for specimen 04-7/8, the leak rate was very low until the temperature reached 684°C (1263°F) at which point the leak rate increased rapidly to 11,650 mg/min and still rising. Under constant temperature hold at 700°C, the leak rate was reduced when the leakage path pressure was reduced to 2000 psi, but began to rise again until the pressure was reduced further to 1500 psi when the leak rate was reduced again but began to rise again until the pressure was finally reduced to 0. The specimen (Fig.7-18) in the post-test condition showed that the collar was oxidized significantly during the test.

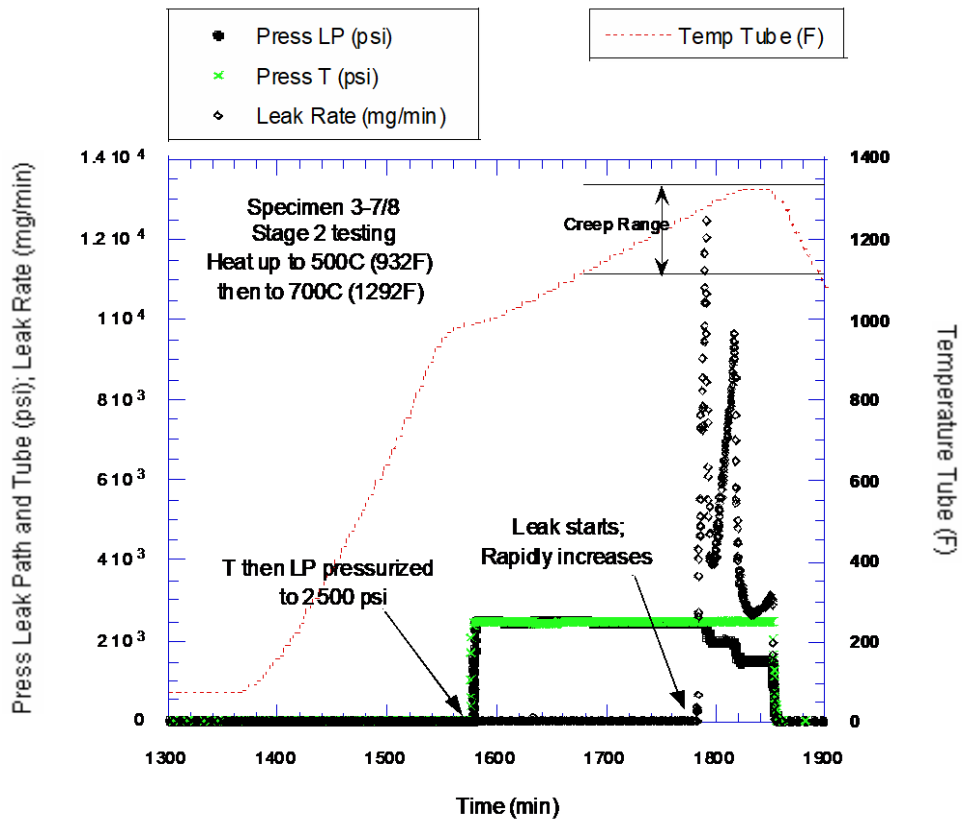


Figure 7-17 Pressure and Leak Rate History of Specimen 03-7/8 at High Temperature during Stages 2-4 Loading



Figure 7-18 Post-test Picture of Specimen 03-7/8

Results from the post-test room temperature pressure cycling under stage 3 are shown in Table 7-14. With the tube pressure at 1500, 2000 and 2500 psi, the leak path pressure was varied between 100 and 450 psi. Comparison of Tables 7-14 and 7-0 shows that the leak rates during stage 3 of the two specimens with 51 mm (2 in.) and 102 mm (4 in.) long leak paths are comparable.

Table 7-14 Stage 3 Final Room Temperature Tests of Specimen 03-7/8

Tube Pressure (T) (psi)	Leak Path Pressure (LP) (psi)	Leak Rate (mg/min)
2510	101	1107
2507	196	2826
2504	298	4946
2501	452	8690
2008	100	1070
2008	199	2942
2008	301	5337
2007	451	9543
1503	94	1157
1505	202	3482
1506	299	6148
1506	451	11,542

7.5.5 Specimen 02-3/4 (NX 8524)

This is a specimen that used 19 mm (0.75 in.) diameter tube with 102 mm (4 in.) long leak path length. The specimen in the as-received state is shown in Fig.7-19. The results of the room temperature tests under step 1 loading are included in Table 7-15, which shows that except for the test at the highest pressure, the leak rates are comparable to those for specimen 05-7/8 (Table11), which is of the same diameter but different material.

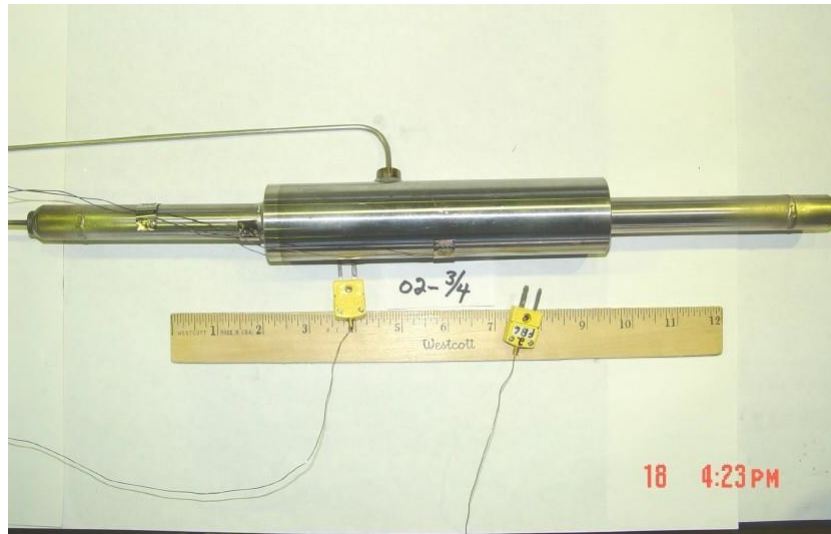


Figure 7-19 Specimen 02-3/4 in the As-received Condition

Table 7-15 Stage 1 Initial Room Temperature Testing of Specimen 02-3/4

Tube Pressure (T) (psi)	Leak Path Pressure (LP) (psi)	Leak Rate (mg/min)
1505	1496	14.4
1998	1996	21.1
2496	2491	30.1

The leak rate and pressure history during the high temperature test under stage 2 are shown in Fig.7-20. As in the case of specimen 05-7/8, the leak rate was very low until the temperature reached 673°C (1244°F) at which point the leak rate increased rapidly to 8517 mg/min in 23 minutes. The temperature still rising at the rate of 50°C/h and the tube pressure held at 2500 psi (17 MPa), as shown in Fig.7-20, the leak rate was reduced significantly when the leakage path pressure was reduced to 2000 psi (14 MPa), but began to rise again until the pressure was reduced further to 1500 psi (10 MPa) when the leak rate was reduced again but began to rise again until the pressure was finally reduced to 0. The specimen (Fig. 7-21) in the post-test state showed that the collar was oxidized significantly during the test.

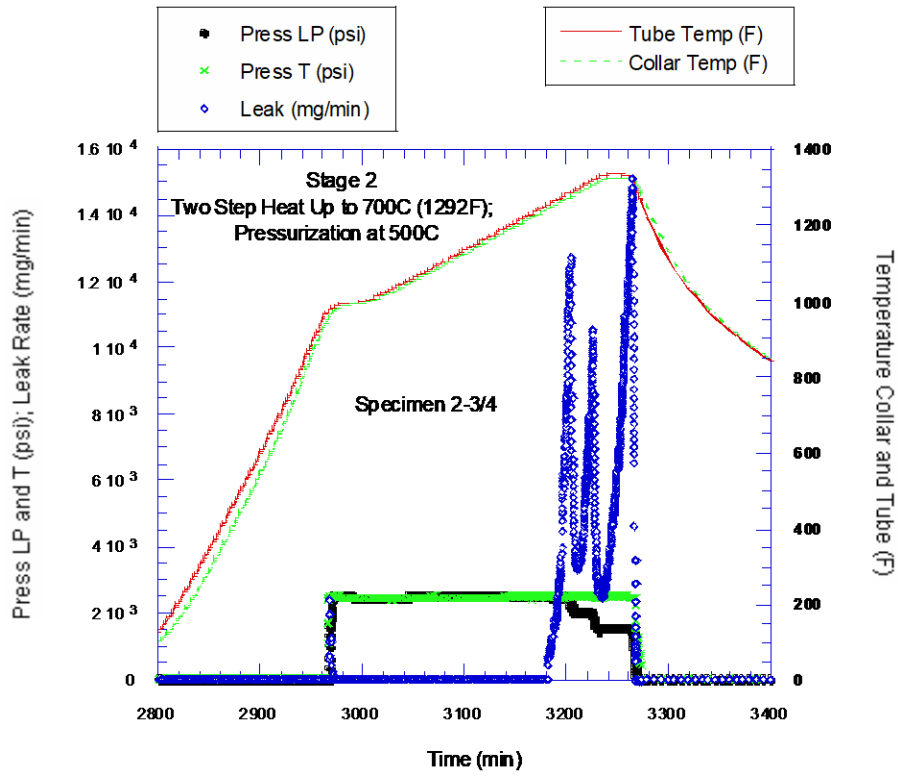


Figure 7-20 Pressure, Leak Rate and Temperature History of Specimen 02-3/4 at High Temperature during Stage 2



Figure 7-21 Post-Test Picture of Specimen 02-3/4

Stage 3 final room temperature testing of specimen 02-3/4 yielded the data shown in Table 7-16. The leak data in this test stage was obtained for three different tube pressurization levels (T) of nominally 2,500, 2,000, and 1,500 psi each involving a range of leak path pressures (LP). A comparison of room temperature data from pre-creep testing from Stage 1 (see Table 15) and post-creep testing Stage 3 (Table 7-16) show that the Stage 2 creep testing has greatly increased specimen leak rates during Stage 3 testing and that creep has permanently decreased the leak path resistance.

Table 7-16 Stage 3 Final Room Temperature Tests of Specimen 02-3/4

Tube Pressure (psi)	Leak Path Pressure (psi)	Leak Rate (mg/min)
2503	204	3221
2501	298	5692
2500	401	8748
2497	497	11,633
2008	499	12,456
2008	404	9325
2008	301	6138
2008	201	3377
1495	199	3660
1495	300	6606
1495	402	10,007
1495	501	13,437

7.5.6 Specimen 07-7/8 (NX 8520)

This is a companion specimen to 04-7/8 both with 102 mm (4 in.) leak path length. The specimen in the as-received state is shown in Fig.7-22. The results of the room temperature tests under stage 1 loading are included in Table 7-17, which shows that, as in the case of its companion specimen 04-7/8 (Table 7-9), the leak rates at all three pressures are relatively low, which is to be expected because the calculated contact pressure is 3 ksi.



Figure 7-22 Specimen 07-7/8 in the As-received Condition

Table 7-17 Stage 1 Room Temperature Testing of Specimen 07-7/8

Tube Pressure (psi)	Leak Path Pressure (psi)	Leak Rate (mg/min)
1500	1504	1.7
2004	2001	3.8
2497	2494	5.2

An earlier test had shown that heating to only 600°C and holding a fully pressurized specimen [2500 psi, 2500 psi] for an hour caused no measurable leakage but upon cooling to room temperature and leak testing, the specimen showed significantly increased leakage compared to that prior to the high temperature excursion. The stage 2 testing of specimen 07-7/8 was modified to confirm this behavior by first including a 1.5 hour hold at 600°C (stage 2) followed by cooling to room temperature (stage 3), which was then followed by the normal protocol, i.e., heating up to 700°C and a 30 minute hold (stage 4) and finally cooling down to room temperature (stage 5). The leak rate results from all five stages are presented in Fig.7-23. As before, no measurable leak rate was detected during the 1.5 hour dwell at 600°C (stage2). However, during the subsequent room temperature testing (stage 3), very large leak rates were observed (Table 7-18).

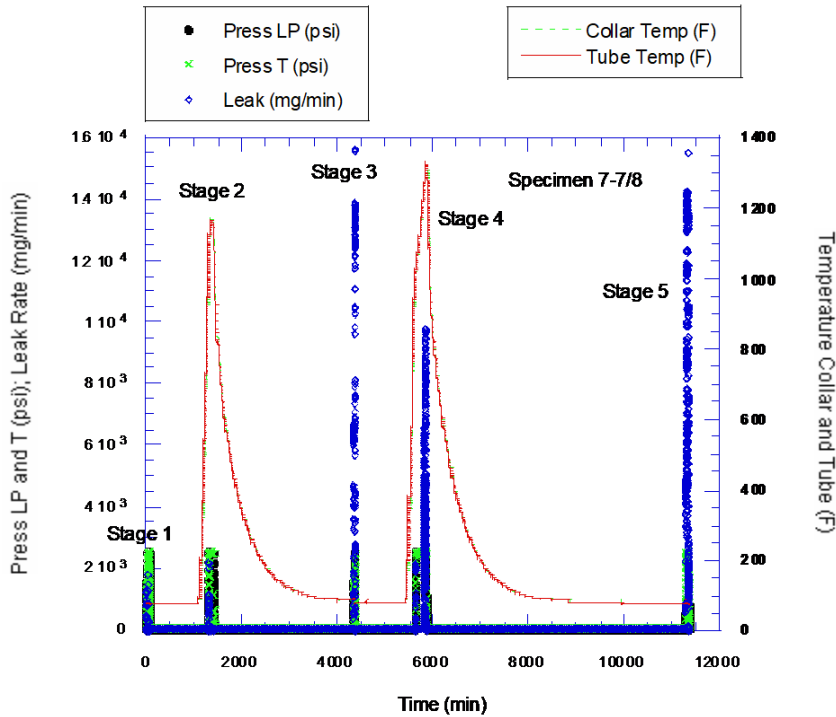


Figure 7-23 Modified Stage 2 (Five Stages) Pressure-temperature Leak Rate History of Specimen 07-7/8

Table 7-18 Stage 3 Room Temperature Testing of Specimen 07-7/8

Tube Pressure (psi)	Leak Path Pressure (psi)	Leak Rate (mg/min)
1509	1494	6467
1997	1984	13,382
2480	2499	Exceeded meter

During Stage 4 testing, just as for previously reported testing on other specimens, during the final 50°C/hr heat up to 700°C, no measurable leak was observed until the specimen temperature reached 677°C (1250°F) at which point the leak rate went from zero to 9824 mg/min in ~ 19 minutes (Table 7-19).

As before, the leak rate was reduced significantly when the leakage path pressure was reduced to 2000 psi (14 MPa), but began to rise again until the pressure was reduced further to 1500 psi (10 MPa) when the leak rate was reduced again but began to rise again until the pressure was finally reduced to 1100 psi (8 MPa). The final room temperature testing of specimen 07-7/8 yielded the data shown in Table 20. The leak data in this test stage was obtained for three different tube pressurization levels (T) of nominally 2500, 2000, and 1500 psi each involving a range of leak path pressures (LP). A comparison of room temperature data from pre-creep

testing from Stage 1 (see Table 7-17) and post-creep testing Stage 3 (Table 7-20) show that the Stage 2 creep testing has greatly increased specimen leak rates during Stage 3 testing and that creep has permanently decreased the leak path resistance. The specimen (Fig. 7-24) in the post-test state showed that the collar was oxidized significantly during the test.

Table 7-19 Stage 4 Discrete Data for Leak Rate Maximums and Minimums of Specimen 07-7/8

Time (min)	Pressure (psi)	Specimen Temp (°F)	Leak Rate (mg/min)
5794	[2508, 2490]	1251 / 1247	~ 0
5813	[2494, 2488]	1280 / 1276	9824
5820	[1997, 2496]	1291 / 1287	2320
5834	[2005, 2493]	1310 / 1305	5145
5834	[1098, 2492]	1325 / 1325	20.8

Table 7-20 Final Room Temperature Testing of Specimen 07-7/8

Tube Pressure (T) (psi)	Leak Path Pressure (LP) (°F)	Leak Rate (mg/min)
2496	194	691
2497	502	4,702
2506	598	6,671
2500	803	11,888
2008	802	14,229
2005	601	8,582
2006	500	6,070
2006	202	1,065
1505	199	1,404
1508	505	7,646
1508	604	10,510
1508	702	13,549

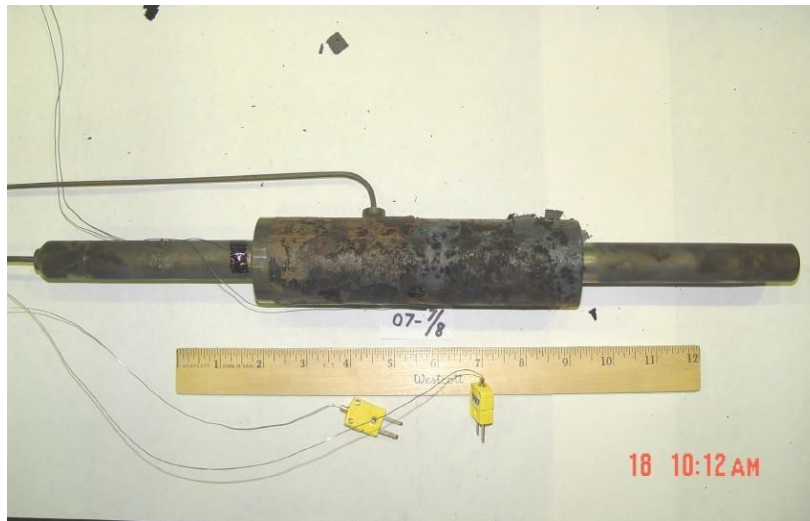


Figure 7-24 Specimen 07-7/8 in the Post-test Condition

7.6 Special Tests Designed to Study Mechanisms

7.6.1 Trends Observed in Leakage Tests and Revised Protocol

All the tests conducted to date, with both the tube side and the leakage path side pressurized to 17.2 MPa (2.5 ksi), showed a small-to-modest leak rate at room temperature, a gradual reduction of leak rate with increasing temperature to almost zero at $\geq 500^{\circ}\text{C}$. When the temperature was increased further, at a certain temperature the leakage started and increased rapidly to rates beyond our measurement capability (13,000 mg/min). The onset of rapid increase of leak rate increased with increasing leak path length, as shown in Fig.7-25. Also, the onset of high leakage can be expected to depend on the tightness of the tube-to-collar joint. A reasonable indicator for the tightness of the joint is the initial leak rate at room temperature. Figure 7-26 shows a plot of the temperature at onset of large leakage vs. the initial leak rate of the same specimen at room temperature. When the initial leak rate is large (> 10 mg/min), the joint is relatively "loose" and the temperature at onset of large leakage is relatively insensitive to it. However, when the initial leak rate is small (< 10 mg/min), that is the joint is relatively "tight", the temperature at onset of large leakage increases significantly.

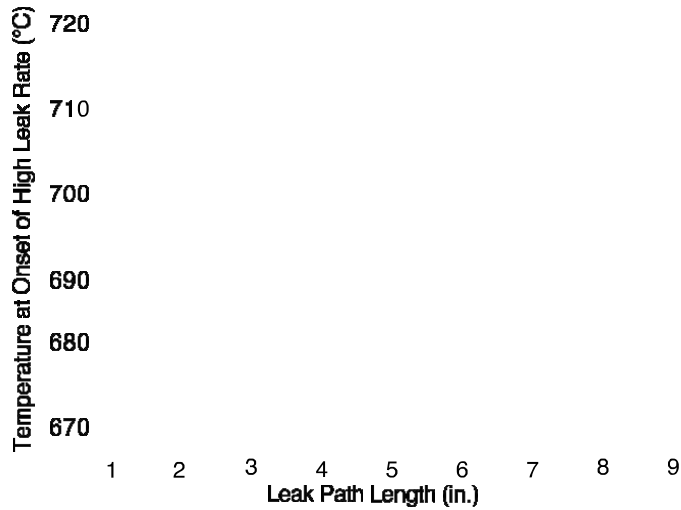


Figure 7-25 Variation of the Temperature at Onset of Large Leakage with Leak Path Length of the Specimens with 22 Mm (0.875 In.) Diameter Tubes

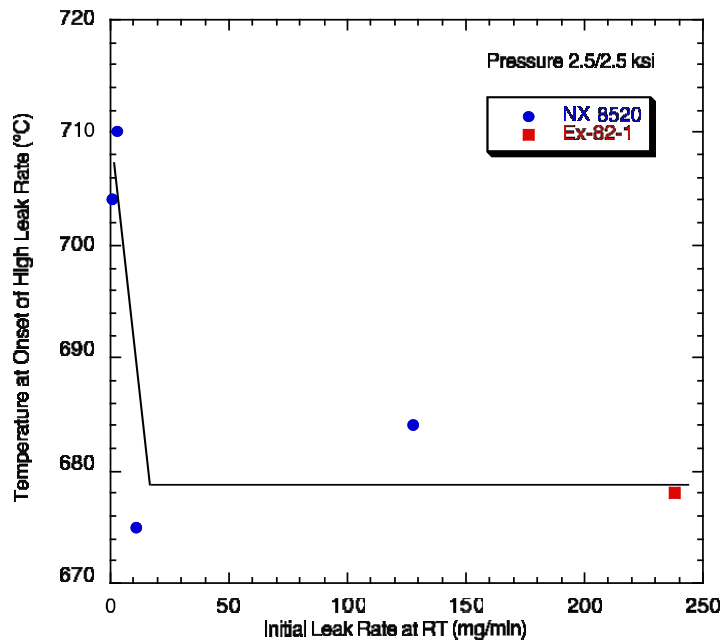


Figure 7-26 Variation of the Temperature at Onset of Large Leakage with Initial Leak Rate at Room Temperature of the Specimens with 22 mm (0.875 in.) Diameter Tubes

Most of the test results are consistent, at least qualitatively with the contact pressure leak model and the expected behavior under creep conditions. However, there was one significant difference that could not be explained satisfactorily - all the specimens were completely leak tight up until the onset of the large leakage. The leakage model predicts that before the gap between the tube and the collar actually opened resulting in large leakage, the contact pressure should have relaxed continuously, which in turn should have led to a small but increasing

leakage during the temperature ramp prior to the onset of large leakage. Such increasing leakage prior to the onset of large leakage was not observed. It was clear that macroscopic creep was occurring in the specimens, because non-leaking specimens (e.g., test 10-7/8) had large leakage when they were cooled down and tested at room temperature. The complete lack of leakage during most of the heat up period suggested that there is a mechanism, e.g., oxidation of collar, other than thermal expansion mismatch, which is responsible for the apparent increase in flow path resistance during the temperature ramp. A new test protocol was developed in which the opening of the gap between the tube and collar by creep due to crevice pressure was minimized. ANL also investigated using air instead of nitrogen for pressurizing the leakage path.

The new protocol called for the specimen to be tested in five stages

Stage 1 Leak rates at room temperature were measured for pressure (psi) pairs [1500, 1500], [2000, 2000], and [2500, 2500] to characterize leakage before creep.

Stage 2 With the specimen un-pressurized, heat at 150°C/hr to 600°C and then at a rate of 50°C/hr to ~ 670°C and then hold for four hours at this temperature. The slower heat up for the last 70°C was to ensure specimen thermal uniformity.

At the beginning of the 4 hour dwell at 670°C, the tube pressure was raised to 2500 psi and held constant for 4 hours. Fifteen minutes into the dwell, the leak path pressure was raised to 2000 psi and if the leak started it was allowed to grow only long enough to get a leak rate reading. If the leak did not start immediately, the leak path was depressurized, and after another 15 minutes, the specimen was pressurized again to 2000 psi; this cycle was repeated for the four hour dwell at 670°C

Stage 3 After cool down to room temperature, measure leak rates at room temperature for tube pressures of 2500, 2000, and 1500 psi for several different leak path pressures.

Stage 4 An additional stage of creep testing at 670°C was added when Stage 2 testing of specimen 01-3/4 produced no leakage over the entire 4 hours of testing with cycling of the leak path pressure between 0 and 2000 psi. During Stage 4 testing, the specimen was pressurized on both sides at [2500, 2000] psi for the entire four hours in contrast to Stage 2 where the specimen only saw leak path pressure of 2000 psi for a few minutes cyclically for 11 cycles over four hours. Thus, in Stage 4, the collar was exposed to more time at constant pressure, which allowed the leak path gap to open up and increase and cause increasing leakage with time.

Stage 5 The final Stage 5 room temperature leak testing was conducted to allow assessment of creep induced changes of leak path flow resistance caused by Stage 4 creep testing.

A question had arisen as to whether the cold gas supply feeding the jet exiting the leakage path during high temperature testing had sufficient residence time within the crevice to reach equilibrium with the specimen temperature. Any deviation of the gas temperature from the specimen temperature would affect the density of nitrogen and influence the mass flow rate calculations. Therefore, ANL conducted a test on a specimen that was instrumented with thermocouples to measure the gas temperature exiting the leakage path.

Finally, in most of our tests, the tube pressure and the leakage path pressure were independently controlled. In reality, the leakage path fluid will be provided by the primary fluid leaking through cracks in the tube wall. Therefore, ANL conducted two tests (Tests 06-7/8 and 02-7/8, discussed later) in which a 0.79 mm (0.03125 in.) diameter hole was drilled through the tube wall within the tube-to-collar junction and the hole that supplied gas to the collar was blocked off. The testing protocols for temperature and tube pressure were kept the same 7.6.2 except that the leakage path pressure was maintained via leakage through the tube cracks.

7.6.2 Specimen 01-3/4 (NX 8524)

This specimen was 19 mm (0.75 in.) in diameter and 102 mm (4 in.) long. The specimen in the as-received state is shown in Fig. 7-27. The results of the room temperature tests under stage 1 loading are included in Table 7-21, which shows that, as in the case of its companion specimen 04-7/8 (Table 7-9), the leak rates at all three pressures are relatively low.

During stage 2, the tube was heated to 670°C, pressurized to 2500 psi and held constant with no pressure applied on the crevice side. Periodically, ANL leak tested the specimen at temperature by applying a short period of 2000 psi pressure on the crevice side every 15 minutes. Our leak rate model predicted a significant relaxation of contact stress during the 4 hour hold with consequent leakage. However, no measurable leakage was observed up to 4 hours. It is conjectured that oxidation of the collar in the crevice was responsible for flow blockage. An old specimen (07-7/8) that was tested under the original protocol was then sliced transversely and axially to free up a piece of the collar from the tube. Visual examination showed extensive oxidation (black) on the collar ID surface. It is suspected that the formation of the oxide layer is primarily responsible for shutting off leakage at high temperature, which is unlikely during accident conditions due to minimal oxygen content in plant water. Although ANL has used high purity nitrogen as the pressurizing gas in all our tests to date, calculations showed that a 4-8 μm of oxide could still be expected to form in 4h in the low partial pressure oxygen atmosphere within the crevice.



Figure 7-27 Specimen 01-3/4 in the As-received Condition

Table 7-21 Stage 1 Initial Room Temperature Testing of Specimen 01-3/4

Tube Pressure (T) (psi)	Leak Path Pressure (LP) (°F)	Leak Rate (mg/min)
1506	1501	9.1
2006	2006	10.5
2501	2503	13.9

The leak test at room temperature during stage 3 showed a large increase in leak rate compared to that before the high temperature excursion (Table 7-21). The results are presented in Table 7-22 for a series of leak path pressures with zero tube pressure and for three different tube pressure levels (T) of nominally 2,500, 2,000, and 1,500 psi each involving a range of leak path pressures (LP). Furthermore, following the test at 400 psi, the leak path pressure was reduced to an earlier value of 96.5 psi and the leak rate was approximately the same as before, showing that the data was reproducible and that possible oxidation products produced by the high temperature testing were not being blown out by the high leak rates in Stage 3. The large increase in leak rate during stage 3 was consistent with the model prediction of accumulating creep strain during stage 2 testing. If collar oxidation is responsible for flow blockage at the elevated temperature during stage 2, it appears that the combined effect of creep and differential thermal strain during cool down was sufficient to overcome the blockage of flow area caused by oxidation.

During stage 4 testing at 670°C, the specimen was pressurized at [2500, 2000] for the entire four hours at 670°C. The pressure and leakage data are plotted in Fig.7-28. For the first 30 minutes under pressure there was no leakage; then a leak started and continued to grow linearly with time for the next 3.5 hours reaching 8352 mg/min.

Table 7-22 Stage 3 Room Temperature Tests of Specimen 01-3/4

Tube Pressure (T) (psi)	Leak Path Pressure (LP) (psi)	Leak Rate (mg/min)
0	49.0	61.5
0	96.7	193.7
0	196.2	728.5
0	297.3	1676.2
0	400.0	3085.6
0	96.5	189.1
2496	99	18.6
2495	200	67.3
2495	300	150.8
2495	402	284.2
2495	600	732.0
2003	600	1164.6
2006	390	430.4
2006	294	227.4
2008	107	31.3
1500	102	45.2
1500	197	162.4
1501	302	419.9
1502	605	2071.8
1503	804	4282.7

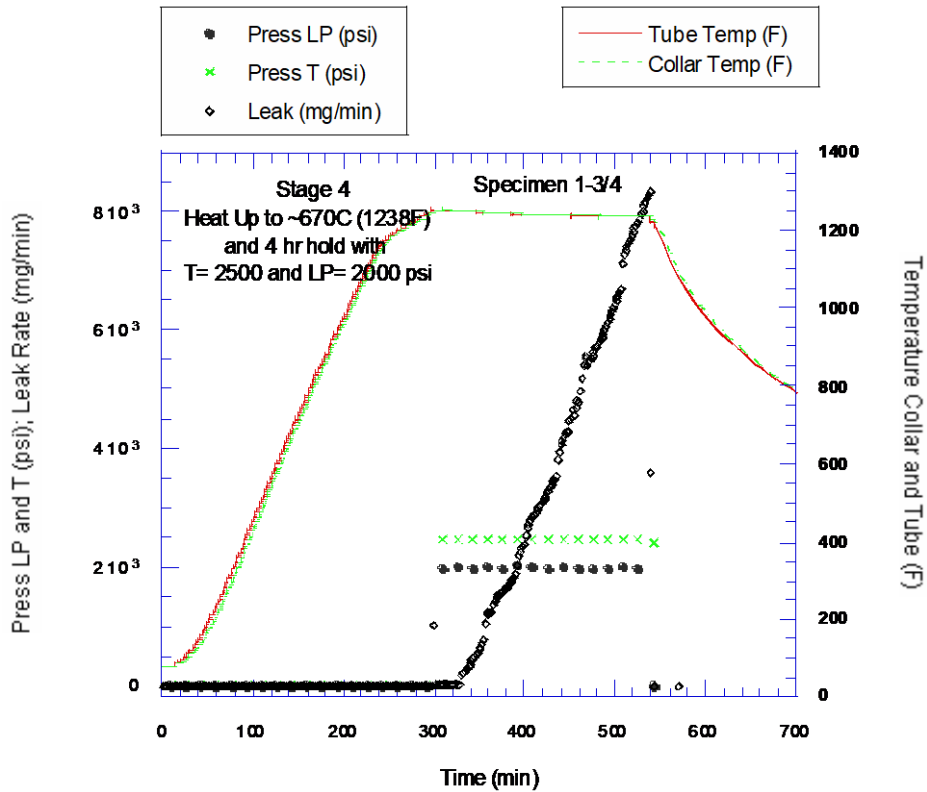


Figure 7-28 Stage 4 Pressure-Temperature-Leak Rate History of Specimen 01-3/4

Table 7-23 shows the final room temperature leak rate test data for specimen 01-3/4. The room temperature leak data taken during Stage 5 testing showed a considerable increase over the room temperature leak data obtained during Stage 3, indicating additional creep strains had occurred during the high temperature excursion in stage 4. The specimen in the post-test condition (Fig.7-29) showed that the collar was oxidized significantly during the test.



Figure 7-29 Specimen 01-3/4 in the Post-test Condition

Table 7-23 Stage 5 Final Room Temperature Tests of Specimen 01-3/4

Tube Pressure (T) (psi)	Leak Path Pressure (LP) (psi)	Leak Rate (mg/min)
0	50.7	333
0	100.6	1037
0	200	3387
0	301	6786
0	401	10724
0	99.5	1019
2497	99.1	302
2494	200	1134
2498	300	2455
2496	401	4282
2495	600	9183
1999	598	10950
2001	400	5307
2003	297	3050
2005	202	1483
1998	100	389
1496	101	534
1496	199	1836
1496	301	3874
1497	401	6494
1497	602	12997
0	98.8	994

7.6.3 Specimen 01-7/8 (NX-8520)

This specimen has alloy 600 SG tubing of 22 mm (0.875 in.) dia. and a 51 mm (2 in.) leak path length. The specimen in the as-received state is shown in Fig.7-30. The protocol involved three test Stages at creep temperatures and used a two-step heat up during which time the specimen was unpressurized. The first step involved furnace heat up at a rate of 150°C/hr to 600°C which was then followed by a slower heat up at a rate of 50°C/hr to a furnace temperature of 670°C (692C actual specimen temperature). The slower heat-up to final desired temperature reduces furnace temperature overshoot and allows the specimen temperature to become uniform. For each creep test, the specimen was held at constant temperature and subjected to low various levels of pressurization for various periods of time which increased in duration for each subsequent test. After each of the three elevated temperature creep tests (Stages 2, 4, 6), ANL measured leak rate when the specimen was cooled to room temperature and compared the leak rates with initial data from Stage 1 room temperature testing. This comparison allowed us to evaluate the influence on leak rate of the permanent changes in leak path flow resistance caused by creep and collar oxidation.



Figure 7-30 Specimen 01-7/8 in the As-received Condition

Stage 1

Stage 1 involved room temperature leak testing using three pressurization (psi) pairs of [T,LP] = [0,100], [0,200], and [0,400]. The testing furnishes leak data prior to creep testing which is used for evaluating permanent changes in leak rate caused by creep. The leak rate data for the three levels of pressurization [T,LP] = to [0,101], [0,203], and [0,403] were 4.6, 4.6, and 5.8 mg/min respectively. These are very small leak levels; higher leak rates were expected under these low leak path pressures.

Upon arrival of the specimens from B&W in 2007 all specimens underwent leak test screening at room temperature. Specimen 01-7/8 in 2007 when tested under 100 psi on the leak path with no tube pressure exhibited a leak rate of 2190 mg/min many times larger than that from the current test. There is the possibility that oxidation of the collar during the intervening months has occurred. It should be noted that the specimen was stored in a plastic bag with desiccant. However, it is possible that the water found in the leak path exit crevice for this specimen upon arrival from B&W may have caused oxidation or corrosion inside the leak path which greatly reduced the flow rate in the current test.

Stages 2 and 3

The specimen was heated up from room temperature at 150°C/hr up to 600°C followed by final heat up at 50°C/hr to a furnace temperature of 670°C (692°C- 1282°F actual specimen temperature). The specimen was then subjected to a 2 hour hold while at 692°C to let oxidation of the collar occur. The specimen was tested unpressurized, so no creep would be induced by pressurization and only the stresses from differential tube/collar thermal expansion and the hydraulic expansion would be relieved by creep. This allowed an easier interpretation of the role collar oxidation maybe playing in influencing leak rate. After the hold, the specimen was cool down to room temperature. It was then leak tested at room temperature with the same pressures as in stage 1. The results are shown in Table 7-24. The leak rates are much greater than those obtained in stage 1. Thus, the relaxation of stresses due to hydraulic expansion and thermal mismatch during heating introduced enough creep deformation to reduce the flow path resistance significantly. Further, the oxidation during the 2 hour hold at 670°C did not have a significant influence on the leakage.

Table 7-24 Stage 3 Room Temperature Tests on Specimen 01-7/8

Tube Pressure (T) (psi)	Leak Path Pressure (LP) (psi)	Leak rate (mg/min)
0	98	404
0	199	1509
0	400	5843

Stage 4

Stage 4 testing involved a second heating of the unpressurized specimen to creep temperatures employing the same two step heat up to 692°C as before. However, Stage 4 involved a 3 hour hold at 692°C instead of the 2 hours used earlier to allow more time for collar oxidation to occur. In addition, during the hold period, three short-duration cycles of leak path pressurization of 100, 200, and 400 psi with no tube pressurization were applied and all the leak rates were measured to be essentially zero. The specimen was then cooled down to room temperature.

Stage 5

Stage 5 testing involved repeating the room temperature leak testing of Stage 1 for the pressurization (psi) pairs of [T,LP] = to [0,100], [0,200], and [0,400]. Stage 5 data, shown in Table 7-25, indicate about 10-20% increase in leak rate compared to those in stage 3.

Table 7-25 Stage 5 Room Temperature Tests on Specimen 01-7/8

Tube Pressure (T) (psi)	Leak Path Pressure (LP) (psi)	Leak rate (mg/min)
0	98	531
0	200	1899
0	401	6386

Stage 6

Stage 6 testing involved a third heating of the unpressurized specimen to 670°C employing the same two step heat up to 692°C as used in Stages 2 and 4. After reaching 692°C, ANL waited for 1 hr. for the specimen to reach thermal equilibrium. Then the tube was first pressurized to 2500 psi followed by a quick pressurization of the leak path to 2000 psi. Both pressures were held constant and the leak rate was monitored.

Figure 7-31 shows the data for Stage 6 testing. As shown, at approximately 2 minutes after pressurization the leak rate was zero and then started to grow. For the next 57 minutes the leak rate grew steadily from zero to 11,126 mg/min at which time the test was stopped, specimen depressurized, and cooled down to room temperature. If testing were continued, the leak rate would have continued to grow.

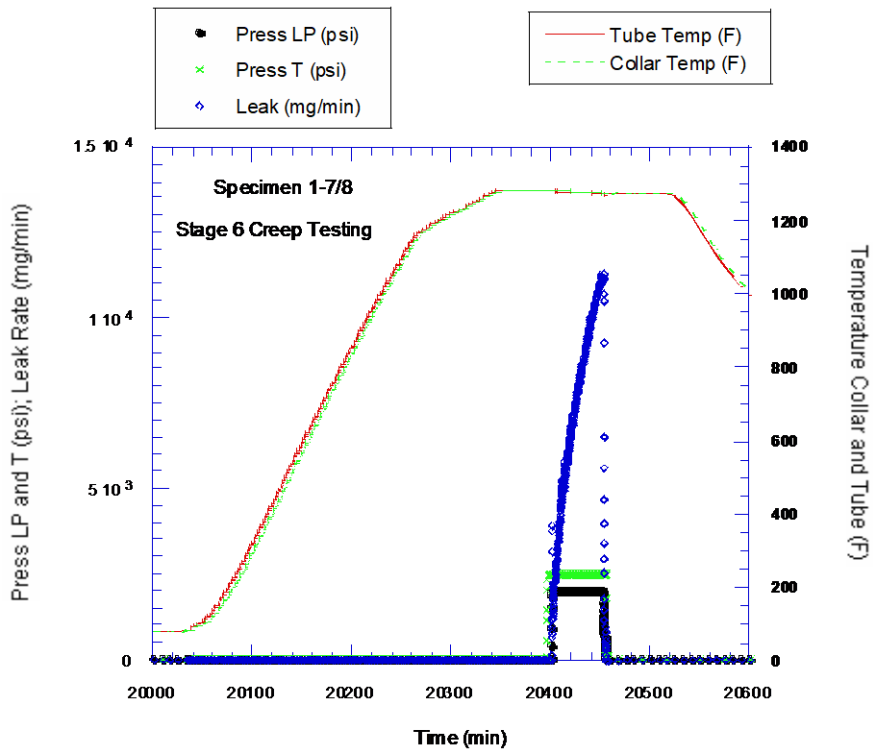


Figure 7-31 Stage 6 Pressure-Temperature-Leak Rate Data for Specimen 01-7/8

Stages 7 and 8

Stage 7 testing involved repeating the room temperature leak testing of Stage 1 for the pressurization (psi) pairs of [T,LP] = [0,100], [0,200], and [0,300]. Because the specimen leak gap had opened so much by creep, ANL could only pressurize the leak path to 300 psi before the leak rate exceeded the flow meter limit. Stage 7 leak data are tabulated in Table 7-26.

Table 7-26 Stage 7 Room Temperature Tests on Specimen 01-7/8 with Nitrogen

Tube Pressure (T) (psi)	Leak Path Pressure (LP) (psi)	Leak rate (mg/min)
0	99	2,504
0	202	6,835
0	305	11,776

In Stage 8, ANL conducted a companion set of leak tests (Table 7-27) which involved the same pressurization pairs and room temperature testing as Stage 7 but a change in pressurization gas from nitrogen to air. This was done to check our flow instrumentation in preparation for testing of our next specimen. Both sets of tests showed much greater leak rates than observed in stage 5. The post-test specimen is shown in Fig. 7-32.



Figure 7-32 Specimen 01-7/8 in the Post-test Condition

Table 7-27 Stage 8 Room Temperature Tests on Specimen 01-7/8 with Air

Tube Pressure (T) (psi)	Leak Path Pressure (LP) (psi)	Leak rate (mg/min)
0	100	2,566
0	199	7,016
0	301	12,137

7.6.4 Specimen 03-3/4 (NX 8524)

This is a 102 mm (4 in.) long, 19 mm (0.75 in.) diameter Alloy 600 tube (Heat NX 8524). The test protocol was modified from that used for previous testing to explore the combined influence of creep and collar oxidation on the leak behavior at elevated temperature. Instead of nitrogen, air was used to pressurize the leakage path. Air is more conducive to collar oxidation than nitrogen and is more representative of the oxidation effects in the prototypic environment of superheated steam. Specimen 03-3/4 had two thermocouples one mounted on the tube and the second on the collar. The thermocouples on the specimen allowed monitoring specimen temperature uniformity. The specimen in the pre-test condition is shown in Fig. 7-33.



Figure 7-33 Specimen 03-3/4 in the Pre-test Condition

Results from the initial Stage 1 room-temperature leak-rate characterization testing are shown in Table 7-28. These pre-creep leak rates are very small.

Table 7-28 Stage 1 Initial Room Temperature Testing of Specimen 03-3/4

Tube Pressure (T) (psi)	Leak Path Pressure (LP) (psi)	Leak Rate (mg/min)
0	103	0
0	203	1.22
0	402	6.1

During stage 2 testing of specimen 03-3/4, the unpressurized specimen was pressurized to [T,LP] = 2500/2000 psi (17.2/13.8 MPa) when the specimen temperature reached 500°C and then heated at a rate of 50°C/h to 700°C. Following that, a 1 hour furnace dwell was maintained, which yielded an actual uniform specimen temperature of 716°C. There was no leakage until 10 minutes after reaching 716°C, at which time the leak path gap opened by macro-creep and the leak rate grew from 0 to 14,308 mg/min over the next 25 minutes (Fig 7-34). During tube leaking, the thermocouples on the specimen collar and tube as well as those in the core tube of the furnace showed no signs of being cooled by gas flow into the specimen from the room-temperature gas supply bottles.

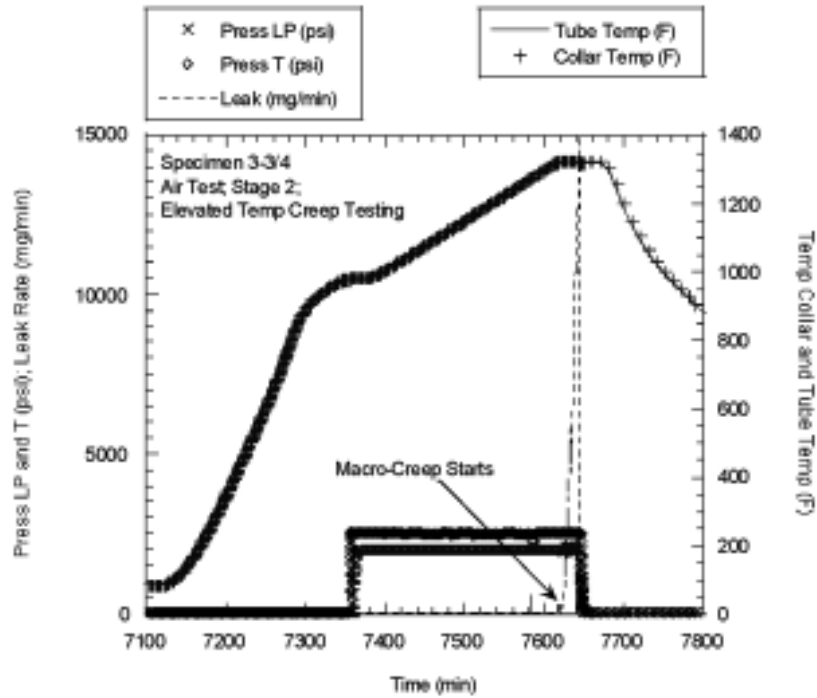


Figure 7-34 Pressure, Leak Rate and Temperature History of Specimen 03-3/4 at High Temperature During Stage 2

During Stage 3 final room-temperature air testing for the three pressure pairs shown in Table 7-29, specimen 03- 3/4 yielded leak rates of 406 mg/min, 1421mg/min, and 5,037 mg/min, respectively. These leak rates are significantly greater than the corresponding leak rates during Stage 1 testing (Table 7-28). However, comparison with the leak rates during stage 3 testing of specimen 02-3/4 (Table 7-29) suggests that oxidation has reduced the leak rates by more than a factor of 2 (note that the application of tube pressure would reduce the leak rates from those shown in Table 7-29). The specimen in the post-test condition is shown in Fig. 7-35.

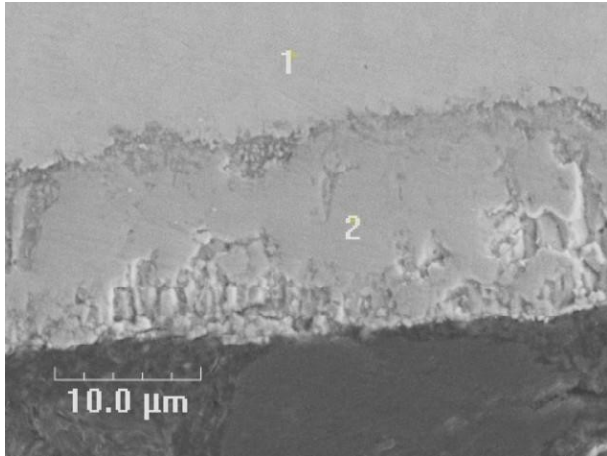
Table 7-29 Stage 3 Room Temperature Tests on Specimen 03-3/4 with Air

Tube Pressure (T) (psi)	Leak Path Pressure (LP) (psi)	Leak rate (mg/min)
0	103	406
0	203	1421
0	402	5037

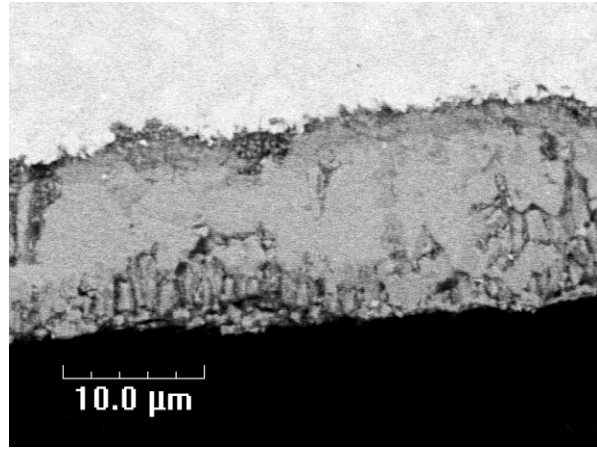


Figure 7-35 Specimen 03-3/4 in the Post-test Condition

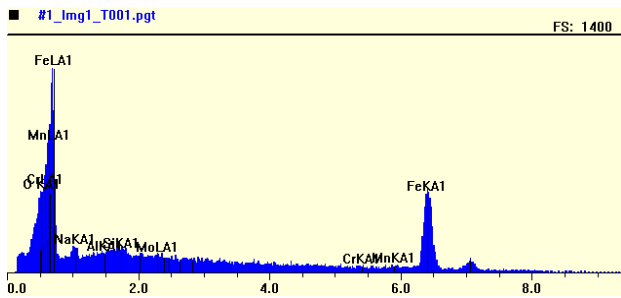
Specimen 3-3/4 was cut open to assess the oxide scale thickness on the inner surface of the collar within the tube-to-collar junction. Figure 7-36a-b show SEM micrographs for the cross-sectional view of the inside surface of the collar. As shown in Fig. 7-36 (b), the oxide layer thickness appears to be about 10 μm . Figures 7-36 (c) and (d) show EDS spectra for the spots "1" and "2" designated in Fig. 7-36 (a). Oxygen peak at the spot "2" is clearly observed. As compared to the oxide thicknesses (1-4 μm) in specimens tested with high purity nitrogen gas, the oxide layer in this specimen is much thicker.



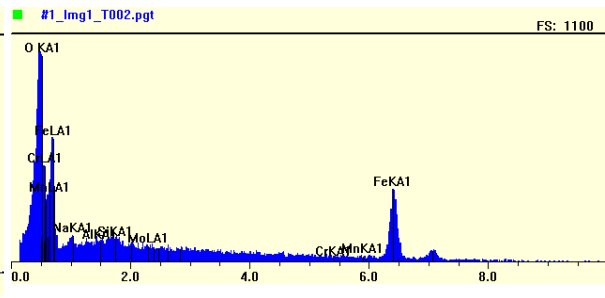
(a) Secondary Electron Image



(b) Back-scattered Electron Image



(c) Spot "1" in (a)



(d) Spot "2" in (a)

Figure 7-36 SEM Micrographs for the Cross-sectional View of the Inside Collar Surface Showing Metal Part (upper) and Mounting Polymer (lower) Region Divided by Oxide Layer with (A) Secondary Electron Image and (B) Back-Scattered Electron Image (3,000X magnification); EDS Analysis for (C) Spot "1" and (d) Spot "2" in (a)

7.6.5 Test 06-7/8 (EX-82-1)

The 101.6 mm (4 in.) long specimen 06-7/8 has a 0.79 mm (0.03125 in.) diameter hole drilled through the tube to simulate a flawed SG tube. The pre-test condition specimen is shown in Fig. 7-37. The tube hole is located in the annular inlet plenum of the leak path directly opposite the original nitrogen supply line entering through the collar used to separately supply the leak path with gas. In this test, the leak path of the specimen was only pressurized by tube pressurization, which is more prototypical under the conditions specified in Case 8b.

The tube hole was machined at ANL. Upon receiving the specimen from the machine shop and prior to leak testing, nitrogen gas was blown through the tube pressurization line and the old leak path supply line hole was monitored for drilling debris. There was no sign of debris, and the specimen was sent back to the shops for placement of a seal weld on the collar supply linehole. Nitrogen gas was blown at 2.76 MPa (400 psi) into the tube and the leak path exit plane was checked for bubbles. Very small bubbles were observed from several locations around the leak path exit circumference, indicating the entrance to the leak path was not blocked by drilling debris. Because questions had been raised as to whether the gas supplied to the specimens

from the high-pressure tanks at room temperature was warmed adequately by the furnace prior to entering the leak path, one of three thermocouples placed on Specimen 06-7/8 was located close to the jet exit plane in the path of the leak jet to monitor gas temperature exiting the specimen during high-temperature testing (Fig. 7-38).

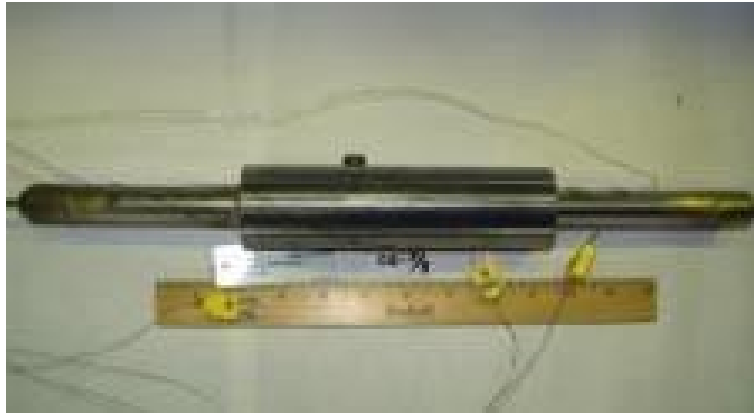


Figure 7-37 Specimen 06-7/8 in the Pre-test Condition

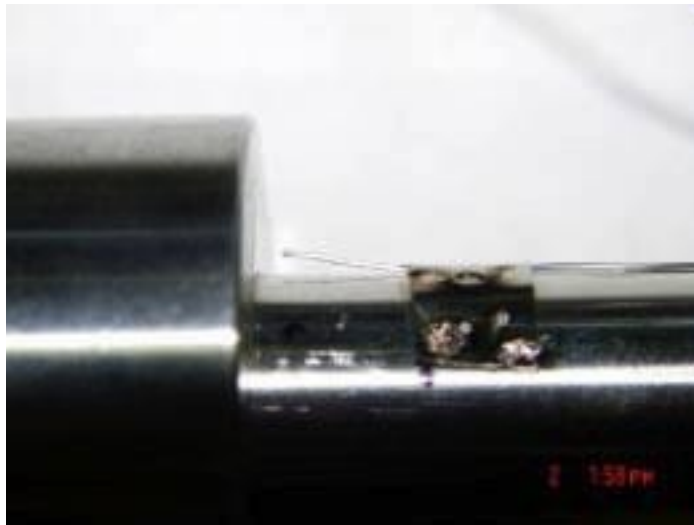


Figure 7-38 Thermocouples Attached to Specimen 06-7/8 Located Near the Jet Exiting the Leakage Path

Specimen 06-7/8 was tested using nitrogen gas pressurization with the following three Stage protocol

1. Initial pre-creep (Stage 1) room-temperature leak rates were measured for a series of tube pressures ranging from 0.69 to 3.45 MPa (100 to 500 psi).
2. For the elevated-temperature creep testing (Stage 2), the specimen was heat up to 500°C with no pressurization and then pressurized to a tube pressure of 17.2 MPa (2500 psi). The furnace heating rate was then reduced from 150°C/hr to 50°C/hr for

final heat-up to a furnace temperature of 700°C, which was followed by a 1 hour dwell at this temperature. During the entire test, the leak rate was monitored until it became too large for the flow meter.

3. Upon specimen cool-down, ANL measured leak rates (Stage 3) for the same range of pressures as for Stage 1 in order to quantify the degree of permanent creep-induced change in the leak path gap and the leak rate.

The results from the Stage 1 testing are given in Table 7-30.

Table 7-30 Stage 1 Initial Room Temperature Testing of Specimen 06-7/8

Tube Pressure (T) (psi)	Leak Rate (mg/min)
101	0
200	0
300	0
401	1.16
500	4.64

Figure 7-39 shows the Stage 2 elevated-temperature pressure and leak rate data for specimen 06-7/8. Upon reaching 500°C, the specimen was pressurized to 17.2 MPa (2500 psi) and the leak rate began oscillating initially between a few hundred mg/min and zero with a few second cycle period. As the specimen underwent further heat-up under furnace programmed control to 700°C (1292°F), the oscillations in leak rate amplitude continued to grow but periodically still went to zero. At a specimen temperature of approximately 650°C (1202°F), the leak rate continued to oscillate but the leak maximum started to grow more quickly, indicating macrocreep had become significant. Upon reaching a temperature of 663°C (1225°F), the leak rate no longer went to zero and the upper value started to grow more quickly and had reached ≈2015 mg/min. Upon further temperature increase to 678°C (1252°F), the leak rate oscillation had almost stopped and the leak rate had reached 4176 mg/min. Upon reaching 687°C (1269°F), the leak rate had increased without oscillation to 10,116 mg/min. Approximately 6 minutes later, the leak had grown to 15,660 mg/min which exceeded our flow meter limit, and the experiment was stopped. Table 31 shows the results from the room temperature testing in Stage 3. The specimen in the post-test condition is shown in Fig. 7-40.

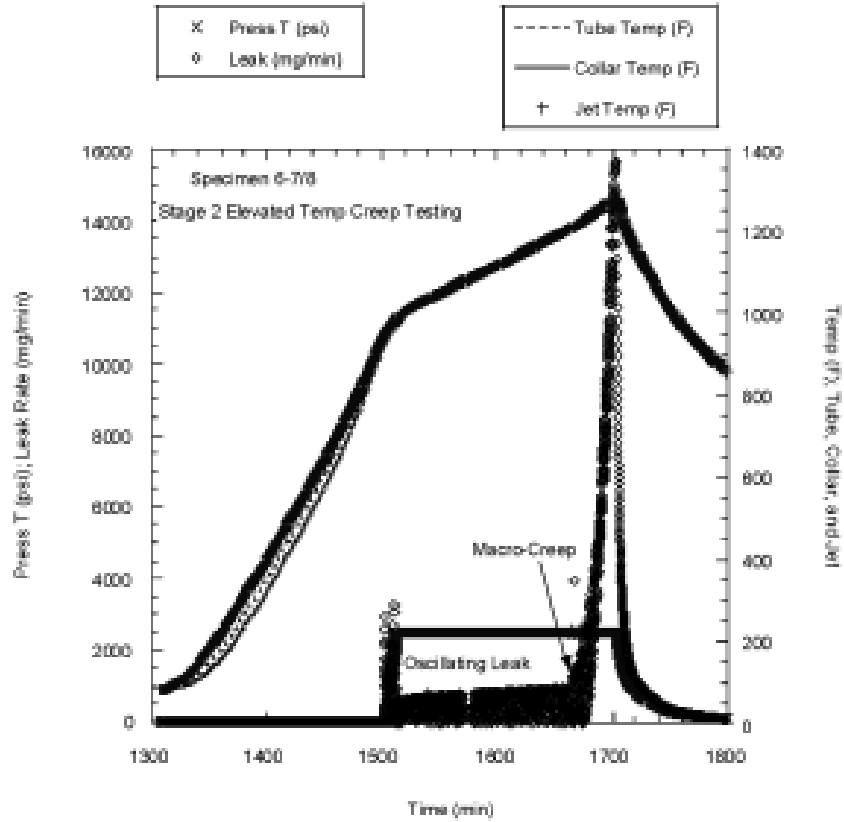


Figure 7-39 Stage 2 Elevated Temperature Testing of Specimen 06-7/8

Table 7-31 Stage 3 Final Room Temperature Testing of Specimen 06-7/8

Tube Pressure (T) (psi)	Leak Rate (mg/min)
99	1268
201	4329
299	8349
405	13,443
500	Too large to measure



Figure 7-40 Specimen 06-7/8 in the Post-test Condition

7.6.6 Test 02-7/8 (EX-82-1)

The 5 mm (2 in.) long specimen 02-7/8 has a 0.79 mm (0.03125 in.) diameter hole drilled through the tube to simulate a flawed SG tube. The specimen in the pre-test condition is shown in Fig. 7-41. Nitrogen gas was blown at 2.76 MPa (400 psi) into the tube and the leak path exit plane was checked for bubbles. Small bubbles were observed from several locations around the leak path exit circumference, indicating the entrance to the leak path was not blocked by drilling debris. As was done for specimen 06-7/8, one of three thermocouples placed on specimen 02-7/8 was located close to the jet exit plane in the path of the leak jet to monitor gas temperature exiting the specimen during high-temperature testing. Specimen 02-7/8 was tested with the following four Stage protocol:

1. Initial pre-creep (Stage 1) room-temperature leak rates were measured for a series of tube pressures ranging from 500 to 2500 psig.
2. For the normal operating temperature testing (Stage 2), the specimen was pressurized at 2500 psig and heated up with the ramp rate of 50° C/hr to 300 C. The leak rate was continuously monitored to 300° C. The temperature at 300° C was held for as long as it was necessary to obtain a reading. Then, the specimen was depressurized and cooled down.
3. For the elevated-temperature creep testing (Stage 3), the specimen was heated up to 500° C with no pressurization and then pressurized to a tube pressure of 17.2 MPa (2500 psig). The furnace heating rate was then reduced from 150° C/hr to 50° C/hr for final heat-up to a furnace temperature of 700° C, which was followed by a 1 hour dwell at this temperature. During the entire test, the leak rate was monitored until it became too large for the flow meter.
4. Upon specimen cool-down, leak rates (Stage 4) were measured for the same range of pressures as for Stage 1 in order to quantify the degree of permanent creep-induced change in the leak path gap and the leak rate.



Figure 7-41 Specimen 02-7/8 in the Pre-test Condition

The test results from the Stage1 testing are shown in Table 7-32. During Stage 2 testing, starting with the specimen pressurized to 2500 psi at room temperature, as it was heated to 300°C, the leak rate reduced from 1800 to 200 mg/min (Fig. 7-42). No leak rate oscillation was observed.

Table 7-32 Stage 1 Initial Room Temperature Testing of Specimen 02-7/8

Tube Pressure (T) (psi)	Leak Rate (mg/min)
500	0
1000	5
1500	64
2000	350
2500	1800

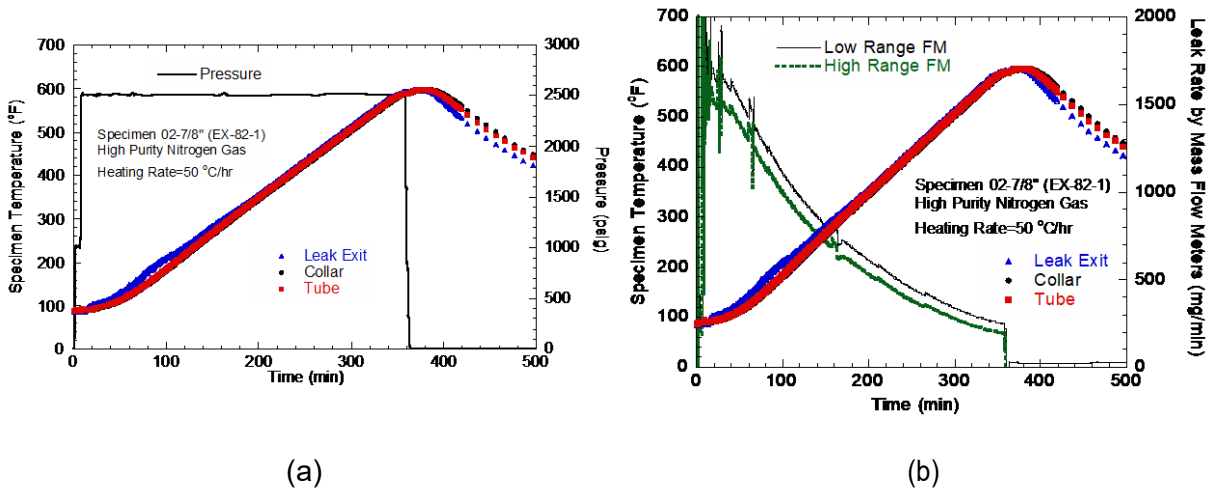


Figure 7-42 Variation of (a) Specimen Pressure and Temperature and (b) Leak Rate and Specimen Temperature with Time for Test 02-7/8 during Stage 2

Figure 7-43a shows the specimen temperatures and pressure as functions of time during Stage 3 elevated temperature leak rate testing. Upon reaching 500°C, the specimen was pressurized to 17.2 MPa (2500 psi). As noted in Fig. 7-43a, the furnace heater power was off for 20 minutes due to the malfunction of high temperature limit controller, but heating was resumed after 20 minutes. Figure 7-43b shows leak rates measured by a high-range mass flow meter, as well as specimen temperatures. The leak rate began oscillating initially between 850 mg/min and zero once every second. As the specimen underwent further heat-up under furnace programmed control to 700°C (1292°F), the oscillations in leak rate amplitude continued to grow to ~1000 mg/min but periodically still went to zero. At a specimen temperature of approximately 662°C (1224°F), the leak rate continued to oscillate but the leak maximum started to grow more quickly, indicating macro-creep had become significant. The leak rate no longer went to zero. Upon further temperature increase to 666°C (1230°F), the leak rate oscillation had almost stopped and the leak rate had reached 6750 mg/min. Upon reaching 679°C (1255°F), the leak rate had increased without oscillation to 10,000 mg/min. Approximately 8 minutes later, the leak had grown to 15,660 mg/min which exceeded our flow meter limit, and the experiment was stopped. As shown in Fig. 7-44, the temperature readings from the thermocouple placed in the leak path exit showed that the gas temperature started to deviate from the specimen and collar temperatures when the leak rate exceeded 8000 mg/min. The alloy 600 tube temperature was almost identical to the carbon steel collar temperature, except that when the leak rate exceeded 10,000 mg/min, the tube temperature began to lag behind the collar temperature possibly because of inadequate heating of the nitrogen gas inside the tube at high leak rates. When the leak rate reached the maximum limiting value, the leak exit, collar, and tube temperatures were 690°C (1274°F), 682°C (1260°F), and 677°C (1251°F), respectively. It appears that nitrogen gas within the crevice was heated sufficiently.

The overall leakage behavior of the specimen 02-7/8 at elevated temperature was qualitatively similar to that of previous specimens tested with separate pressurization of the tube and leak path. The overall behavior of the two specimens with the drilled 0.8 mm (0.03125 in.) diameter holes, 02-7/8 and 06-7/8, are very similar. Stage 1 testing at 500 psi pressure showed that specimen 02-7/8 initially had a tighter joint than 06-7/8. As a result, the temperature at which the leak rate started to grow during high temperature testing was 662°C for specimen 02-7/8 and 650°C for specimen 06-7/8. However, the temperature at which the leak rate reached

10,000 mg/min was 679°C for specimen 02-7/8 and 687°C for specimen 06-7/8, possibly reflecting the longer leak path of 06-7/8 relative to 02-7/8.

Both tests suggest that there is a tube/collar structure and leakage gas dynamic instability at $\geq 500^\circ\text{C}$ which causes the leakage path pressure to oscillate and which persists until a physical gap opens up at the tube-to-collar interface. The amplitude and the period of the pressure oscillation in the shorter leakage-path-specimen (02-7/8) are comparable to those in the longer leakage-path-specimen (06-7/8). Interestingly, during Stage 2 testing of specimen 02-7/8 when the leak rate gradually decreased from 1800 to 200 mg/min as the specimen temperature was raised from room temperature to 310°C, such oscillations did not occur, as shown in Fig. 7-42b. It is not clear whether and when such oscillations would initiate if specimen 02-7/8 had been pressurized from the beginning of Stage 3 testing.

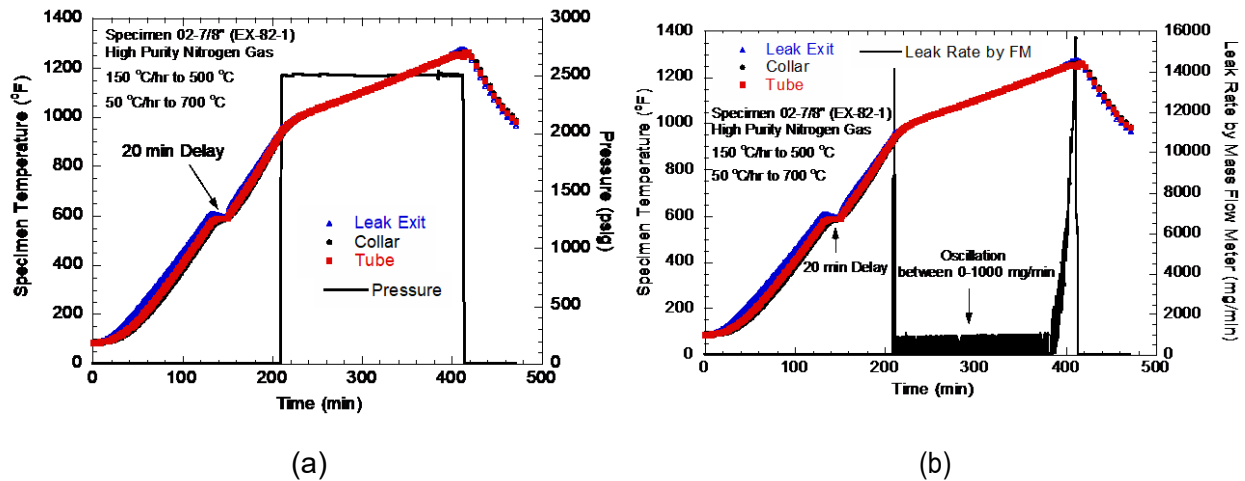


Figure 7-43 Variation of (a) Specimen Pressure and Temperature and (b) Leak Rate and Specimen Temperature with Time for Test 02-7/8 during Stage 3

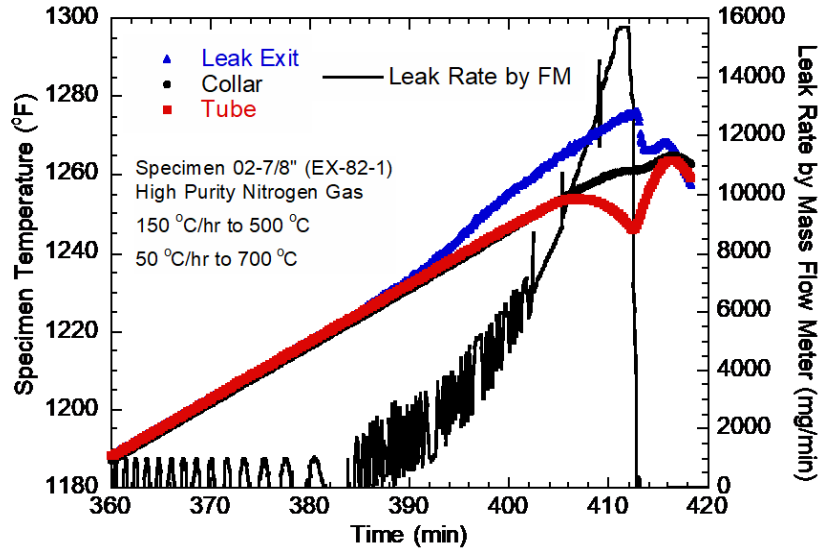


Figure 7-44 Expanded View of Variation of Specimen, Collar and Gas Temperatures and Leak Rate for Test 02-7/8 during Stage 3

The leakage rates measured during the final Stage 4 room temperature testing are shown in Table 7-33. Comparison of Tables 7-33 and 7-31 show that the leak rates in specimen 06-7/8 were greater than those in specimen 02-7/8, possibly because specimen 06-7/8 was heated to a higher temperature [687°C (1269°F)] than specimen 02-7/8 [680°C (1256°F)] during stage 3 testing.

Table 7-33 Stage 4 Final Room Temperature Testing of Specimen 02-7/8

Tube Pressure (T) (psi)	Leak Rate (mg/min)
102	870
202	2800
305	5600
408	8800
504	12,000

8 ANALYSIS OF TESTS

8.1 Contact Pressure and Gap Analysis

Contact pressures for all the specimens were analyzed by FEA that took into account the effects of hydraulic expansion, gas pressure, thermal expansion mismatch between the tube and the collar and relaxation of stresses due to creep. A simplified 1-dimensional model for calculating contact pressure was also developed with the objective of combining it with our 1-dimensional leak rate model developed in Section 5.3 so that leak rates for the tube-to-collar specimens can be predicted under creeping conditions at high temperature.

8.1.1 1-Dimensional Model for the Tube-to-Collar Junction

Nomenclature

α_t and α_c	Average thermal expansion coefficients of tube and collar
α'_t and α'_c	Incremental thermal expansion coefficients of tube and collar
$\dot{\delta}_t$ and $\dot{\delta}_c$	Radially outward displacement rates of tube and collar
Δ	Free tube hydraulic expansion
Δ_{th}	Interference due to free radial thermal expansions of tube and collar
Δ_p	interference due to pressure-induced free radial expansions of tube and collar
Δ_{pt} and Δ_{pc}	Free pressure-induced radial expansions of tube and collar
σ_t and σ_c	Average hoop stresses in tube and collar
σ_{to} and σ_{co}	Initial average hoop stresses in tube and collar
A_t and A_c	Steady state creep rate coefficients for tube and collar
B_t and B_c	Primary creep rate coefficients for tube and collar
E_t and E_c	Elastic moduli of tube and collar
h_t and h_c	Wall thicknesses of tube and collar
K_t and K_c	Elastic stiffnesses of tube and collar
n_t and n_c	Stress exponents for steady state creep rates of tube and collar
m_t and m_c	Stress exponents for primary creep rates of tube and collar
p_f and p_1	Fluid pressures in the crevice and tube
P_c and P_{co}	Contact pressure and initial contact pressure
\dot{P}_c	Rate of increase of contact pressure
r_t and r_c	Radii of the tube and collar
r_{int}	Radius at the interface between tube and collar
t	Time
t_{ot} and t_{oc}	Primary creep time constants for tube and collar

T and \dot{T} Temperature and temperature ramp rate

Initial Conditions at $t=0$

Total radial lack of fit = $\Delta + \Delta_{th} + \Delta_p$ where

Δ is the lack of fit due to hydraulic expansion of the tube, $\Delta_{th} = (\alpha_t - \alpha_c)(T - T_{ref})r_{int}$ and $\Delta_p = \Delta_{pt} - \Delta_{pc}$.

$\Delta_{pt} = (p_1 - p_f)/K_t$ and $\Delta_{pc} = p_f/K_c$, where

$$K_t = \frac{E_t h_t}{r^2} \text{ and } K_c = \frac{E_c h_c}{r^2}$$

Compatibility of deformation requires that at $t=0$

$D + D_{th} + D_p = P_c/K_t + P_c/K_c$ which gives the initial contact pressure as

$$P_c = P_{co} = \frac{\Delta + \Delta_{th} + \Delta_p}{\frac{1}{K_t} + \frac{1}{K_c}}, \quad (20)$$

$$\text{Initial tube stress} = \sigma_w = -\frac{(P_{co} + p_f - p_1)r_t}{h_t}, \text{ and} \quad (21a)$$

$$\text{Initial collar stress} = \sigma_{co} = \frac{(P_{co} + p_f)r_c}{h_c}. \quad (21b)$$

The value of Δ was determined for each tube diameter and material by correlation of contact pressure calculated by FEA and the model.

Relaxation of Contact Pressure at High Temperature by Creep ($t > 0$)

Considering creep strain to be the sum of primary and steady state creep strains as discussed in section 4.2, the equations are reproduced here.

$$\epsilon_c = \epsilon_{c,p} + \epsilon_{c,s} \quad (22)$$

where $\epsilon_{c,p}$ = primary creep strain and $\epsilon_{c,s}$ = steady state creep strain,

$$\epsilon_{c,p} = A_1 \sigma^n \exp\left(-\frac{Q_1}{T}\right) \left[1 - \exp\left(-\frac{t}{t_0}\right)\right] \quad (23a)$$

and

$$\epsilon_{c,s} = A_2 t \sigma^n \exp\left(-\frac{Q_2}{T}\right) \quad (23b)$$

Substituting

$$A = A_1 \exp\left(-\frac{Q_1}{T}\right) \text{ and } B = A_2 \exp\left(-\frac{Q_2}{T}\right),$$

and using Eqs. 23a and 23b, Eq. 22 reduces to

$$\varepsilon_c = A\sigma^n t + B\sigma^m \left[1 - \exp\left(-\frac{t}{t_0}\right)\right], \quad (24a)$$

which can be differentiated to give

$$\dot{\varepsilon}_c = A\sigma^n + B\sigma^m \frac{1}{t_0} \exp\left(-\frac{t}{t_0}\right) \quad (24b)$$

The average tube and collar stresses are given by

$$\text{Tube stress } \sigma_t = -\frac{(P_c + P_f - P_1)r_t}{h_t} \quad (25a)$$

and

$$\text{collar stress } \sigma_c = \frac{(P_c + P_f)r_c}{h_c} \quad (25b)$$

Radially outward displacement rates of tube and collar = $\dot{\delta}_t$ and $\dot{\delta}_c$, where

$$\dot{\delta}_t = -A_t \sigma_t^n r_t - B_t \sigma_t^m \frac{1}{t_{0t}} \exp\left(-\frac{t}{t_{0t}}\right) r_t - \frac{\dot{P}_c}{K_t} + \alpha'_t r_{im} \dot{T} \quad (26a)$$

and

$$\dot{\delta}_c = A_c \sigma_c^n r_c + B_c \sigma_c^m \frac{1}{t_{0c}} \exp\left(-\frac{t}{t_{0c}}\right) r_c + \frac{\dot{P}_c}{K_c} + \alpha'_c r_{im} \dot{T} \quad (26b)$$

Equating the radial displacement rates gives

$$\frac{d}{dt}(P_c) + \frac{A_t r_t \sigma_t^n + A_c r_c \sigma_c^n + B_c r_c \sigma_c^m \frac{1}{t_{0c}} \exp\left(-\frac{t}{t_{0c}}\right) + B_t r_t \sigma_t^m \frac{1}{t_{0t}} \exp\left(-\frac{t}{t_{0t}}\right) + (\alpha_c - \alpha_t) r_{im} \dot{T}}{\frac{1}{K_t} + \frac{1}{K_c}} = 0 \quad (27)$$

For a given p_1 , Eq (27) can be solved for P_c as a function of t and p_f , i.e.,

$$P_c = P_c(t, p_f) \quad (28)$$

If the temperature T were constant and the collar perfectly creep resistant, i.e., $A_c = 0$, then the long term solution of Eq. (27) is

$$P_c = p_1 - p_f \quad (29),$$

indicating that all the thermal and mechanically (hydraulic expansion) induced contact pressure would relax out leaving only that due to the fluid pressures. On the other hand, if the tube were perfectly creep resistant, i.e., $A_t = 0$, then although $P_c = -p_f$ is a solution of Eq. (27), it is not permissible because P_c cannot be negative. Thus, Eq. (27) is applicable until P_c is reduced to 0 beyond which the collar would lose contact with the tube and a gap would open up as the collar grows away from the tube.

Gap Opening after Loss of Contact

Following loss of contact between the tube and the collar, the contact pressure P_c is zero. The radial rate of separation (i.e., gap opening rate) between the tube and the collar is given by

$$\dot{\delta} = \dot{\delta}_c - \dot{\delta}_t \quad (30a)$$

where

$$\dot{\delta}_c = A_c \sigma_c^n r_c + B_c r_c \sigma_c^m \frac{1}{t_{0c}} \exp\left(-\frac{t}{t_{0c}}\right) + \alpha'_c \dot{T} r_{int} \quad (30b)$$

and

$$\dot{\delta}_t = A_t \sigma_t^n r_t + B_t r_t \sigma_t^m \frac{1}{t_{0t}} \exp\left(-\frac{t}{t_{0t}}\right) + \alpha'_t \dot{T} r_{int} \quad (30c)$$

Validation of One-Dimensional Model

Hold at constant temperature

Comparisons of the 1-D model-calculated and FEA-calculated variations of contact pressure in the tube-to-collar specimen with time for a constant temperature hold at 700°C with various pressures acting on the tube interior and leakage path side are shown in Fig. 8-1. The predictions by the 1D model are reasonably close to the FEA results. Note that significant relaxation of contact pressure occurs at 700°C even without any applied pressure (green lines in Fig. 8-1). If both sides of the tube are pressurized to 17.2 MPa (2.5 ksi) at 700°C, contact pressure is totally relaxed out by about 20 minutes (red lines).

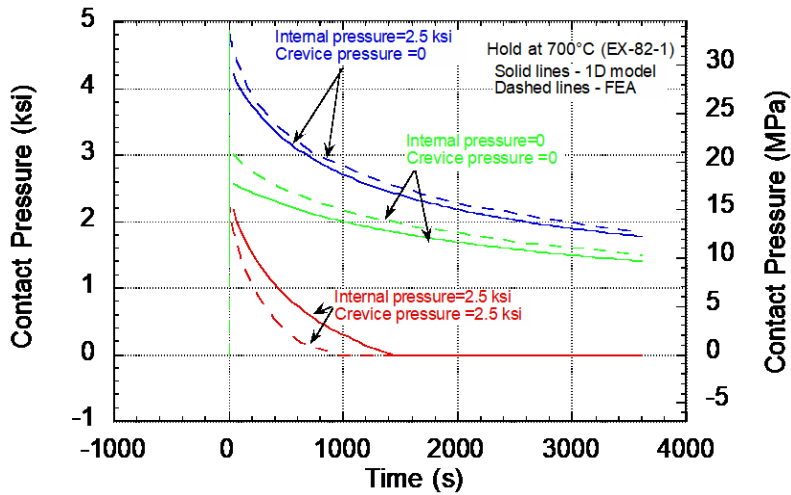


Figure 8-1 Variation of Contact Pressure with Time -1D Model vs. FEA

A comparison of the 1-D model-calculated and FEA-calculated variations of gap opening in the tube-to-collar specimen with time after contact pressures are relaxed out for a constant temperature hold at 700°C are shown in Fig. 8-2. The initiation time for contact opening are over predicted by the 1-D model, but the rate of gap opening is predicted reasonably well.

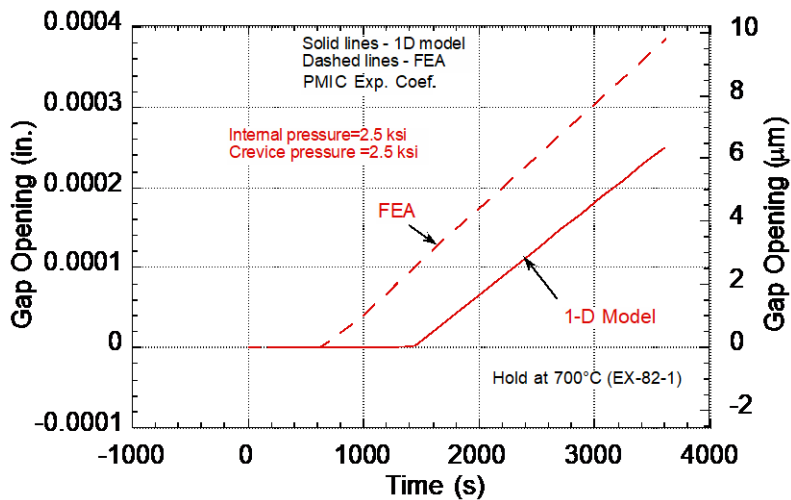


Figure 8-2 Variation of Gap Opening with Time -1D Model vs. FEA

Fixed temperature ramp rate

The test on the tube-to-collar specimen 05-7/8 was conducted on a 101 mm (4 in.) long specimen with 22 mm (0.875 in.) diameter (Heat EX-82-1) Alloy 600 tube. This specimen was heated to 500°C without any pressure. After thermal equilibration, it was pressurized on both the tube side and the leakage path side to 17.2 MPa (2.5 ksi) and then its temperature was

ramped at 50°C/h. The test showed that the specimen leakage was essentially zero up until the temperature reached 676°C beyond which it increased rapidly. The variations of contact pressure and gap opening with temperature calculated by FEA and the 1-D model are plotted in Fig. 8-3. The temperatures at which complete loss of contact pressure is predicted are 680°C (by FEA) and 695°C (by 1-D model). The predicted variation of contact pressure with temperature by the 1-D model is reasonably close to that predicted by FEA.

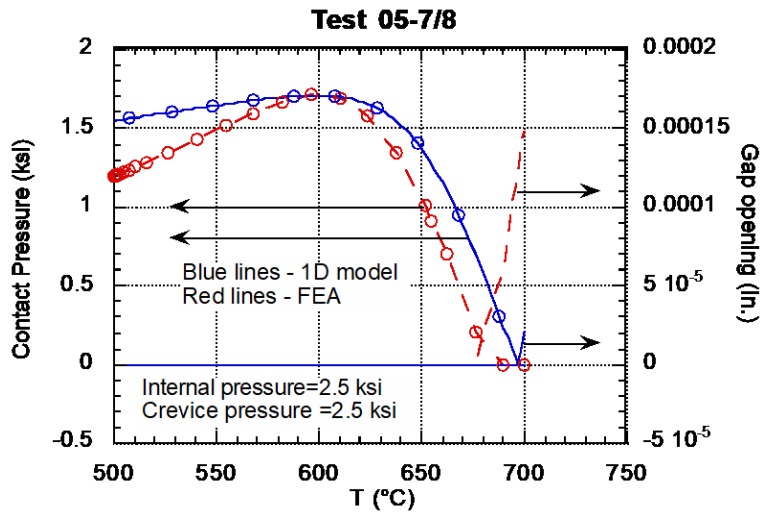


Figure 8-3 Variations of Contact Pressure and Gap Opening with Temperature for Test 05-7/8

8.1.2 Transition from Closed to Open Contact

There is a divergence with using the correlation for the effective gap (Eq. (15)), when the contact can open for part of the time. This is because as the contact pressure approaches zero, the effective gap width approaches infinity (Fig. 8-4, thin blue line). To maintain continuity between when the gap is closed to when the gap is open, ANL set the effective gap width to the constant Gaussian width value of 2. Note that when the gap calculated with FEA (red line) is less than the Gaussian width, the effective gap width is assumed to be equal to the Gaussian width. The predicted leak rates using this assumption are reasonably close to the observed leak rates.

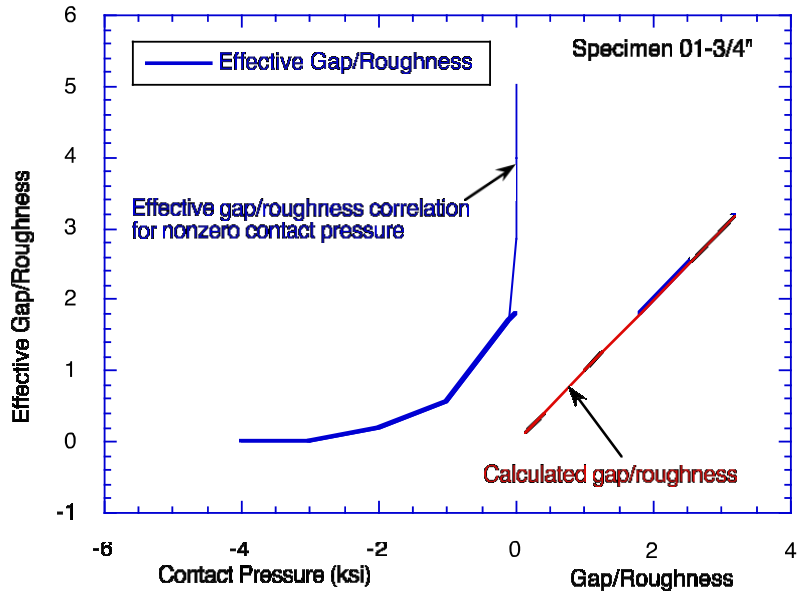


Figure 8-4 Effective Gap Width Used When the Contact Changes between Closed and Open

8.2 Leakage Analysis of Tests

A rigorous calculation of the leak rate through the annulus between the tube and collar requires a coupled thermal hydraulic and structural analysis of the specimen, because the leak rate depends on the contact pressure as well as gas pressure variation along the annulus which are interdependent. For most calculations, an approximate "ring assembly" model was used to compute the changes in contact pressure and flow resistance with fluid pressure. This model is shown in Fig. 8-5 and discussed more fully in the next section. p_c denotes the contact pressure and p_f the fluid pressure. The gaps between the tube and the collar are shown greatly enlarged for clarity. In rough surface contact, asperities on the collar and tube are in contact. In annular flow, there is an actual gap between the collar and tube.

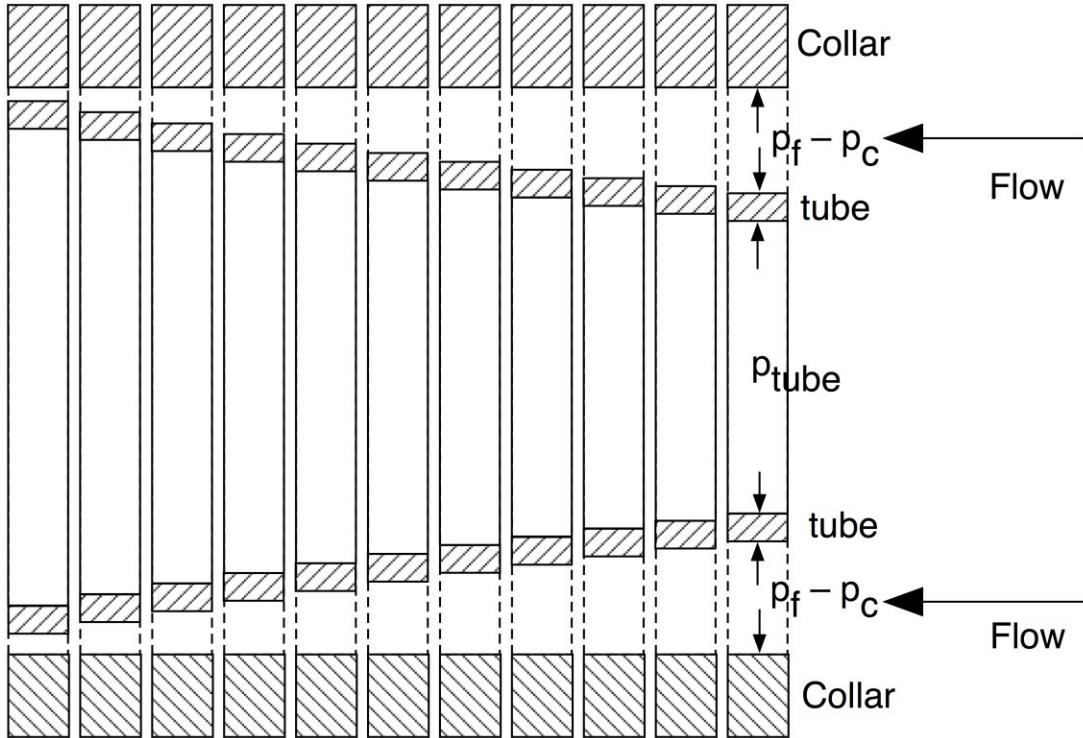


Figure 8-5 Specimen Divided into a Number of Composite Rings

8.2.1 Ring Assembly Model

ANL divided the specimen axially into a number of independent rings of length dz as shown in Fig. 8-5 and made the following assumptions

- (1) Each ring behaves structurally independent of the other rings,
- (2) For situations in which creep is occurring, at any time t , the steady state leak rate is achieved on a time scale in which additional creep deformations are negligible (i.e., the time scale for leak rate equilibration is small compared to the time scale for creep),
- (3) The z -variation of the loss coefficient K (i.e., contact pressure) is entirely due to the z -variation of the gas pressure, i.e., the contact pressure does not depend explicitly on z (e.g., due to tubesheet bowing),
- (4) After the passage of a minimum (expected to be short) time, the pressure distribution along the length reaches a steady state profile (i.e., p_f is not a function of time), and
- (5) The inlet and outlet gauge pressures are for all time equal to p_1 and 0 , respectively.

If the above assumptions are made, then the time-dependent leak rate $q(t)$ is given by Eq. (11), which is

$$q \int_0^L dz = -\frac{\rho_1}{\mu} \int_{p_1}^{p_2} \left(\frac{\rho(p_f)}{K\rho(p_1)} \right) dp_f = \frac{-1}{v_1} \int_{p_1}^{p_2} \left(\frac{p_f}{Kp_1} \right) dp_f \quad (31)$$

where q = mass flow rate, ν_1 =kinematic viscosity of the gas inside the tube at pressure p_1 , L is the leakage path length and K is the flow resistance.

The axial distribution of fluid pressure (the "steady state profile") at any time t can be obtained by computing z for a given $p_f = p$ from the following equation

$$z = -\frac{1}{\nu_1 q} \int_{p_1}^p \frac{\left(\frac{p_f}{p_1}\right)}{K} dp_f \quad (32)$$

If the profile changes significantly with time, then this approach will fail. The reasonable correlation of the test results with this approach suggests that the profile does not change significantly.

8.2.2 Initial Room Temperature Tests

The initial screening test measurements of leak rate of the B&W specimens were used to get initial estimates of the fitting parameters in the leak rate model. In the leak rate model, the leak rates depend on the surface roughness, the contact pressure, the fluid driving pressure, and the fluid physical properties. The contact pressure depends on the initial contact pressure from expansion, the internal pressure in the tube, and the temperature. The fluid properties are also temperature dependent. The model also contains two fitting parameters. In analyzing the experimental data on leak rates, it is assumed that the contact pressure, roughness, fluid driving pressure, and temperature are known or can be estimated for each test. The two fitting parameters are assumed to be global variables; if the model is successful, one set of values of these parameters should be able to describe the results of the entire set of leak tests.

In practice, neither the contact pressure nor the roughness are known very well for each specimen. The fabrication conditions are used to determine the initial contact pressures through finite element analysis. However, as exemplified by specimen 01-7/8, the control of the fabrication conditions may not be good enough to ensure that consistent values of the contact pressure are achieved.

The experimental results for leak rates from the screening tests were summarized in Table 8-1. The initial contact pressures are finite element estimates based on the tube mechanical properties and the fabrication process followed by B&W. For two of the specimens, in addition to the data for 3.45 and 6.89 MPa (500 and 1000 psig), leak rates were also measured at pressures intermediate to those values. The experimental data for these tests are shown in Fig. 8-6. The predicted values have been scaled to match the observed flow rate at one value of the driving pressure and the value of one of the fitting parameters, the cutoff value for the Gaussian distribution of the roughness, has been chosen to be 5.0 to get reasonably close dependence on the driving pressure.

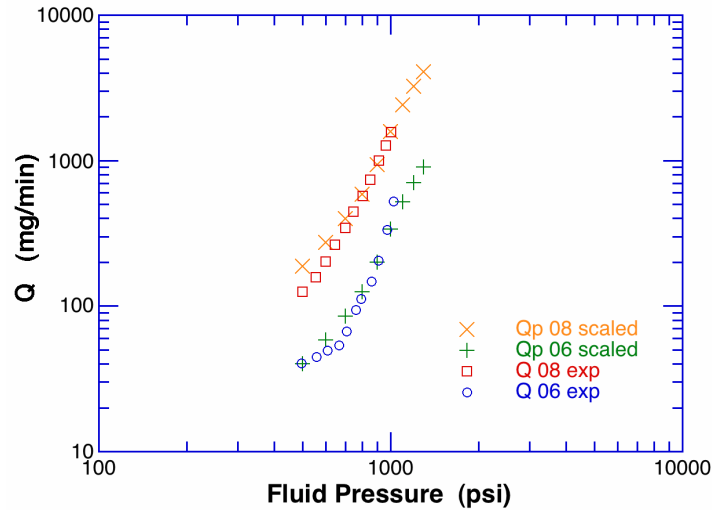


Figure 8-6 Flow Rates as a Function of Fluid Driving Pressure for Specimens 06-7/8 and 08-7/8

The dependence of the flow on the fluid driving pressure follows a power law reasonably well (straight lines on a log-log plot such as Fig. 8-6). The predicted values, shown as X and +, have been scaled to match the observed flow rate at one value of the driving pressure. The slopes are 3.5 and 3.7 for Specimens 06-7/8 and 08-7/8, respectively. Power law slopes can be computed for the other specimens, but with only two data points, the slopes are highly uncertain and vary from 2.2 to 6.1. However, the average value is 3.9, reasonably close to that for the two specimens for which enough data are available to compute more reliable values.

To estimate the second fitting parameter α of Eq. (15), values of the parameter were chosen, and then a value of the roughness was selected to match the observed flow rate at 6.89 Mpa (1000 psig). These roughness values are shown for two values of the fitting parameter are shown in the last two columns of Table 8-1. The average values of the fitted roughness are 2.1 ± 0.6 and 2.2 ± 0.7 μm . The average value of the measured roughness is 2.2 ± 0.7 . Thus, both values of the fitting parameter give average values of the roughness consistent with the measured value. The fitting parameter values were refined after more tests were completed.

The leak rates and computed roughness for Specimens 03-3/4 and 03-7/8 are large compared to other specimens and the measured roughness. It is suspected that the initial contact pressure for these two specimens is less than the 20.6 MPa (3000 psi) predicted by the analysis and the roughness values for these two specimens were not included in the averages. However, inclusion of the values (which are roughly 95th and 99th percentile values) still gives average values within the uncertainty of measured value.

8.2.3 Leakage Analysis of Tests with Creep

FEA can be used to analyze each ring. Alternatively, a spreadsheet was written which uses the 1-D model to calculate the contact pressure (and gap opening, if any) as a function of time, temperature, tube pressure and crevice pressure loading for any of the rings depicted above,

$$P_c = P_c(t, p_1, p_f, T) \quad (33)$$

Table 8-1 Initial Estimates of Roughness for B&W Specimens

#01-3/4 (NX8524)	2.2	
#02-3/4 (NX8524)	3.4	
#03-3/4 (NX8524)	5.5?	
#01-7/8 (NX8520 LT)		
#02-7/8 (EX-82-1)		2.1
#03-7/8 (NX8520 LT)		4.9?
#04-7/8 (NX8520 LT)		
#05-7/8 (EX-82-1)		1.0
#06-7/8 (EX-82-1)		2.3
#07-7/8 (NX8520 LT)		
#08-7/8 (EX-82-1)		4.0
#09-7/8 (NX8520 LT)		
#10-7/8 (EX-82-1)		1.5
#11-7/8 (NX8520 LT)		

^aComputed with $\log_{10} \alpha = 2.40$

^bComputed with $\log_{10} \alpha = 2.45$

As an example, consider a tube with an internal pressure of 17.2 MPa (2.5 ksi) that is subjected to the temperature ramp shown in Fig. 8-7. The spreadsheet uses the 1-D model to calculate variations of contact pressure with time as functions of the crevice pressure, as shown in Fig. 8-8a. The spreadsheet then replots the data in Fig 8-8a as variation of contact pressure with crevice pressure at various times (Fig. 8-8b). A similar plot for gap opening can also be generated (Fig. 8-9). The integral in Eqs. 31-32 can then be carried out if K is known as a function of p_f at each of the times shown in Fig. 8-8b.

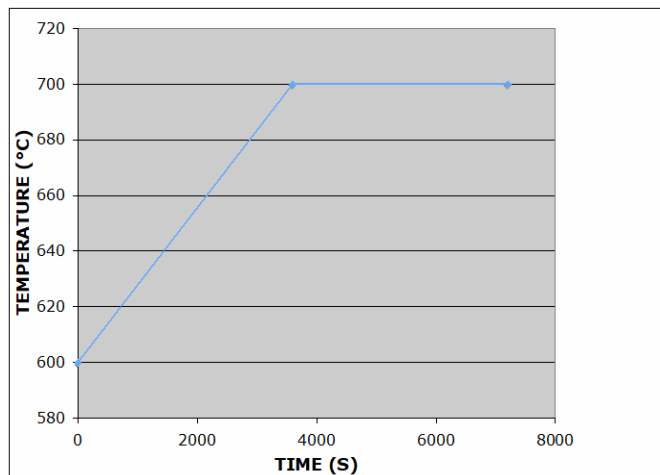


Figure 8-7 Time vs. Temperature Plot for a Tube with an Internal Pressure of 17.2 MPa (2.5 ksi)

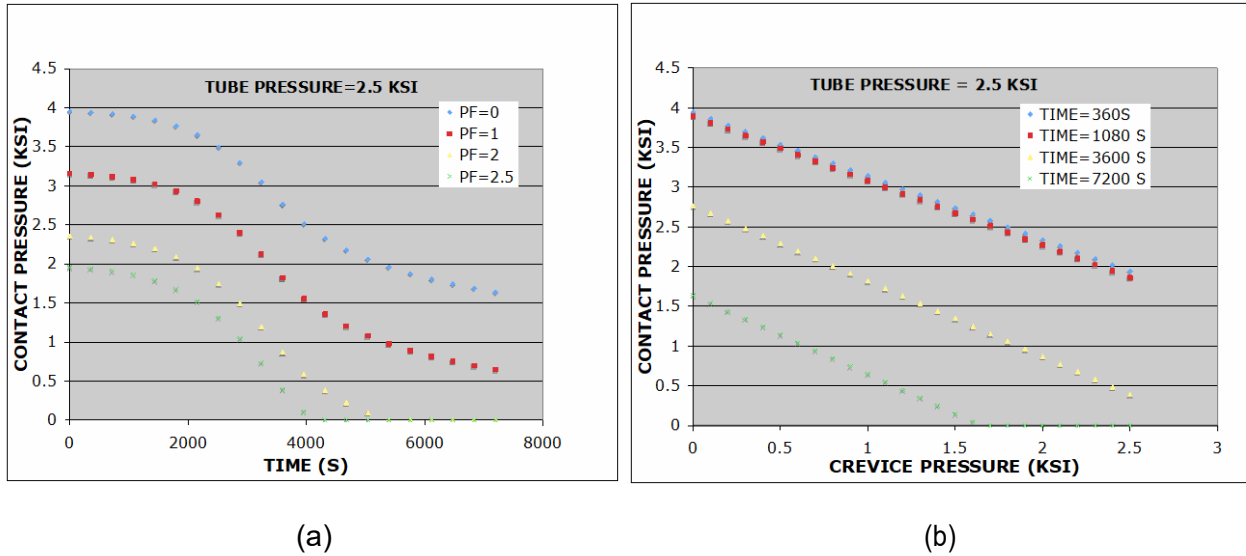


Figure 8-8 (a) Calculated Variation of Contact Pressure with Time for Various Values of Crevice Pressure and (b) the Data Replotted as Variation of Contact Pressure with Crevice Pressure at Various Times

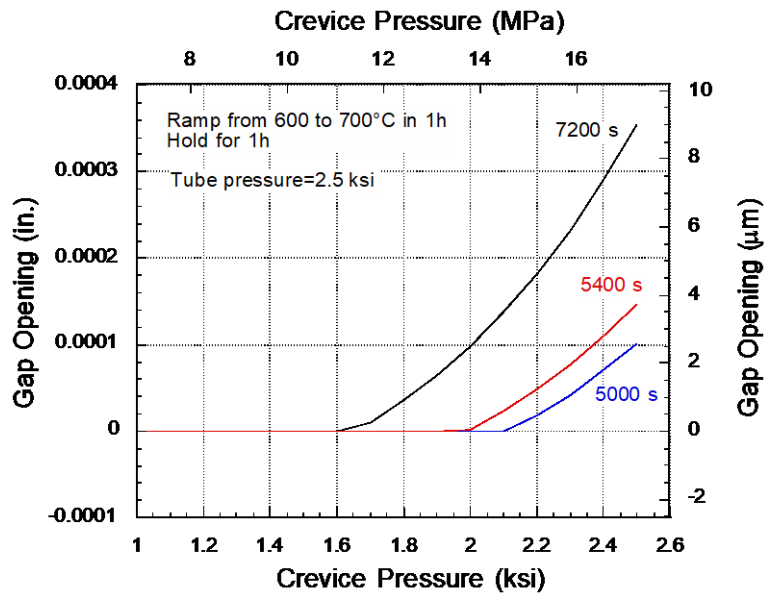


Figure 8-9 Variation of Gap Opening with Crevice Pressure at Various Times

8.2.4 Crevice Gas Pressure Distribution

Test 11-7/8 (Section 7.5.1) was analyzed using the ring assemblage model (with FEA) to calculate the gas pressure variations in the crevice at room temperature before (stage 1) and after (stage 5) the specimen was exposed to high temperature. The results are shown in Fig. 8-10. During stage 1 of the test, the tube and the collar were in positive contact with high contact pressure while in stage 5 a physical gap was created by the creep deformation during prior high

temperature excursion. The gas pressure profile in stage 1 (low leak rates) is almost constant through the entire length, irrespective of the tube and crevice pressures. Most of the flow path resistance (pressure drop) occurs at the exit end. The gas pressure profiles during stage 5 (high leak rates) are close to the parabolic profile (Eq. (14)) derived in section 5.2.1.2 for a uniformly wide rigid gap.

Therefore, for the FEA of the full specimen, it was assumed that the crevice pressure distribution is uniform as long as the contact is closed with positive contact pressure. At the other extreme, when the gap is physically open with zero contact pressure, it was assumed that the crevice pressure distribution is parabolic. This assumption was also used for FEA of the Model 51 tube-to-tubesheet junction during severe accidents.

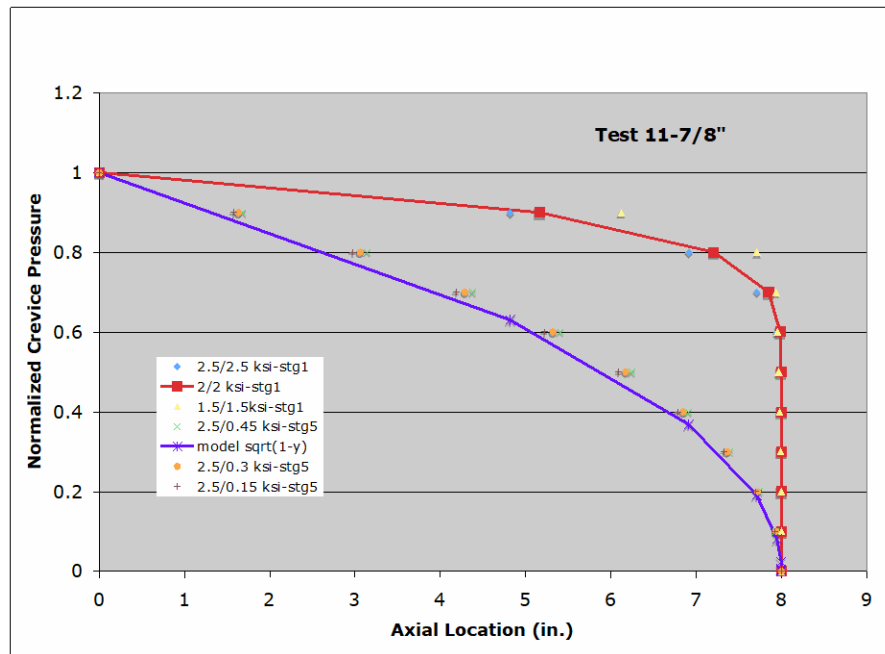
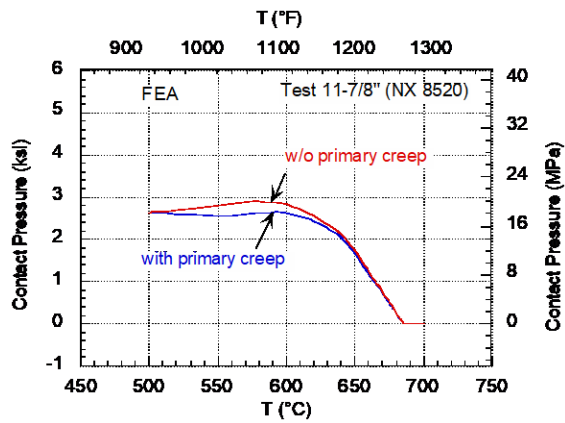


Figure 8-10 Axial Variation of Normalized Crevice Gas Pressure in Specimen 11-7/8 During Stage 1 and Stage 5 Testing

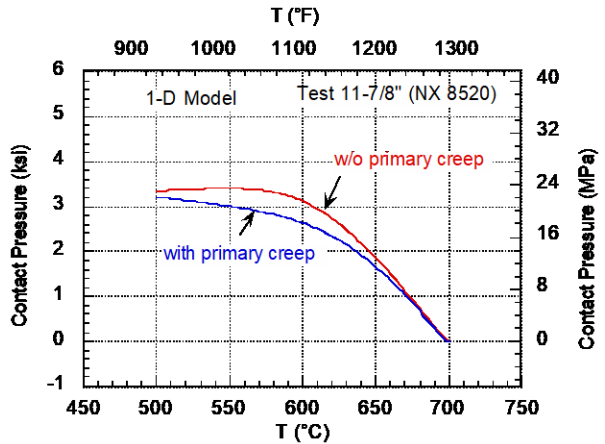
8.2.5 Detailed Analysis Results of a Representative Sample of Tests

Test 11-7/8 (NX 8520)

This specimen (203 mm [8 in.] long) was heated to 500°C without any pressure at a rate 150°C/hr, following which both the tube and the crevice were pressurized to 2500 psi; then the specimen was heated to 700°C at 50°C/hr. Comparisons of the FEA-calculated and 1-D model-calculated variations of contact pressure with time are shown in Figs. 8-11a-b, respectively. The predictions by the 1D model are reasonably close to the FEA results. Note that inclusion of primary creep does not affect the final temperature by either the FEA or the model. The test indicated a rapid increase of leakage at 710°C.



(a)



(b)

Figure 8-11 Variation of Contact Pressure with Temperature for Test 11-7/8 Calculated by (a) FEA and (b) 1-D Model

The room temperature stage 1 leak rate tests were fitted with the leak rate parameters shown in Table 8-2. The same parameter α and a surface roughness value of $5 \mu\text{m}$ was used for predicting the leak rates of the rest of the tests.

Table 8-2 Leak Rate Parameters Determined from Room Temperature Stage 1 Tests on Specimen 11-7/8

Tube Pressure (ksi)	Crevice Pressure (ksi)	Test Leak Rate (mg/min)	Parameter α (Eq. (15))	Roughness (μm)
2.5	2.5	2.5	5136	1.05
2.0	2.0	2.3	5136	1.15
1.5	1.5	1.2	5136	1.12

Figure 8-12 shows a comparison between the test leak rates during stages 4 and 5 testing with a tube internal pressure of 17.2 MPa (2.5 ksi) and the leak rates predicted by FEA and the 1-D model, both using the ring assembly approximation for the specimen. The FEA analysis (ignoring primary creep) prediction for the high temperature test was significantly over that measured. The 1-D model (including primary creep) predicts all the leak rates quite accurately when the tube pressure is 17.2 MPa (2.5 ksi), including the leak rate at high temperature. However, although the 1-D model predicts the leak rates for the stage 5 tests with lower tube pressures reasonably well, it tends to over predict the leak rates at the highest crevice pressures (Figs 8-13a-b).

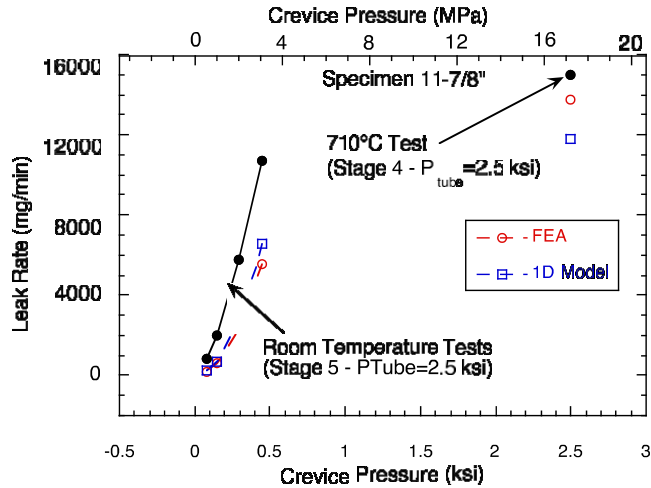


Figure 8-12 Comparison of Test Leak Rates at Room Temperature and 710°C with Those Predicted by FEA and the 1-D Model for Specimen 11-7/8

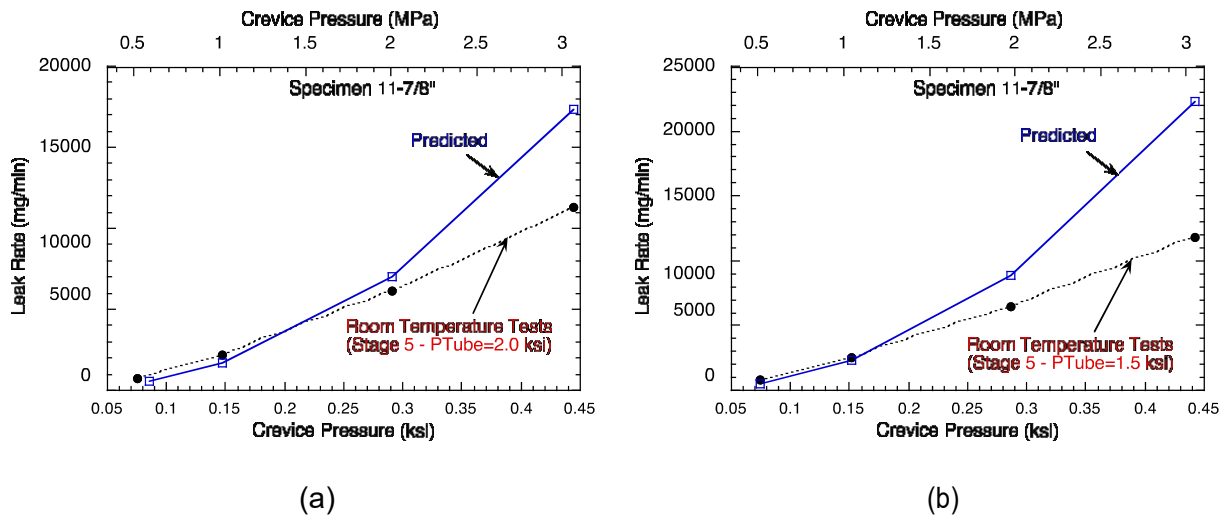


Figure 8-13 Comparison of Test Leak Rates (Specimen 11-7/8, Stage 5) at Room Temperature with those Predicted by the 1-D Model at Tube Pressures of (a) 14 MPa (2 ksi) and (b) 10.3 MPa (1.5 ksi)

Test 01-3/4 (NX 8524)

This 102 mm (4 in.) long specimen (unpressurized) was heated to 670°C, following which the tube was pressurized to 2500 psi and the leakage path was left unpressurized and the specimen was held at constant conditions for 4 hours without any measurable leakage. It was then cooled down and leak tested at room temperature (Stage 3). Later, it (unpressurized) was heated to 670°C, and the tube was pressurized to 2500 psi and the leakage path was pressurized to 2000 psi and the specimen was held at constant conditions (Stage 4) for another 4 hours during which the leak rate was measured. It was then cooled down and leak tested at room temperature (stage 5).

The room temperature stage 1 leak rates were fitted with the ring assembly FEA model using leak rate parameters shown in Table 8-3. The same parameter α and a surface roughness value of 2 μm was used for predicting the leak rates of the rest of the tests.

Table 8-3 Leak Rate Parameters Determined from Room Temperature Stage 1 Tests of Specimen 01-3/4

Tube Pressure (ksi)	Crevice Pressure (ksi)	Test Leak Rate (mg/min)	Parameter α (Eq. (15))	Roughness (μm)
2.5	2.5	13.9	2560	2.0
2.0	2.0	10.5	2560	1.5
1.5	1.5	9.1	2560	1.2

During the first 4h hold at 670°C, the computed contact pressure relaxes as shown in Fig 8-14. The relatively high contact pressure at the end of the hold time is consistent with the lack of large leakage. A comparison of the experimentally measured leak rates for stage 3 of specimen 01-3/4 with the leak rates predicted by FEA and the 1-D model is shown in Figs. 8-15a-b, respectively. Similar comparisons between test and predicted leak rates for stage 5 tests are shown in Figs. 8-16a-b, respectively. In both cases, the predicted leak rates by FEA and the 1-D model are slightly different but are within a factor of 2 of the observed leak rates.

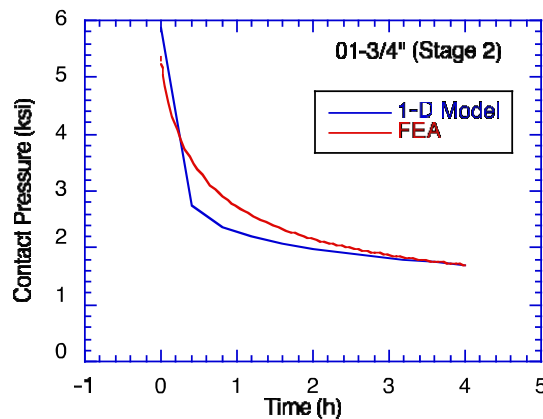
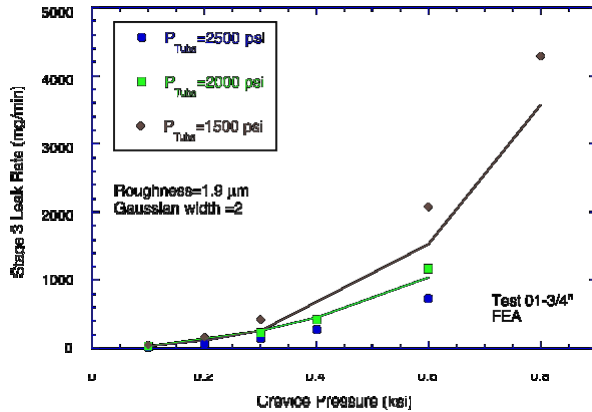
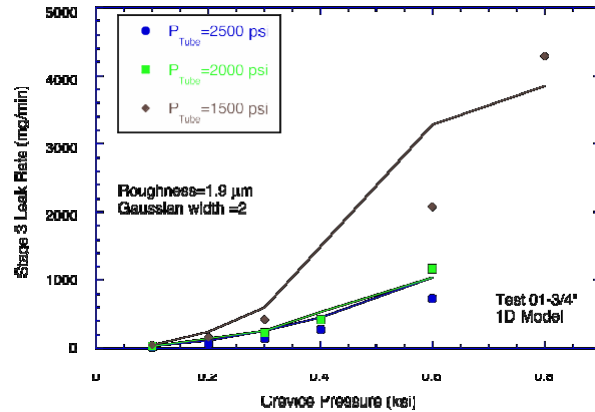


Figure 8-14 Computed Relaxation of Contact Pressure of Specimen 01-3/4 During the First 4 hour Hold at 670°C

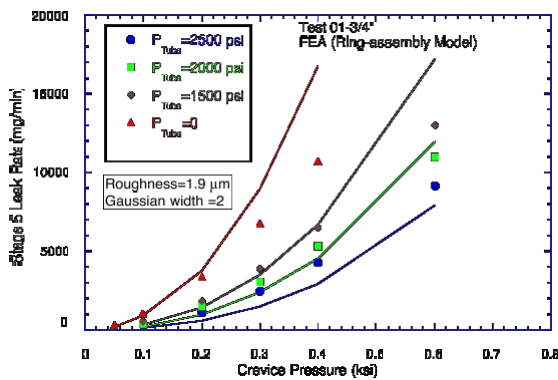


(a)

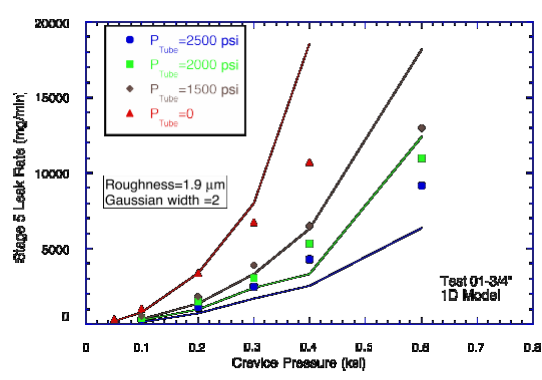


(b)

Figure 8-15 Comparison of Test Leak Rates (symbols) at Room Temperature during Stage 3 Testing of 01-3/4 vs. Crevice Pressure with those Predicted by (a) FEA and (b) 1D Model



(a)



(b)

Figure 8-16 Comparison of Test Leak Rates (symbols) at Room Temperature during Stage 5 Testing of 01-3/4 vs. Crevice Pressure with those Predicted by (a) FEA and (b) 1D Model

Comparison of test leak rates ($P_{\text{tube}}=17.2 \text{ MPa}$ (2.5 ksi)) and predicted leak rates using 1-D model and FEA (both using ring assembly model) vs. crevice pressure for the tests at room temperature and 670°C are shown in Fig. 8-17. The leak rates predicted by FEA (ring assembly model) are within a factor of 2 of the test leak rates at both temperatures. However, the test leak rate at 670°C is significantly under-predicted by the 1-D model.

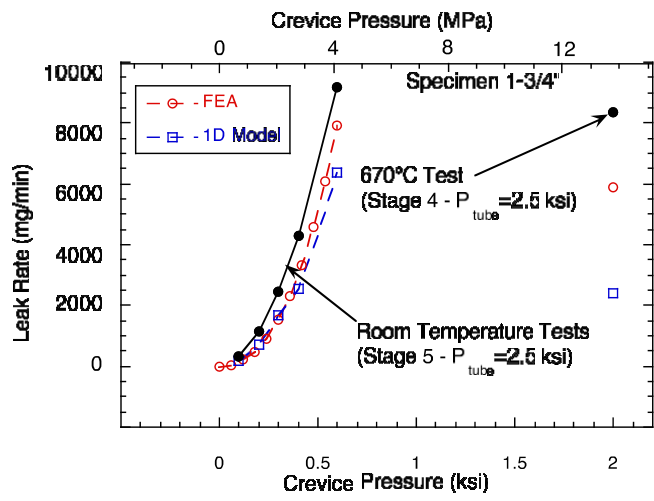


Figure 8-17 Comparison of Test Leak Rates at Room Temperature and 670°C vs. Crevice Pressure with those Predicted by FEA and the 1-D Model for Specimen 01-3/4

Test 02-7/8 (EX-82-1)

The room temperature stage 1 leak rates on this 51 mm (2 in.) long specimen were fitted with the 1-D model to determine the leak rate parameters shown in Table 8-4. The same parameter α and a surface roughness value of 2.7 μm was used for predicting the leak rates of the rest of the tests.

Table 8-4 Leak Rate Parameters Determined from Room Temperature Stage 1 Tests of Specimen 02-7/8

Tube Pressure (ksi)	Crevice Pressure (ksi)	Test Leak Rate (mg/min)	Parameter α (Eq. (15))	Roughness (μm)
2.5	2.5	1800	4517	2.7
2.0	2.0	350	4517	1.8
1.5	1.5	64	4517	1.2

Thermal Ramp to 300°C

Before subjecting the specimen to the high temperature ramp, specimen 02-7/8 was slowly heated to 300°C with both the tube and the crevice pressures held constant at 17.2 MPa (2.5 ksi) and the leak rate was monitored continuously. This test provided an opportunity to test the adequacy of the thermal expansion coefficients and the leak rate model at the temperatures of interest to MSLB conditions. Recently, P. King of B&W, Canada reanalyzed ANL's thermal expansion coefficient data for A508 steel measured by PMIC in the temperature range of room

temperature to 400°C, using a piecewise polynomial fit that would presumably represent the data better than the 4th order polynomial fit over the entire temperature range (room temperature to 700°C) that PMIC used. The original data on A508 between room temperature and 800°F reported by PMIC, together with the fits proposed by B&W and ANL are presented in Fig. 8-18. Note that the B&W fit to the A508 data at around 400°F has an upward jog in the curve that is missing in the ANL fit. Also included in Fig 8-18 are the data measured by PMIC for Alloy 600. The variations of contact pressure and leak rate with temperature were calculated with the 1-D model using the B&W fit as well as the ANL fit shown in Fig. 8-18. Variation of the calculated contact pressures with temperature are plotted in Fig. 8-19, which shows that the two curves are coincident from room temperature to 400°F, but the contact pressures calculated with the B&W fit has a peak at 400°F (corresponding to the upward jog in Fig. 8-18) while the ANL-predicted contact pressure increases monotonically with temperature. This difference in the calculated contact pressures leads to the predicted leak rates shown in Fig. 8-20, which also includes the test data. It is clear that the test data are in agreement with the predictions based on the ANL fit to the expansion data but deviate from those based on the B&W fit at $\geq 450^\circ\text{F}$. In all leakage calculations for the in-house tests, the ANL fit to the PMIC thermal expansion coefficient data for A 508 and the PMIC thermal expansion coefficient data for Alloy 600 was used.

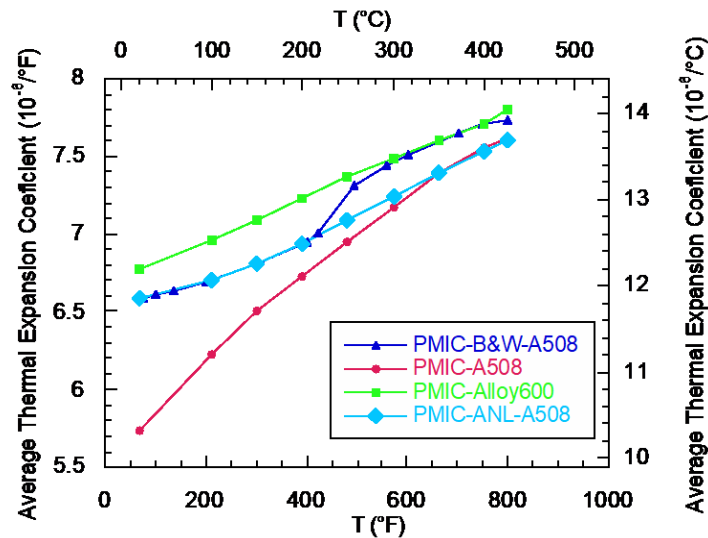


Figure 8-18 Original PMIC Data for Thermal Expansion Coefficient of A508 (red filled circles), B&W Fit to the Data (deep blue filled triangle), ANL Fit to the Data (light blue filled diamond), and PMIC Data for Alloy 600 (green filled squares)

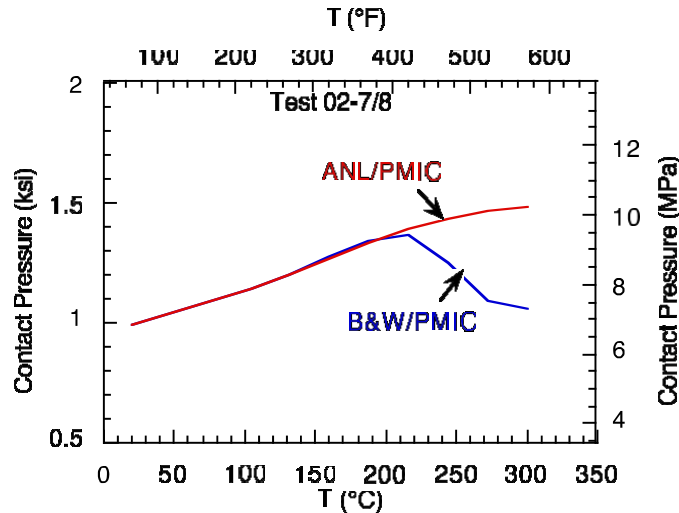


Figure 8-19 Calculated Contact Pressures using B&W and ANL Fits to the PMIC Expansion Coefficient Data for A508

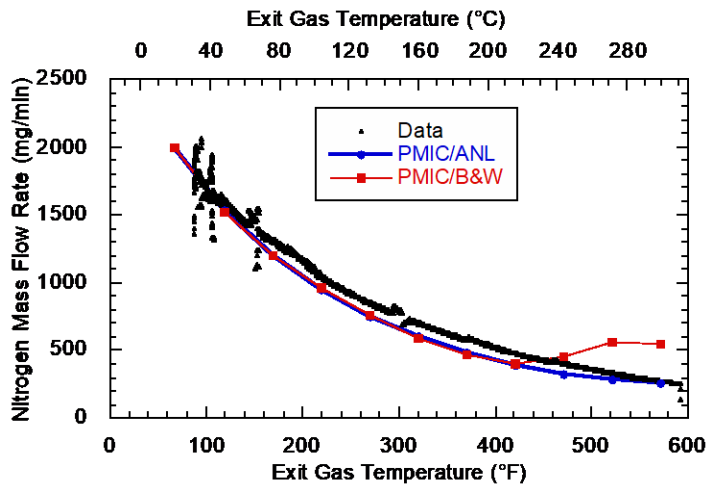


Figure 8-20 Comparison of the Measured Leak Rates with Those Predicted by the 1-D Model using the B&W and ANL Fits to the PMIC Thermal Expansion Coefficient Data for A508

Thermal Ramp to 700°C (Stage 3)

Specimen 02-7/8 was next heated to 500°C with zero pressure, tube was then pressurized to 2500 psi and the temperature ramp continued at 50°C/hr to 700°C. Because of the drilled hole in the tube wall, it was assumed that the crevice pressure was equal to the tube pressure. The predicted leak rate with time is compared with the test results in Fig.8-21. Except for the leak rate oscillations, the general trend of the leak rate is predicted reasonably well.

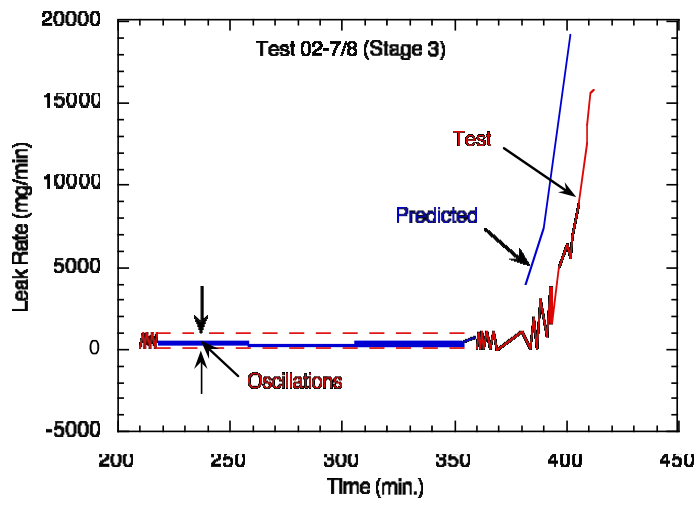


Figure 8-21 Predicted vs. Observed Leak Rate for Test 02-7/8

9 LEAKAGE PREDICTIONS FOR TUBE-TO-TUBESHEET JUNCTIONS DURING DESIGN BASIS ACCIDENTS

9.1 Assessment of Leak Model for Design Basis Accidents

A model for leakage between rough surfaces under pressure with two phase flow conditions was described in Section 5.2. No experiments with liquids or two phase flows were performed as part of this program, but industry data were presented in a public meeting at Waltz Mill, PA on November 19, 2008 [10]. The empirical “universal constants” in the model were taken to be the same as determined in the tests with nitrogen gas described in Section 7.

The experimental samples were intended to have relatively low contact pressures. The hydraulic expansion pressures used are known. The actual yield stresses of the tubes used for the tests are unknown, but it is assumed that they are typical of Westinghouse SG tube materials. This suggests that the initial contact pressures in the specimens are low and for comparison with the experiments they were assumed to be zero. Parametric calculations were performed to assess the effect of higher initial stresses. The surface roughness of the tubes and collars are also unknown. In the calculations, the roughness was assumed to be dominated by the machining roughness of the collar and was taken to be typically 3–6 μm. Thus, variations in surface roughness could be expected to lead to variations in leak rate between specimens on the order of a factor of 10–20.

9.1.1 Comparison to Room Temperature Tests with Water

Westinghouse performed leak rate experiments on tube–collar specimens at room temperature with internal pressures of []^{a,c,e}. [10] The design of the specimen assured that the fluid driving pressure was the same as the internal pressure. For comparison between the model and the Westinghouse predictions, the surface roughness of each specimen was varied to obtain the best agreement with the experiments. The values obtained in this manner ranged from 2.9-6.4 μm, consistent with values that might be expected. Figure 9-1 shows a comparison of the predicted and observed leak rates for the room temperature tests.

In an actual application, the actual leak rates under normal operating conditions can be measured. Of interest is the change in leak rate as conditions are changed. In the room temperature tests, the predicted and observed leak rates can be normalized in terms of the leak rate at 6.9 MPa (1000 psi), and the relative changes in the predicted and observed leak rates compared. An error factor is defined as

$$\text{error factor} = \frac{\text{observed change in leak rate}}{\text{predicted change in leak rate}} \quad (34)$$

The error factors for the room temperature tests are shown in Fig. 9-2. The error factor compares the observed increase in leak rate as the pressure is increased to the predicted increase in leak rate. In addition to the error factors determined for each test, the estimated 95th percentile value of the error factor is shown. The solid line in the figure is an estimated bound fitted between the value of 1 and the estimate 95th percentile values at the pressure ratios of 1.91, 2.65, and 3.11. The error factor is somewhat greater than 1, i.e., the model is underpredicting the changes in leak rate as the pressure is increased. The results show the model predictions are slightly non-conservative.

[

]a,b,c

Figure 9-1 Comparison of Observed and Predicted Leak Rates for Tests with Water at Room Temperature (The dashed lines indicate a factor of 1.5)

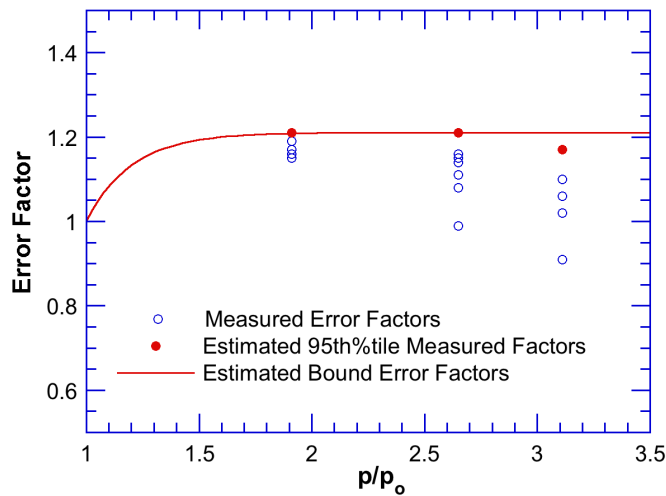


Figure 9-2 Leak Rate Error Factors for Tests with Water at Room Temperature

The actual leak rate from a tube–collar specimen is strongly dependent on initial contact pressure and the roughness h . It scales with roughness as h^3 . The predicted dependence on initial contact pressure is shown in Fig.9-3.

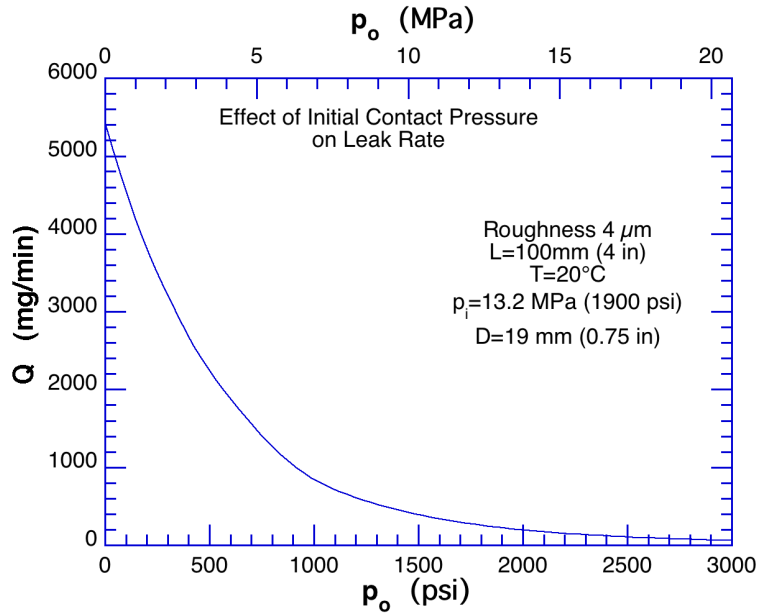


Figure 9-3 Dependence of Leak Rate of Water at Room Temperature and an Internal Pressure $p_i = 13.2 \text{ MPa}$ with Initial Contact Pressure

As the temperature is increased, the leak rate from a tube–collar is expected to increase as the viscosity of water decreases with increasing temperature. At higher temperatures the flow in the crevice between the tube and the collar may become two phase. The predicted behavior of the flow with increasing temperature is shown in Fig. 9-4 for flow in tube–collar specimen with an internal pressure of 13.2 MPa (1900 psi) and exiting to the atmosphere. The leak rate is normalized to the leak rate at room temperature. As the temperature increases, the leak rate at first increases. At higher temperatures, the water flashes before the exit, and the higher the temperature, the farther down the crevice, flashing occurs. The predicted leak rate in this region decreases with increasing temperature. The missing segments are not calculated because the thermodynamic data for this range is not included in the spreadsheets used for the calculation.

The initial contact pressure has little effect at lower temperatures but becomes more significant at higher temperatures. It should be noted that Fig. 9-4 indicates relative flow rates. The absolute flow rate at the higher contact pressure will be much lower as suggested by the results shown in Fig. 9-3.

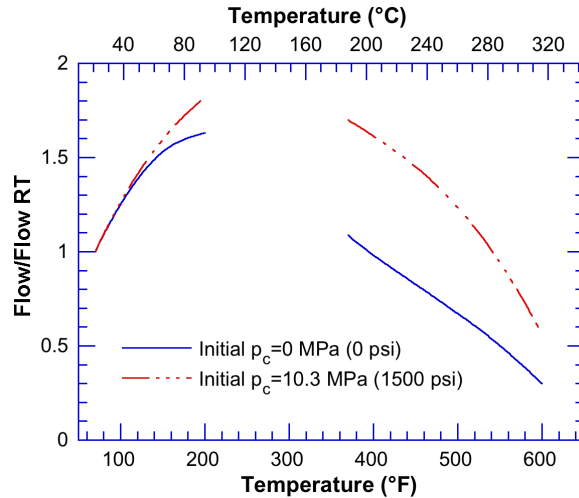


Figure 9-4 Dependence of Normalized Flow Rate on Temperature for Two Initial Contact Pressures

In some of the Westinghouse tests used the same specimens were tested at 70°F (21.1°C) and 600°F (315.6°C). Figure 9-5 shows a comparison of the relative leak rates at the two temperatures with the predicted values. In one set of tests at higher temperature performed by Westinghouse, crevice pressures were measured. The tests were performed on 2 different specimens with different internal pressure, exit pressure, and temperature conditions representing normal operating conditions (NOP) and main steam line break conditions (SLB). The test conditions are summarized in Table 9-1.

[

]a,b,c

Figure 9-5 Comparison of Measured Leak Rates at 70°F (21.1°C) and 600°F (315.6°C) at Different Internal Pressures with the Corresponding Predicted Values

Table 9-1 Conditions for Tube–Collar Crevice Pressure Profile Tests

Test Type, No.	Temperature, °C (°F)	Internal Pressure, MPa (psi)	Exit Pressure, MPa (psi)
NOP 1	317.8 (604)	15.7 (2279)	5.5 (799)
2	318.3 (605)	15.5 (2254)	5.5 (792)
3	310 (590)	20 (2899)	10 (1453)
SLB 1	241.7 (467)	19.4 (2810)	0.2 (23)
2	216.1 (421)	19.6 (2846)	0.2 (23)
3	203.9 (399)	17.8 (2582)	0.1 (21)
4	247.8 (478)	19.7 (2857)	0.2 (31)
5	194.4 (382)	19.5 (2827)	0.2 (26)
[

The measured crevice profiles in these tests are compared with those predicted by the model in Figs. 9-6–9-14. The linear chain dotted profiles show linear pressure drops based on $p-p_{\text{exit}}$ and $p-p_{\text{sat}}$. [

[

Figure 9-6 Comparison of the Predicted Measured Pressure Distributions for Test NOP 1

[

Figure 9-7 Comparison of the Predicted Measured Pressure Distributions for Test NOP 2

[

Figure 9-8 Comparison of the Predicted Measured Pressure Distributions for Test NOP 3

[

Figure 9-9 Comparison of the Predicted Measured Pressure Distributions for Test SLB 1

[

Figure 9-10 Comparison of the Predicted Measured Pressure Distributions for Test SLB 2

[

Figure 9-11 Comparison of the Predicted Measured Pressure Distributions for Test SLB 3

[

Figure 9-12 Comparison of the Predicted Measured Pressure Distributions for Test SLB 4

[

Figure 9-13 Comparison of the Predicted Measured Pressure Distributions for Test SLB 5

.

[

Figure 9-14 Comparison of the Predicted Measured Pressure Distributions for Test SLB 6

The error factors for predicted changes in leak rate as the fluid pressure is changed for the tests at 600°F are shown in Fig. 9-15. The error factor compares the observed increase in leak rate as the pressure is increased to the predicted increase in leak rate. There is considerable more scatter in data at 600°F than in the corresponding room temperature data shown in Fig. 9-16. The model in some cases overpredicts the change in leak rate by an order of magnitude, although the estimated 95/95 confidence limits are greater than 1, i.e., the predicted result could sometimes be nonconservative and underpredict the increase in leak rate. The calculations were performed for zero initial contact stress due to expansion and for nominal values of the thermal stress. Varying the initial stress and the thermal stress values does not change the relative values significantly.

Also shown in Fig. 9-15 are the statistical 95/95 upper confidence bounds on the error factor and an estimated bound on the error factor as a function of pressure increase. The solid curve in the figure is a simple linear fit chosen to bound the 95/95 values of the error factor. Although it may appear somewhat conservative relative to the data, because the available tests involve only changes in pressure while potential applications could involve changes in both temperature and pressure, some conservatism may be warranted to address uncertainty not represented in the available data.

Although the model is predicting the pressure profiles reasonably well, the leak rate predictions are less satisfactory. It is not surprising that the actual flow rates are overpredicted, since the flow area could be reduced by factors not addressed in the model such as corrosion of the tube collar or plugging by debris.

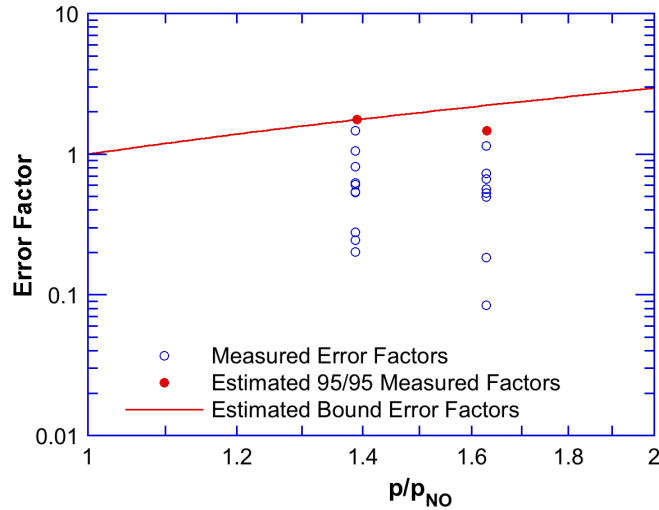


Figure 9-15 Leak Rate Error Factors for Tests with Two Phase Flows At 600°F

In laboratory tests performed by Westinghouse, the contact pressure is a function of the initial contact pressure due to hydraulic expansion, the internal pressure, and the temperature. In design basis accidents, the contact pressure is also a function of the overall deformation of the tube sheet. The potential effect of such deformations on the contact pressures is discussed in Section 9.2.2. Such structurally induced changes in contact pressure could have large effects on leak as shown in Fig. 9-16. The dependence of the relative change on the nominal values is weak.

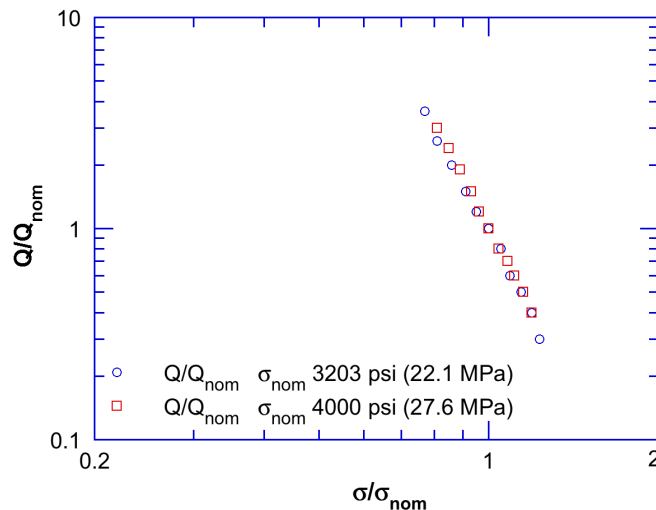


Figure 9-16 Change in Leak Rate as the Contact Pressure is Changed with the Temperature and Fluid Driving Pressure Fixed at Nominal Values

Parametric calculations for the change in leak rate associated with a set of design basis accidents were performed for two different assumptions about the contact stress. In one case (Case 1), the contact stress was fixed at its value under normal operation. The changes in contact stress due to changes in pressure in the primary and secondary systems, temperature, and the deformation of the tube sheet were assumed to “cancel out”. This would be appropriate if it could be shown that the combined effects of the pressure, temperature, and structurally induced changes in contact stress always resulted in an increase in contact stress. In the other case (Case 2), the changes in contact pressure due to pressure changes in the primary and secondary systems and temperature were included. This would be appropriate if it could be shown that the deformation of the tube sheet always produced an increase in the contact stress. Table 9-2 summarizes results for normal operations (NO), steam line break (SLB), feed line break (FLB), locked rotor (LR), and control rod ejection (CRE). The table give model predictions for the two contact stress assumptions along with a 95th percentile based on the error factor results shown in Fig. 9-15. For the constant contact stress assumption, the limiting accident (largest increase in leak rate) is the control rod ejection. If the structurally induced contact stress is additive to the pressure and temperature induced contact stresses, the increase in leak rate is about half that for the limiting accident for Case 1, and the limiting accident is the SLB.

Table 9-2 Parametric Estimates of Changes in Leak Rate (LR) During Design Basis Accidents Under Two Different Contact Stress Assumptions

	p/pNO	LR Ratio 1 Constant Contact Stress	LR Ratio 1 95th percentile	LR Ratio 2 Contact Stress includes p, T effects	LR Ratio 2 95th percentile
NO	1.0	1.0	1.0	1.0	1.0
SLB	1.1	1.9	2.4	2.6	3.3
FLB	1.2	1.6	2.2	0.8	1.1
LR	1.2	2.4	3.5	1.2	1.7
CRE	1.3	4.1	6.9	1.2	1.9

9.2 Contact Pressure Analysis

9.2.1 Effective Plastic Properties of Tubesheet

A series of elastic-plastic FEAs were conducted on the unit cells to determine the effective plastic properties of the tubesheet. The stress-strain curves used for the SA508 steel in the FEA are plotted in Fig. 9-17. Hill’s formulation was used to represent the yield surface of an anisotropic material, as follows

$$f(\sigma) = \sqrt{F(\sigma_r - \sigma_\theta)^2 + G(\sigma_z - \sigma_r)^2 + H(\sigma_\theta - \sigma_z)^2 + 2L\sigma_{r\theta}^2 + 2M\sigma_{rz}^2 + 2N\sigma_{z\theta}^2} \quad (35)$$

where

$$F = \frac{(\sigma^0)^2}{2} \left[\frac{1}{\sigma_{r,y}^2} + \frac{1}{\sigma_{\theta,y}^2} - \frac{1}{\sigma_{z,y}^2} \right] = \frac{1}{2} \left[\frac{1}{R_{11}^2} + \frac{1}{R_{33}^2} - \frac{1}{R_{22}^2} \right], \quad (36a)$$

$$G = \frac{(\sigma^0)^2}{2} \left[\frac{1}{\sigma_{r,y}^2} + \frac{1}{\sigma_{z,y}^2} - \frac{1}{\sigma_{\theta,y}^2} \right] = \frac{1}{2} \left[\frac{1}{R_{11}^2} + \frac{1}{R_{22}^2} - \frac{1}{R_{33}^2} \right], \quad (36b)$$

$$H = \frac{(\sigma^0)^2}{2} \left[\frac{1}{\sigma_{z,y}^2} + \frac{1}{\sigma_{\theta,y}^2} - \frac{1}{\sigma_{r,y}^2} \right] = \frac{1}{2} \left[\frac{1}{R_{22}^2} + \frac{1}{R_{33}^2} - \frac{1}{R_{11}^2} \right]. \quad (36c)$$

$$L = \frac{3}{2} \left(\frac{\tau^0}{\sigma_{r,\theta,y}} \right)^2 = \frac{3}{2R_{13}^2} \quad (36d)$$

$$M = \frac{3}{2} \left(\frac{\tau^0}{\sigma_{r,z,y}} \right)^2 = \frac{3}{2R_{12}^2} \quad (36e)$$

$$N = \frac{3}{2} \left(\frac{\tau^0}{\sigma_{z\theta,y}} \right)^2 = \frac{3}{2R_{23}^2} \quad (36f)$$

with $\sigma_{r,y}$, $\sigma_{\theta,y}$, $\sigma_{z,y}$, $\sigma_{r\theta,y}$, $\sigma_{z\theta,y}$, and $\sigma_{rz,y}$ = normal flow stresses in the r (radial), θ (hoop), z (thickness) directions, and shear flow stresses in the r θ , z θ , and rz planes respectively.

σ^0 and τ^0 are reference normal and shear yield stresses, with $\tau^0 = \sigma^0 / \sqrt{3}$. The anisotropic yield stress ratios are defined as follows

$$R_{11} = \frac{\sigma_{r,y}}{\sigma^0} \quad (37a)$$

$$R_{22} = \frac{\sigma_{z,y}}{\sigma^0} \quad (37b)$$

$$R_{33} = \frac{\sigma_{\theta,y}}{\sigma^0} \quad (37c)$$

$$R_{12} = \frac{\sigma_{rz,y}}{\tau^0} \quad (37d)$$

$$R_{13} = \frac{\sigma_{r\theta,y}}{\tau^0} \quad (37e)$$

and

$$R_{23} = \frac{\sigma_{z\theta,y}}{\tau^0} \quad (37f).$$

In ABAQUS, the reference stress-strain curves and the anisotropic yield stress ratios R_{ij} are input as functions of temperature. For transversely isotropic materials, such as a tubesheet with square hole array, $\sigma_{r,y} = \sigma_{\theta,y}$ and $\sigma_{rz,y} = \sigma_{z\theta,y}$, or equivalently $R_{11} = R_{33}$, $R_{12} = R_{13}$. Note that a basic assumption in ABAQUS is that the anisotropic yield stress ratios R_{ij} are constants at any given temperature and do not vary with plastic strain.

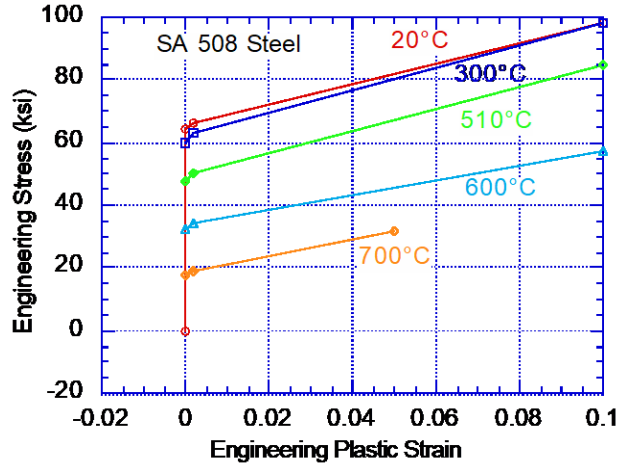


Figure 9-17 Average Stress-Strain Curves of SA508 Steel Used for Deriving Equivalent Stress-Strain Curves of the Tubesheet

The calculated in-plane and transverse yield stresses for the tubesheet with 19.4 mm (0.765 in.) diameter holes (pitch= 27.2 mm [1.07 in.]) and 22.6 mm (0.891 in.) diameter holes (pitch=32.5 mm [1.28 in.]) arranged in square arrays are plotted in Figs 9-18a-b, respectively. A comparison with the parent SA508 yield properties shows that the tubesheet yield strengths are significantly reduced by the presence of the holes, more so in the in-plane than in the transverse direction.

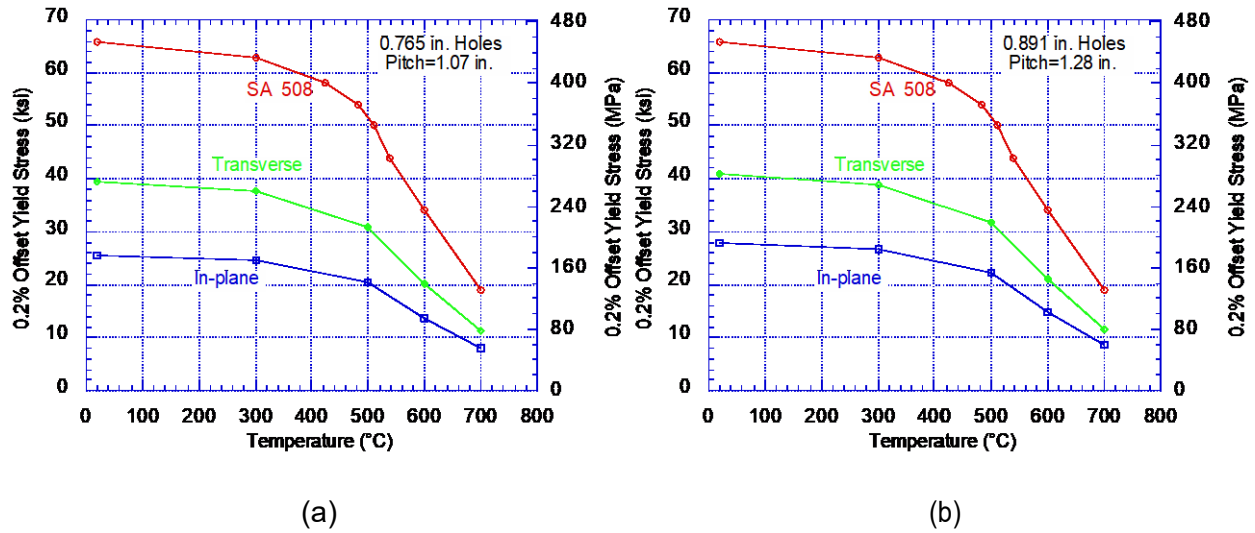


Figure 9-18 Variation of Yield Stress of SA508 and Effective Tubesheet Material with Temperature for Hole Diameter Of (A) 19.4 Mm (0.765 In.) and (B) 22.6 Mm (0.891 In.)

Calculated equivalent stress-strain curves in the in-plane and transverse directions of the tubesheet with 19.4 mm (0.765 in.) holes are plotted in Figs 9-19a-b, respectively. Similar curves for the tubesheet with 22.6 mm (0.891 in.) holes are plotted in Figs. 9-20a-b. A comparison of Figs 9-19a-b and 9-20a-b shows that the two sets of curves for the two different hole sizes are very similar. The in-plane stress-strain curves at various temperatures were input as reference stress-strain curves in ABAQUS (i.e., $R_{11}=1$).

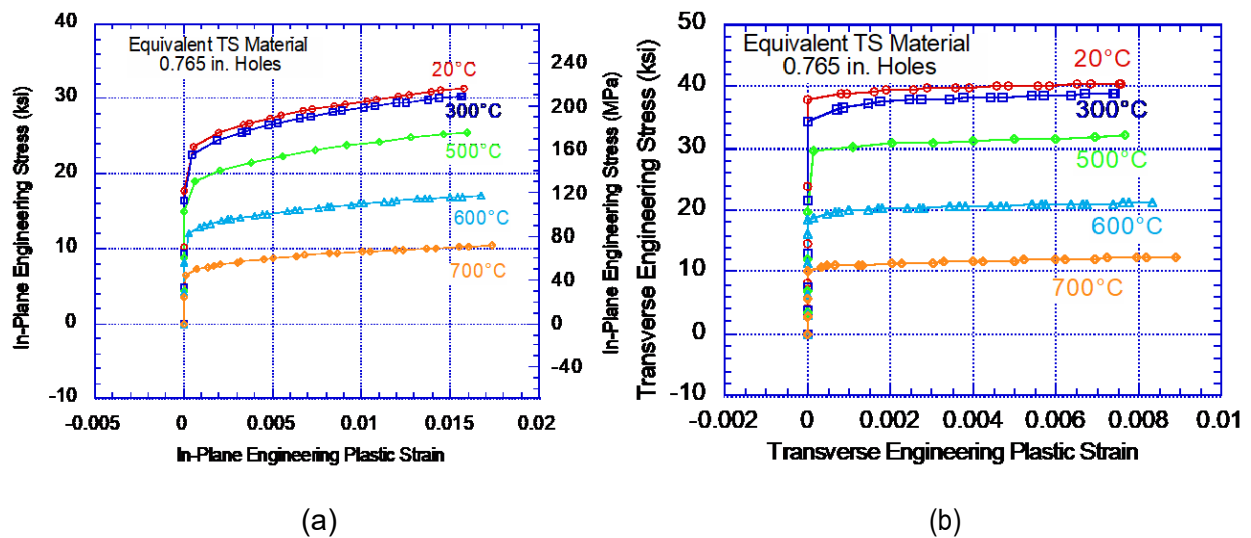


Figure 9-19 Calculated Equivalent Stress-Strain Curves at Various Temperatures of the Tubesheet with 19.4 Mm (0.765 In.) Holes in the (a) in-Plane and in the (b) Transverse Directions

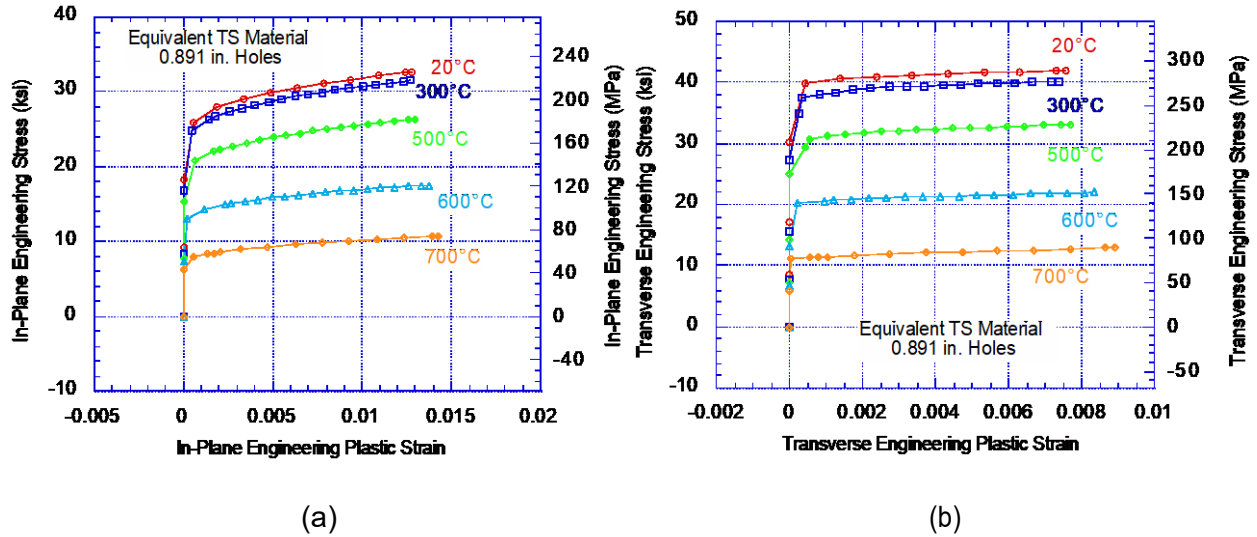


Figure 9-20 Calculated Equivalent Stress-Strain Curves at Various Temperatures of the Tubesheet with 22.6 Mm (0.891 In.) holes in the (a) in-Plane and in the (b) Transverse Directions

Calculated shear stress-strain curves for in-plane and transverse shear loading of the tubesheet with 19.4 mm (0.765 in.) holes are plotted in Figs 9-21a-b, respectively. Similar curves for the tubesheet with 22.6 mm (0.891 in.) holes are plotted in Figs. 9-22a-b. A comparison of Figs 9-21a-b and 9-22a-b shows that the two sets of curves for the two different hole sizes are very similar. The anisotropic factors R_{ij} (with $R_{11} = R_{33} = 1$) at various temperatures were calculated from the data shown in Figs. 9-19 - 9-22 using Eqs. 37a-f and were input in ABAQUS.

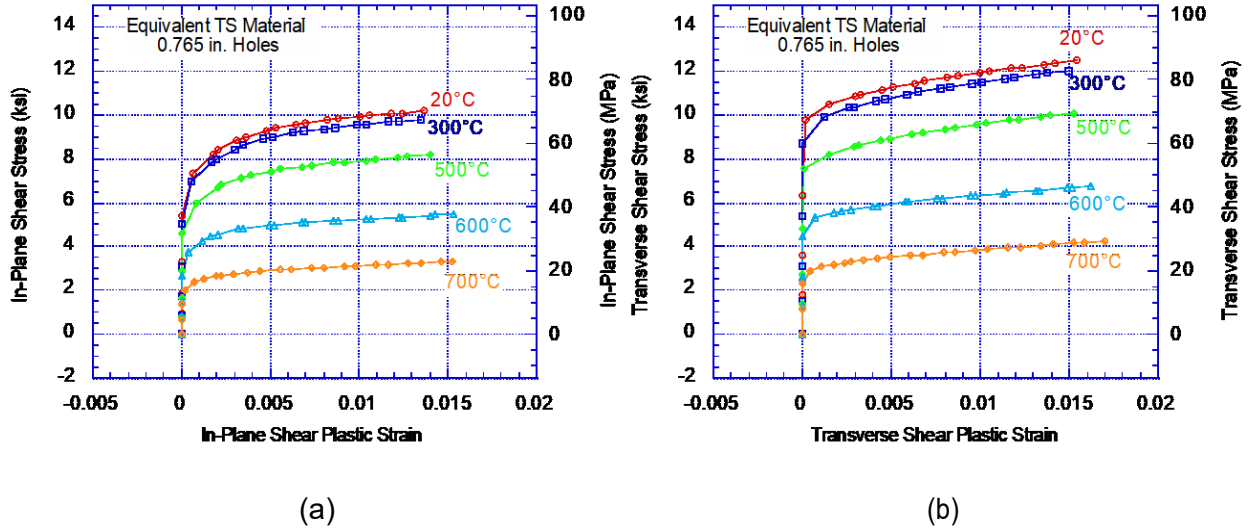


Figure 9-21 Calculated Shear Stress-Plastic Strain Curves at Various Temperatures of the Tubesheet with 19.4 Mm (0.765 In.) Holes for (a) in-Plane Shear and (b) Transverse Shear Loading

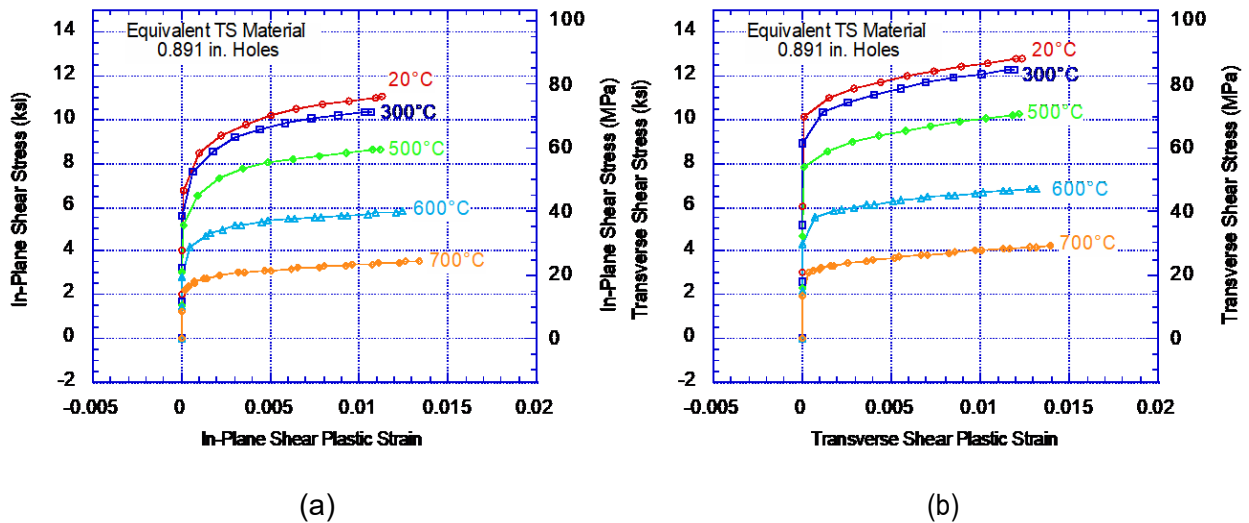


Figure 9-22 Calculated Shear Stress-Plastic Strain Curves at Various Temperatures of the Tubesheet with 22.6 Mm (0.891 In.) Holes for (a) in-Plane Shear and (b) Transverse Shear Loading

9.2.2 FEA Results

For the purpose of this report, EX-82-1 Alloy 600 was selected as the tube material (yield = [because its flow stress properties are representative of those of many of the heats of tubes in the field. The mechanical properties of the tubesheet material (A508) were obtained from the literature. The thermal expansion coefficients for both materials were obtained from the ASME Code, Section II. Stress analyses were carried out for a Model 51 SG subjected to loadings

during normal operation (NO) and main steam line break (MSLB) accident. The various loading parameters used in the analyses are tabulated in Table 9-3. Note that the temperature is assumed to be uniformly distributed throughout the tube-to-tubesheet junction in both cases. A preliminary analysis showed that tubesheet bowing due to primary pressure has a bigger effect on leakage than the temperature drops through the tubesheet during NO and MSLB. Therefore, the assumption of uniform temperature distribution should not affect the results significantly.

Table 9-3 Loading Assumed for Stress Analyses of Model 51 SG with [je Diameter Alloy 600 Tubes

Loading Parameter		NO	MSLB
Hydraulic Expansion Pressure (ksi)		[
Primary Pressure (ksi)		2.25	2.5
Secondary Pressure (ksi)		0.8	0.023
Temperature (°C)		315	232
Saturation Pressure (ksi)		1.541	0.422

An FEA was originally conducted where the FEM did not represent the connections between the tubesheet, solid rim and the SG shell adequately. As a result, the bending displacements in the tubesheet during MSLB were overestimated, which affected the distribution of the contact pressure at the tube-to-tubesheet interface significantly. After a meeting with Westinghouse, an updated FEM model was created and used in the FEA. An analysis with a quarter of the updated model showed that, in contrast to the prediction of the original analysis using the inaccurate model, the contact pressure near the top of tubesheet was not reduced to zero during a postulated MSLB, because the transverse bending of the tubesheet was significantly reduced in the updated model.

The distribution of contact pressure after hydraulic expansion predicted by the updated full model is not changed compared to that by the old model (Fig.9-13), because the tubesheet does not bend during hydraulic expansion. However, the distributions are significantly different during NO and MSLB because the tubesheet experiences significantly different amounts of bending under these situations (Fig. 9-14a-b). The reduction in the contact pressure near the top of the tubesheet for both NO and a MSLB predicted by the old model is greater than that by the updated quarter or updated full model. In particular, while the old model predicted that the contact pressure would be reduced to zero and the contact would open up near the top of tubesheet during MSLB, the updated models predict that the contact will remain closed (with positive contact pressure) along the entire tube-to-tubesheet interface. Except near the free edges, the predicted contact pressure distributions by the updated quarter model and the updated full model are identical, because the spatial distribution of temperature is assumed to be uniform in both cases.

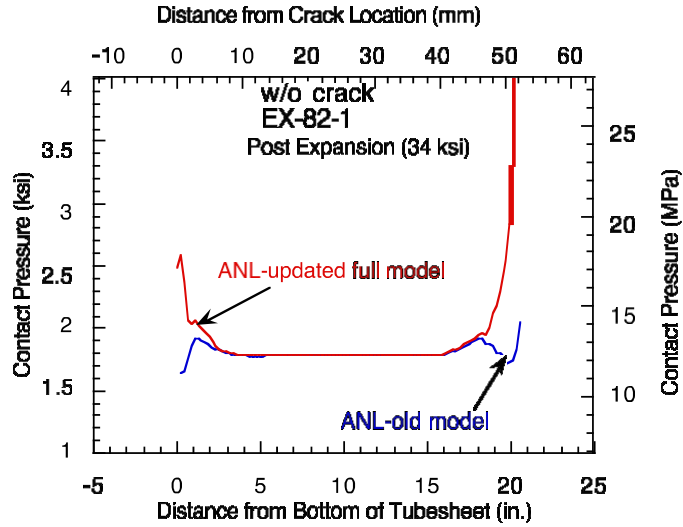


Figure 9-23 Comparison of Distributions of Contact Pressure at the Tube-to-Tubesheet Interface Following Hydraulic Expansion Computed by the Old Model and the Updated Model

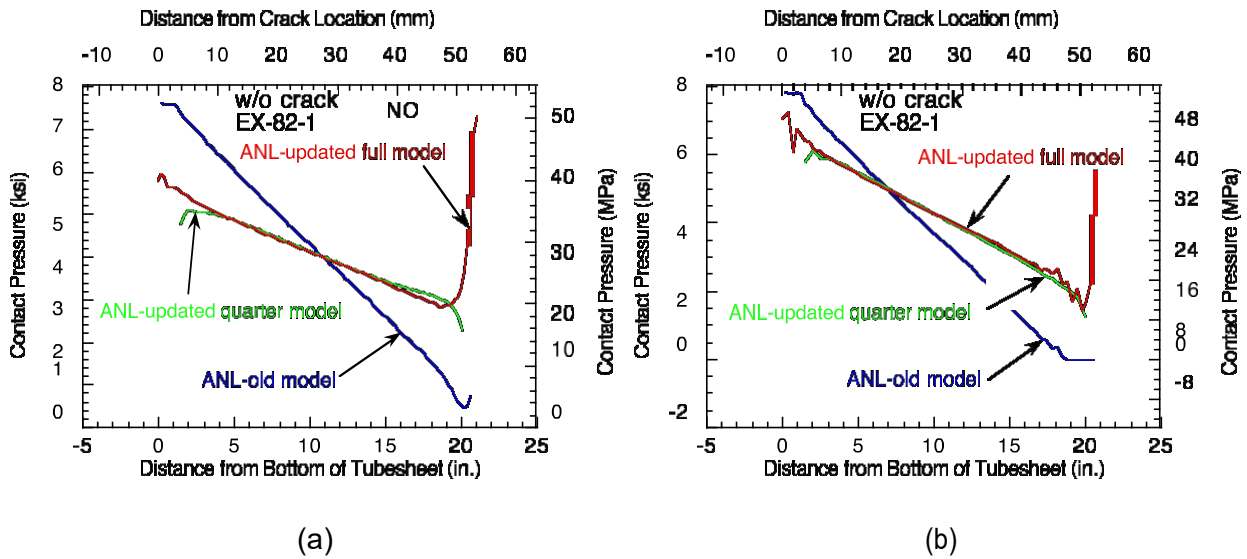


Figure 9-24 Comparison of Distributions of Contact Pressure Computed by the Old Model, the Updated Quarter Model and the Updated Full Model Due to Loadings During (a) NO and (b) MSLB

The displaced shapes of the cross-section of the tube at the top of tubesheet during NO and MSLB are shown in Figs. 9-25a-b, respectively. Note that the diametral growth of the tube in the tubesheet radial direction is less than that in the orthogonal direction. The ovalization of the tube cross-section at the tubesheet mid-surface and at the top of tubesheet is further illustrated in Figs. 9-26a-b, respectively, which shows that the diameter at 0°/180° grows significantly less

than that in the 90°/270° direction. It should be noted that Figs 9-27a-b include thermal growth of the tube that is larger during NO than during MSLB because the temperature during NO is higher than that during MSLB. However, the thermal growth should not add to the ovalization of the tube cross-section significantly. Owing to the tubesheet bowing, the degree of ovalization is less at the tubesheet midsection than at the top of tubesheet. However, the circumferential variation of the contact pressure is quite modest, as shown in Fig. 9-27. The maximum circumferential variation in contact pressure is 0.03 ksi at the tubesheet mid-surface and 0.15 ksi at the top of tubesheet for both NO and MSLB. Such variations are not resolvable in Fig. 9-27, which shows plots of the axial variation of contact pressure along four axial paths along the tube OD surface during MSLB. Note that the contact pressures during MSLB are higher than those during NO provided the crevice is assumed to be uniformly pressurized by the secondary fluid.

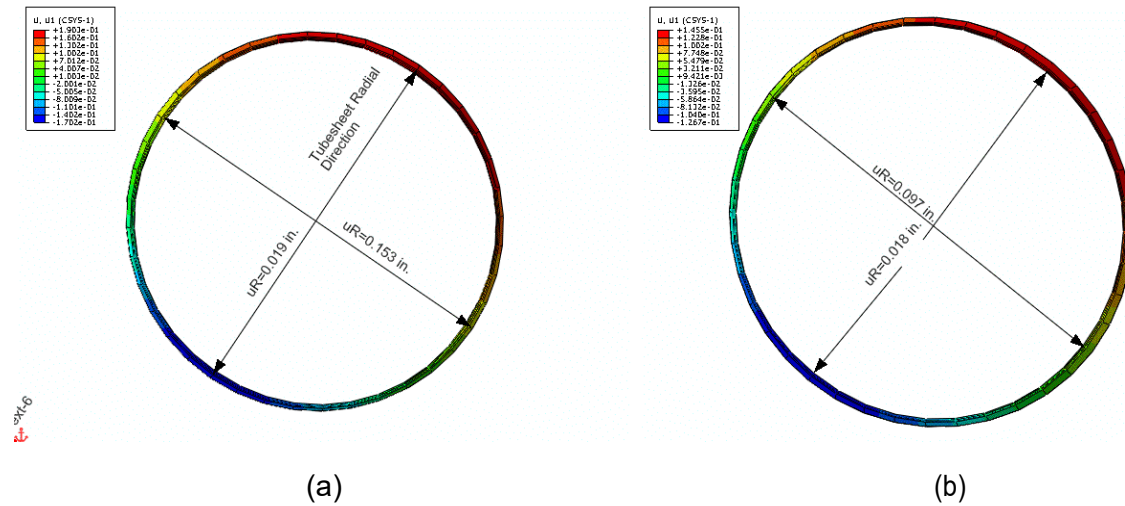


Figure 9-25 Displaced Shape of the Tube Cross-section at the Top of Tubesheet during (a) NO and (b) MSLB (The Diametral Expansion (uR) of the Tube along a Tubesheet Radial Direction is less than that in the Orthogonal Direction, Suggesting a Small Ovalization of the Tube Cross-section)

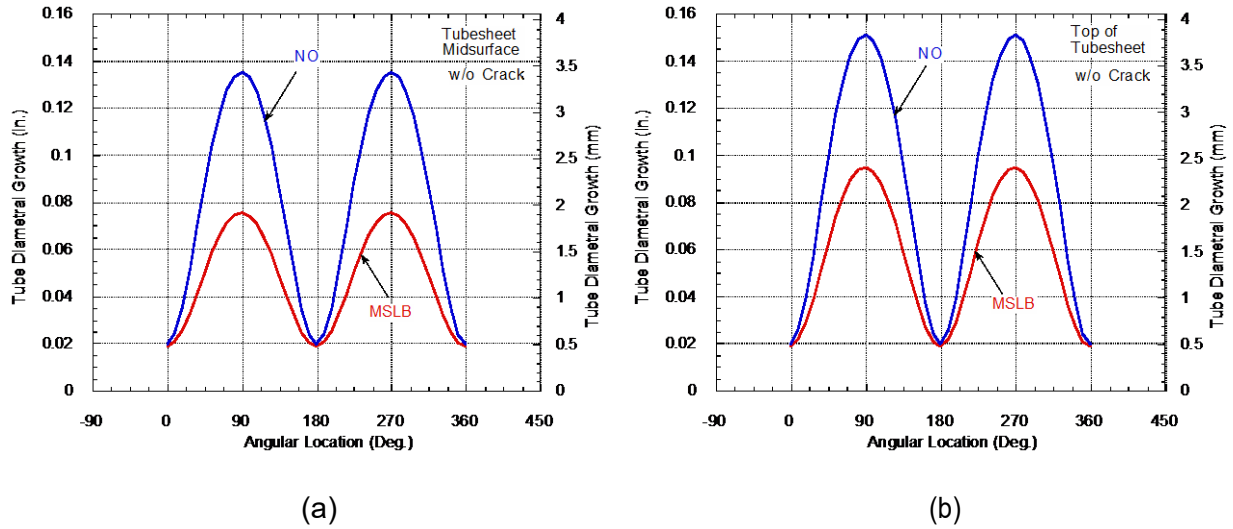


Figure 9-26 Variation of Diametral Growth of the Tube Cross-Section with Angular Location During NO and MSLB at (a) Tubesheet Midsurface and (b) Top of Tubesheet

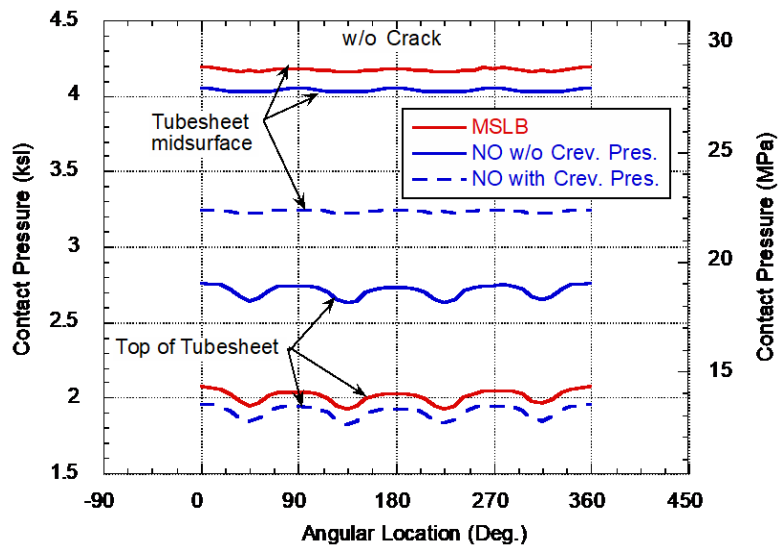


Figure 9-27 Circumferential Variation of Contact Pressure at the Tubesheet Midsurface and at the Top of Tubesheet during NO and MSLB (Dashed lines indicate contact pressures calculated assuming that the crevice is pressurized with the secondary fluid)

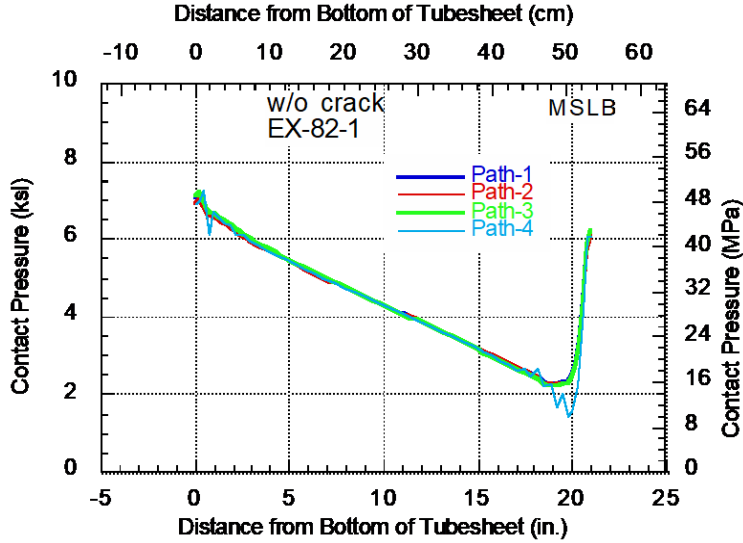


Figure 9-28 Axial Distribution of Contact Pressure along Four Paths Situated 90° Apart in the Circumferential Direction of the Tube during MSLB

9.3 Leak Rate Predictions for Normal Operation and Design Basis Accidents

For calculation purposes, it was assumed that the tube has a full 360° TW circumferential crack located at the mid plane of the tubesheet. The basic leak rate equation for two-phase flow is Eq. (5) from Section 5.2, which is renumbered here as Eq. (38)

$$q = -\frac{1}{K} \frac{\rho(p_f)}{\mu} \frac{dp_f}{dz} \quad (38)$$

where, in general, the loss coefficient K , dependent on the contact pressure, is a function of z (axial distance through the tubesheet thickness), the density ρ is a function of pressure and temperature, but for water it is approximately independent of pressure (incompressible), μ is coefficient of viscosity, p_f is the fluid pressure in the crevice. The subcooled water after entering the crevice at the crack location (assumed to be at the tubesheet mid-surface location) flows upwards and flashes to steam at a location in the crevice where the fluid pressure equals the saturation pressure. Assuming that the subcooled liquid flashes to steam instantaneously as soon as saturation pressure is reached and that steam is a perfect gas, integration of Eq. ((38)) gives the following equation for mass flow rate q

$$q = \frac{\Delta p_f}{v_{liq} \int_0^{L_{sat}} K(z) dz + v_{sat} \int_{L_{sat}}^L \frac{K(z)}{\frac{p_f}{p_{sat}}} dz} \quad (39)$$

where Δp_f is the inlet to outlet pressure drop in the crevice fluid, v_{liq} denotes kinematic viscosity of the liquid, v_{sat} denotes the kinematic viscosity of the saturated gas and the subscript "sat" denotes conditions at saturation condition. To obtain the crevice pressure distribution along the length, the continuity requires the mass flow to be constant along the length and the crevice pressure distribution, given by

$$P_1 - P_f = q \begin{cases} v_{liq} \int_0^z K(z) dz & \text{for } z < L_{sat} \\ v_{liq} \int_0^{L_{sat}} K(z) dz + v_{sat} \int_{L_{sat}}^z \frac{P_{sat}}{P_f} K(z) dz & \text{for } z \geq L_{sat} \end{cases} \quad (40)$$

where p_1 is the crevice inlet pressure and the flow rate q is obtained from Eq. (39).

Initially, the distribution of crevice pressure p_f , the values of L_{sat} and q are unknown. However, Eq. (39) can be solved iteratively with two nested loops, as follows

- (1) For a given crevice pressure distribution (initially, a constant crevice pressure distribution can be assumed), use FEA to obtain the contact pressure distribution from which $K(z)$ can be determined by using Eqs. (15)-(16).
- (2) Crevice pressure distribution gives L_{sat} , which, together with $K(z)$, determined in step 1, can be substituted into Eq. (39) and integrated to give q .
- (3) Use Eq (40) to obtain a new distribution of crevice pressure $p_f(z)$, which is generally different from that assumed previously.
- (4) Repeat steps 2-3, holding $K(z)$ fixed, until the mass flow rate $q(z)$ across every cross-section of the tube is constant (i.e., $q(z)=q$, independent of z) and the crevice pressure distribution $p_f(z)$ converges.
- (5) Until the overall solution has converged, the new crevice pressure distribution is, in general, not compatible with the contact pressure distribution that was determined in step 1 and was held constant during steps 2-4.
- (6) Repeat steps 1-5 until both the crevice pressure distribution and the contact pressure distribution converge and are mutually compatible.

Figure 9-29 shows the calculated leak rates as functions of the iteration number for both NO and MSLB conditions. Although the leak rate for NO converged, that for MSLB showed oscillations varying between 650 and 1550 mg/min. The reason for the difference in behavior can be traced to the axial variations of the contact pressure and crevice pressure for the two cases. The axial variations of contact pressure and crevice pressure during NO reach relatively stable values, as shown in Figs.9-30a-b, respectively. In contrast, during MSLB the axial variations of contact pressure and crevice pressure show cyclic variations with iteration number, as shown in Figs. 9-30a-b, respectively. During NO, the water flashes to steam close to the exit end with a steep pressure drop through the gaseous phase. Although the behavior during MSLB is qualitatively similar, there is a much steeper pressure drop in the gaseous phase and flashing occurs almost at the exit plane (over a single element). The calculated leak rate is very sensitive to the location of the flashing point. To obtain a more stable result for the MSLB case, a finer mesh may be required near the exit plane.

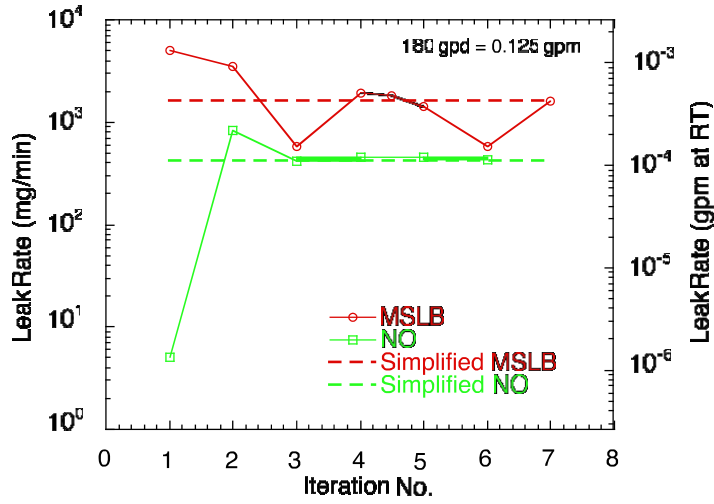


Figure 9-29 Calculated Leak Rate vs. Iteration Number for Normal Operation and Main Steam Line Break Conditions (Dashed lines show predictions by a simplified model)

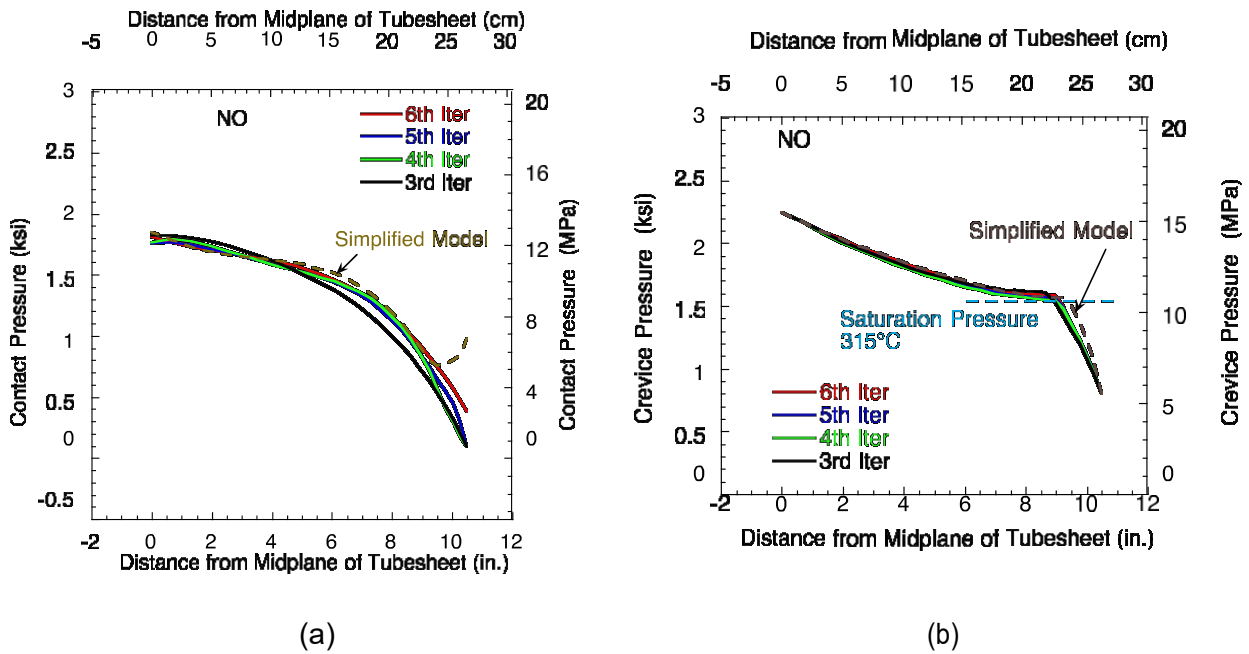


Figure 9-30 Distribution of (a) Contact Pressure and (b) Crevice Pressure along the Length of the Tube during NO

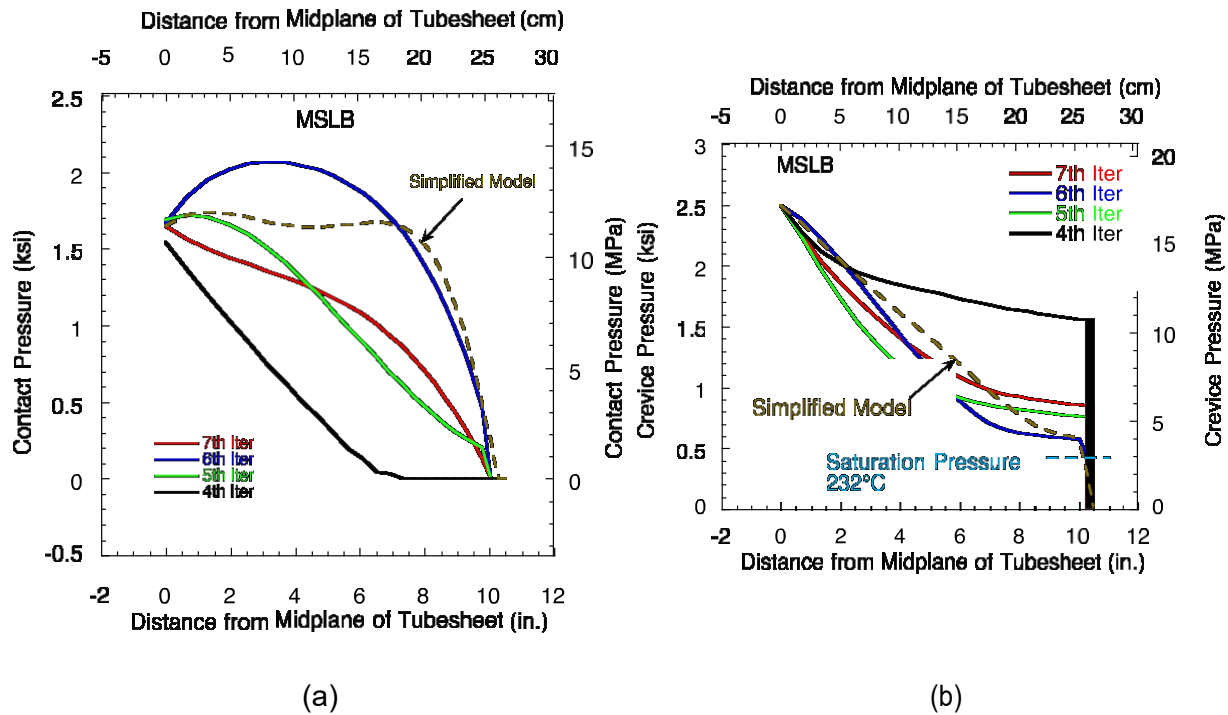


Figure 9-31 Distribution of (a) Contact Pressure and (b) Crevice Pressure along the Length of the Tube during MSLB

9.3.1 Simplified Leak Rate Model

To avoid time-consuming iterative FEAs, a simplified model was developed. It was assumed that the effective contact pressure at any axial location (z) is obtained by subtracting the crevice coolant pressure at that location from the contact pressure at that location calculated assuming zero crevice pressure. This model is inapplicable when the effective contact pressure is <0 and a gap opens up. The leak rates were calculated using steps 1-4 until the crevice pressure distribution converged. The contact pressure distribution corresponding to the new crevice pressure distribution was not recalculated, thus the results were obtained with a single iterative loop, rather than the two nested loops that were used in the previous case. The effective contact pressure and crevice pressure distributions for NO are plotted as dashed lines in Figs. 9-30a-b, respectively, and the same for MSLB are plotted as dashed lines in Figs. 9-31a-b, respectively. The calculated leak rates are shown by dashed lines in Fig. 9-29. Note that the effective contact pressure and crevice pressure distributions for NO calculated by the simplified model are very close to those predicted by the more rigorous model. Also, the leak rate predicted by the more rigorous model converges to the leak rate predicted by the simplified model (1×10^4 gpm at room temperature). The effective contact pressure and crevice pressure for MSLB calculated by the simplified model are reasonably close to those predicted by the final iterations of the more rigorous model. The leak rate during MSLB predicted by the simplified model is close to the upper value of the oscillatory leak rates predicted by the more rigorous model (4×10^{-4} gpm at room temperature).

9.3.2 Approximate Bounds to Leak Rates

Bounds to leak rates under NO and MSLB can be derived by assuming fixed crevice pressure distributions to calculate the contact pressures and gaps, if any, by FEA. Leak rates are calculated iteratively by using steps 1 through 3 of Section 9.3, without changing the contact pressure distribution. Figures 9-32a-b show the calculated crevice pressure distributions for NO and MSLB when the contact pressures are calculated assuming a uniform crevice pressure distribution (equal to the primary pressure). Similarly, Figs 9-33a-b show the calculated crevice pressure distributions for NO and MSLB when the contact pressures are calculated assuming a parabolic crevice pressure distribution (varying parabolically from primary pressure at the crack location to the secondary pressure at the crevice outlet). Note that when a uniform crevice pressure distribution is assumed (Figs. 9-32a-b) for calculating the contact pressures, the calculated crevice pressures are less than the assumed crevice pressures for both NO and MSLB. On the other hand, when a parabolic crevice pressure distribution is assumed for calculating the contact pressures, the calculated crevice pressure distribution can be slightly less or slightly greater than the assumed crevice pressure for NO (Fig. 9-33a), but the calculated crevice pressure distribution is significantly greater than the assumed crevice pressure for MSLB (Fig. 9-33b). These observations suggest that the leak rates calculated on the basis of a uniformly distributed crevice pressure for calculating the contact pressure should be upper bounds. This is to be expected because the true crevice pressure at any axial location must be less than or equal to the crevice inlet (primary) pressure and the assumption of a uniformly distributed crevice pressure equal to the primary pressure necessarily leads to an upper bound to the crevice opening displacement (and/or lower bound to the contact pressure). On the other hand, the leak rate calculated on the basis of a parabolically distributed crevice pressure is not necessarily a lower bound to the true leak rate, although our tests did suggest that the crevice pressure distribution is close to parabolic when the crevice is fully open and the leak rate is high.

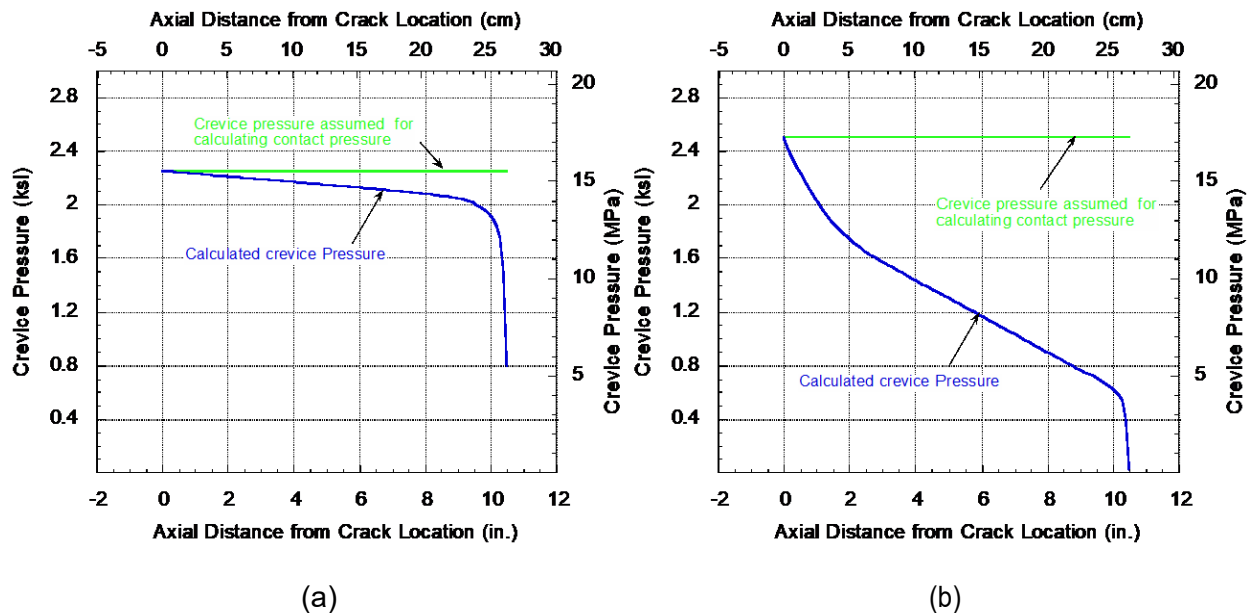


Figure 9-32 Calculated Crevice Pressure Distribution and the Uniform Crevice Pressure Distribution Assumed for Calculating the Contact Pressures during (a) NO and (b) MSLB

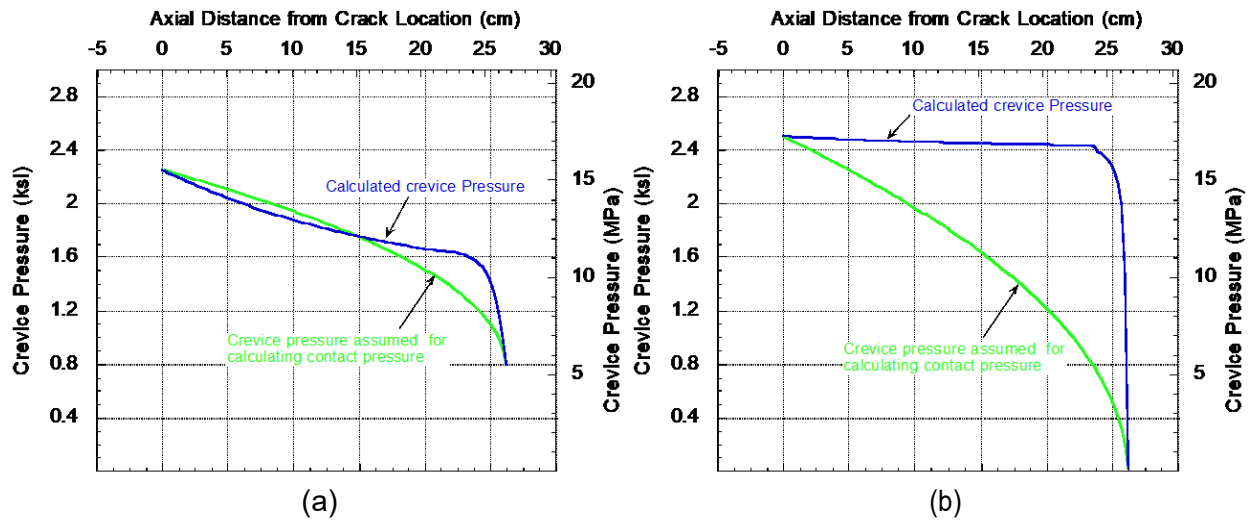


Figure 9-33 Calculated Crevice Pressure Distribution and the Parabolic Crevice Pressure Distribution Assumed for Calculating the Contact Pressures during (a) NO and (b) MSLB

Figures 9-34a-b show upper and lower leak rate bounds (dashed lines) calculated on the basis of a uniform crevice pressure distribution (equal to the primary pressure) and a parabolic crevice pressure distribution (varying parabolically from primary pressure at the crack location to the secondary pressure at the crevice outlet) for NO and MSLB, respectively. The upper bounds based on a uniform crevice pressure distribution provide conservative bounds to the leak rates calculated by the more rigorous model. Although not necessarily true in general, parabolic crevice pressure distribution in the present case provides a conservative lower bound to the leak rate under MSLB, but is close to the leak rate predicted by the more rigorous model for NO.

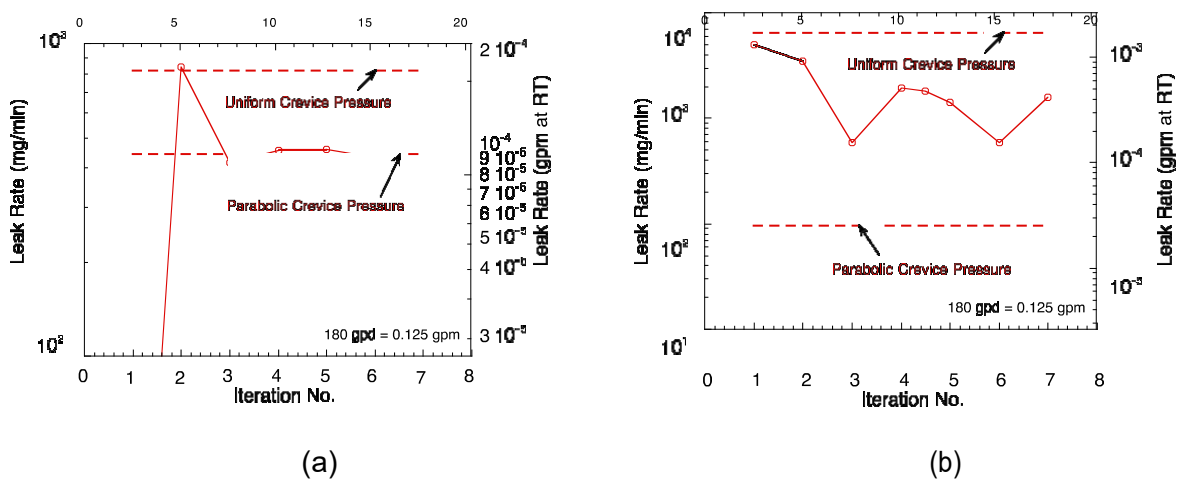


Figure 9-34 Calculated Leak Rate vs. Iteration Number (solid lines) for (a) Normal Operation and (b) Main Steam Line Break Conditions (Dashed lines represent bounds)

10 LEAKAGE PREDICTIONS FOR TUBE-TO-TUBESHEET JUNCTIONS DURING SEVERE ACCIDENTS

In previous experience with tube-to-collar testing, it was observed that large leakages occurred when the crevice at the tube-to-tubesheet interface was pressurized such that the collar crept away from the tube. Under Case 8B accident conditions, pressurization will occur through tube cracks, and subsequently into the crevices, rather than independently pressurized, as in some of the above testing. Thus, in section 7.6.5, where the crevice was not independently pressurized, the tube behaved in a prototypical fashion.

For the purpose of this report, EX-82-1 Alloy 600 was selected as the tube material (yield = 514 MPa (2 ksi)), because its flow stress properties are representative of the heats of tubes in the few remaining Westinghouse SGs with Alloy 600 tubes. ANL considered leakage from a 360° throughwall circumferential crack in the tube located at the mid thickness level of the tubesheet, i.e., 267 mm (10.5 in.) below the top of tubesheet and assumed that the total leakage through all similar cracks in the SG has negligible effect on the progress of the severe accident transient.

10.1 Thermal Analysis

The thermal analysis of the tube-to-tubesheet junction during the accident was conducted with a fairly crude model of the tubesheet using RELAP5. Heat transfer coefficients (HTCs) and gas temperatures were calculated for an average tube and the hottest tube. The analysis did not provide any information on the distribution of temperature in the tubesheet either in the thickness direction or in the plane of the tubesheet. To develop a more realistic temperature distribution in the tubesheet, FEAs were conducted with thermal inputs from more detailed computational fluid dynamics (CFD) analyses of the hot inlet quadrant of the tubesheet provided by NRC-RES. The average thermal loadings in the other three quadrants of the tubesheet were provided by Information Systems Laboratories. [3]

The actual geometry of the tubesheet is quite complex, with the core region consisting of thousands of tube holes arranged in a regular array (Fig. 10-1). To consider the detailed geometry and input history of heating of each tube hole individually in a finite element model (FEM) would be impractical. In this case, as in the previous analyses for normal operation and design basis accidents, a single tube located within a tubesheet hole was included, while replacing the rest of the tubesheet by a homogeneous equivalent tubesheet material (Fig. 10-2). Detailed distributions of local heat transfer coefficients (HTCs) and gas temperatures were input as a function of time in the tube that was considered in the FEM. The heating load on the rest of the tubes was smeared out in the tubesheet material as volumetric heating. A detailed analysis, to be discussed later, showed that such an approach is reasonable. The divider plate was also included, the lower head and 152 mm (6 in.) of the SG shell immediately above the tubesheet in the FEM.

In the thermal FEAs, it was assumed that there is no thermal gap resistance between the SG tube OD surface and the tubesheet hole inner surface. This is a simplification of the real situation, which is a coupled heat transfer-structural analysis problem, because the gap thermal resistance across the tube-to-tubesheet interface is a function of contact pressure or gap opening. In the subsequent structural FEAs, the tube-to-tubesheet interface was modeled with gap elements that have sliding and friction capabilities and allow the contact to open (i.e., create a gap) after the contact pressure reduces to zero. However, the error in the thermal analysis introduced by our simplifying assumption is somewhat self-correcting because the opening of a gap would tend to

increase the gap thermal resistance which would tend to increase the tube temperature which in turn would tend to close the gap, reduce the gap thermal resistance and reduce the tube temperature.

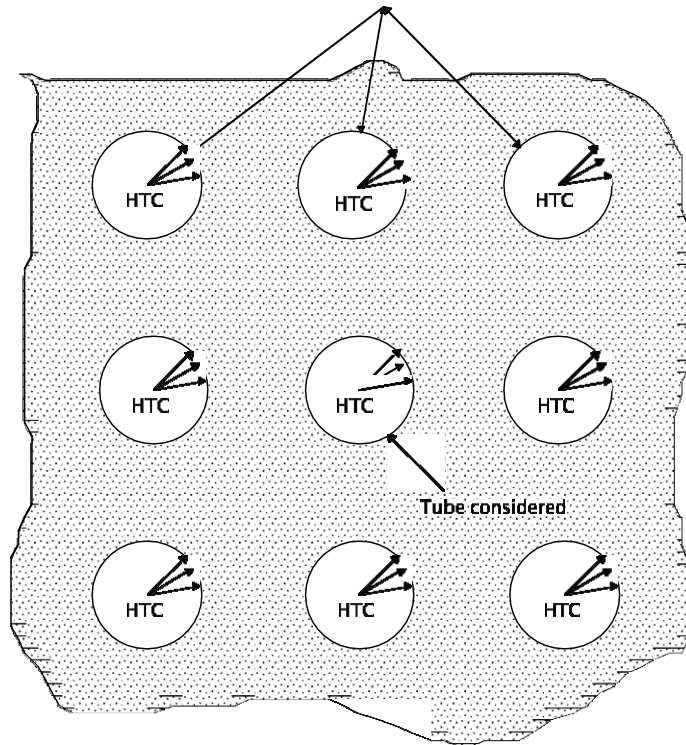


Figure 10-1 Thermal Loading of Tubes and Tubesheet

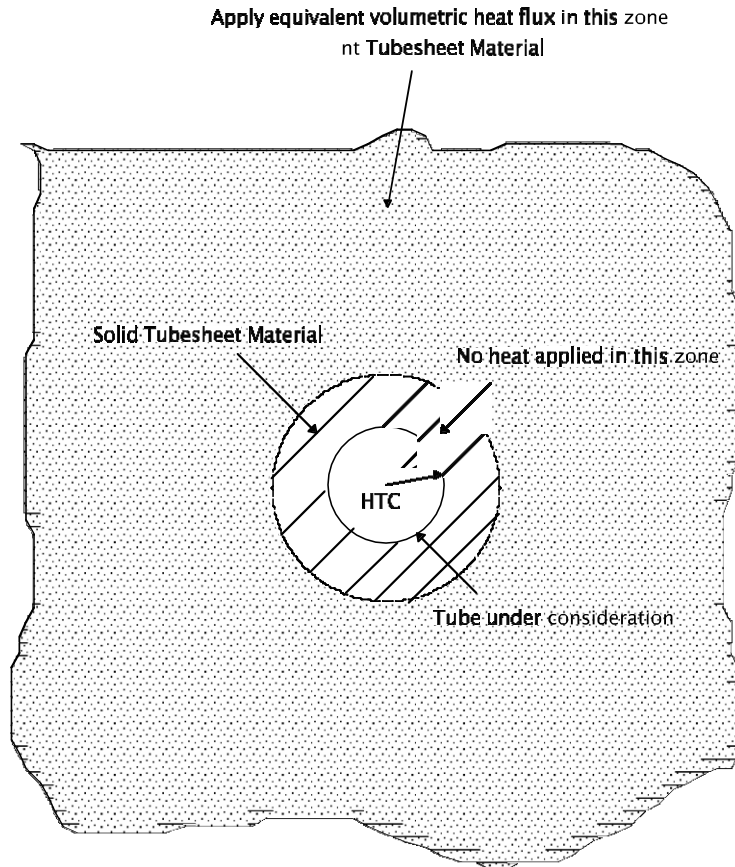


Figure 10-2 Thermal Loading of a Single Tube under Consideration and of the Equivalent Tubesheet Material

10.1.1 Thermal Hydraulic Input Data from CFD and RELAP 5 Analysis

CFD calculations were performed to get a more detailed understanding of the temperature distribution in the tubesheet. Distributions of the HTCs and gas temperatures at the inlet and outlet ends for the hot inlet (cells h1-h21) were provided by Boyd.* The CFD-generated heat transfer data for the tubesheet in the hot inlet quadrant of the tubesheet is shown in Fig.10-3. RELAP5 calculations for thermal input data for the hot outlet (cell h22), cold outlet (cell h23) and cold inlet (cell h24) as functions of time during the severe accident (Base Case) were also available. [3] Each cell represents a tubesheet region containing a group of tubes. Plots of the inlet gas temperature for the various cells in the hot inlet quadrant and the heat transfer coefficient, which is the same for all the cells, are shown in Figs. 10-4a and 10-4b. To maximize the creep relaxation effects without being unduly conservative, the selected reference tube was located within cell 16. In the thermal conduction analysis, the portion of the tube inner surface located in the lower half of the tubesheet was subjected to the inlet gas temperature and HTC of cell 16, which are shown in Figs. 10-4a-b, and the portion of the tube inner surface located in the upper half of the tubesheet was subjected to the outlet gas temperature and HTC of cell 16. Also, it was assumed that there is no resistance to heat flow at the interface between the tube

* C. Boyd, Thermal Boundary Conditions for Tube Sheet during a Severe Accident, Personal Communication to S. Majumdar, October 2006.

OD surface and the tube hole surface in the tubesheet. The tubesheet, the divider plate and the location of the tube hole under consideration in the FEM are shown in Fig. 10-5.

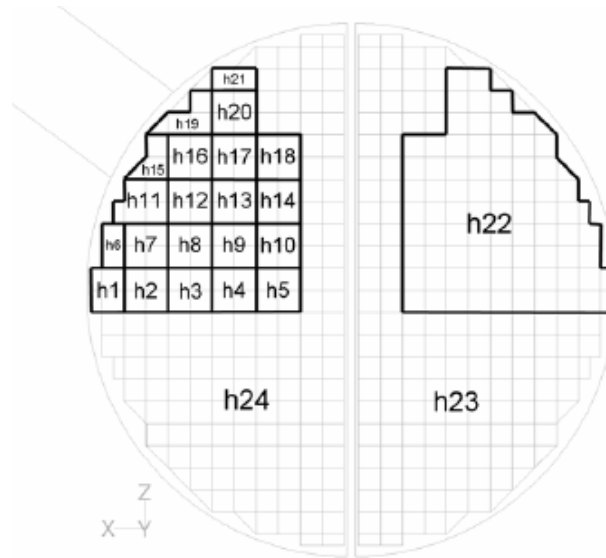


Figure 10-3 Definition of Tubesheet Cells H1-H24 Used in CFD Analysis

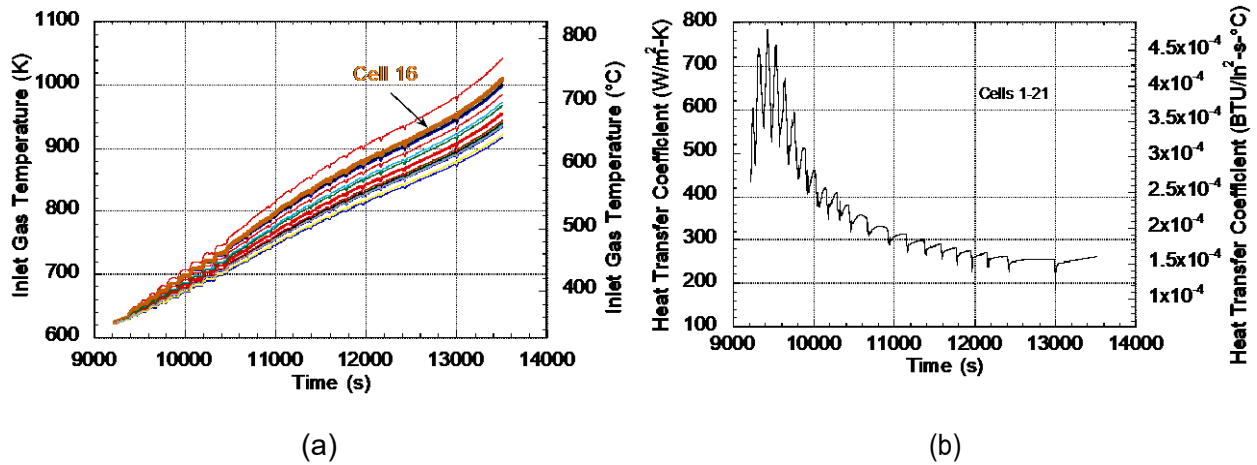


Figure 10-4 Variations of (a) Inlet Gas Temperatures and (b) Heat Transfer Coefficient with Time for Tubesheet Cells 1-21 Obtained from CFD Analysis

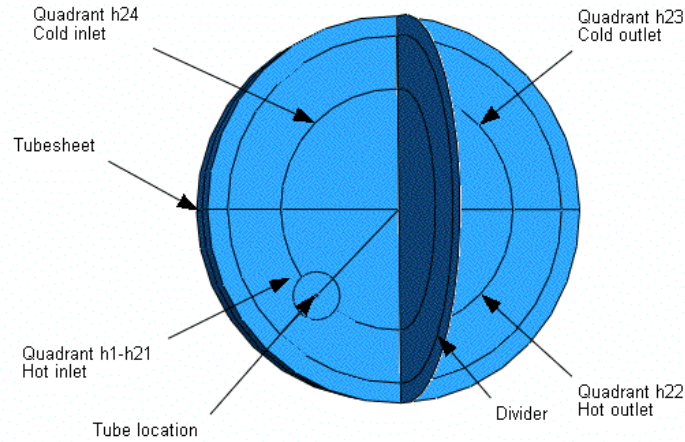


Figure 10-5 Finite Element Model of Model 51 SG Showing the Tubesheet, Location of the SG Tube, Divider Plate and the Various Cells used in the CFD Analysis

10.1.2 Development of Thermal Properties for Equivalent Tubesheet Material

10.1.2.1 Thermal Conductivity

The anisotropic thermal conductivity properties of the equivalent homogeneous tubesheet material are related to the heat flux and temperature gradient vectors by Eq. (41)

$$\begin{Bmatrix} h_r \\ h_z \\ h_\theta \end{Bmatrix} = \begin{bmatrix} k_{rr} & 0 & 0 \\ 0 & k_{zz} & 0 \\ 0 & 0 & k_{\theta\theta} \end{bmatrix} \begin{Bmatrix} \frac{\partial T}{\partial r} \\ \frac{\partial T}{\partial z} \\ \frac{1}{r} \frac{\partial T}{\partial \theta} \end{Bmatrix} \quad (41)$$

where h_r , h_z and h_θ denote the heat flux vectors in the radial, axial (through thickness) and circumferential directions and $\frac{\partial T}{\partial r}$, $\frac{\partial T}{\partial z}$ and $\frac{1}{r} \frac{\partial T}{\partial \theta}$ are the corresponding temperature gradient vectors. For the square arrays under consideration, $k_{rr}=k_{\theta\theta}$.

The effective thermal conductivity properties of the tubesheet were calculated by applying unit temperature drops across the opposite faces of the unit cell and then conducting FEAs to determine the corresponding heat flux vectors. The variations of the thermal conductivities with temperature for the tubesheet with 22 mm (0.875 in.) diam. tubes (23 mm [0.891 in.] diam. holes at 33 mm [1.28 in.] square pitch) and 19 mm (0.75 in.) diam. tubes (19 mm [0.765 in.] diam. holes at 27 mm [1.07 in.] square pitch) are plotted in Fig. 10-6. It is evident that the thermal conductivity properties of both arrays are comparable. Fig. 10-6 also shows the thermal conductivity of A508 steel. Compared to the conductivity of solid A508 steel, both the radial (r)

and the axial (z) thermal conductivities of the equivalent tubesheet material are reduced significantly, the in-plane properties more so than the through-thickness properties.

10.1.2.2 Specific Heat and Mass Density

The specific heats in BTU/lb-C (J/kg-C) of the tubesheet and A508 steel are the same (Fig.10-7), but the effective mass density of the tubesheet for both arrays is 5.5 g/cm³ (0.2 lbs/in³) compared to 7.8 g/cm³ (0.282 lbs/in³) of solid A508 steel.

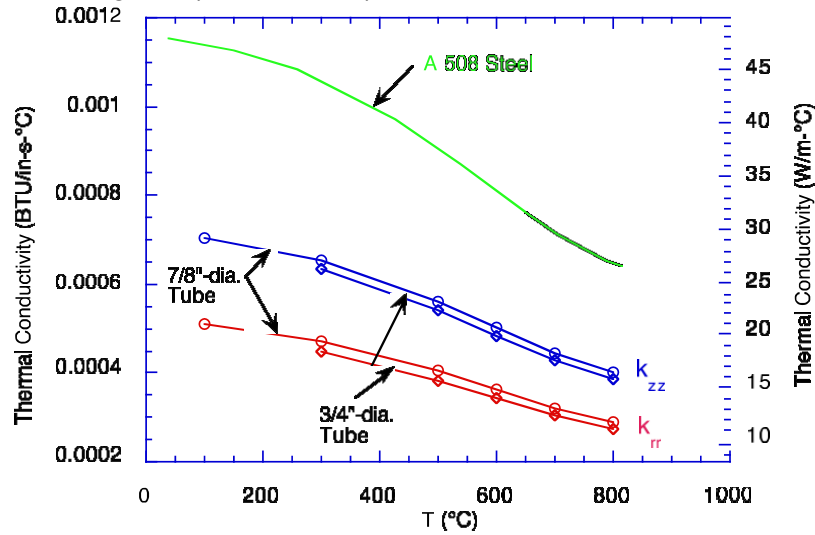


Figure 10-6 Variation of Effective Thermal Conductivity Properties of Tubesheet with Temperature

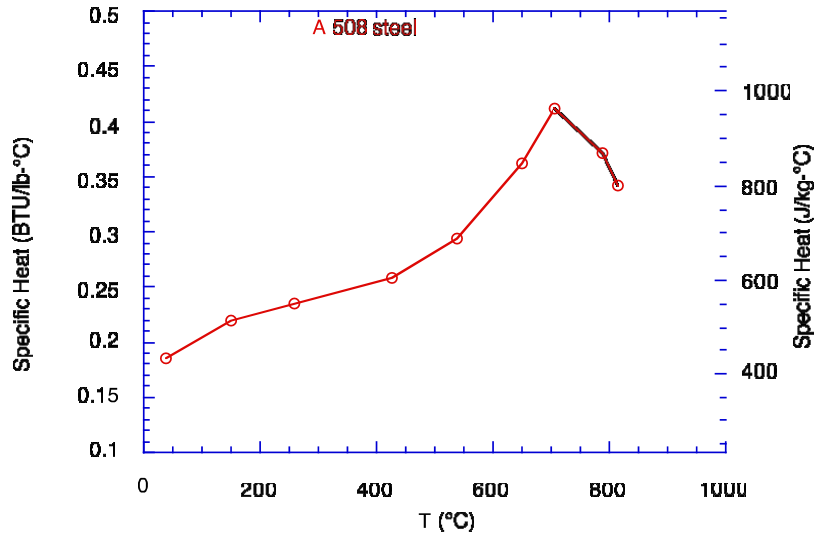


Figure 10-7 Variation of Specific Heat of A508 with Temperature

10.1.2.3 Volumetric Heating Rate (Base Case) for the Equivalent Tubesheet Material

To simplify the analysis of the heat transfer from the SG tubes to the tubesheet away from the SG tube under consideration, instead of using the HTC data from the CFD analysis, the total heat transferred from each fluid cell to the tubesheet (total of eight fluid cells - two fluid cells per quadrant) calculated by RELAP5 for the base case was input as a volumetric heat source. The total heat transferred was divided by the fluid volume and multiplied by the fluid volume fraction (relative to the unit cell) to obtain the volumetric heating rate for the equivalent homogeneous tubesheet structure. Two sets of ABAQUS transient thermal conduction analyses for the unit cell of the tubesheet were conducted to compare the accuracy of the simplified approach with a more detailed analysis. In the first analysis, the inside surface of the tube in the unit cell was subjected to time varying but spatially uniform gas temperature and HTC for the hot inlet plenum obtained from the CFD analysis. In the second analysis, the unit cell was replaced by an equivalent homogeneous solid cube with the same exterior dimensions but with effective values of thermal conductivity and density to account for the void volume inside the unit cell and subjected to the calculated volumetric heating. The calculated temperature fields in the two analyses differed by at most 1 or 2 degrees over the duration of the severe accident (Fig. 10-8). The temperatures in the unit cell in the first analysis were quite uniform radially, confirming the expected high heat transfer properties of the perforated tubesheet (Fig. 10-9a); the temperature field inside the equivalent solid cell was perfectly uniform (as expected) (Fig. 10-9b). The small radial temperature gradient (2°C from coldest to hottest) in the unit cell makes the use of the equivalent solid in a global analysis viable without significant loss of accuracy.

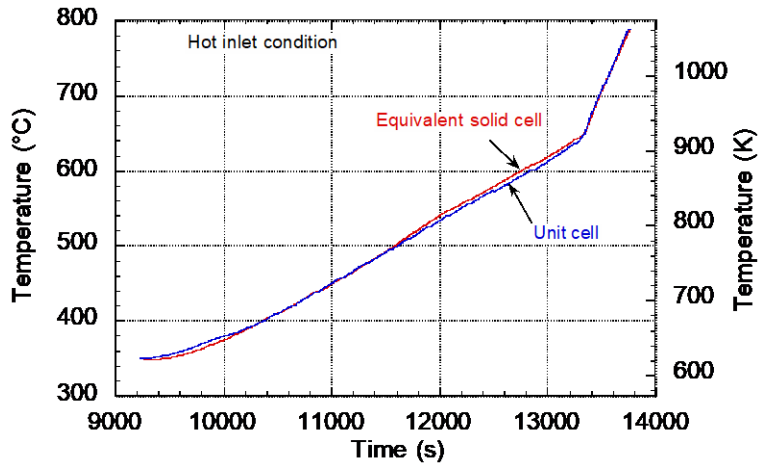


Figure 10-8 Time Variation of the Maximum Temperatures in the Unit Cell and the Equivalent Solid Cell Subjected to Hot Inlet Conditions

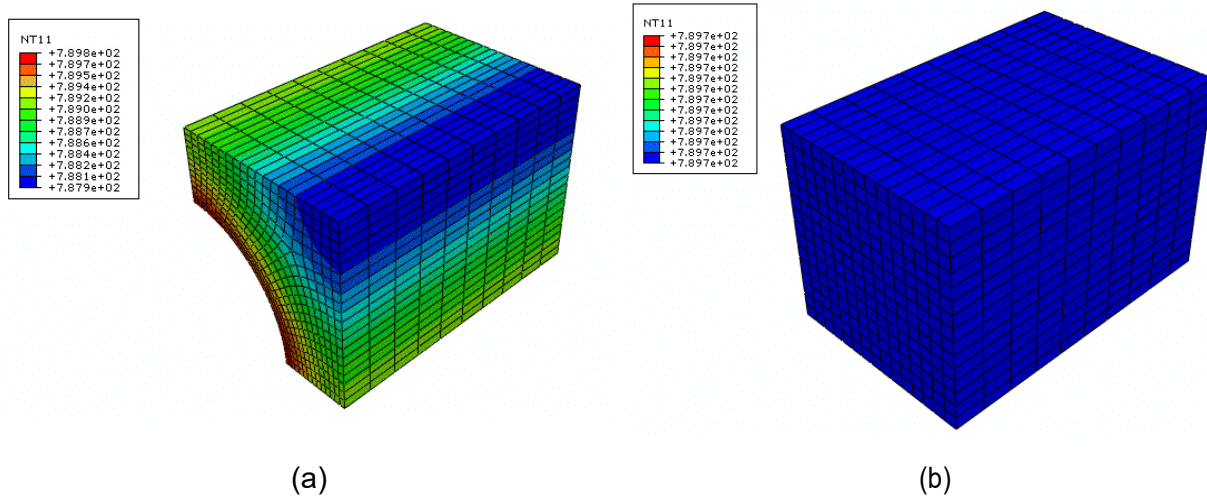


Figure 10-9 Temperature Distribution (In °C) at 13,760 S in (a) Tubesheet Unit Cell Subjected to HTC and Gas Temperature Corresponding to Hot Inlet Condition and (b) Tubesheet Equivalent Solid Cell Subjected to Equivalent Volumetric Heating Rate

For the rest of the components (i.e., lower head, divider plate and SG shell), the HTC and gas temperature data calculated by RELAP 5 were used. The exterior surfaces of the lower head and the SG shell were subjected to ambient conditions.

10.1.3 Thermal Analysis of Tube-to-Tubesheet Junction

10.1.3.1 Tube Located in the Hot Inlet Quadrant

Typical temperature distributions in the lower head inside surface and the tubesheet lower surface are shown in Figs 10-10, respectively. The temperature variations at two different times along the radial path identified in Fig. 10-12 are plotted in Fig. 10-12. The solid rim because of its mass and lack of volumetric heating stays cool throughout the severe accident transient. The tube temperature is slightly higher than the tubesheet temperature during the early period of the transient (≤ 12966 s). However, the tube temperature lags behind the temperature of the tubesheet at ≥ 13505 s.

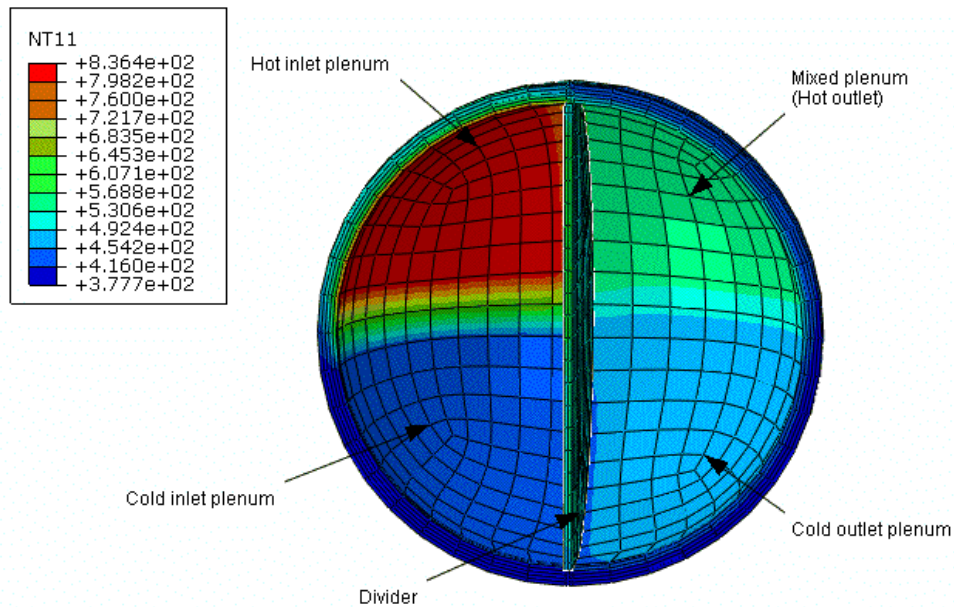


Figure 10-10 Temperature Distribution at the Inside Surface of the Lower Head of a Model 51 SG at Time $t=13,760$ s

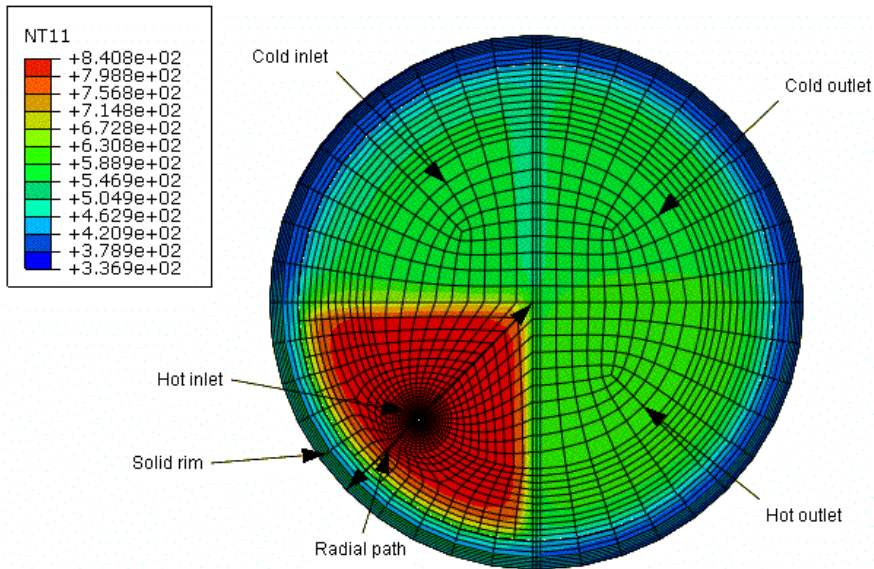


Figure 10-11 Temperature Distribution at the Bottom Surface of a Model 51 Tubesheet at 13,760 S (The line with the arrowheads represent the radial path along which the temperatures in Fig. 10-12 are plotted)

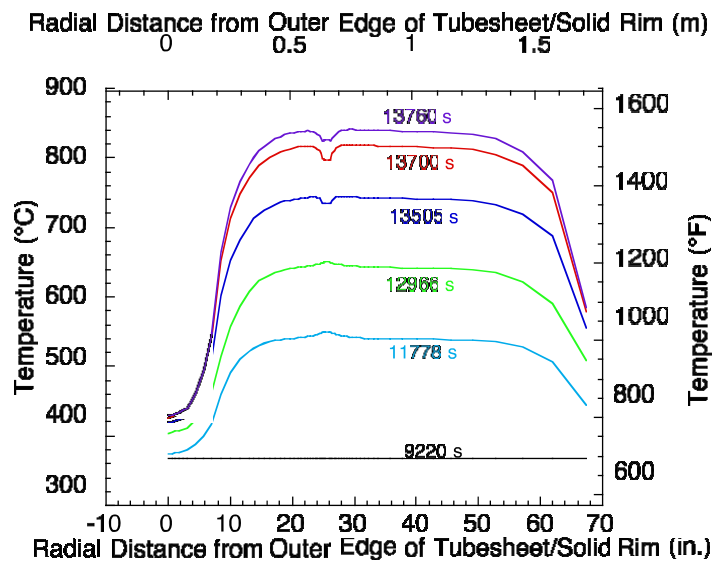


Figure 10-12 Temperature Distribution in the Solid Rim, Tubesheet and Tube Wall along the Radial Path through the Hot Region of the Tubesheet Bottom Surface Shown in Fig. 10-11 during the Severe Accident

10.1.3.2 Hottest Tube Temperature

The axial temperature distribution in the hottest tube is plotted in Fig. 10-13 as a function of time. The exposed portion of the tube ($z > 533$ mm [21 in.]) above the top of tubesheet is typically (except at 13,700 s) about 50°C hotter than the tube within the tubesheet.

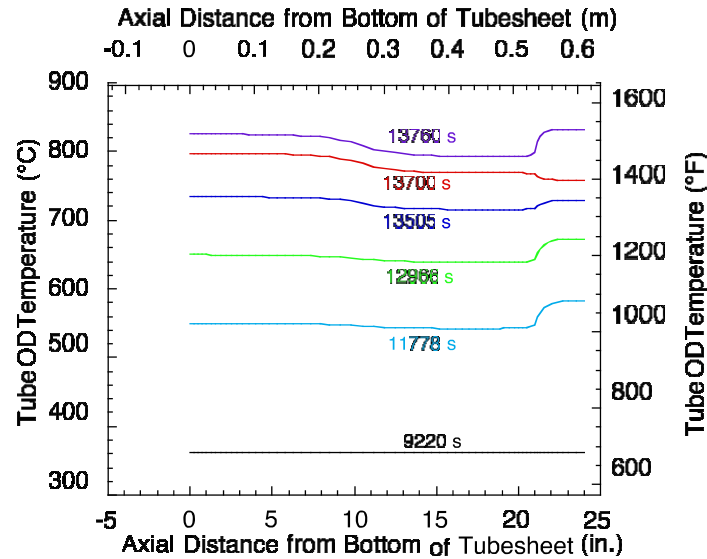


Figure 10-13 Axial Temperature Distribution in the Tube at Various Times

The temperature ramp rate of the hottest tube and the gas inside the hottest tube in the Model 51 SG are plotted in Fig. 10-14. Although the hottest tube temperature lags behind the gas temperature by 250°C , the temperature ramp rates of the gas and the metal are approximately the same. Our tube-to-collar leak tests were conducted with a ramp rate of $5^{\circ}\text{C}/\text{min}$, which is the same as that of the tube inside the tubesheet in the range of 500 - 650°C . The ramp rate in the tests did not represent the predicted higher ramp rate at $>650^{\circ}\text{C}$, and the effect of the difference in ramp rate has to be accounted for by analyses.

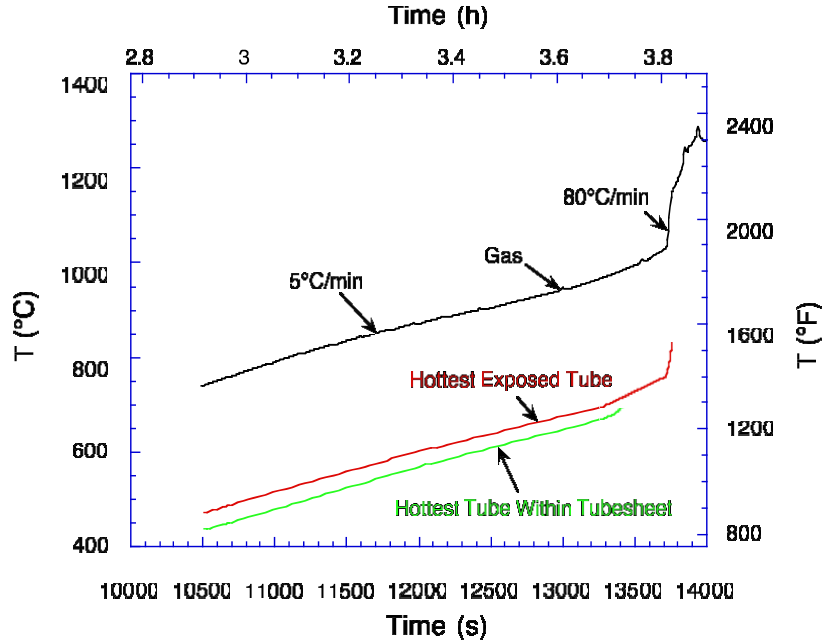


Figure 10-14 Comparison of Temperature Histories of the Gas Inside the Hottest Tube, Hottest Tube (ID) within the Tubesheet and Exposed Part of the Hottest Tube (ID)

10.2 Contact Pressure Analysis

10.2.1 Development of Creep Properties of Tubesheet

The built-in equation for the creep strain rate in the finite-element program ABAQUS can be either in the time-hardening form, i.e.,

$$\dot{\epsilon}_c = A\sigma^n t^m \quad (42a)$$

or in the strain-hardening form, i.e.,

$$\dot{\epsilon}_c = \left(A\sigma^n [(m+1)\epsilon_c]^m \right)^{1/(m+1)}, \quad (42b)$$

where A, n, and m are functions of temperature, σ is stress, ϵ_c is creep strain, $\dot{\epsilon}_c$ is creep strain rate, and t is time.

ABAQUS allows anisotropic creep properties using Hill's standard function similar to the anisotropic plasticity case.

$$q(\sigma) = \sqrt{F(\sigma_r - \sigma_\theta)^2 + G(\sigma_z - \sigma_r)^2 + H(\sigma_\theta - \sigma_z)^2 + 2L\sigma_{r\theta}^2 + 2M\sigma_{rz}^2 + 2N\sigma_{z\theta}^2} \quad (43)$$

where

$$F = \frac{(q)^2}{2} \left[\frac{1}{\sigma_r^2} + \frac{1}{\sigma_\theta^2} - \frac{1}{\sigma_z^2} \right] = \frac{1}{2} \left[\frac{1}{R_{11}^2} + \frac{1}{R_{33}^2} - \frac{1}{R_{22}^2} \right], \quad (44a)$$

$$G = \frac{(q)^2}{2} \left[\frac{1}{\sigma_r^2} + \frac{1}{\sigma_z^2} - \frac{1}{\sigma_\theta^2} \right] = \frac{1}{2} \left[\frac{1}{R_{11}^2} + \frac{1}{R_{22}^2} - \frac{1}{R_{33}^2} \right], \quad (44b)$$

$$H = \frac{(q)^2}{2} \left[\frac{1}{\sigma_z^2} + \frac{1}{\sigma_\theta^2} - \frac{1}{\sigma_r^2} \right] = \frac{1}{2} \left[\frac{1}{R_{22}^2} + \frac{1}{R_{33}^2} - \frac{1}{R_{11}^2} \right]. \quad (44c)$$

$$L = \frac{3}{2} \left(\frac{r}{\sigma_{r\theta}} \right)^2 = \frac{3}{2R_{13}^2} \quad (44d)$$

$$M = \frac{3}{2} \left(\frac{r}{\sigma_{rz}} \right)^2 = \frac{3}{2R_{12}^2} \quad (44e)$$

$$N = \frac{3}{2} \left(\frac{r}{\sigma_{z\theta}} \right)^2 = \frac{3}{2R_{23}^2} \quad (44f)$$

with σ_r , σ_θ , σ_z , $\sigma_{r\theta}$, $\sigma_{z\theta}$, and σ_{rz} = normal stresses in the r (radial), θ (hoop), z (thickness) directions, and shear stresses in the $r\theta$, $z\theta$, and rz planes respectively. q and r are reference normal and shear stresses, with $r = q / \sqrt{3}$. The anisotropic creep stress ratios are defined as follows

$$R_{11} = \frac{\sigma_r}{q} \quad (45a)$$

$$R_{22} = \frac{\sigma_z}{q} \quad (45b)$$

$$R_{33} = \frac{\sigma_\theta}{q} \quad (45c)$$

$$R_{12} = \frac{\sigma_{rz}}{r} \quad (45d)$$

$$R_{13} = \frac{\sigma_{r\theta}}{r} \quad (45e)$$

and

$$R_{23} = \frac{\sigma_{z\theta}}{r} \quad (45f).$$

In ABAQUS, the reference creep rate curves (i.e., A, m and n) and the anisotropic creep stress ratios R_{ij} are input as functions of temperature. For transversely isotropic materials, such as a tubesheet with square hole array, $A_r = A_\theta$, and $A_{rz} = A_{z\theta}$, or equivalently $R_{11} = R_{33}$, $R_{12} = R_{13}$. Note that a basic assumption in ABAQUS is that the anisotropic creep stress ratios R_{ij} are constants at any given temperature and do not vary with plastic strain. For isotropic materials (like A 508), all the R_{ij} s = 1.

Similar to the analysis performed for the tube-collar specimens, the available literature creep rate data for A508 steel at high temperatures were fitted to the following equation

$$\dot{\epsilon}_c = B \exp\left(-\frac{Q}{T}\right) \sigma^n t^m \quad (46)$$

where $B=1 \times 10^{18}$, $n=5.1686$, $Q=55,991$, and $m=0$ with creep rate in 1/s, stress in ksi, time in s and temperature in K. Comparing Eqs (46) and (42a), $A = B \exp\left(-\frac{Q}{T}\right)$.

The effective creep rate for the tubesheet were determined by applying given loads to the opposite faces of the unit cell, conducting FEAs to determine the displacement rates, and calculating the stresses and the creep strains as functions of time. The calculations were repeated for various temperatures and applied loads. The resulting creep curves could be fitted by Eq. 42a, with $m=0$ and $n=5.1686$ and values of A that depended on the unit cell geometry and temperature.

The calculated in-plane and transverse creep rate coefficients (A) for the tubesheet with 23 mm (0.891 in.) diameter holes (pitch=33 mm [1.28 in.]) and 19 mm (0.765 in.) diameter holes (pitch=27 mm [1.07 in.]) arranged in square arrays are plotted in Figs 10-15a-b, respectively. A comparison with the parent SA508 creep rate coefficient A shows that the tubesheet resistance to creep deformation is significantly reduced by the presence of the holes, more so in the in-plane than in the transverse direction.

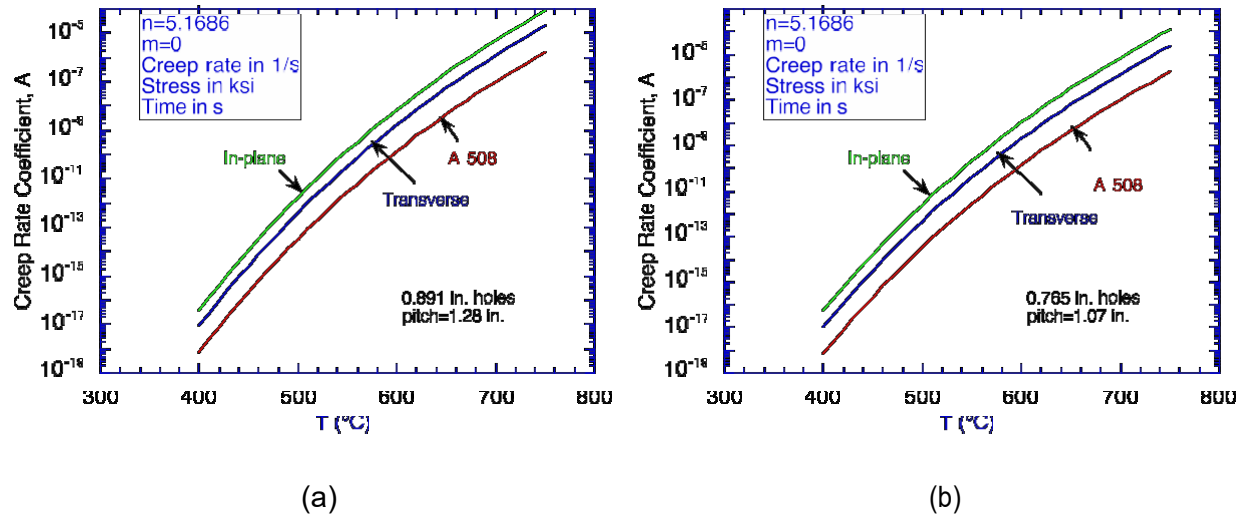


Figure 10-15 Variation of Creep Rate Coefficient A with Temperature for Tubesheets with (a) 23 mm (0.891 in.) Diam. Holes at a Pitch of 33 mm (1.28 in.) and (b) 19 mm (0.765 in.) Diam. Holes at a Pitch of 27 mm (1.07 in.) (Parameter units are as labelled)

10.2.2 Results from FEA

The thermal analysis results for the hot tube of Model 51 were incorporated into the structural analysis FEM. The analysis included elastic, plastic, and creep deformation of all the components. The pressure loading included the tube internal pressure (16.2 MPa (2.35 ksi)), lower head internal pressure and an upward pressure (16.2 MPa (2.35 ksi)) acting on the lower surface of the tubesheet. Because the secondary side of the SG is assumed to depressurize during the accident, the shell side internal pressure acting on the tubesheet is equal to zero. The hydraulic expansion pressure for the 22 mm (0.875 in.) diameter tube is 234 MPa (34 ksi). The mechanical properties of the tubesheet material (A508) were obtained from the literature. The mechanical properties of the Alloy 600 heat EX-82-1 were used for the SG tube. The thermal expansion coefficients for both materials were obtained from the ASME Code, Section II.

As noted earlier, the tubesheet bowing has an important effect on the contact pressure distribution during accidents that involve depressurization of the secondary side, such as MSLB. The bending deformation of the tubesheet during such accidents is approximately axisymmetric, as shown in Fig. 10-16. However, during the high temperatures excursion of severe accidents when creep deformation becomes significant, the hot quadrant of the tubesheet undergoes an additional local bending deformation, as shown in Figs. 10-17a-b. This local deformation creates additional bending of the SG tube, which results in a non-axisymmetric variation of contact pressure at the tube-to-tubesheet interface. Such non-axisymmetric distributions of contact pressure are not present to any appreciable extent in our tube-to-collar junction test specimens.

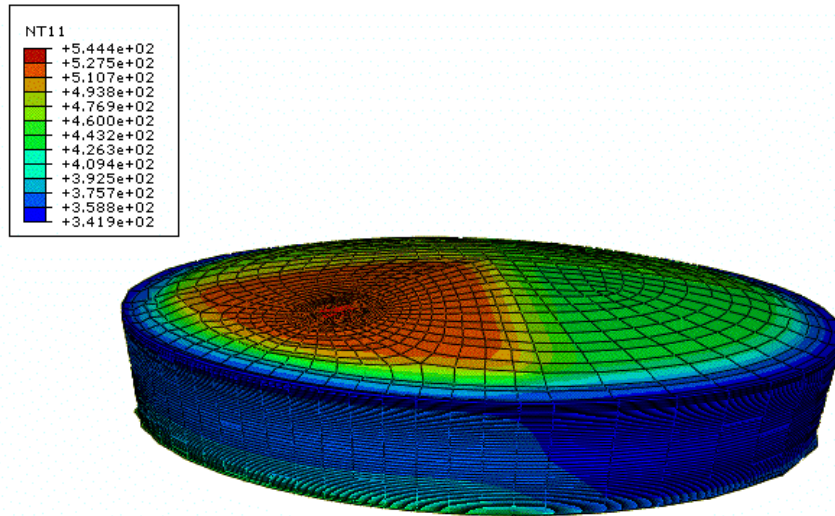


Figure 10-16 Deformation of the Top Surface of the Tubesheet at 11,700 s

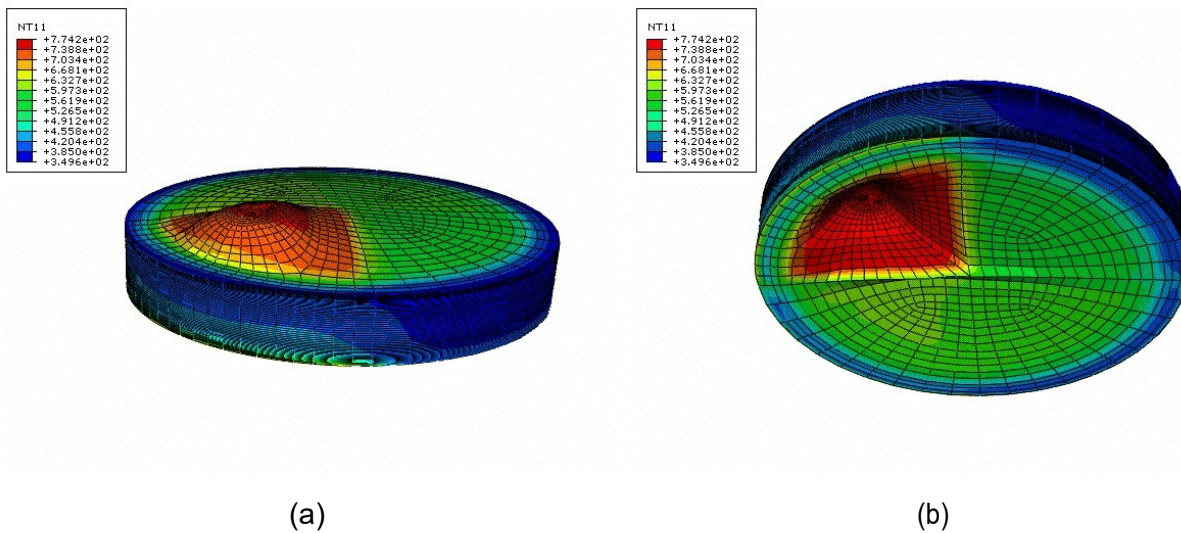


Figure 10-17 Tubesheet Deformation at 13,590 s at the (a) Top and (b) Bottom Surfaces, Showing Enhanced Deformation in the Hot Inlet Zone Due to Creep

Our experience with tube-to-collar tests has shown that in order to get large leakages during severe accidents, the crevice at the tube-to-tubesheet interface needs to be pressurized so that the collar creeps away from the tube. Although the crevices of most of our tube-to-collar specimens were pressurized independently, a non-prototypical situation, pressurization will occur in tubes with through-wall cracks. As discussed in Section 7.6.5, to demonstrate that

external pressurization of the crevice is not necessary to get large leaks, in specimen 02-7/8 it was deliberately chosen not to pressurize the crevice independently (i.e., the crevice pressure inlet was sealed off) but instead had a 0.8 mm (0.03125 in.) diameter hole drilled in the tube wall to determine whether the gas leaking through the drilled hole was sufficient to pressurize the crevice. This test behaved essentially in the same fashion as the tests in which the crevice was independently pressurized to the same level as the tube. Therefore, it is very likely that if the tube in a SG in the field has a through-wall crack within the tubesheet region, the crevice region will be pressurized. Therefore, crevice pressures were included to act on the tube outer diameter surface and the tube hole surface within the tubesheet to simulate leakage from a crack situated at the mid thickness level of the tubesheet.

10.2.2.1 Tube Without Crack (Unpressurized Crevice)

At design basis accident temperatures, the contact pressure is a function of the hydraulic expansion pressure, the internal pressure, and the temperature. Early in the event, the leak rates are relatively small and depend on the contact pressure and the roughness of the machined surfaces of the tube sheet and the tube. As the temperature rises with time, the contact pressure profile changes because of creep and changes in the relative thermal expansion coefficients between the tube and the tubesheet. The analyses focus on the time after 9173 s when the liquid is boiled off, only steam and hydrogen are flowing through the SG tubes, and the temperatures begin to rise significantly above those associated with design basis conditions (350°C). The contact pressure initially increases from that at 9220 s due to the thermal expansion mismatch between the tube and tubesheet. Beyond a certain time, the contact pressure decreases because of the relaxation effect of creep of both the tubesheet and the tube. Also, the time-dependent bowing of the tubesheet, which experiences bending creep deformation due to the primary pressure acting on it, causes the contact pressures to vary. However, if there is no leaking crack, the annulus is not pressurized by the primary coolant, the component of the contact pressure due to tube internal pressure at the tubesheet midplane (where tubesheet bowing effect is minimum) is maintained at all times. But, in the upper half of the tube-to-tubesheet interface, the contact pressure can be reduced further due to tubesheet bowing effect.

Axial variations of the contact pressure along four azimuthally located paths (paths 1-4) on the tube OD surface are plotted in Fig. 10-18a. Note that path 1 is situated at $\theta=0^\circ$, path 2 at $\theta=90^\circ$, path 3 at $\theta=180^\circ$, and path 4 at $\theta=270^\circ$. The plane defined by axial paths 1 and 3 passes through the center of the tubesheet. The variations of contact pressure with time at the tubesheet midplane at four circumferential locations on the tube OD surface are plotted in Fig. 10-18b. Initially, the contact pressure increases with time because of thermal expansion mismatch, reaching a maximum at $t=11,038\text{s}$, beyond which creep becomes significant and the contact pressure is reduced. However, Fig. 10-18a shows that the contact pressure remains positive along the entire tube surface until about time $t=13760\text{ s}$ when the top 25 mm (1 in.) of the interface has lost contact and the crevice opens up. The circumferential variation of contact pressure at the tubesheet mid plane, plotted in Fig 10-9a, is uniform until creep becomes significant, at which time the contact pressure distribution becomes sinusoidal, suggesting slight ovalization of the tube. A highly magnified view of the deformed tube cross-section shows the ovalized tube (Fig. 10-19b). The axial variations of the crevice opening displacement along four azimuthally located paths (paths 1-4) and circumferential variation of crevice opening displacement at the top of the tubesheet at various times are plotted in Figs. 10-20a-b, respectively, showing that non-zero crevice opening occurs for times $\geq 13445\text{ s}$. Both the maximum crevice opening displacement and the length of the loss of contact zone increase with time until the maximum crevice opening displacement attains a value of 0.48 mm (0.019 in.) and

the length over which contact is lost reaches a value of 51 mm (2 in.) at $t=13760$ s. Fig. 10-20b shows that there is a significant circumferential variation in the crevice opening displacement, suggesting that the ovality of the tube cross-section is maintained even in the non-contacting region of the crevice.

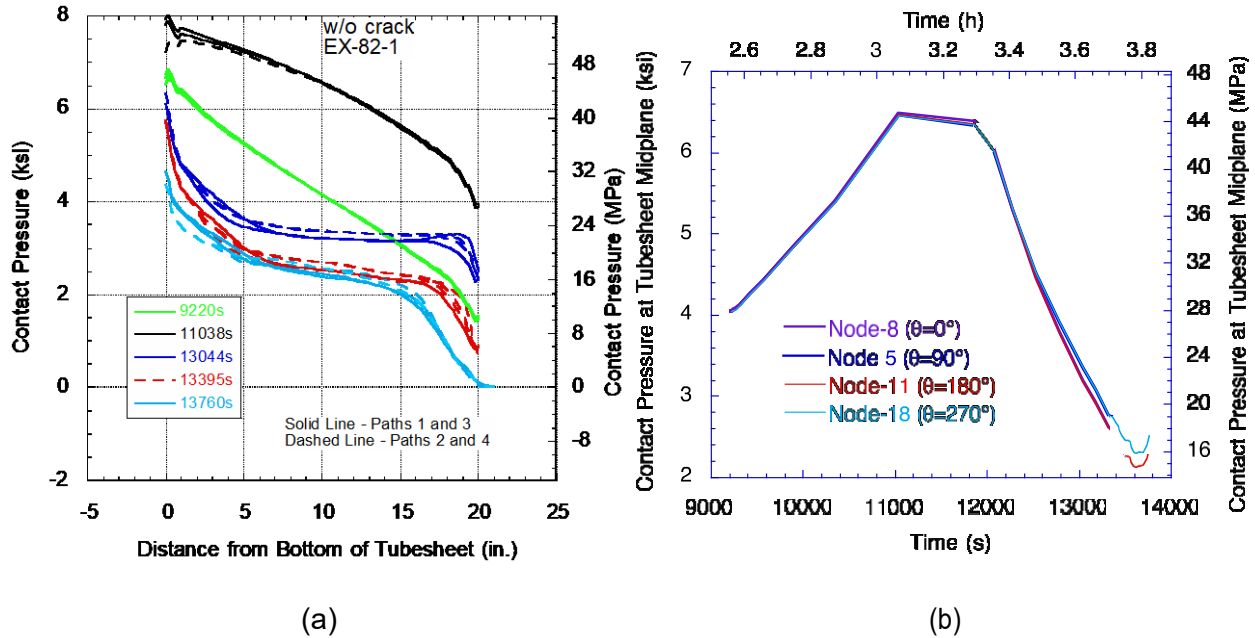


Figure 10-18 Variations of Contact Pressure (a) Along Four Axial Paths at Various Times and (b) With Time at Four Circumferential Locations at the Tubesheet Midplane during the Severe Accident (Crevice pressure = 0)

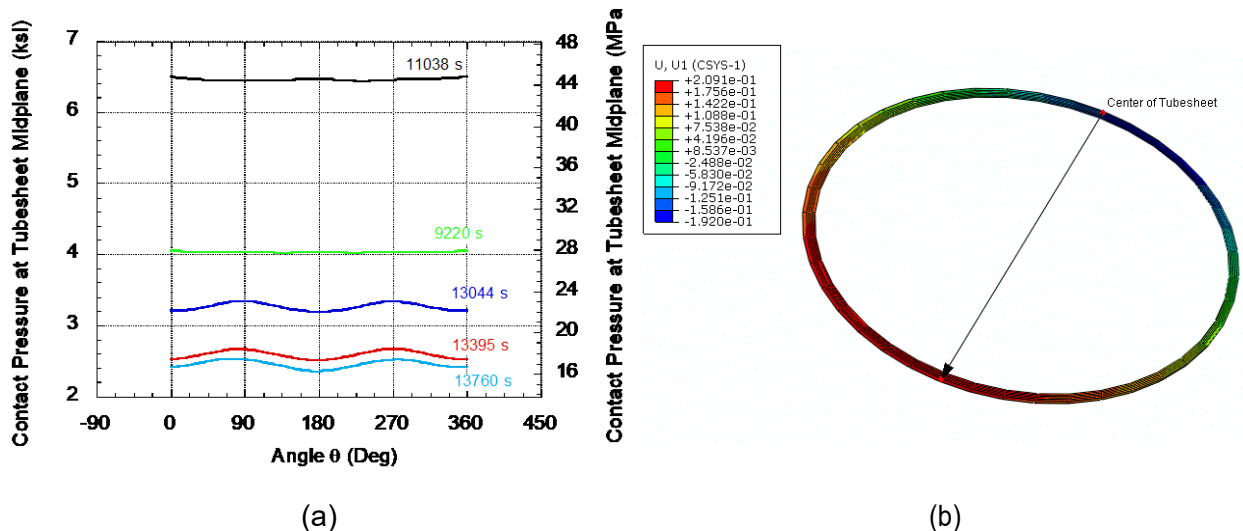


Figure 10-19 (a) Circumferential Variations of the Contact Pressure at the Tubesheet Mid Plane at Various Times during the Severe Accident and (b) Highly Magnified Deformed Tube Cross-section at the Tubesheet Mid Plane at $t=13760$ s (The arrow points toward the center of the tubesheet)

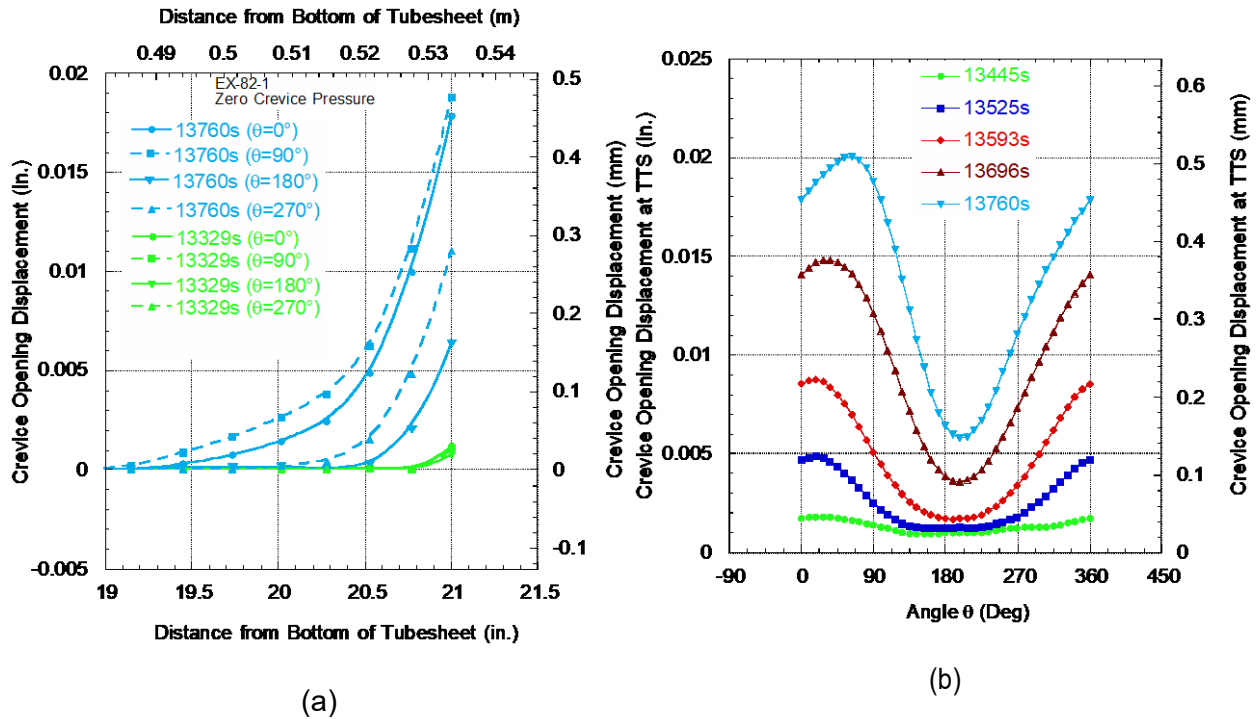


Figure 10-20 (a) Axial Variation of Crevice Opening Displacement along Four Paths at Two Times and (b) Circumferential Variation of Crevice Opening Displacement at the Top of Tubesheet at Various Times during the Severe Accident (Crevice Pressure = 0)

The variations of the crevice opening displacements with time at the top of tubesheet at four circumferential locations are plotted in Fig. 10-21, which shows that the crevice opening displacements begin to increase at a rapid rate at 13400s.

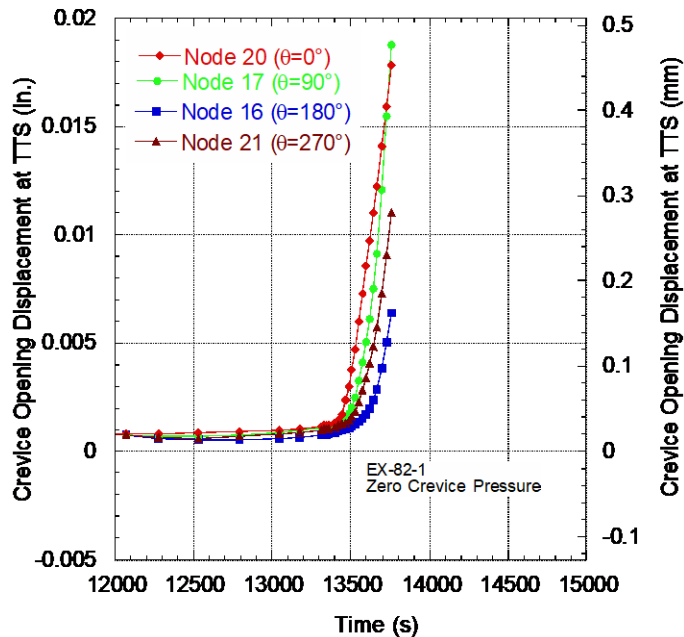


Figure 10-21 Time Variations of Crevice Opening Displacements at Four Circumferential Locations at the Top of Tubesheet (Crevice pressure = 0)

10.2.2.2 Tube with a TW Circumferential Crack at the Mid Plane (Pressurized Crevice)

Ideally, the pressure distribution in the crevice is approximately uniform as long as the contact pressure between the tube/tubesheet is positive and parabolic when a physical gap is opened at the interface (Section 8.2.2). However, instead of attempting to compute the transition of the crevice pressure distribution from uniform to parabolic in a single analysis, two limiting crevice pressure distributions were considered – a uniform pressure distribution and a parabolic pressure distribution. In Section 9.3.2, it was reported that the uniform crevice pressure distribution would provide an upper bound to the crevice opening displacements and thus an upper bound to the leak rate. The parabolic pressure distribution is used here as a reference case and the leak rate based on it may not necessarily provide a lower bound.

Uniform Crevice Pressure

Axial variations of the contact pressure along four azimuthally located paths (paths 1-4) on the tube OD surface are plotted in Fig. 10-22a. The variations of contact pressure with time at the tubesheet midplane at four circumferential locations on the tube OD surface are plotted in Fig. 10-22b. Initially, the contact pressure increases with time because of thermal expansion mismatch, reaching a maximum at $t=11,500$ s, beyond which creep becomes significant and the contact pressure is reduced. Figure 10-22a shows that the contact pressure remains positive along the entire tube surface until about time $t=13,267$ s, beyond which an increasing portion of the interface at the top loses contact and the crevice opens up. Note that the magnitude of the contact pressure is lower than when the crevice is unpressurized (cf. Figs. 10-18a-b). As a result, the time at which the top of tubesheet loses contact is earlier than when the crevice is unpressurized. The circumferential variation of contact pressure at the tubesheet mid plane, plotted in Fig. 10-23, is uniform until creep becomes significant, at which time the contact

pressure distribution becomes slightly sinusoidal (not resolvable at the magnification of Fig.10-23), suggesting slight ovalization of the tube. The axial variations of the crevice opening displacement along four azimuthally located paths (paths 1-4) and circumferential variation of crevice opening displacement at the top of the tubesheet at various times are plotted in Figs. 10-24a-b, respectively, showing that non-zero crevice opening occurs for times $\geq 13,267$ s. Both the maximum crevice opening displacement and the length of the loss of contact zone increase with time until the maximum crevice opening displacement attains a value of 2.15 mm (0.085 in.) and the length over which contact is lost reaches a value of 102 mm (4 in.) at $t=13760$ s. Fig. 10-24b shows that there is a significant circumferential variation in the crevice opening displacement, suggesting that the ovality of the tube cross-section is maintained even in the non-contacting region of the crevice.

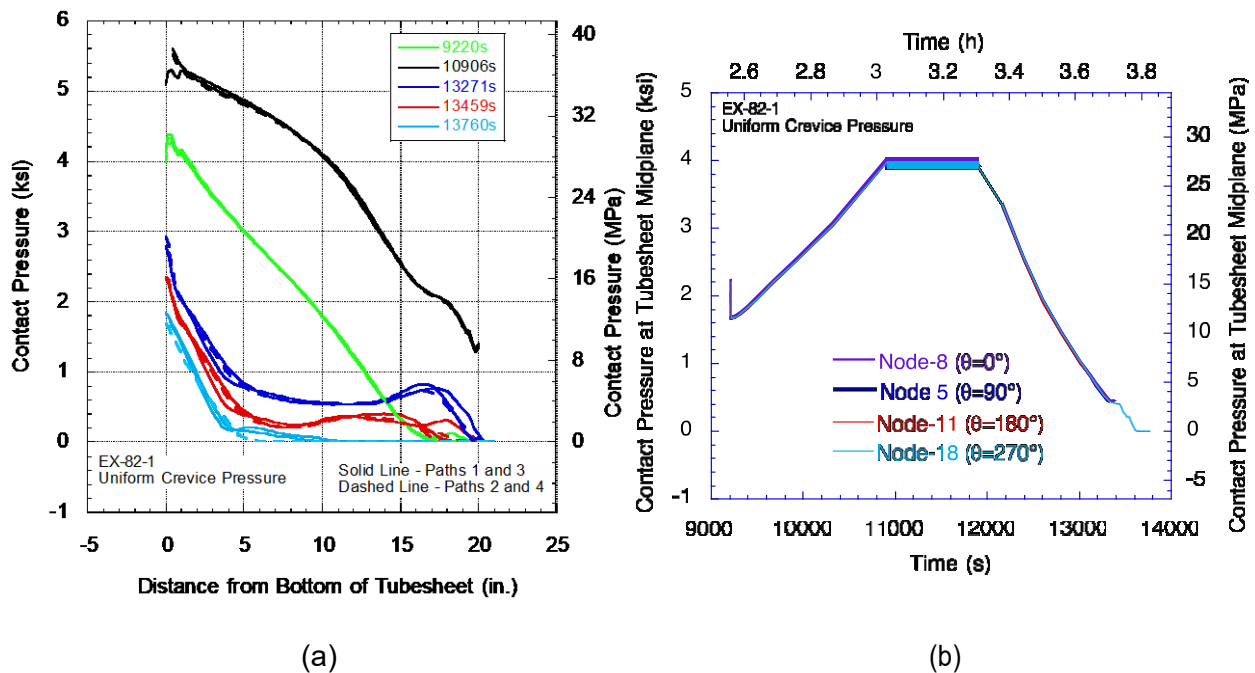


Figure 10-22 Variations of Contact Pressure (a) Along Four Axial Paths at Various Times and (b) With Time at Four Circumferential Locations at the Tubesheet Midplane during the Severe Accident [Uniform crevice pressure = 16.2 MPa (2.35 ksi)]

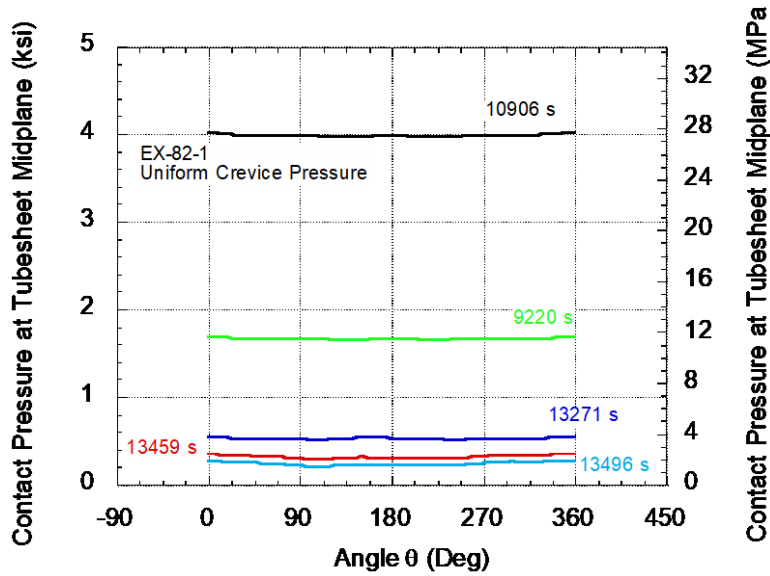


Figure 10-23 Circumferential Variations of the Contact Pressure at the Tubesheet Mid Plane at Various Times during the Severe Accident [Uniform crevice pressure = 16.2 MPa (2.35 ksi)]

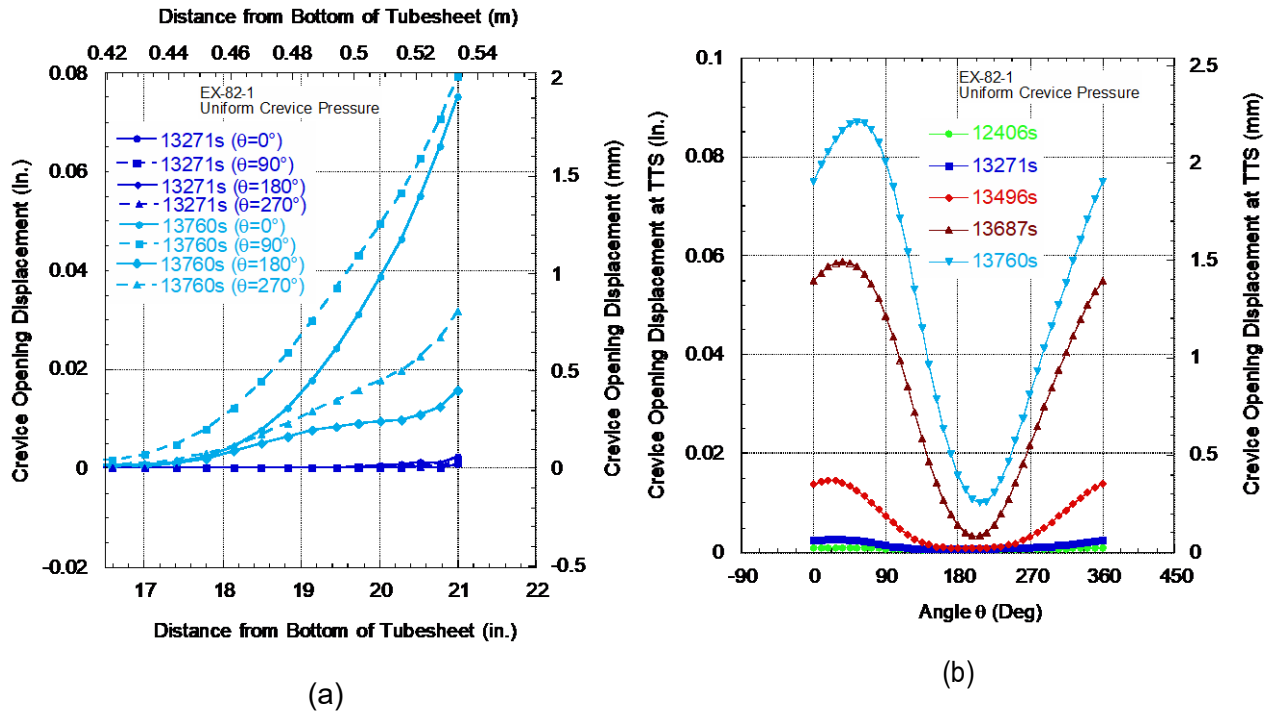


Figure 10-24 (a) Axial Variation of Crevice Opening Displacement Along Four Paths at Two Times and (b) Circumferential Variation of Crevice Opening Displacement at the Top of Tubesheet at Various Times during the Severe Accident [Uniform crevice pressure = 16.2 MPa (2.35 ksi)]

The variations of the crevice opening displacements with time at the top of tubesheet at four circumferential locations are plotted in Fig. 10-25, which shows that the crevice opening displacements begin to increase at a rapid rate at 13,200s. As expected, the crevice opening displacements are higher than when the crevice is unpressurized (cf. Fig. 10-21).

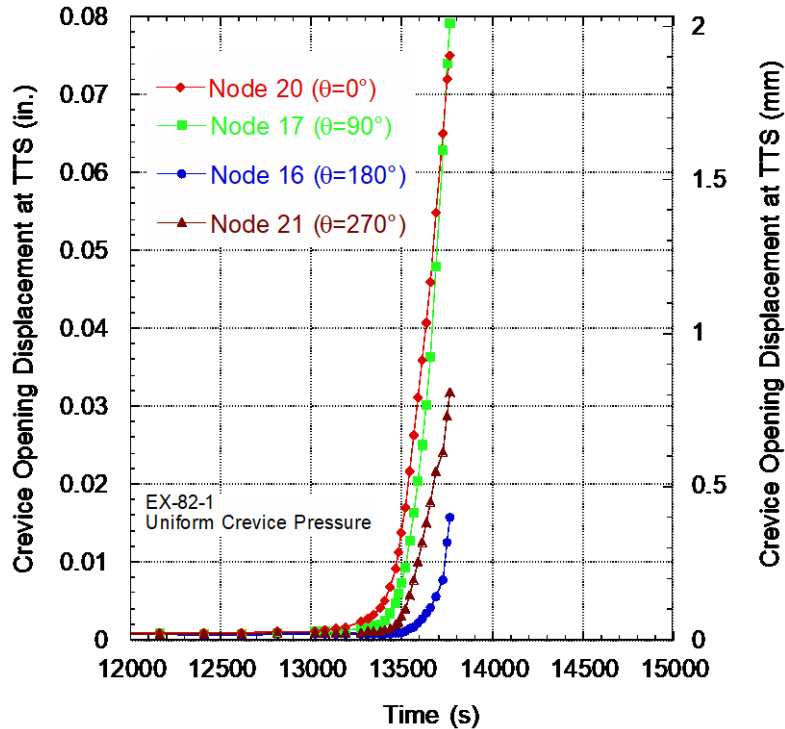


Figure 10-25 Time Variations of Crevice Opening Displacements at Four Circumferential Locations at the Top of Tubesheet [Crevice pressure = 16.2 MPa (2.35 ksi)]

Parabolic Crevice Pressure

Axial variations of the contact pressure along four parallel azimuthally located paths (paths 1-4) on the tube OD surface are plotted in Fig. 10-26a. The variations of contact pressure with time at the tubesheet midplane at four circumferential locations on the tube OD surface are plotted in Fig. 10-26b. Initially, the contact pressure increases with time because of thermal expansion mismatch, reaching a maximum at $t=12,000$ s, beyond which creep becomes significant and the contact pressure is reduced. Figure 10-26a shows that the contact pressure remains positive along the entire tube surface until about time $t=13,467$ s, beyond which an increasing portion of the interface at the top loses contact and the crevice opens up. Note that the magnitude of the contact pressure is lower than when the crevice is unpressurized (cf. Figs.10-18a-b). As a result, the time at which the top of tubesheet loses contact is shorter than when the crevice is unpressurized. The circumferential variation of contact pressure at the tubesheet mid plane, plotted in Fig 10-27, is uniform until creep becomes significant, at which time the contact pressure distribution becomes slightly sinusoidal (not resolvable at the magnification of Fig. 10-27), suggesting slight ovalization of the tube. The axial variations of the crevice opening displacement along four parallel azimuthally located paths (paths 1-4) and circumferential variation of crevice opening displacement at the top of the tubesheet at various times are plotted

in Figs. 10-25a-b, respectively, showing that non-zero crevice opening occurs for times $t \geq 13,467$ s. Both the maximum crevice opening displacement and the length of the loss of contact zone increase with time until the maximum crevice opening displacement attains a value of 0.76 mm (0.03125 in.) and the length over which contact is lost reaches a value of 102 mm (4 in.) at $t=13,760$ s. Fig. 10-28b shows that there is a significant circumferential variation in the crevice opening displacement, suggesting that ovality of the tube cross-section is maintained even in the non-contacting region of the crevice.

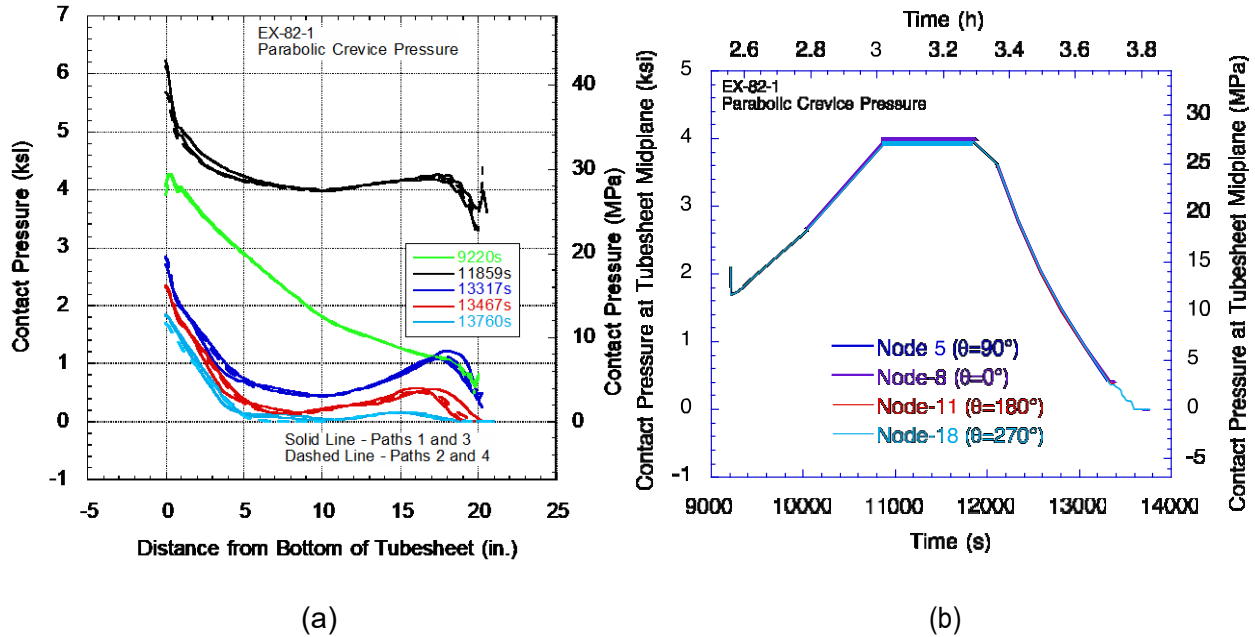


Figure 10-26 Variations of Contact Pressure (a) Along Four Axial Paths at Various Times and (b) With Time at Four Circumferential Locations at the Tubesheet Midplane during the Severe Accident [Parabolic crevice pressure distribution with maximum crevice pressure = 16.2 MPa (2.35 ksi)]

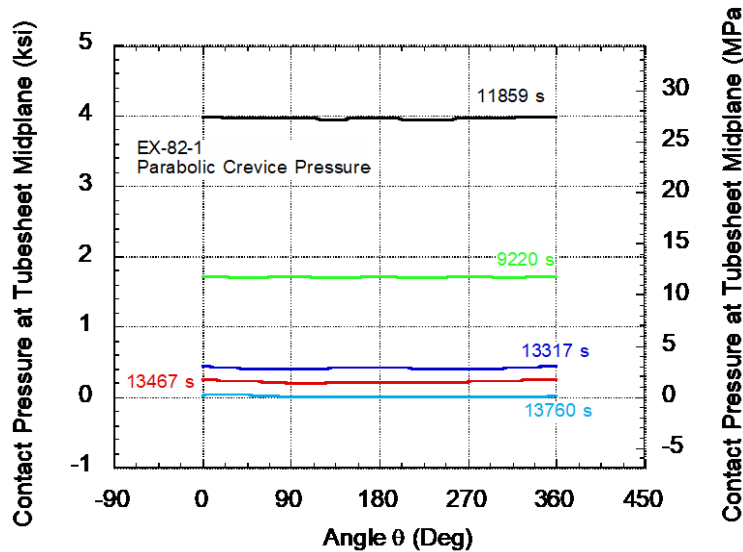


Figure 10-27 Circumferential Variations of the Contact Pressure at the Tubesheet Mid Plane at Various Times during the Severe Accident [Parabolic crevice pressure distribution with maximum crevice pressure = 16.2 MPa (2.35 ksi)]

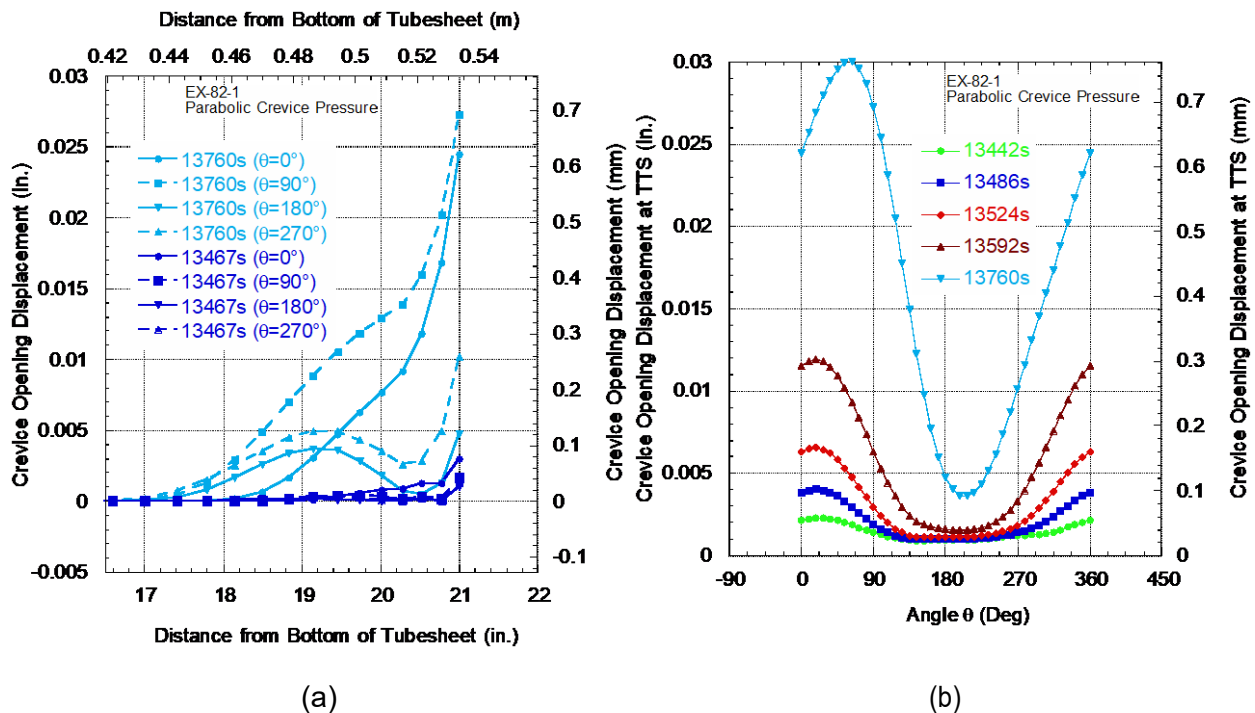


Figure 10-28 (a) Axial Variation of Crevice Opening Displacement Along Four Paths at Two Times and (b) Circumferential Variation of Crevice Opening Displacement at the Top of Tubesheet at Various Times during the Severe Accident [Parabolic crevice pressure distribution with maximum crevice pressure = 16.2 MPa (2.35 ksi)]

The variations of the crevice opening displacements with time at the top of tubesheet at four circumferential locations are plotted in Fig. 10-29, which shows that the crevice opening displacements begin to increase at a rapid rate at time $t \geq 13300$ s. As expected, the crevice opening displacements are higher than when the crevice is unpressurized (cf. Fig. 10-21) but smaller than when the crevice is uniformly pressurized (cf. Fig. 10-25)

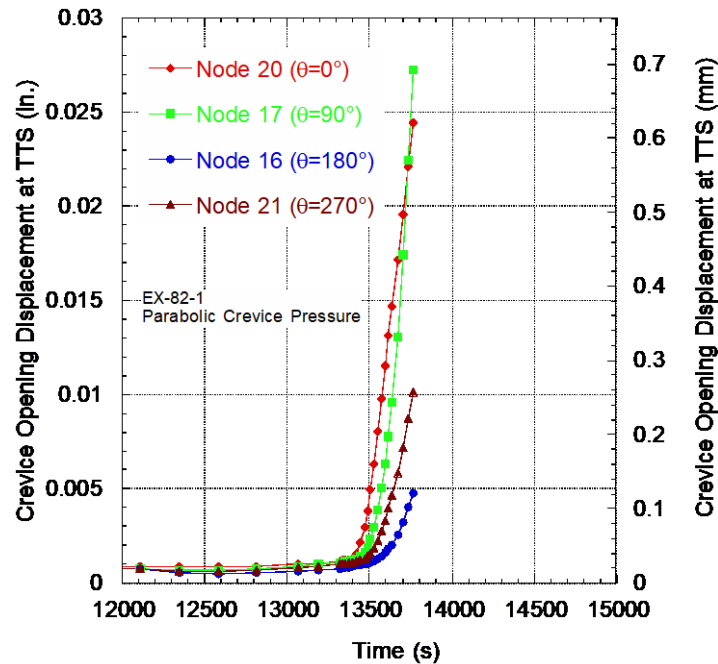


Figure 10-29 Time Variations of Crevice Opening Displacements at Four Circumferential Locations at the Top of Tubesheet [Parabolic crevice pressure distribution with maximum crevice pressure = 16.2 MPa (2.35 ksi)]

10.3 Leak Rate Prediction for Severe Accident

10.3.1 Leak Rate Model

As stated before, it was assumed that a full 360° TW circumferential crack is located at the mid plane of the tubesheet. Also, it can be assumed that the rate at which the gas pressure distribution in the crevice equilibrates is faster than the rate at which the contact pressure (or gap) distribution changes due to creep. The basic leak rate equation for single-phase (superheated steam) flow, which is Eq. (5) from Section 5.2, can be specialized for the current conditions as Eq. (47).

$$q(t) = -\frac{1}{K} \frac{\rho(p_f)}{\mu} \frac{\partial p_f}{\partial z} \quad (47)$$

where, in general, the loss coefficient K , dependent on the contact pressure, is a function of time t , axial location z (axial distance measured from the crack location through the tubesheet thickness). The density ρ and dynamic viscosity μ , both of which are in general functions of the pressure p_f and temperature of the gas in the crevice, are, therefore, also functions of t and z . The correlations for density and dynamic viscosity of superheated steam as functions of

pressure and temperature were obtained from Ref. 11. At any time t , integration of Eq. ((47)) gives the following equation for mass flow rate $q(t)$

$$q(t) = \frac{\Delta p_f}{\int_0^L \frac{\mu(z)}{\rho(z)} K(z) dz} \quad (48)$$

where Δp_f is the inlet to outlet pressure drop in the crevice gas. To obtain the crevice pressure distribution along the length, the continuity requires the mass flow to be constant along the crevice length and the crevice pressure distribution is given by

$$p_1 - p_f(t) = q(t) \int_0^z \frac{\mu(z)}{\rho(z)} K(z) dz \quad (49)$$

where p_1 is the crevice inlet pressure and the flow rate $q(t)$ is obtained from Eq. (48).

Solving Eq. (48) as rigorously as in the case of MSLB (Section 9.3) would require an iterative procedure that, using two nested loops at every time step, would be very labor intensive. Instead, leak rates were calculated by using the contact pressure (and gap) distributions that correspond to uniform and parabolic crevice pressure distributions and following a procedure analogous to that outlined in section 9.3.2. As mentioned earlier, the use of a uniform pressure distribution equal to the primary pressure to calculate the crevice opening should provide an upper bound to the leak rate.

10.3.2 Predicted Leak Rates

A further complication for predicting the leak rate for the Model 51 SG tube arises because the contact condition of the tube in the SG, in contrast to the tube-to-collar specimens, is non-axisymmetric (e.g., Figs. 10-19a and 10-20b). As a result, our leak rate model, which is based on axisymmetric contact conditions, predicts leak rates that depend on the circumferential location of the axial path. The predicted leak rates along four axial paths separated from each other by 90° in the circumferential direction as functions of time are plotted in Figs. 10-30a-b for the two different distribution of crevice pressure. There is significant variation in the predicted leak rates depending on the leakage path. In reality, the leakage flow will occur circumferentially from high flow resistance to low flow resistance regions before flowing axially. For the current work, the linear averages of the leakage rates was used as the probable leak rates and the cumulative leakages are plotted in Fig. 10-31. The curve corresponding to the uniform crevice pressure distribution should be upper bound to the true leak rate. Although the curve corresponding to parabolic crevice pressure distribution is not necessarily a lower bound to the true leak rate, our tests suggested that the crevice pressure distribution is close to parabolic when the crevice is fully open and the leak rate is high.

The leak rates and cumulative leakages reported here are our current best estimates, keeping in mind the lack of any relevant test data.

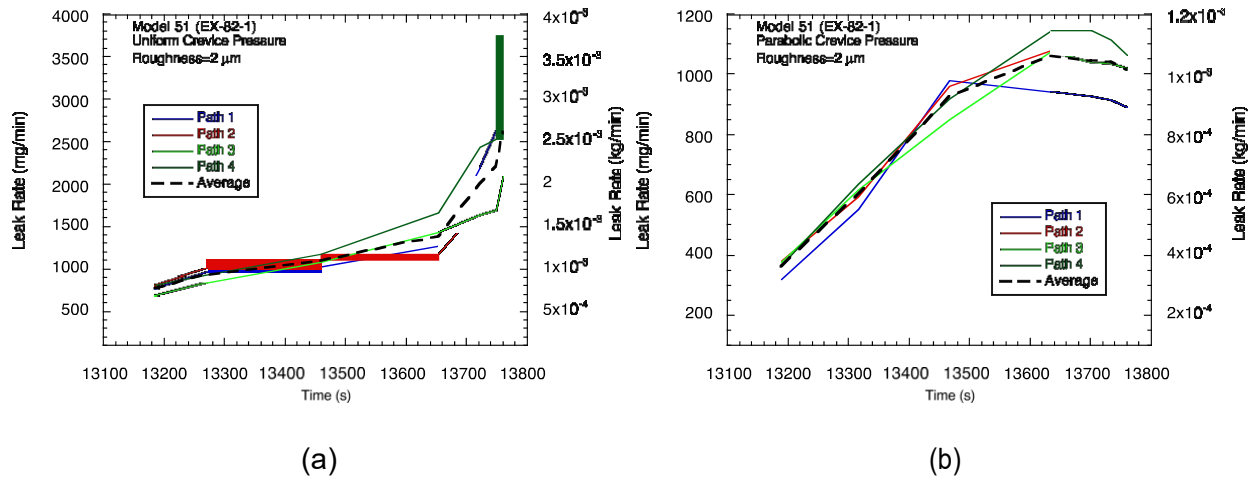


Figure 10-30 Calculated Leak Rate (using roughness= μ 2m) vs Time for Model 51 SG with (a) Uniform Crevice Pressure Distribution and (b) Parabolic Crevice Pressure Distribution Along Four Axial Paths

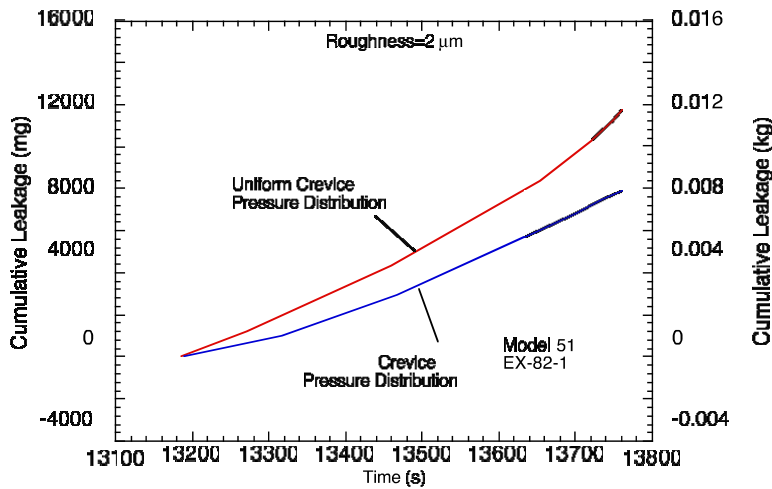


Figure 10-31 Calculated Cumulative Leakage vs Time for a Model 51 SG for Two Types of Crevice Pressure Distribution (roughness=2 μ m)

Correlation of predicted leak rate with the leak rates obtained from our tube-to-collar test specimen tests showed that the roughness parameter could vary between 2 and 5 μ m. Therefore, the leak rates were recalculated with a roughness parameter of 5 μ m. The results for leak rates corresponding to a uniform and parabolic crevice pressure distributions are plotted in Figs. 10-33a-b, respectively. The cumulative leakage vs. time plot for both crevice pressure profiles are shown in Fig. 10-33. Comparison of Figs 10-30a-b with Figs. 10-32a-b shows that the leak rates are increased by about a factor of 10 when the roughness is increased from 2 to

5 μm . A comparison of Fig. 10-31 with Fig. 10-33 shows that the cumulative leakage is also increased by a similar factor.10-33

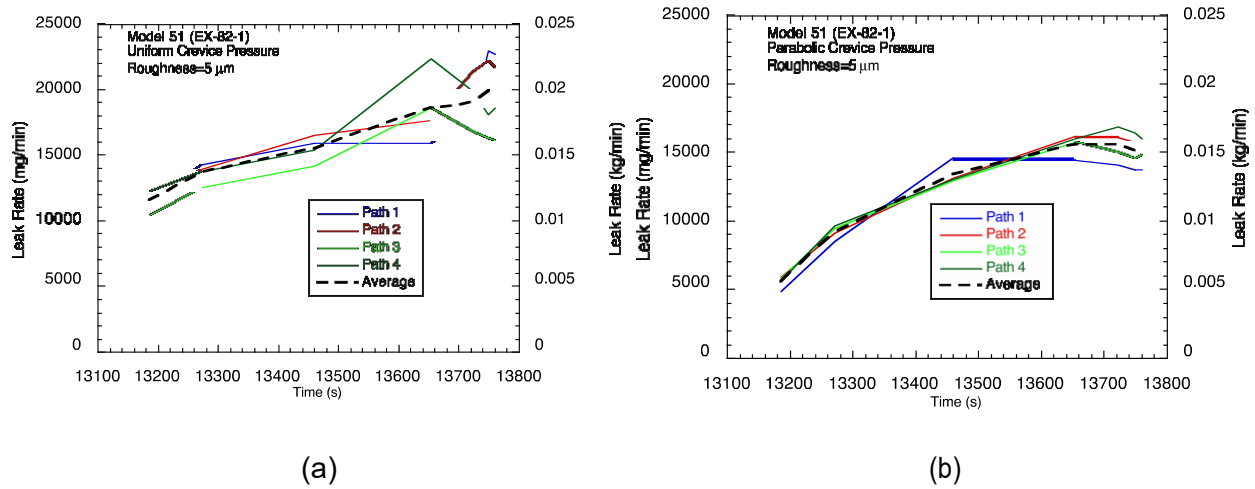


Figure 10-32 Calculated Leak Rate (using roughness=5 μm) vs. Time for Model 51 SG with (a) Uniform Crevice Pressure Distribution and (b) Parabolic Crevice Pressure Distribution Along Four Axial Paths

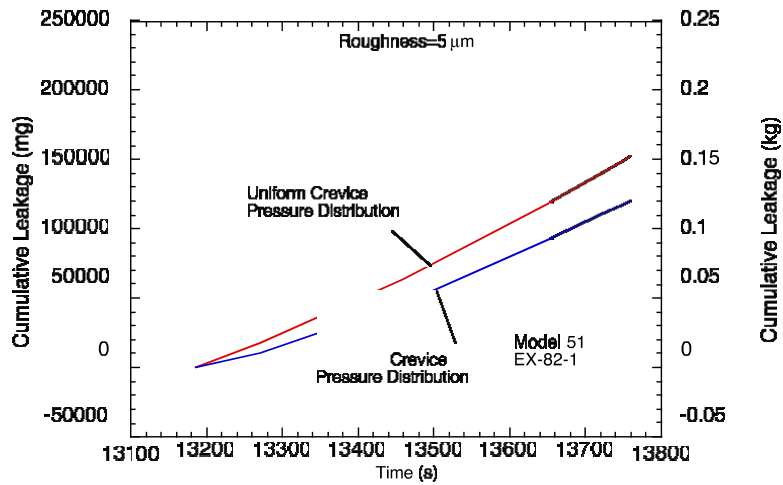


Figure 10-33 Calculated Cumulative Leakage (roughness=5 μm) vs. Time for a Model 51 SG for Two Types of Crevice Pressure Distribution

10.4 Tube Rupture/Pullout During Severe Accidents

An alternative path for getting large leakages from the tube-to-tubesheet junctions during severe accidents is to have tube pullouts occurring prior to tube rupture in the free span region. Tube pullout is a realistic possibility because SGs are allowed to operate with severed tubes under the tubesheet as long as they are demonstrated not to experience tube pullout during NO and MSLB transients. To explore the possibility of tube pullouts before tube rupture in the free span, the following two sets of analyses were conducted to calculate and compare the results:

- Calculate the time to ligament rupture of a tube with a PTW crack in the free span region
- Calculate the time to cause tube pullout from the tubesheet

10.4.1 Free Span SG Tube Rupture

The times to creep rupture of 22.2 mm (0.875 in.) diameter Alloy 600 SG tubes were calculated using the procedure outlined in Ref. 12. To account for the variability of material properties, three PTW crack lengths were selected with depths such that a range of $3\Delta p_{NO}$ (or $1.4 \Delta p_{MSLB}$) criterion for ligament rupture was satisfied. The corresponding range of ligament stress magnification factor m_p was selected for the severe accident calculations (Fig. 10-34). As a reminder, the time to creep rupture is controlled by m_p , which combines the damaging influence of both the crack length and crack depth into a single factor for stress magnification. The pressure differential and average tube wall temperature history of an average tube and the hottest tube are plotted in Fig. 10-35.

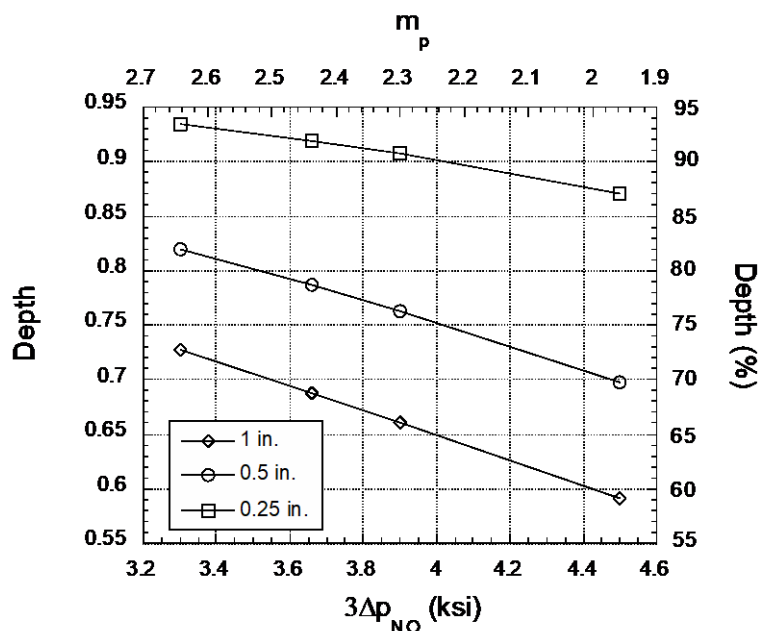


Figure 10-34 Variation of Crack Depth and m_p with $3\Delta p_{NO}$ for Three Different Crack Lengths (1ksi=6.895 MPa)

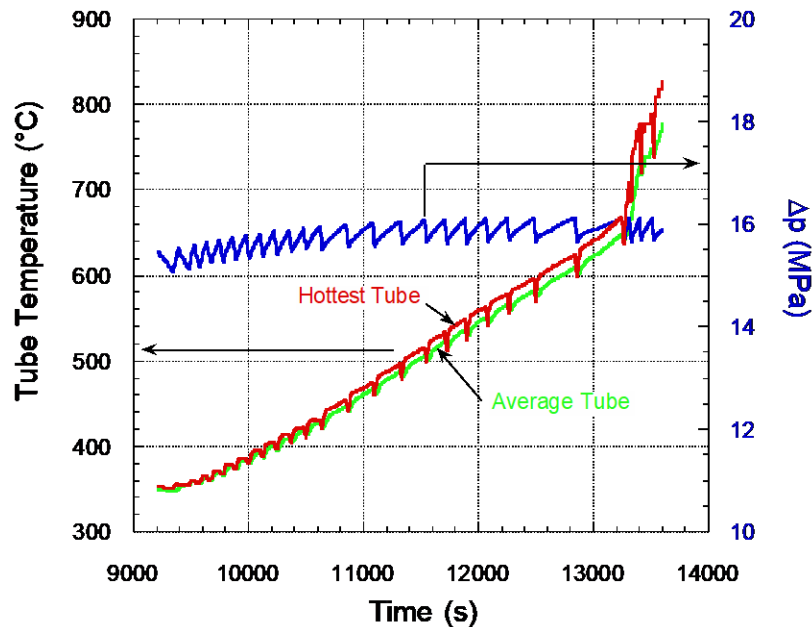


Figure 10-35 Variations of Pressure Differential Δp and Average Tube Wall Temperatures of an Average and the Hottest Tube with Time during the Severe Accident

The mean value together with confidence bounds of the time to rupture of the hottest tube is plotted against m_p in Fig. 10-36a. A similar plot for the average tube is given in Fig. 10-36b. Note that the mean value of time to rupture of the hottest tube decreases from 13,450 s for a virgin tube (i.e., $m_p=1$) to 12,900 s for a crack with $m_p=2.7$. The corresponding times for an average tube are 14,400 and 13,500 s, respectively. Due to the nature of the scatter in the creep rupture data, the spread in the predicted rupture times for the hottest tube increases with increasing m_p , whereas the same for the average tube decreases with increasing m_p .

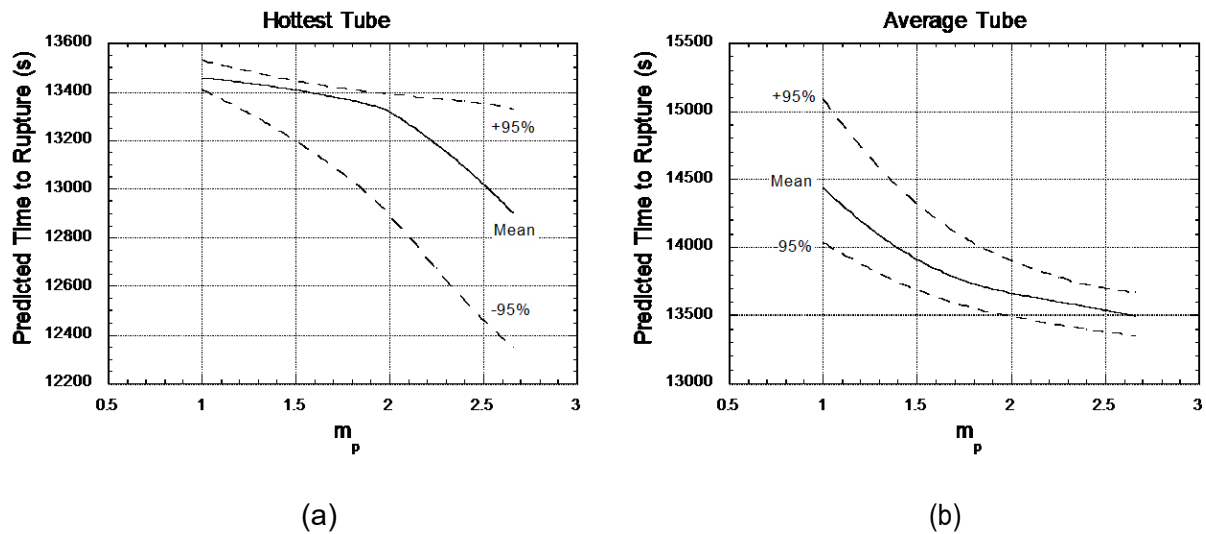


Figure 10-36 Mean and $\pm 95\%$ Confidence Bonds Values of Time to Rupture vs Stress Magnification Factor for (a) the Hottest and (b) Average Tubes Containing Cracks in the Free Span Region

10.4.2 Tube Pullout

Tube pullout is promoted by the end cap pressure loading on the tube. The pullout force is resisted by the frictional forces acting at the tube-to-tubesheet interface. The frictional force depends on the contact pressure, contact length and the friction factor μ . The contact pressure distribution in turn depends on whether the crevice at the tube-to-tubesheet interface is or is not pressurized. For the current work, $\mu = 0.2$ and a contact length equal to $H^* = 0.45$ m (17.75 in.) were used.** The contact pressures corresponding to unpressurized and pressurized crevice with parabolic pressure distribution were obtained from Figs. 10-18a and 10-31a, respectively, which were calculated for the hottest tube only. For frictional force calculations, the average contact pressures along the four paths presented in these figures were integrated. The variations of the tube pullout force due to end cap pressure loading and friction forces corresponding to zero and parabolic crevice pressure distribution with time are plotted in Fig. 10-37. Note that the tube pullout force remains less than the resisting friction force at all time if the crevice is unpressurized. When the crevice is pressurized, the pullout load exceeds the resisting frictional force at times $t \geq 13,700$ seconds. From a comparison of Fig. 10-37 with Fig. 10-36a it can be seen that any hot tube containing PTW cracks within the range of m_p of interest in the free span region will rupture prior to pullout. However, the same is true for the average tube only if it is assumed that the contact pressures calculated for the hottest tube are also applicable to the average tube (Fig. 10-36b), and also only if the mean value of m_p is > 2 , which occurs for 6 mm (0.25 in.) long cracks $> 87\%$ deep, or for 13 mm (0.5 in.) long cracks $> 70\%$ deep, or for 25 mm (1 in.) long cracks $> 60\%$ deep (Fig. 10-34).

** Emmett Murphy, NRC, Personal Communication to S. Majumdar, July 1, 2011.

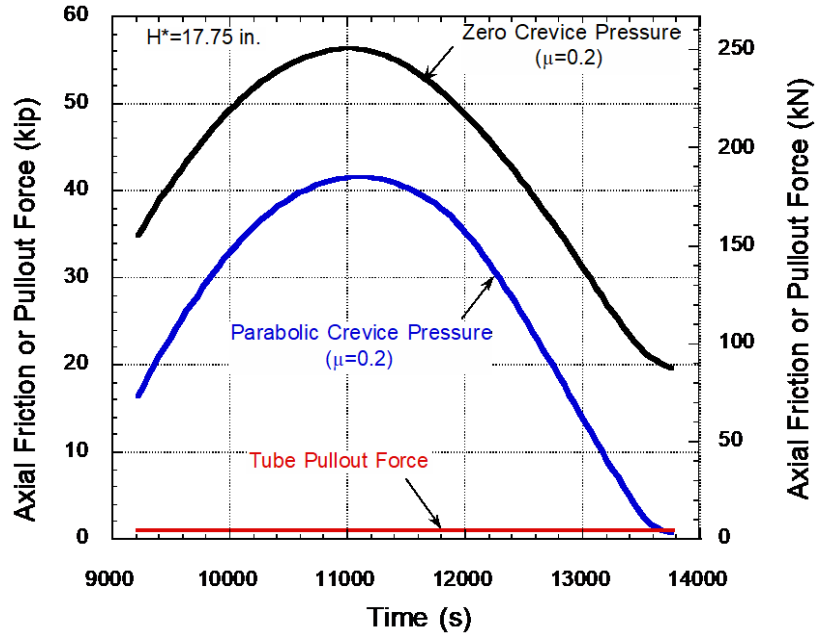


Figure 10-37 Variation of Pullout Force and Frictional Resistant Force with Time (The frictional forces are computed from contact pressures predicted by FEA with zero and a parabolic distribution of crevice pressure)

11 CONCLUSIONS

Under station blackout severe accident conditions, the SG tube-to-tubesheet junction may provide a leakage path due to creep and depressurization of the crevice. This work summarizes possible scenarios and leakage rates using a combined experimental-analytical approach performed by both ANL and the NRC. Pursuant to Title 10 of the *Code of Federal Regulations*, Appendix A to Part 50, the General Design Criteria, Criteria 14, 15, 30, 31, and 32, licensees are required to ensure the integrity of the reactor coolant system boundary, which includes the tubesheet and SG tubing. The work described in this report summarizes potential challenges to RCS integrity through a potential leakage pathway.

Tube-to-collar test specimens were designed to simulate the contact pressures generated in a real SG tube-to-tubesheet junction due to hydraulic expansion and thermal expansion mismatch between the tube and the tubesheet. However, the specimens were not designed to simulate the more complex behavior of a real SG tube-to-tubesheet junction, such as, tubesheet bowing, tube hole ovalization, etc. Twelve tube-to-collar joint specimens were fabricated by B&W, Canada and ANL conducted pressure and leak rate tests on them at high temperatures representative of thermal transients during severe accidents. The tubes and the leakage paths (crevices) in the specimens were independently pressurized. The tests showed a steady decrease of leak rate with increasing temperature from room temperature and reduced to almost zero at $\geq 500^{\circ}\text{C}$. In tests where the crevice pressure was held constant and the temperature of the specimen ramped, the leak rate resumed at temperatures between $670\text{--}690^{\circ}\text{C}$ and increased at an increasing rate with temperature to high values ($>5000\text{ mg/min}$) until the test was stopped. However, if the crevice was mostly depressurized and a crevice pressure applied only intermittently to measure the leak rates, no such large leakage was observed. Thus, it was concluded that large leakage is not possible unless the crevice is pressurized for a sufficiently long time to relax the contact pressure and open a gap at the tube-to-collar interface by deforming the collar by creep.

Specimens with 19 mm (0.75 in.) diameter tubes behaved essentially the same way as 22 mm (0.875 in.) diameter tubes. Also, specimens with three different heats of Alloy 600 tubes behaved essentially the same way. The onset of large leakage during the temperature ramp increased slightly with increasing leakage path length.

A test, in which the crevice pressure inlet was sealed off and a 0.8 mm (0.03125 in.) hole was drilled in the tube wall, behaved essentially the same way as specimens whose tubes and crevices were pressurized independently. It is thus very likely that crevices in tubes containing throughwall cracks within the tubesheet of a real SG will also be pressurized.

A 2-D axisymmetric finite element model and a simplified 1-dimensional model of the specimen were developed and used to calculate the variation of contact pressure and gap at the tube-to-collar interface with time. The analyses included stresses due to hydraulic expansion, thermal stresses due to mismatch in thermal expansion coefficients between the tube and the collar and stresses induced by tube and crevice pressures. The high temperature mechanical properties needed for analysis were obtained from literature as well as a limited number of tensile and creep tests conducted on three heats of Alloy 600 tubes and a single heat of A508 steel. Thermal expansion coefficient data for a single heat of Alloy 600 and A 508 steel were obtained as functions of temperature up to 700°C . Both models were successful in predicting the temperature at which there was a complete loss of contact pressure leading to onset of large leakage.

A 1-D leak rate model was developed based on incompressible plane Couette-Poiseuille flow applied to the case of the interface between two plane rough surfaces in contact. The leak rates of most of the tests could be predicted to within a factor of 2-3 by appropriate choices of three adjustable parameters of the model. All three parameters were determined from the initial leak rate tests at room temperature before the high temperature tests were performed.

A finite element model of a Westinghouse Model 51 tube-to-tubesheet joint was developed. The model included a single SG tube (hot tube) embedded inside the tubesheet (with a solid rim), the divider plate, the lower head and a short segment of the SG shell. The inhomogeneous tubesheet with tube holes was replaced by a homogeneous tubesheet with equivalent anisotropic properties. The anisotropic properties were determined from FEA of the tubesheet unit cell. The heat transfer from the tube to the tubesheet for the single tube was analyzed in details, while the heat flow from the rest of the tubes to the tubesheet was approximated by volumetric heat fluxes. The heat transfer data for the hot tube was obtained from a CFD analysis performed by NRC/RES, and those for the rest of the components were obtained from RELAP 5 model. First, a thermal conduction analysis was conducted with FEM. The temperature data from the thermal conduction analysis were input into a elastic-plastic-creep structural FEM that included the tube pressure, crevice pressure and the primary pressure acting on the lower surface of the tubesheet. The analysis provided the contact pressure and interfacial gap variation along the length of the tube as functions of time.

The stress analysis result showed a significant variation of contact pressure and gap in the tube circumferential direction, suggesting that circumferential flow would occur. However, since our leak rate model is based on axisymmetric geometry and ignores any circumferential flow, leak rates were calculated for four axial paths located 90° apart in the circumferential direction of the tube for a throughwall circumferential crack located at the mid thickness level of the tubesheet. There was significant variation in the leak rates calculated for the four paths. The results showed that the predicted path-averaged leak rate remains low ($<10^{-3}$ kg/min) until 13,460 s (-95% confidence limit rupture time for the hottest tubes is 13740s). For a surface roughness of 2 μm , by 13460 s, the leakage rate from a tube within the tubesheet is predicted to be between 9×10^{-4} and 1.1×10^{-3} kg/min and the cumulative leakage is predicted to be between 2.9×10^{-3} and 4.4×10^{-3} kg per tube. By 13760s, the leak rate is predicted to be between 1×10^{-3} and 3×10^{-3} kg/min and the cumulative leakage is predicted to be between 8×10^{-3} and 12×10^{-3} kg per tube. The leakage numbers should be multiplied by approximately a factor of 10 if the surface roughness is increased to 5 μm . In the absence of tests with realistic interface and boundary conditions, the present results should be considered as best estimates to approximate potential field conditions. However, these leakages, even if multiplied by a factor of 5000, are too small to cause a change in the progress of the severe accident transient or to depressurize the primary side significantly.

A tube pullout analysis showed that the end cap pressure loading acting on the hottest tube is insufficient to overcome the fictional resistant force (using $H^*=0.45$ m [17.75 in.]) and cause a pullout before a free span crack of interest will rupture during the severe accident.

12 REFERENCES

1. NUREG-1570, Risk Assessment of Severe Accident-Induced Steam Generator Tube Rupture, U.S. Nuclear Regulatory Commission, March 1998.
2. C. D. Fletcher, R. W. Shumway and D. L. Barber, Revised SCDAP/RELAP5 Base Case Calculation for Zion TMLB Station Blackout Event, ISL-NSAD-TR-03-18, Information Systems Laboratories, Inc., Idaho Falls, ID, October 2003.
3. C.D. Fletcher and R.M. Beaton, Evaluation of Uncertainties in SCDAP/RELAP5 Station Blackout Simulations, ISL-NSAD-TR-06-04, Information Systems Laboratories, Inc., Idaho Falls, ID, May 2006.
4. J. L. Rempe et al., Light Water Reactor Lower Head Failure Analysis, NUREG/CR-5642, Idaho National Engineering Laboratory, October 1993.
5. H. F. P. Purday, An Introduction to the Mechanics of Viscous Flow, Dover, p. 173, 1949.
6. W. F. Hughes and J. F. Osterle, On the Adiabatic Couette Flow of a Compressible Fluid, Zeitschrift für Angewandte Mathematik und Physik (ZAMP), v 8, pp 89–96, 1957.
7. J. A. Greenwood, and J. B. P. Williamson, Contact of Nominally Flat Surfaces, Proc. R. Soc. London, Ser. A, A295, pp. 300–319, 1966,
8. N. Patir and H. S. Cheng, An Average Flow Model for Determining Effects of Three-Dimensional Surface Roughness on Partial Hydrodynamic Lubrication, Journal of Lubrication Technology, v 100, pp. 12–17, 1978.
9. WCAP-15932-P, Improved Justification of Partial-Length RPC Inspection of Tube Joints of Model F Steam Generators of Ameren-UE Callaway Plant, public version of the affidavit and topical report are available on ADAMS system, ML031980099 and ML032320341.
10. Westinghouse Presentations, Waltz Mills, November 19, 2008.
11. V. I. Lachkov, A. I. Lysenkov and Yu. V. Mamonov, Expressions for Thermophysical Properties of Superheated Steam, Measurement Techniques, Vol. 42, No. 1, pp. 58-60, 1999.
12. S. Majumdar, W. J. Shack, D. R. Diercks, K. Mruk, and J. Franklin, Failure Behavior of Internally Pressurized Flawed and Unflawed Steam Generator Tubing at High Temperatures – Experiments and Comparison with Model Predictions, NUREG/CR-6575, Argonne National Laboratory, March, 1998.

BIBLIOGRAPHIC DATA SHEET

(See instructions on the reverse)

1. REPORT NUMBER
(Assigned by NRC, Add Vol., Supp., Rev.,
and Addendum Numbers, if any.)
NUREG/CR-7210

2. TITLE AND SUBTITLE

**Development and Validation of Models for Predicting Leakage from Degraded
Tube-to- Tubesheet Joints During Severe Accidents**

3. DATE REPORT PUBLISHED

MONTH

YEAR

July

2020

4. FIN OR GRANT NUMBER

Y6582

5. AUTHOR(S)

Saurin Majumdar, Kenneth Kasza, Chi Bum Bahn, William J. Shack

6. TYPE OF REPORT

Technical

7. PERIOD COVERED (Inclusive Dates)

8. PERFORMING ORGANIZATION - NAME AND ADDRESS (If NRC, provide Division, Office or Region, U. S. Nuclear Regulatory Commission, and mailing address; if contractor, provide name and mailing address.)

Argonne National Laboratory
Argonne, IL 60439

9. SPONSORING ORGANIZATION - NAME AND ADDRESS (If NRC, type "Same as above", if contractor, provide NRC Division, Office or Region, U. S. Nuclear Regulatory Commission, and mailing address.)

Division of Engineering
Office of Nuclear Regulatory Research
U.S. Nuclear Regulatory Commission
Washington, DC 20555

10. SUPPLEMENTARY NOTES

11. ABSTRACT (200 words or less)

This report documents the development and validation of analytical models to predict steam generator (SG) tube leakage that can be expected from cracks within the tube-to-tubesheet junction at high temperature. Pressure and leak rate tests were conducted at high temperatures on 12 tube-to-collar junction specimens with independent pressurization of the tube and the leakage path (crevice). A finite element model of the specimen was used to calculate the variation of contact pressure and tube-to-tubesheet gap over time. A leak rate model was developed based on plane Couette-Poiseuille flow along the interface between two rough contacting surfaces. The model parameters were determined from the leak rate tests.

A finite element model was developed for a Westinghouse Model 51 SG tube-to-tubesheet interface, including the divider plate, lower head and a short segment of the SG shell. The model was used to analyze first, the spatial variation of the temperature with time, and second, the variations of contact pressure and gap along the tube-to-tubesheet interface as functions of time during the postulated station blackout severe accident. The leak rate model was used to predict the leak rates during the severe accident. Results in this report indicate that leakage could occur through the tube-to-tubesheet joints in station blackout accident conditions, and there are significant variations in the leak rates calculated for different paths. In addition, results show that the leak rate remains low for three hours, after which the rate is predicted to increase. In the absence of tests with realistic interface and boundary conditions, the present results should be considered as best estimates

12. KEY WORDS/DESCRIPTORS (List words or phrases that will assist researchers in locating the report.)

PWR
steam generator (SG)
steam generator tube
steam generator inspection
finite element modeling
severe accidents

13. AVAILABILITY STATEMENT

unlimited

14. SECURITY CLASSIFICATION

(This Page)

unclassified

(This Report)

unclassified

15. NUMBER OF PAGES

16. PRICE



Federal Recycling Program



UNITED STATES
NUCLEAR REGULATORY COMMISSION
WASHINGTON, DC 20555-0001
OFFICIAL BUSINESS



©NRCgov

NUREG/CR-7210

**Development and Validation of Models for Predicting Leakage from
Degraded Tube-to-Tubesheet Joints During Severe Accidents**

July 2020